POWER OPTIMISATION CONTROL OF A GUIDE-VANES INTEGRATED EXHAUST AIR TURBINE GENERATOR BASED ON VIENNA RECTIFIER

YIP SOOK YEE

INSTITUTE OF GRADUATE STUDIES
UNIVERSITY OF MALAYA
KUALA LUMPUR

2018

University of Malaya

POWER OPTIMISATION CONTROL OF A GUIDE-VANES INTEGRATED EXHAUST AIR TURBINE GENERATOR BASED ON VIENNA RECTIFIER

YIP SOOK YEE

THESIS SUBMITTED IN FULFILMENT OF THE REQUIREMENTS FOR THE DEGREE OF DOCTOR OF PHILOSOPHY

INSTITUTE OF GRADUATE STUDIES
UNIVERSITY OF MALAYA
KUALA LUMPUR

2018

University of Malaya

UNIVERSITY OF MALAYA

ORIGINAL LITERARY WORK DECLARATION

Name of Candidate: Yip Sook Yee

Matric No: HHD120002

Name of Degree: Doctor of Philosophy (Ph.D)

Title of Project Paper/Research Report/Dissertation/Thesis ("this Work"):

Power optimisation control of a guide-vanes integrated exhaust air turbine generator based on Vienna rectifier

Field of Study: Power system protection (*electronics and automation*)

I do solemnly and sincerely declare that:

(1) I am the sole author/writer of this Work;
(2) This Work is original;
(3) Any use of any work in which copyright exists was done by way of fair dealing and for permitted purposes and any excerpt or extract from, or reference to or reproduction of any copyright work has been disclosed expressly and sufficiently and the title of the Work and its authorship have been acknowledged in this Work;
(4) I do not have any actual knowledge nor do I ought reasonably to know that the making of this work constitutes an infringement of any copyright work;
(5) I hereby assign all and every rights in the copyright to this Work to the University of Malaya ("UM"), who henceforth shall be owner of the copyright in this Work and that any reproduction or use in any form or by any means whatsoever is prohibited without the written consent of UM having been first had and obtained;
(6) I am fully aware that if in the course of making this Work I have infringed any copyright whether intentionally or otherwise, I may be subject to legal action or any other action as may be determined by UM.

Candidate's Signature Date:

Subscribed and solemnly declared before,

Witness's Signature Date:

Name:

Designation:

University of Malaya

POWER OPTIMISATION CONTROL OF A GUIDE-VANES INTEGRATED EXHAUST AIR TURBINE GENERATOR BASED ON VIENNA RECTIFIER

ABSTRACT

Exhaust air recovery system is a concept recently introduced to generate electrical power from cooling towers. It is an onsite energy generating system that consists of a vertical axis wind turbine (VAWT) connected to a permanent magnet synchronous generator (PMSG) and its power electronics converter. This system was designed to be retrofitted above exhaust air outlets of cooling towers to harness the discharged wind. While preliminary studies confirmed the feasibility of the concept, power optimization of the exhaust air recovery system is yet to be attempted. In this project, power optimization of the wind energy generated from the exhaust air recovery system was investigated based on both mechanical and electrical approaches.

In this work, mechanical improvement was made by mounting guide-vanes between the exhaust air outlet and VAWT, with the purpose of augmenting wind power generation. Guide-vanes also help to divide the wind into several channels of airflow, whereby if they set at the correct angle, it would result in the induced wind being more uniform and better directed towards the optimized angle of attack of the wind turbine. By analyzing the discharge air profile of the exhaust air outlet, the optimized positions and angles of the guide-vanes were obtained. Experimental results based on a lab-scale turbine and the guide-vane system were validated with double multiple stream tube theory (DMST).

On the electrical side, power optimization was made possible via efficient control of the PMSG and its power electronics converter. The Vienna rectifier was proposed to be used as the power electronics converter as a trade-off between cost and performance. Firstly, direct torque control (DTC) based on Vienna rectifier was investigated. An improved look-up table (LUT) was proposed to improve the overall control accuracy of the existing DTC in order to reduce the generated torque and stator flux ripples. The

University of Malaya

improvement was performed by increasing the comparing conditions of the torque comparator with more accurate selection of switching vectors. Meanwhile, computation delay compensation was also considered for digital implementation of the DTC.

One drawback of the LUT-DTC is that the switching vector selection is done on an off-line basis, which is not optimized for all operating conditions. To further improve the effectiveness of the control method, a finite-set model predictive direct torque controller (MPDTC) was developed. To mitigate the well-known high computation burden problem of the MPC, a LUT was proposed to reduce the number of candidate switching vectors based on DC-link voltage errors. Simulation and experimental results confirmed the effectiveness of the proposed hybrid LUT-MPDTC method in regulating the torque and flux of the machine while maintaining a balanced DC-link.

A maximum power point tracker was used on top of the developed MPDTC strategy to optimize the power extracted from the wind turbine. A lab-scale wind turbine emulator was developed using an induction motor that was controlled using field-oriented control. Electrical tests were conducted with the developed turbine emulator to verify the performance of the overall power optimization mechanism using the electrical approaches.

Keywords: Power optimization, guide-vane, wind turbine generator, model predictive direct torque control, Vienna rectifier.

University of Malaya

KAWALAN PENGOPTIMUMAN KUASA UNTUK TURBIN ANGIN EKZOS YANG BERINTEGRASI DENGAN SUDUT BILAH PANDUAN ANGIN MELALUI PENERUS VIENNA

ABSTRAK

Sistem pemulihan angin ekzos ialah konsep yang diperkenalkan untuk menjana kuasa eletrik daripada menara penyejuk. Ia adalah satu sistem yang terdiri daripada turbin angin yang berpaksi tegak (VAWT) dan disambung dengan penjana jenis magnet kekal (PMSG) dan penukar kuasa elektronik. Sistem ini dicadangkan untuk dipasang di atas menara penyejuk untuk mengekstrakkan sumber angin yang berciri angin yang lebih baik berbanding dengan angin semula jadi. Walaupun kajian awal telah mengesahkan konsep tersebut, pengoptimuman kuasa sistem pemulihan ekzos angin masih belum dilaksanakan. Oleh itu, pengoptimuman kuasa yang dijana daripada sistem pemulihan angin ekzos akan dikaji dalam projek ini dari segi mekanikal dan elektrikal.

Pengoptimuman kuasa dari segi mekanikal adalah dikemukakan dengan memasangkan sudut bilah panduan arah di antara saluran ekzos angin dengan VAWT dengan tujuan mengawal arah angin ekzos. Di samping itu, sudut bilah pandu arah akan membahagikan angin kepada beberapa saluran aliran angin yang lebih seragam. Apabila sudut bilah panduan arah dilaraskan kepada kedudukan dan sudut yang optimum, angin akan diarahkan kepada sudut kritikal penjana turbin angin ekzos dan menghasilkan daya yang lebih tinggi. Dengan menganalisa profil penglepasan angin dari saluran angin ekzos, padanan optima posisi dan sudut bilah panduan arah dengan VAWT diperolehi. Keputusan eksperimen berdasarkan turbin skala makmal dan sistem panduan udara digunakan untuk mengesahkan penemuan teori.

Dari segi elektrikal, pengoptimuman kuasa dijalankan melalui kawalan di atas PMSG dan penukar elektronik kuasa. Dengan mengambil kira keseimbangan antara kos dan pretasi, penerus Vienna dicadangkan sebagai kuasa penukar elektronik. Kajian kawalan

University of Malaya

histerisis tork secara langsung (hysteresis DTC) dengan menggunakan penerus Vienna dijalankan sebagai langkah pertama. Jadual “lookup” yang lebih baik untuk kaedah histerisis kawalan tork secara langsung dikemukakan untuk meningkatkan ketepatan kawalan keseluruhan DTC yang sedia ada dengan mengurangkan penjanaan tork dan fluks riak. Penambahbaikan pretasi kawalan ini diperolehi dengan meningkatkan tahap histerisis untuk tork (torque comparator). Selain itu, faktor-faktor yang boleh menjejaskan operasi DTC telah diambil kira untuk memilih vektor voltan yang tepat untuk pembinaan jadual. Di samping itu, pampasan untuk kelambatan pengiraan juga diambil kira untuk pelaksanaan digital histerisis tork secara langsung dengan memaklum-balas perubahan tork dan flux yang disebabkan oleh vector voltan yang dipilih ke sampel seterusnya.

Salah satu kelemahan DTC dengan penggunaan jadual “lookup” adalah jadual yang dibina tidak optima untuk semua keadaan operasi penjana turbin. Ini disebabkan oleh pembinaan jadual dilaksanakan secara *off-line*. Untuk peningkatan yang ketara untuk kuasa kawalan, kawalan tork secara langsung dengan model penganggaran (MPDTC) telah diusulkan. Satu jadual berdasarkan ralat voltan DC juga dicipta agar mengurangkan calon vektor voltan yang digunakan untuk model penganggaran. Oleh itu, masalah beban pengiraan akibat daripada MPDTC dapat dikurangkan. Simulasi dan eksperimen telah dijalankan untuk mengesahkan kesan kawalan tork dan fluks mesin di samping mengekalkan keseimbangan voltan DC dengan pengunnaan kaedah hibrid kawalan tersebut. Pengesan titik kuasa maksimum digunakan bersama dengan strategi MPDTC untuk mengoptimumkan kuasa yang dijanakan daripada turbin angin. Sebuah emulator turbin angin skala makmal yang berciri-ciri turbin angin telah dibina dengan menggunakan motor aruhan. Ujian makmal telah dijalankan dengan emulator turbin untuk mengesahkan prestasi pengoptimuman kuasa keseluruhan dari segi elektrikal.

Kata Kunci: Pengoptimuman kuasa, sudut bilah panduan angin, turbin angin penjana electrik, kawalan tork langsung, kawalan penerus Vienna.

University of Malaya

ACKNOWLEDGEMENTS

I would like to express my greatest gratitude to my supervisors, late Prof. Ir. Dr. Hew Wooi Ping, Prof. Dr. Chong Wen Tong and Dr. Tan Chee Pin for their continuous guidance and advice, which have motivated me throughout the research project duration.

I would also like to thank the Malaysian Ministry of Education Malaysia and University of Malaya for providing financial support through MyPhD scholarship, High Impact Research Grant and PPP research grant, without which will not be possible for me to complete this project

Besides, I would like to seize this opportunity to thank all the staffs in UMPEDAC, especially Dr. Che Hang Seng and my colleagues who have given me encouragement and endless hour of discussion whilst conducting this research. Last but not least, my sincere gratitude goes to my family who had always never failed to support me until the completion of this thesis.

University of Malaya

TABLE OF CONTENTS

University of Malaya

University of Malaya

University of Malaya

University of Malaya

University of Malaya

LIST OF FIGURES

University of Malaya

University of Malaya

University of Malaya

University of Malaya

LIST OF TABLES

University of Malaya

University of Malaya

LIST OF SYMBOLS AND ABBREVIATIONS

Symbols:

V_{rated}	:	Rated wind speed
$V_{cut\text{-}in}$	:	Cut-in wind speed
$V_{cut\text{-}out}$	:	Cut-out wind speed
w	:	Width of deflector
h	:	Height of deflector
l	:	Distance from deflector to VAWT
λ	:	Tip speed ratio
R	:	Radius of wind turbine
ω	:	Turbine rotational speed
V	:	Free stream wind speed
C_p	:	Power coefficient
β	:	Pitch angle
P	:	Wind turbine mechanical power
ρ	:	Air density
A	:	Swept area of wind turbine
h	:	Height of wind turbine blade
ωR	:	Tip speed
V_R	:	Relative velocity
V_a	:	Induced velocity
θ	:	Blade's azimuth angle
a	:	Induction factor
α	:	Angle of attack
C_l	:	Lift coefficient
C_d	:	Drag coefficient

University of Malaya

C_t : Tangential force coefficient

C_n : Normal force coefficient

F_t : Tangential force

F_{ti} : Instantaneous tangential force

F_{ni} : Instantaneous normal force

τ_i : Instantaneous torque

τ : Torque

c : Chord length

N : Number of turbine blade

θ_{GV} : Guide-vane angle

ϕ : Induced wind flow angle

V_{a_down} : Induced wind at downwind side of turbine

q : Quarter number

$\theta_{\omega R}$: Tip speed angle

Q : Volume flow rate

V_{outlet} : Average discharged wind speed

A_{outlet} : Discharge air outlet area

L_s : Stator inductances

ω_s : Stator rotational speed

ω_r : Rotor rotational speed

φ_s : Stator flux

φ_r : Rotor flux

R_s : Stator resistance

δ : Load angle

θ_s : Stator angle

θ_r : Rotor angle

University of Malaya

T_e	:	Electromagnetic torque
p	:	Pole pairs
V_{DC}	:	DC-link voltage
i	:	Phase index
S_i	:	Switching signal
n	:	Binary representative index of the switching signals
γ	:	Phase angle
Δ_{sec}	;	Change sector between stator current and stator flux
$\Delta\delta$	:	Change of load angle
r	:	Radius of voltage vector from origin
k	:	Sector index
ΔT	:	Time interval
V_p	:	Upper capacitor voltage
V_n	:	Lower capacitor voltage
V_{pn}	:	DC-link voltage error
h	:	Error band
$\underline{\Delta}V_{pn}$	:	Change in DC-link voltage
φ_s'	:	Estimated stator flux with delay compensation
T_e'	:	Estimated torque with delay compensation
C_1	:	Upper capacitance
C_2	:	Lower capacitance
N	:	Number of samples
x_i	:	Instant value of variable
$\bar{x}$	:	Mean of collected samples
CF	:	Cost function
T_s	:	Sampling time

University of Malaya

k	:	Weighing factor
n_{max}^{*}	:	Optimal switching vector
C	:	Change of rotor speed
$\underline{\Delta}\omega_r$	:	Step-size of rotor speed

Abbreviations:

PMSG	:	Permanent magnet synchronous generator
WECS	:	Wind energy conversion system
WRSG	:	Wound rotor synchronous generator
VAWT	:	Vertical axis wind turbine
HAWT	:	Horizontal axis wind turbine
MSC	:	Machine side converter
GSI	:	Grid side inverter
PWM	:	Pulse-width modulation
CB-PWM	:	Carrier based pulse-width modulation
SVM	:	Space vector modulation
FOC	:	Field oriented control
MPPT	:	Maximum power point tracker
MPP	:	Maximum power point
OT	:	Optimum torque
PSF	:	Power signal feedback
VOC	:	Voltage oriented control
DPC	:	Direct power control
CFD	:	Computational fluid dynamic
ODGV	:	Omni-directional-guide-vane
ANN	:	Artificial neural network

University of Malaya

MPTA	:	Maximum power torque per ampere
PCC	:	Predictive current control
PTC	:	Predictive torque control
FS-MPC	:	Finite set model predictive control
DTC	:	Direct torque control
MPDTC	:	Model predictive direct torque control
MPC	:	Model predictive control
LUT	:	Lookup table
TSR	:	Tip Speed Ratio
THD	:	Total harmonic distortion
DMST	:	Double multiple stream tube theory
AOA	:	Angle of attack
VFD	:	Variable frequency driver
MH	:	Martin Hepperle
PI	:	Proportional Integrator
IM	:	Induction motor
P&O	:	Perturbed-and-observed

University of Malaya

LIST OF APPENDICES

University of Malaya

CHAPTER 1: INTRODUCTION

1.1 Overview

With the rapid growth of the global human population, the demand for safe, secure and affordable energy supply continues to increase for modern civilization and industrial development. In Malaysia, total energy demand had grown by 4% in the year 2016 as compared to 2.2% for the year 2015 along with 1.5% average annual population growth rate (Department of Statistical Malaysia, 2016; Suruhanjaya Tenaga, 2017). At this rate, Malaysia may turn out to be a net energy importer by the year of 2020 with the energy demand about 971 TWh along with 33.4 million of populations. (Ali, Daut, & Taib, 2012).

Fossil fuels serve as the dominant source of the existing energy resources for electricity generation. It represents 94.5% of the total electricity capacity in Malaysia whilst the rest is generated from solar, hydroelectricity or others (biogas and etc.) (Shafie, Mahlia, Masjuki, & Andriyana, 2011). Nevertheless, the consumption of fossil fuels can result in undesirable effects to the environment for example, greenhouse gases emission. There was a study revealed that over 90% of the global energy-related greenhouse gasses emission is due to the by-product of fuel combustion (i.e. carbon dioxide) (Ahmad, Kadir, & Shafie, 2011). Currently, global warming is already at an alarming rate and it will continue to intensify due to the growing concentration of greenhouse gases emission. The extensive melting of ice at the polar caps due to the considerable increase of temperature in the earth's atmosphere exacerbates the rising of sea level and coastal flooding, along with the climate change. The consequences of climate change had already been seen in Malaysia. Recently, a devastating flood hit in Kedah and Penang with an abnormal downpour, averaged more than 250 mm within a day causing loss of lives and properties ("After deadly flood", 2017).

University of Malaya

In addition to that, it is anticipated that the cost of electricity generation using fossil fuels will only continue to increase in the future, given the limited supply of fossil fuel sources. For instances, the general commercial tariff of electricity in Peninsular Malaysia under the category of medium voltage is currently fixed at 36.5 sen/kWh (RM) (Tenaga Nasional [TN], 2017) but is projected to rise by 10% per annum (Chong, Naghavi, Poh, Mahlia, & Pan, 2011).

In order to ensure the sustainability and cost effectiveness of energy supply, while fulfilling the overwhelming increase of energy demand in parallel with the rapid growth in a country, a paradigm shift is necessary by incorporating renewable energy systems for electricity generation. This is also aligned with one of the goals of the eleventh Malaysia plan (2016-2020) in which renewable energy generation is targeted to be 11% of the electricity generation by 2020 (renewable energy capacity is projected to be reached 2,080 MW) (TN, 2017).

1.2 Problem Statements

Among the popular renewable energy sources, wind energy has been placed in the limelight and it is the most rapid growing of renewable energy (Schiffer, 2016). Harnessing wind energy provides the means to reduce the dependency on fossil fuels. Installation of wind turbine in the urban environment seemed to have picked up its pace due to the incorporation of wind turbine into the building eliminates the need for supporting tower to raise the wind turbines to a reasonable height, where the wind speed is higher. On-site renewable energy generation is useful for sustainable electrical power generation leading to the abatement of carbon dioxide emission as well as the reduction in consumer's electricity cost (Bahaj, Myers, & James, 2007). The electrical power generated can directly supply to the building and hence, lower power loss due to the long distance of grid line power transmission can be omitted. Nevertheless,

University of Malaya

various problems such as safety, land size, and the random behavior of renewable energy resources are essential to be addressed if the system is installed near to the energy demand. Wind resources in urban area is generally weak, turbulent, and unstable in terms of speed and direction due to the presence of building and other adjacent of obstruction (Li, Wang, & Yuan, 2010). A wind assessment study conducted in urban area revealed that the free-stream wind speed in Malaysia is less than 4 m/s for more than 90% of total wind hours throughout the year. (Chong, Poh, Fazlizan, & Pan, 2012). With such unfavorable wind condition, most of the existing wind turbines cannot be used in Malaysia since they are designed to operate at higher wind speed.

Instead of harvesting natural wind, a promising alternative sources of wind energy that has not been harnessed are the systems that generate exhaust air, for instance, cooling tower. Cooling towers are widely used at the factories, hospitals and large office buildings (Jeong, Chung, Bae, Kim, & Shin, 2005), and they are considered as an essential part of building in a tropical region like Malaysia. Comparatively, the exhaust air speed is generally more consistent and higher to the natural wind with the measured value of approximately 9 m/s (Chong, Poh, Fazlizan, Oon, & Tiah, 2011).

An exhaust air energy recovery system, which made up of a vertical axis wind turbine (VAWT) coupled to a generator with its power electronics converter and controller can be retrofitted above the outlet of a cooling tower to extract the discharged wind (Chong et al., 2014; Chong et al., 2013; Fazlizan, 2016). It is a kind of building integrated wind turbine that utilized the unnatural wind resource for electricity generation. The preliminary studies on such exhaust air wind turbine generator confirmed the feasibility of the concept. The results revealed that it can be recovered up to 13% of the cooling fan's motor power consumption, without exerting undesired effect to the performance of the cooling tower (Chong et al., 2013). Nevertheless, previous studies had always focused on the mechanical geometrical and configuration optimization without taking into account

University of Malaya

the control aspects. Furthermore, the discharged air speed will vary as the cooling tower changes its fan speed in order to suit the cooling demand, causing the wind turbine to operate under suboptimal conditions. Hence, power optimization control of the exhaust air turbine generator, similar to normal wind energy conversion system, is expected to have a profound impact on improving the power extraction. This project intends to bridge this knowledge gap by investigating the power optimization of a guide-vanes integrated exhaust air wind turbine generator system.

1.3 Project Overview

In this project, the purpose is to optimize the wind power generation from the exhaust air turbine generator and it is an extension of the preliminary study on the exhaust air turbine generator (Fazlizan, 2016). Figure 1.1 shows the overall setup of the guide-vanes integrated exhaust air turbine used for the proposed power optimization study. The setup consists of an exhaust air turbine located at the top of a cooling turbine and coupled to a permanent magnet generator with its power electronics converter (Vienna rectifier).

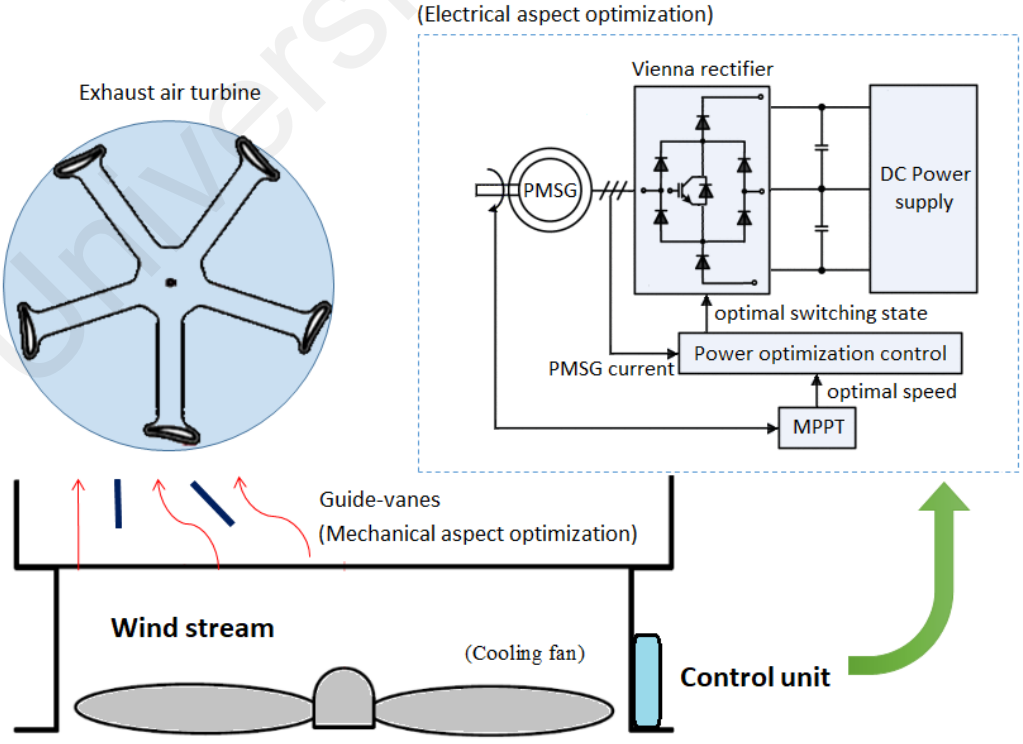

Figure 1.1: Overall proposed optimization approach.

University of Malaya

In order to harvest maximum wind energy from a wind turbine, one of the ways to improve wind power is to focus on the aerodynamic behavior of the wind turbine. Guide-vanes which are created by using two wind deflector plates were arranged in between the wind turbine and wind source, such that the local wind flow can be adjusted to achieve a better angle of attack with respect to the turbine blades. In this project, an aerodynamic model was derived to calculate angle of attack while taking into consideration the guide-vane angle. The efficacy of the proposed solution on the VAWT was confirmed by using both experiment and double multiple stream tube (DMST) theory.

Apart from mechanical means of power optimization via guide-vanes integration, the power captured by the wind turbine can also be optimized by the proper control of the generator. This can be done by controlling the electrical power of the generator, such that the wind turbine rotational speed is maintained at an optimum tip speed ratio as the discharged wind speed varies. In this project, Vienna rectifier was used as the machine side converter which controls the electrical power generated by the permanent magnet synchronous generator (PMSG). An improved lookup table based direct torque control (LUT-DTC) strategy was first developed for effective control of the PMSG. Subsequently, a lookup table-based model predictive direct torque control (LUT-MPDTC) was developed to further improve the control performance. Both control methods were first simulated in Matlab Simulink to confirm their performance before verifying using experimental results. The maximum power point tracker (MPPT) and turbine emulator were also developed in this project to further validate the overall power optimization mechanism using the proposed LUT-MPDTC method with the guide-vanes integrated exhaust air wind turbine generator.

University of Malaya

1.4 Objectives of Research

The objectives of this research are as follows:

1) To determine the optimum position and angle of guide-vanes configuration experimentally to improve the total wind power generation.
2) To analyze and validate the behavior of the guide-vanes integrated exhaust air turbine generator using double multiple stream tube (DMST) theory.
3) To improve the switching vector lookup table (LUT) for direct torque control of permanent magnet synchronous generator based on Vienna rectifier.
4) To develop a model predictive torque control method for permanent magnet synchronous generator based on Vienna rectifier.
5) To build a lab scale wind turbine emulator with perturbed-and-observed based maximum power point tracker for the verification of the overall power optimization mechanism.

1.5 Research Contributions

The major contribution of this research is to optimize the wind power generation from the exhaust air turbine generator based on mechanical and electrical approaches. Following are the contributions provided by this dissertation: -

1) Wind power augmented device (guide-vanes) was developed to improve the discharged air flow near the exhaust air turbine. The optimized configuration of the guide-vane with VAWT was determined for maximum wind power extraction.
2) The aerodynamic model for VAWT which takes into consideration of the guide-vane angles was developed. This developed model offers an analytical approach to obtain the aerodynamic parameters of the VAWT at different azimuth angle. It can be used in the conjunction with DMST theory to anticipate the generated power from a VAWT.

University of Malaya

3) Direct torque control (DTC) of PMSG using Vienna rectifier was investigated where a guideline for the design and implementation of lookup table for DTC was presented. A standardized generator voltage model which considers the switching vector coordinates was developed for easy analysis of the switching vector effect on the performance of the DTC. The developed voltage model can be used in both conventional DTC and model predictive direct torque control (MPDTC) approach.
4) As an improvement to the LUT based DTC method, a hybrid LUT-MPDTC method was developed for the control of PMSG using Vienna rectifier. Compared to conventional LUT-DTC, the proposed control method uses predictive model to automate the optimization of switching vector selection hence, achieving better performance. On the other hand, the integration of a LUT into the MPDTC reduces the computational burden of the proposed method compared to conventional MPC approach.

1.6 Thesis Outline

This thesis is divided into six chapters and it is organized as follows:

Chapter 1 presents an introduction to the research project which includes the background and problem statements of the research. Subsequently, it is followed by the project overview, objectives, research contributions and the thesis outline.

Chapter 2 reviews the existing literature related to the topics covered in this research project. Firstly, an overview on the existing studies related to wind energy conversion system is presented. Subsequently, literature on power optimization methods for wind energy conversion method is given, covering both mechanical and electrical approaches.

Chapter 3 covers the mechanical power optimization using guide-vanes integrated exhaust air turbine generator. The first part of this chapter explains the theoretical background of a wind turbine. The general model for the angle of attack calculation is

University of Malaya

modified with the consideration of guide-vane angle. The fabrication of the test rig for a laboratory test is also presented. The theoretical discussion is validated by comparing the behavior of the exhaust air wind turbine with and without the guide-vanes integration, and then evaluating the results using DMST analysis.

Chapter 4 is about the power optimization using DTC based on Vienna rectifier. It provides an in-depth analysis on the effect of the switching vectors of the Vienna rectifier on the performance of direct torque control in terms of torque, stator flux, and DC-link voltage variation. An improved lookup table is then developed with computation delay compensation to improve the overall control efficiency of existing DTC. Finally, simulation and experimental results are used to compare to the improved LUT-DTC with the existing approach where the former is found to outperform the latter.

Chapter 5 proposed a model predictive direct torque control (MPDTC) to further improve control efficiency of the conventional DTC. The design requirements as well as the implementation issues of the MPDTC are also presented. A lookup table (LUT) is used with the MPDTC to reduce the computation burden. Simulation and experimental evaluation are conducted using the same test-rig which runs on the classic DTC (Chapter 4). The obtained experimental results i.e. torque, and stator flux is compared to the conventional DTC approach. Then, a wind turbine emulator is developed with the consideration of guide-vanes integration. The perturbed-and-observed (P&O) maximum power point tracker (MPPT) method is adopted to validated overall power optimization mechanism using electrical approach.

The thesis ends with Chapter 6 which outlines the conclusions and future works for this project. Matlab Simulation models, Vienna rectifier prototype schematics, wind turbine specification, details related to the development of wind turbine emulator and airfoil database are attached in the Appendices for reference purposes.

University of Malaya

CHAPTER 2: LITERATURE REVIEW

In this chapter, a brief overview of the wind energy conversion system (WECS) is first provided. Subsequently, a review on the optimization approaches for improving the total power captured from the WECS is presented. It is divided into two major aspects, i.e. mechanical and electrical in order to establish a better correlation between the surveyed literature and the thesis's objectives.

2.1 Overview of wind energy conversion system (WECS)

A WECS converts the kinetic energy contained in the oncoming wind stream into mechanical energy which then runs the generator to create electrical energy. The oncoming wind resources can be either natural or man-made wind resources depending on the installation site. This energy conversion process is done through two subsystems as illustrated in Figure 2.1. First, the mechanical subsystem consists of a wind turbine that is connected to a generator via an optional gearbox. A gearless configuration is possible by increasing the number of pole-pair of the generator to reduce the difference in rotor and generator speed range. The mechanical subsystem harnesses the kinetic energy from the wind and converts it into rotational motion at the shaft of the generator. The electrical subsystem of WECS consists of a generator and its power electronics converter. The generator is an electro-mechanical energy conversion device that converts the mechanical energy into electrical energy. This energy is conditioned by the power electronics converter to ensure that the generated electrical power can be used by the utility grid, electrical load or energy storage device.

University of Malaya

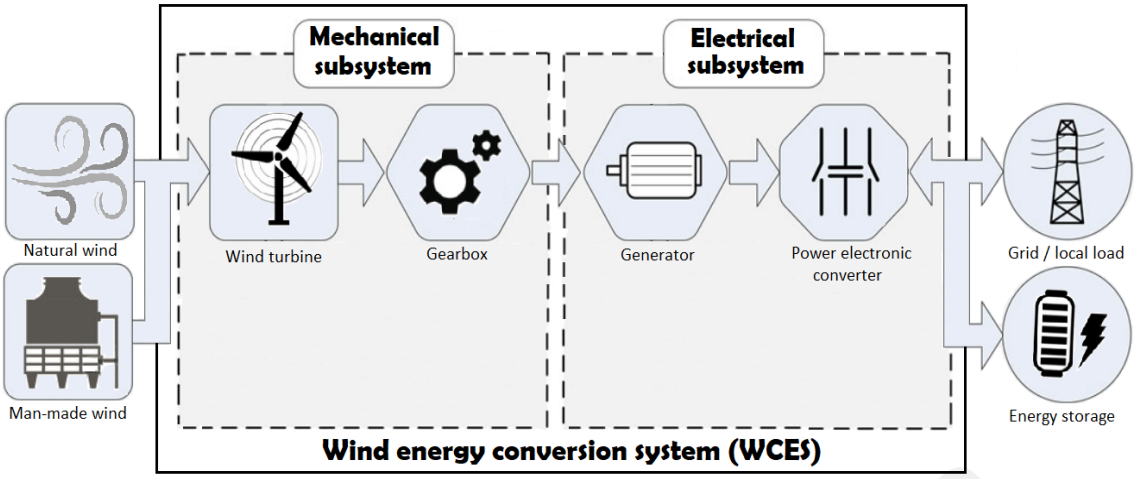

Figure 2.1: Wind energy conversion system (WECS).

The wind turbine in a WECS can be operated in two ways, which are constant speed operation and variable speed operation. Variable speed operation gains more popularity as it presents more advantages over constant speed operation such as higher energy gain, lesser component stress, and better power quality (Abdullah, Yatim, Tan, & Saidur, 2012). The wind turbine is expected to be operated differently according to different regions of wind speed, bounded by cut-in wind speed, $V_{cut\text{-}in}$ and cut-out wind speed, $V_{cut\text{-}out}$ as shown in Figure 2.2.

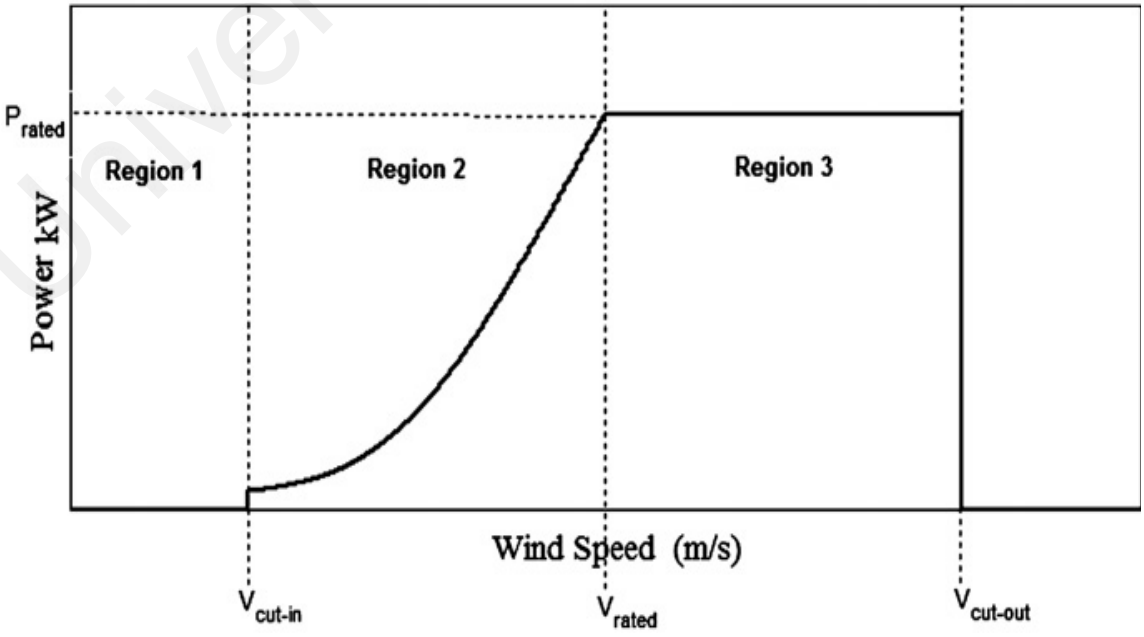

Figure 2.2: Typical power output for a variable speed operated wind turbine. (Abdullah et al., 2012).

University of Malaya

The operation of the wind turbine with its related power optimization approaches can be distinguished by the 3 main operational regions based on the wind speed which are: -

1) Region 1: Low wind speed range

There is no output power generation in this region from a wind turbine as the oncoming air stream speed has fallen below the minimum speed for the turbine to start, i.e. cut-in wind speed ($V_{cut\text{-}in}$). An improvement on the available wind resource quality can be performed here to assist the turbine's start-up performance by passively adding a wind power augmentation device.

2) Region 2: Moderate wind speed range (partial load regime)

The second region describes the operation of a wind turbine between the cut-in wind speed and the rated wind speed where wind turbine starts to operate at $V_{cut\text{-}in}$ and generates its maximum power at rated wind speed, V_{rated}. Power optimization through electrical control system should be employed here, where the wind turbine is controlled to rotate at different speeds in such a way that the power captured is maximized until the operational limit reached.

3) Region 3: High wind speed

In this operating region, the oncoming wind speed that flows to the turbine is above the rated wind speed. Adjustment must be done to the WECS such that the generated power from the wind turbine is restricted to its rated value to avoid the generated power from exceeding the mechanical and electrical limits of the system. This can be done by activating pitch control system to limit the aerodynamic power to alleviate the mechanical loads on the wind turbine. The turbine blade can adjust facing or away from the wind according to the desired aerodynamic behavior of the turbine. Hence, the wind turbine speed will be limited to avoid over-spinning which in turn can cause the mechanical failure.

University of Malaya

Several structures of WECS had been proposed in the literature to achieve the optimized performance at different operational regions of the wind turbine. The classification can be based on the types of wind turbine, wind power augmentation device, types of generator and power electronics converter employed. These topics will be covered in the subsequent sections.

2.2 Types of wind turbine used in WECS

There are two different types of wind turbine available as shown in Figure 2.3 which classified based on its aerodynamic characteristic: -

1) Horizontal axis wind turbine (HAWT)
2) Vertical axis wind turbine (VAWT)

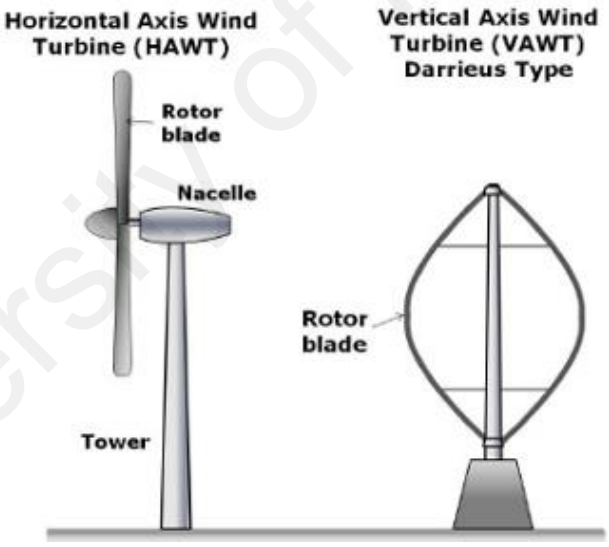

Figure 2.3: Types of the commercially available wind turbine.

2.2.1 Horizontal axis wind turbine (HAWT)

HAWT is designed to face directly into the wind where the axis of rotation is parallel to the ground. It consists of the main rotor shaft and electrical generator at the top of a tower. Usually, this kind of turbines are equipped with a yaw system to orient the turbine towards the wind for maximum power extraction. However, HAWTs are not suitable in urban areas due to their size and geometry (Martin & Roux, 2010).

University of Malaya

2.2.2 Vertical axis wind turbine (VAWT)

VAWT is a type of wind turbine where the axis of rotation is perpendicular to the wind stream. The major advantage of the VAWT is that it is inherently omni-directional and thus, obviates the need for yaw mechanism. With a simpler structural design, lesser acoustic noise and smaller operation space, VAWT is deemed to be more suitable for complex wind flow and hence, urban application. VAWT also has better aesthetics in terms of integrating into architectural structures. Thus, VAWT is chosen to integrate with the exhaust air system as an exhaust air energy recovery system (Chong et al., 2013). Nevertheless, the efficiency and low self-start ability of VAWT are always the main drawbacks, especially for lift-type VAWT. Unlike HAWT, the interaction of this kind of wind turbine with the environment is a complex system. The rotor blades experience a rapid change of angle of attack and hence, VAWT does not always produce positive torque during operation. The negative torque generated at the downwind side of the turbine reduces the overall performance of the VAWT. Therefore, much of the effort devoted to research and design of the VAWT towards the aim of performance improvement.

2.3 Types of generator in wind energy conversion systems (WECS)

Various electrical generator types can be used in conjunction with the wind turbine for a WECS. The right choice of generator depends on the available wind resource speed range (cut-in wind speed to rated wind speed), types of load or application (standalone or grid connected), and the speed of the wind turbine.

Fix speed WECS is the simplest and very first WECS configuration (“Danish” concept) which makes up the biggest share of the smaller WECSs that already installed and scattered on the network (Hansen & Hansen, 2007). The system essentially works without any power converter. However, it suffers from the drawbacks of high mechanical

University of Malaya

stress, large power fluctuations and reactive power burden on the power grid (Wang, Yuwen, Lang, & Cheng, 2013).

Alternatively, variable speed WECS can be used which allows rotor to rotates at different speeds via a power electronics converter. The power electronics converter gives the controllability of rotor speed, thereby, the performance of the WECS can be enhanced. Generally, there are three types of variable speed WECS which have been used commercially. The pros and cons of each type of WECS are summarized in Table 2.1. It also shows different possible technological options such as with or without a gearbox, using synchronous or induction machines and different power converter topologies (full rated converter or partially rated converter).

Variable speed WECS is preferred in this work since the exhaust air energy recovery system is designed to be retrofitted above the cooling tower. In an energy-concious world, it is logical to use the variable frequency drive (VFD) controlled cooling tower which operated over many speeds as opposed to those with the cooling fan on single or two-speed motors. The cooling fan operation speed is heavily dependent on the demand cooling load; As such, the exhaust air turbine will be acted as the conventional variable speed wind turbine. Among different types of generators, PMSG is particularly favored in the small-scale direct-drive WECS due to it offers the merits of high efficiency and reliability, gearless construction, light weight and self-excitation features with better grid support capability. As compared to other types of WECS, the cost of the overall system using PMSG increases due to the need to use full rated power converters that is rated equivalent to the generator capacity. Nevertheless, the cost is only a small fraction (approximately 7%–12%) of the whole wind turbine cost (Carrasco et al., 2006). For these reasons, PMSG is used for the development of the power optimization and WECS in this work.

University of Malaya

Table 2.1: Pros and cons of each type of WECS.

Types of WECS	Pros	Cons
Fixed-speed WECS with an asynchronous squirrel cage induction generator	• Low initial cost. • Simple and reliable operation for the stiff grid.	• Small speed variation (±1%). • Capacitor banks required. • Need soft-starters to smoothen the inrush current during start-up. • Gearbox is needed to match the difference in rotor and generator speed range. • Voltage quality easily deteriorated in the case of a weak grid. • Need a strong mechanical structure to withstand the wind speed variation.
Semi-variable speed (±10%) WECS with wound rotor induction generator	• Sufficient range of variable speed from super-synchronous to sub-synchronous speeds, usually up to 10% above the grid angular frequency (Cheng & Zhu, 2014)	• Smooth grid connection by incorporating the soft starter. • Capacitor banks are required for power factor correction. • Higher energy losses due to the rotor resistance. • Gearbox required.

University of Malaya

Table 2.1, continued: Pros and cons of each type of WECS.

Types of WECS	Pros	Cons
Semi-variable speed (±30%) WECS with double-fed induction generator	• Variable speed range about ± 30% of the synchronous speed (Hansen, Iov, Blaabjerg, & Hansen, 2004; Lie & Cartwright, 2006) • Rotor energy is captured instead of dissipated as heat in the controllable rotor resistance. • Inexpensive small capacity converter. • Does not need reactive power compensation. • Soft-starter is not required.	• Use of slip rings and brushes. (connection of power converter to the rotor winding). • Protection schemes for converter under the case of faulty grids (Cheng & Zhu, 2014) • Gearbox incurs the increase in the overall cost, weight and as well as the demand for frequent maintenance.
Full variable speed WECS with PMSG, WRSG, or WRIG	• Full speed ranges from standstill to full rated speed. • Highest wind energy conversion efficiency. • Complete control of active and reactive power. • Possibility eliminates the gearbox with direct-driven coupling. • Brushless, lower maintenance cost.	• Size, cost and the complexity of the system increase. • Multipole generator (bigger size and cost)

University of Malaya

2.4 Types of converter used for WECS

As mentioned earlier, one of the important components of the variable speed WECS is the power electronics converter. The advantages and disadvantages of the different converter topologies are compared to identify the most appropriate topology for the exhaust air turbine generator. There are mainly three power converter topologies which are commonly used for machine side converter (MSC), i.e.: -

1) Uncontrollable diode rectifier
2) Fully controlled active rectifier
3) Semi-controlled Vienna rectifier

2.4.1 Passive diode rectifier with boost converter

For simple and low-cost WECS, the PMSG can be controlled using a diode-rectifier cascaded with a boost converter. It is the most common set-up found in commercial micro-wind systems. The basic rectifier topologies are given in the circuit diagrams in Figure 2.4. The power electronics converter comprises of two converters i.e. machine side converter (MSC) and grid side inverter (GSI). The main function of the MSC is to control the AC power generated by the generator whilst the GSI interacts with the load by controlling the DC-link voltage. A passive diode rectifier which three-phase voltage from the generator can be easily rectified to the form of DC but there is no controllability on the output. A braking chopper is usually installed on the DC link to dissipate the electrical energy during wind gusts and grid faults. Nevertheless, the use of such topology has several disadvantages. The generator currents contain significant 5th and 7th harmonics with the THD of approximately 30% (Kolar & Friedli, 2013) and this can result in distortion in the electromagnetic torque. Furthermore, the power factor of the converter is unable to be controlled, resulting in non-optimized operation of the generator.

University of Malaya

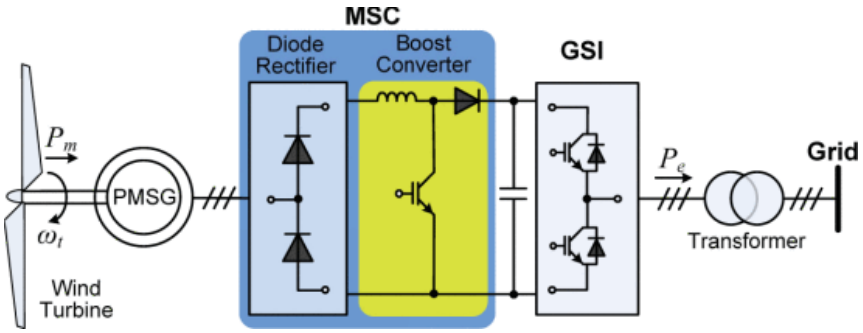

Figure 2.4: PMSG with uncontrollable diode rectifier.

2.4.2 Fully controlled active rectifier

The other types of converter for WECS is the active rectifier, which has better controllability over the generator. Instead of using diodes, power electronics switches such as MOSFET and IGBTs are used such that voltages applied to the generator can be controlled without relying on the polarity of the generator current. The three-phase two level six-switch rectifier is commonly used for controlling three-phase PMSG and its topology is depicted in Figure 2.5 (Xia, Wang, Wang, & Shi, 2016). Fully decoupled control of active and reactive power can be achieved, resulting in better generator speed control and higher quality of generator current.

Multilevel converters have also been proposed for WECS. Comparatively, it has three or more voltage levels over the back-to-back PWM rectifier. There have been various design for multilevel converters such as a neutral-point-clamped converter, cascade half-bridge converter and flying capacitor converter (Rodriguez, Bernet, Steimer, & Lizama, 2010). Neutral-point-clamped converter is commonly used in WECS out of these three multilevel converters due to its maturity (Rodriguez et al., 2010). The utilization of multi-level converter is beneficial in terms of higher power ratings and improved power quality. It allows the utilization of lower switching voltage which has lower resistance and switching loss with additional advantages on EMI filter design (Friedli, Hartmann, & Kolar, 2014). However, the large number of power switches do significantly increases the cost and control complexity.

University of Malaya

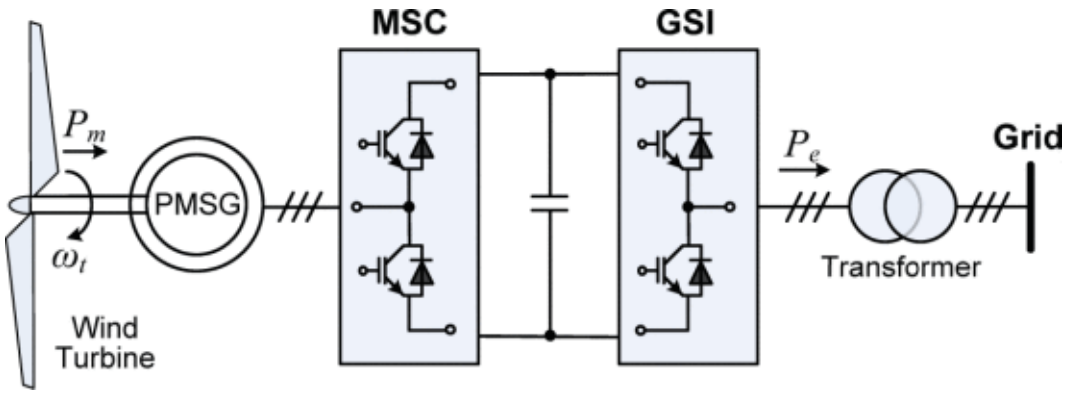

Figure 2.5: A fully controlled active rectifier.

2.4.3 Semi-controlled Vienna rectifier

By taking consideration the tradeoff between cost and performance, Vienna rectifier (three-switch/three-level PWM rectifier) as shown in Figure 2.6 can be an ideal choice for MSC in WECS. The Vienna rectifier mainly uses diodes for its power conversion but include switches to allow certain level of control over the current waveforms, thus can be considered as a semi-controlled rectifier. It is a non-generative boost type converter which has been used in telecommunication power systems, grid-connected system with power factor correction, and recently being implemented for wind turbine system (Kolar & Zach, 1994). This topology can produce 3 voltage levels with only 3 controlled power switches, thereby reducing the overall cost and simplifying the control complexity even though more diodes are required (Kolar, Ertl, & Zach, 1996; Kolar & Zach, 1994).

At the same time, the three-level structure of the Vienna rectifier reduces blocking voltage stress on the power switches by half, allowing enhancement in reliability. It is important to underline that Vienna rectifier is a unidirectional converter and thus, it is impossible to use it as a GSI. Instead, a conventional six-switch converter or another multi-level converter can be used. In this work, an effort is made to investigate the deployment of a Vienna rectifier as MSC in an exhaust air turbine with a PMSG.

University of Malaya

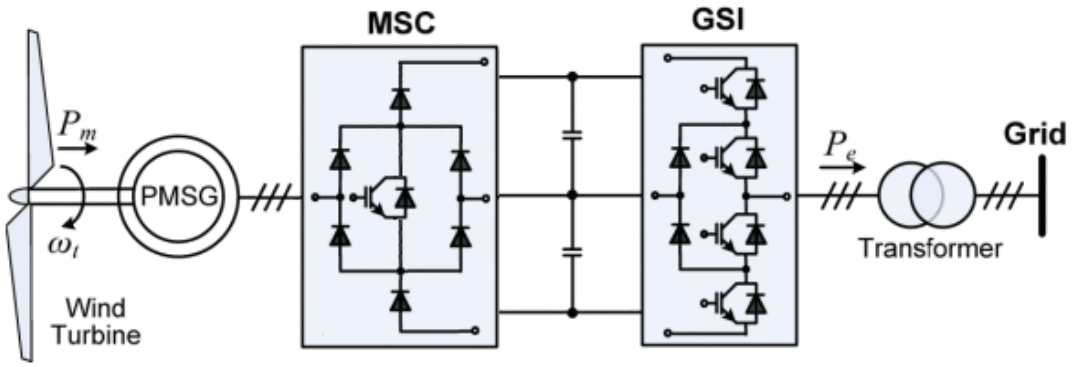

Figure 2.6: Semi-controlled Vienna rectifier.

2.5 Power optimization strategies of WECS

The maximization of the power coefficient is the fundamental concept in optimizing the extraction of wind energy. More and more studies have been published to further improve the power generation from WECS, covering methods from both mechanical and electrical aspects. Figure 2.7 presents the different optimization strategies for a variable speed WECS which are divided into the two approaches, i.e. mechanical approach and electrical approach.

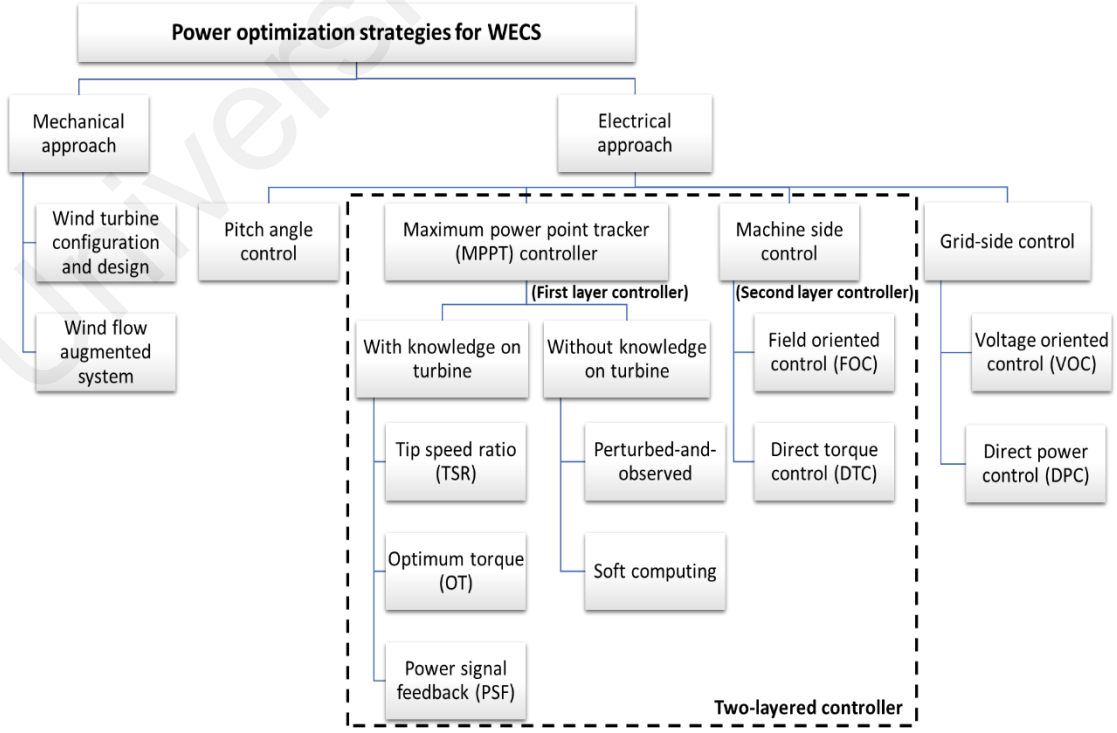

Figure 2.7: Power optimization strategies of WECS.

University of Malaya

Firstly, the aerodynamic performance of the VAWT can be enhanced by modifying turbine blade or configuration of the turbine. The details of VAWT design improvement, which is beyond the scope of this project, can be found in the literature (Aslam Bhutta et al., 2012; Chong et al., 2017; Shikha, Bhatti, & Kothari, 2005). Another mechanical way to increase the extraction of wind power is by the deployment of appropriate aerodynamic devices. The oncoming wind flow near the VAWT can be improved without modifying the basic structure of turbine by integrating it with a wind flow augmentation system.

In terms of electrical aspect optimization, there are three levels of control systems for a WECS, which are: pitch angle control, generator speed control and grid interface control. In this project, focus is given to the generator speed control. The WECS generator speed control can be realized by a two-layered controller in a cascaded structure. The first layer determines the reference signal (speed or torque) via a maximum power point tracker (MPPT) and another layer receives a reference signal from the first layer and executes accordingly using machine side control strategies.

The most common control strategies for the full rated MSC are field-oriented control (FOC) and direct torque control (DTC). The FOC consists of a dual loop outer controller technique for generator speed control. The disadvantage of the FOC is the controlled current is subjected to the coordinate transformation to yield the pair of -*dq* currents. The PMSG's stator flux is controlled by regulating the I_d with the *d*-axis is aligning to the rotor flux. Meanwhile, the torque is controlled by varying the I_q. On the contrary, the use of DTC method eliminates the inner current control loops and transformation between reference frames. The torque can be altered directly which in turn gives faster response and less complexity (Tiwari & Babu, 2016). Besides, it also appears to be a better solution for high performance application because the DTC possesses high robustness towards uncertainties and parameter variation without the needs of rotor position sensor (Rajaei, Mohamadian, & Varjani, 2013; Xia et al., 2016; Zhong, Rahman, Hu, & Lim, 1997).

University of Malaya

2.5.1 Wind flow augmentation system

As mentioned earlier, the major setback of the VAWT is its efficiency in capturing power from the wind. Indeed, the efficiency of the wind turbine can be improved by wind flow augmenting system which concentrates and increases the mass flow through the area of augmented devices. The augmented device can be a diffuser, duct, guide-vanes, stator and other devices.

Guide-vane is a set of fixed structure arranged around the rotor or placed at the upwind side of the wind turbine that guides the oncoming wind into the moving turbine's blades with minimum loss of energy. Guide-vane or sometimes known as stator or guide deflector can be a flat-plate, curved-plate or any other geometries. It can be also used as a shield to reduce VAWT's negative torque. (Wong et al., 2017). The guide-vanes help to divide the fluid into several flow channels which directed to the optimum angle of attack of the turbine blades (Chong, Fazlizan, Poh, Pan, & Ping, 2012). Generally, the main function of the guide-vane is to channel the air flow to a better angle of attack and enhance the velocity of the wind flow by concentrating more wind towards the wind turbine.

One of the first research studied on guide-vane was carried out back on 1978 by Alexander and Holownia (1978). The effect of different stators on the air flow for a Savonius rotor was investigated. The implementation of guide-vane is capable of changing the geometric and air flow characteristic and hence, increasing the VAWT's performance up to 50% (Akwa, Vielmo, & Petry, 2012). Besides, there was a study conducted on a straight-bladed VAWT and the results indicated that the performance of the VAWT can be enhanced by the directed guide-vane row in terms of power coefficient and torque coefficient (Takao et al., 2009). The existence of guide-vanes generates wakes in its downstream and the whirl velocity of inlet flow to the rotor is increased. As a result,

University of Malaya

the VAWT's maximum power coefficient increased by approximately 1.5% over the case without guide-vanes.

The improvement of power output with the guide-vanes installation is also dependent on the geometry of the guide-vane and the VAWT's position relative to the guide-vane (Kim & Gharib, 2013). Based on the study conducted by Kim and Gharib (2013) on a VAWT, the presence of a straight deflector plate at the accurate position in front of a VAWT helped to tailor the free stream flow. However, the VAWT performance became worsen if the deflector plate was placed too near to the VAWT or inside the streamline. Figure 2.8 shows the arrangement of a single flat deflector with its geometry parameters that were investigated includes width (*w*), the height of the deflector (*h*) and the distance between the deflector and VAWTs (*l*). The optimum configuration of deflector improved the maximum power coefficient from 0.031 to 0.101 which is approximated triple of the bare turbine unit. A similar study was carried out experimentally to find the optimal position of a straight deflector plate for the Savonius turbine at the upstream flow (Golecha, Eldho, & Prabhu, 2011). The maximum coefficient of power was found to be 0.21 at a TSR of 0.82 with the presence of deflector plate, which is equivalent to 50% higher in power coefficient. This has reached a consensus with Kim and Gharib (2013) that the coefficient of power can be improved significantly with the optimum configuration of guide-vane.

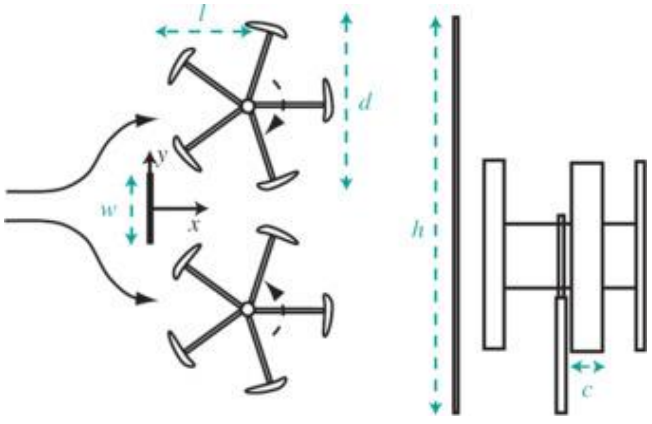

Figure 2.8: Top and side view of the single flat deflector. (Kim & Gharib, 2013)

University of Malaya

In-depth analysis was also conducted through numerical computational fluid dynamic (CFD) to investigate the effect of guide-vane implementation with the VAWT. The optimum configuration of a straight plate can increase the power output coefficient of the Savonius turbine by more than 27% (Mohamed, Janiga, Pap, & Thevenin, 2010, 2011). Meanwhile, the self-starting behavior also improved for almost all of the guide-vane configurations. Similarly, the CFD results of the installed stator vane on flow field had been compared with the experimental wind tunnel testing (Burlando, Ricci, Freda, & Repetto, 2015). The result disclosed that the wind flow at the gaps between the stator vanes was accelerated by approximately 10%.

Besides, other shapes of stator vanes had also been introduced. A V-shaped deflector was designed to be installed at the upstream of the Savonius wind turbine (Shikha, Bhatti, & Kothari, 2003b). The experimental results revealed that the enhancement of maximum power was possible to be improved by 20% when the deflector was positioned at the angle of 37^{o}. Likewise, the effects of the deflecting plate parameters had also been examined in order to enhance the output of the Savonius turbine using circular guide-vanes (Ogawa, Yoshida, & Yokota, 1989). In the study, the output power improved by approximately 30% as compared to a rotor without the deflecting plate. One of the most recent approaches, which a few of curved shape deflectors were used at the upstream of a three-blades Darrius VAWT (Stout et al., 2017). A marginal increment of 1.266% in turbine performance was observed with the use of such deflector.

Other than placing plates or vanes in front of the wind turbine, different configuration of two or more plates can be formed to become a wind power augmentation system. A curtain plate design which made up of two deflecting flat plates as shown in Figure 2.9 helps in guiding the oncoming wind to the advancing blades (Altan, Atılgan, & Özdamar, 2008). The wind flow to the turbine can be increased due to the entrance of wind is narrowed by the curtain plate. As a consequence. the maximum power coefficient of a

University of Malaya

Savonius turbine was improved about 38.5% when the optimum arrangement of curtain plate is installed as compared to a standard turbine.

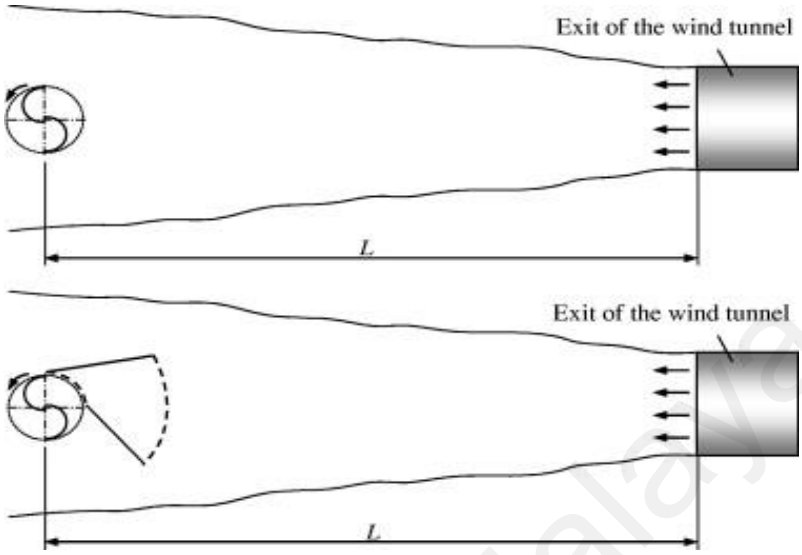

Figure 2.9: Schematic of the rotor with or without curtain arrangement. (Altan et al., 2008)

A similar approach was introduced which two flat plates are used as nozzles for a six blades Savonios turbine to improve the power extraction at low wind speed areas (Shikha, Bhatti, & Kothari, 2003a; Shikha et al., 2003b). A good balance between the number of blades and nozzle dimensions (includes length and ratio between inlet and outlet) have to be achieved for a high efficiency and good performance system. From the study, the highest wind speed improvement can be obtained, which is 3.7 times higher with a nozzle of 55 cm in length and 0.15 of inlet and outlet ratio.

An innovative conveyer-deflector curtain system was proposed that is capable of self-aligning relative to the oncoming wind direction. This system allowed the increment of flow interaction angle of the Savonius turbine's advancing blade. Through the experiment and CFD analysis, the adoption of such system gave higher maximum power, which is 20% greater than a bare unit of the wind turbine. To further extract the output power from the wind, an omni-direction-guide-vane (ODGV) had been developed which is able to collect the oncoming wind from any direction. The ODGV system was built with four

University of Malaya

pairs of guide-vane that surrounded a H-rotor VAWT and they were held by an upper and lower wall duct. The ODGV creates venturi effect as the oncoming wind enters from a wider to a narrower space, improving the wind speed. The study revealed that the output power of a VAWT was enhanced by 206% at TSR of 0.4 with the installation of the ODGV through CFD simulations (Chong et al., 2012). As a continuing work, the ODGV system was modified by dividing the guide-vanes into two segments with a tilted angle of 10^{o} each as shown in the Figure 2.10. The left side figure is the original design and the other is the new design. The CFD simulation results shown that the power coefficient of the turbine was able to increase by 31.65% as compared to the original design of the ODGV system.

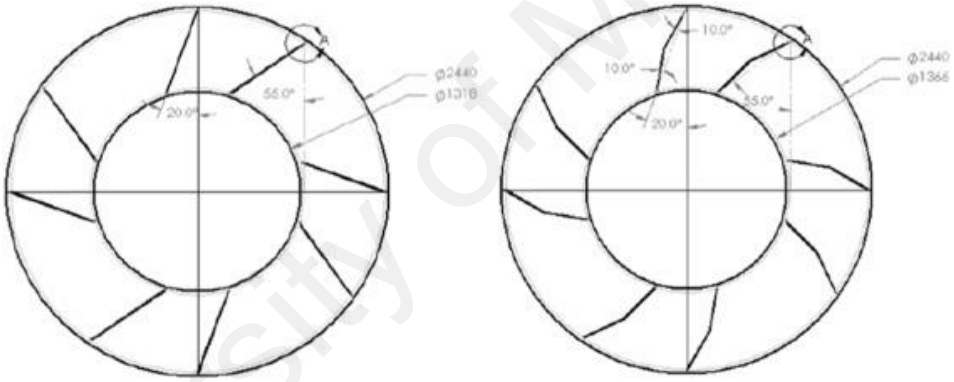

Figure 2.10: The old and new design of ODGV system. (Chong et al., 2012)

These researches had shown through experiment and CFD simulation that the deployment of guide-vane can produce a positive effect on the performance of VAWT in terms of power gain and oncoming wind speed. Nevertheless, these studies are limited to a specific model of the wind turbine and the wind directional augmented system make the analysis of VAWT becomes more intricate. In order to implement guide-vanes to the exhaust air turbine generator, a precise investigation on guide-vanes geometry, position and its distance from the turbine have to be investigated as suggested by the previous researches.

University of Malaya

2.5.2 Maximum power point tracker (MPPT) techniques for wind energy

The performance of a WECS is generally governed by a wind turbine power characteristic curve as shown in Figure 2.11. For optimization control purpose, there is an optimal power curve (which is the trajectory of the optimal tip speed ratio, λ_{opt} under different wind speeds as seen in Figure 2.11) which gives maximum conversion efficiency for the wind turbine at different wind speed. Hence, the generated power from the WECS can be maximized when the generator is controlled to rotate at the optimum rotational speed. MPPT scheme is essential for a WECS to track the optimum rotational speed which changes dynamically with wind speed. It can be classified into two groups (Mirecki, Roboam, & Richardeau, 2007), namely: -

1) MPPT with knowledge on the wind turbine characteristic.
2) MPPT without the knowledge on the wind turbine characteristic.

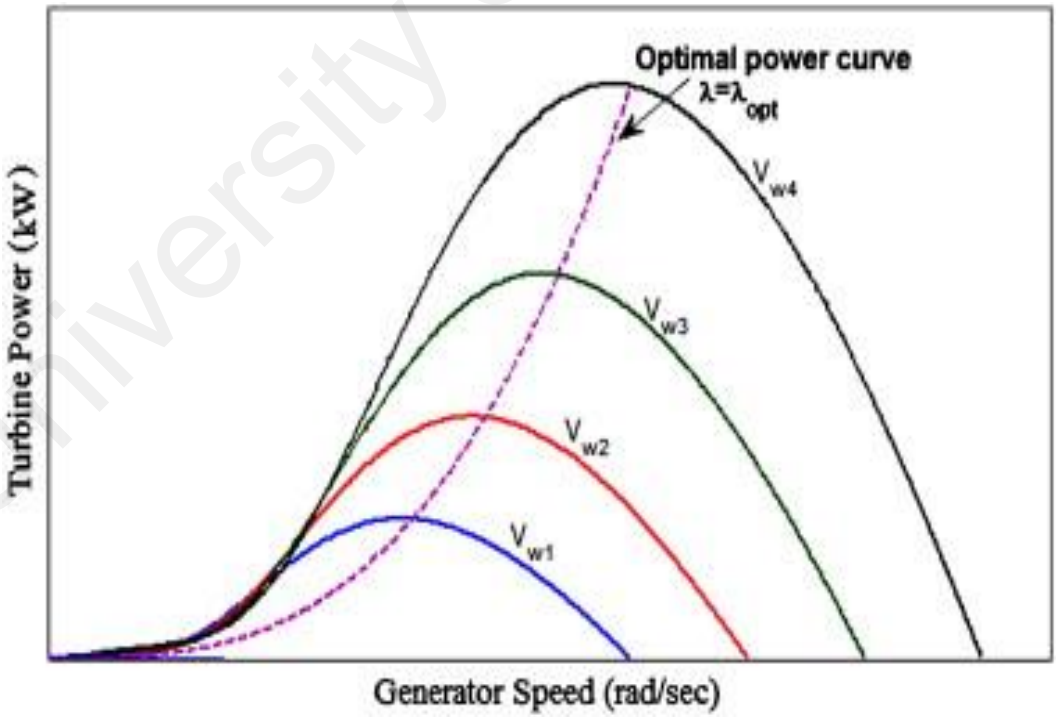

Figure 2.11: Wind turbine power against generator speed at various wind speeds.
(Abdullah et al., 2012)

University of Malaya

2.5.2.1 MPPT with knowledge on the wind turbine characteristic

The foremost MPPT algorithms which are widely used with the knowledge of turbine characteristic are tip speed ratio (TSR) control, optimal torque control (OT), and power signal feedback (PSF) control.

At a given wind speed, the mechanical power from a wind turbine changes drastically with TSR. The extraction of maximum wind power can only occur at an optimal TSR for a specific wind speed. Therefore, one of the straightforward MPPT method is to control the TSR (Nasiri, Milimonfared, & Fathi, 2014). By manipulating the rotor speed of the wind turbine with wind speed, the TSR can be maintained at its optimal value at all time. This method is direct and has good response. However, it requires accurate knowledge of the turbine parameters and precise measurement of the wind speed in order to ensure the wind turbine operates close to the maximum power point (Arifujjaman, Iqbal, & Quaicoe, 2008). Typically, two control sensors are crucial for this MPPT control which are anemometer and encoder. These sensors increase the overall implementation cost of the MPPT.

Other than TSR control, OT control was suggested as an alternative control for MPPT. The difference of OT over TSR control is the input reference signal. OT control regulates the generator torque instead of TSR. Since the wind speed measurement does not require for OT control, it is generally simple, easy and fast. Nevertheless, the tabulation for reference torque requires the accurate knowledge of turbine torque-speed characteristic, which it is hard to acquire and each of the turbines possesses its own constant value. Moreover, the wear and tear of the turbine can cause the torque-speed characteristic changes, reducing the effectiveness of the OT method (Novaes Menezes, Araújo, & Bouchonneau da Silva, 2018).

Apart from TSR and OT method, PSF control can also be used for the MPPT. A lookup table (LUT) was used to obtain the optimal power accordance to wind turbine rotational

University of Malaya

speed. The LUT can be constructed based on off-line experiment, simulation or using datasheet of the wind turbine. There is a more advanced technique for PSF control which uses DC voltage and DC current for LUT development and therefore, allowing the control becomes encoderless (Barakati, Kazerani, & Aplevich, 2009). PSF method offers the advantage of being independent of the wind speed measurement. However, as with OT and TSR method, the characteristic recorded in the LUT may change over time, degrading its performance.

2.5.2.2 MPPT without knowledge on wind turbine characteristic

For control method without prior knowledge on aerodynamic characteristic of the wind turbine, an adaptive MPPT algorithms is needed. It is designed based on an iterative search for its maximal power point by changing the control variables. One of the most popular control methods is the perturbed-and-observed (P&O) / gradient method (Gitano-Briggs, 2010; Kot, Rolak, & Malinowski, 2013; Tiwari & Babu, 2016). In the P&O control, the suitable change of the control variables for the subsequent cycle is determined by the location of the operating point and the relation between the changes in power and control variables. The control variables can be turbine rotational speed, ω or converter duty cycle, D. At any wind speeds, the generated power will be maximum when $\Delta P/\Delta\omega$ or $\Delta P/\Delta D$ is equivalent to 0 (as indicated with the red line in Figure 2.12). The basic principle for the perturbation activity is explained here with Figure 2.12. When the operating point is located in the yellow zone with $\Delta P/\Delta\omega > 0$ at the left, the rotor speed will be perturbed in the increasing direction. It is known that such perturbation is moving towards to the optimal point ($\Delta P/\Delta\omega = 0$) and thus, the subsequent step change will be in the same direction. When wind speed changes from high to low, the operating point will be moved away from the optimal point and $\Delta P/\ \Delta\omega$ becomes <0 as shown in the green zone at the right. The next perturbation of the rotor speed to be applied will be reversed, which is in decreasing direction. As a result, this method has some limitations. It fails to

University of Malaya

track and diverge from the optimal point under fast varying of wind speed. Besides, oscillation at the optimal point is also inevitable.

Some researchers suggested the use of variable or adaptive step-size for the improvement of tracking, such as the advanced hill climbing method (Hong, Lu, & Chiou, 2009; Joseph, Foreman, & McIntyre, 2012). With such improvement, it eliminates the oscillation once the maximum power point found.

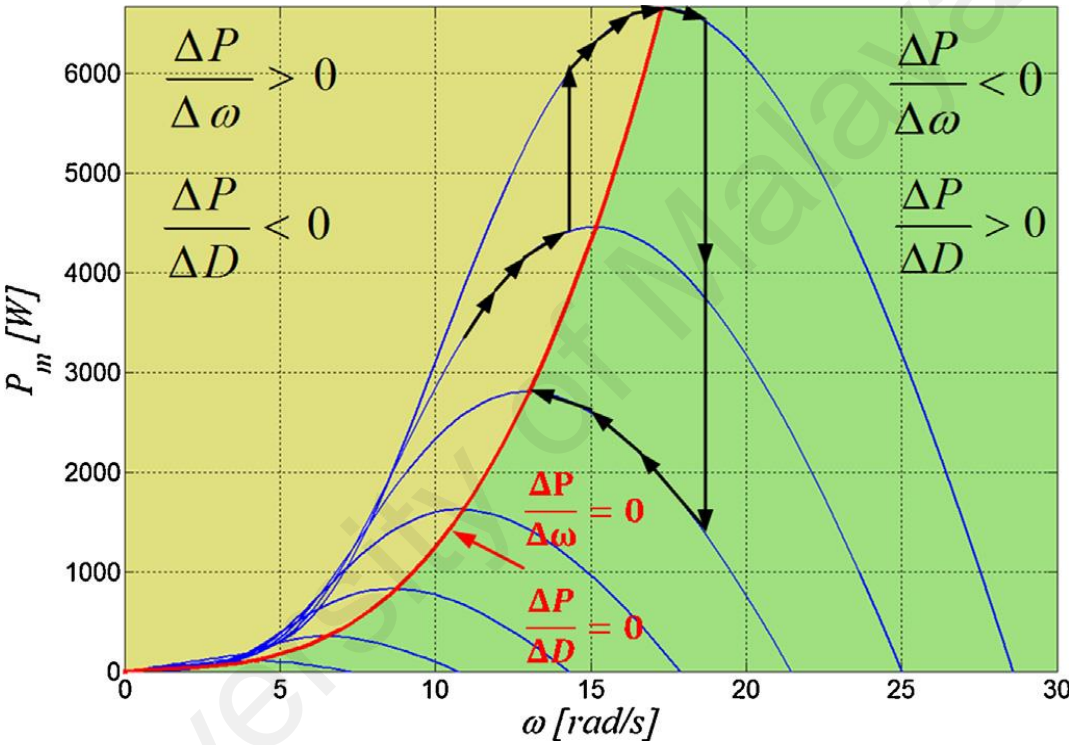

Figure 2.12: P&O method control algorithm for WECS. (Kot et al., 2013)

Soft computing or intelligent system was also utilized in solving the non-linear and the complex MPPT control of a WECS. Artificial intelligent tools include fuzzy logic, neural networks, evolutionary algorithm or hybrid of those methods (e.g. Neuro-Fuzzy interference system) and etc. had been explored for the WECS. Mirecki et al. (2007) investigated the application of fuzzy logic for wind turbine MPPT control. This method deals with reasoning rather than an exact model by using an operational seeking method based on the behavior rules related to both of the input variables (power and speed

University of Malaya

variation). It offers the advantages of fast convergence, parameter insensitivity, and acceptance of noisy and inaccurate signals. Additionally, it can be also use to obtain an optimal step-size for the conventional hill climbing method (Trinh & Lee, 2010). However, this method gives some shortcomings, such as a reduction in accuracy due to fuzziness. System complexity is also increased as additional processing for accuracy is required during the low intensity of wind.

P. Flores et. al used artificial neural network (ANN) based on a back-propagation algorithm to build wind speed prediction model (Zheng, Chen, Huo, & Zhao, 2011). There were three layers of an ANN i.e. input layer, hidden layer, and output layer. The convergence speed of the ANN controller to the optimum point is highly dependent on the weights which allocated for each layer, type of algorithm used in the hidden layer and the training of the system (Tiwari & Babu, 2016). Table 2.2 shows the comparison of the different MPPT techniques presented for WECS.

For simple and fast implementation, a variable step-size of P&O is chosen for the exhaust air turbine generator since prior knowledge of the turbine does not require, though it has low efficiency.

Table 2.2: Comparison of different MPPT for WECS.

MPPT	**TSR**	**OTC**	**PSF**	**P&O**	**Soft computing**
Efficiency	Very high	Very high	Moderate	Low	High
Convergence speed	Fast	Fast	Fast	Low	Medium
Anemometer	Yes	No	No	No	No
Tolerance to rapid variation	Moderate high	Moderate high	Moderate	Low	High
Prior knowledge of the system	Yes	Yes	Yes	No	No
Complexity	Simple	Simple	Simple	Simple	Complex

University of Malaya

2.5.3 Optimization control strategies using Vienna rectifier

While the MPPT controller can identify the optimal operating speed/torque for a generator in a WECS, the generator must be controlled by the MSC to track this speed/torque reference from the MPPT controller. An effective control method for the generator via the MSC is hence a critical part of the electrical power optimization in WECS. Depending on the type of generator and the MSC used, the choice of control method can be quite different. Since Vienna rectifier is used as the MSC in this project, the discussion here focuses on generator control using Vienna rectifier.

Vienna rectifier was designed with the aim of maximizing the power density of the three-phase power supplies (Burgos et al., 2007). MSC control technique performance is typically assessed through ripples in current and torque. Thus, various research activities on modeling and control for Vienna rectifier have significantly proliferated to achieve higher efficiency and lower total harmonics distortion (THD).

Due to its unique features of reduced switches, the Vienna rectifier can only operate in rectifying mode, with the current phase shift from the voltage restricted to $\pm\pi/3$ radians (Radomski, 2007). Furthermore, the access to DC-link midpoint makes Vienna rectifier susceptible to DC-link voltage unbalance, and hence it is vital to include DC-link voltage balancing control for Vienna Rectifier (Lee & Lee, 2016b). The simplest way to control Vienna rectifier can be performed by hysteresis switching method (Kolar et al., 1996; Kolar & Zach, 1994). The three-phase current is regulated by the means of switching on and off of the switches to maintain it within the pre-set hysteresis band in the inner loop whilst the DC-link output voltage is controlled in the outer loop. It has some noteworthy benefits such as easy to implement and fast dynamic response. A more advanced hysteresis current controller was introduced to ensure the continuity of power flow throughout the full range of operation (Foureaux, Oliveira, De-Oliveira, Filho, & De-Faria, 2015). The generation of the reference is dependent on the power level where a

University of Malaya

quasi-sinusoidal current reference and pulse width control was suggested for low power demand whilst sinusoidal for high-level power.

A carrier-based pulse width modulation method (CB-PWM) was presented in (Lee & Lee, 2016a) to maintain the operation of Vienna rectifier with variable power factor so that it becomes suitable for the application in WECS. Conventional CB-PWM can cause Vienna rectifier to operate under non-unity power factor condition. Thus, a compensation voltage is added to the three-phase reference voltages by the proposed CB-PWM to eliminate the range, where the topology constraint of the Vienna rectifier does not comply. From the experiment and simulation results, the proposed CB-PWM allowed the full range of power factor operation (from 0.866 – 1) with the current THD reduced significantly as compared to conventional CB-PWM from 12.82 % to 3.58%. Meanwhile, the two DC-link voltages remained balanced throughout the variable power factor operation.

Space vector modulation (SVM) for Vienna rectifier had also been investigated to explore the boundaries and restrictions of the continuous and discontinuous scheme (Alahuhtala, Virtakoivu, Viitanen, Routimo, & Tuusa, 2007; Dalessandro, Round, Drofenik, & Kolar, 2008). SVM aids in the utilization of the DC-link voltage and hence, it provides better flexibility in control as compared to CB-PWM, resulting in a higher quality in the three-phase current. The dwell time of the redundant switch (small switching vectors) can be adjusted to solve the issue of the unbalanced load for DC-link voltage balancing control (Hang, Zhang, Li, Huang, & Liu, 2013). Meanwhile, the impact of the zero crossing can be reduced by expanding the period of zero duty ratios in the vicinity of current zero crossing. The employment of redundant vector in SVPWM scheme mitigated the problem of current distortions at the points of zero crossing (Wenxi, Zhengyu, Ming, & Zhuang, 2014). The simulation result showed that the current distortions were removed completely with one-degree sensing error in current zero

University of Malaya

crossing. Nevertheless, SVM is difficult to implement in real systems because of its complexity. R. Burgos et al. (2007) presented a simplification for SVM with two- and three-level converter equivalent which it was capable of complementing previous carrier based SVM method.

Previous studies had demonstrated the feasibility of the Vienna rectifier for WECS with induction generator (Chen & Aliprantis, 2011) as well as PMSG (Hu & Liaw, 2013; Hu & Liaw, 2015a, 2015b), based on field-oriented control (FOC) with hysteresis current controller. Despite hysteresis comparator, SVM had also implemented to control PMSG based on Vienna rectifier (Chen, David, & Aliprantis, 2013). A reference current command LUT was developed by using the maximum torque per ampere (MTPA) curve and voltage limit which are analytically tractable. The results revealed that Vienna rectifier outperforms the classical six switches two-level converter with 0.9% increment in energy yield annually. Figure 2.13 and Figure 2.14 depict the block diagram for the two control approaches (i.e. hysteresis current control and SVM control) with different types of generators. There was another study conducted which focused on the erroneous voltage space vector generated when phase current is in the vicinity of zero crossing (Johnson & Aliprantis, 2014). From the investigation, the current and torque ripple was mitigated by engaging a clamp signal when the current is expected to cross zero, improving the THD of current from 5% to 2% at rated speed.

Vienna rectifier was employed to operate as a loss-free resistor for PMSG by the means of three-phase sliding mode control with hysteresis comparator on both current and voltage (Flores-Bahamonde, Valderrama-Blavi, Martínez-Salamero, Maixé-Altés, & García, 2014). The input impedance of the rectifier can be regulated to achieve the desired power delivered by the PMSG with ideal power factor correction. The feasibility of the concept was validated experimentally, and the system can still be operated properly even in the case of sudden loss of one of the phases of AC generator.

University of Malaya

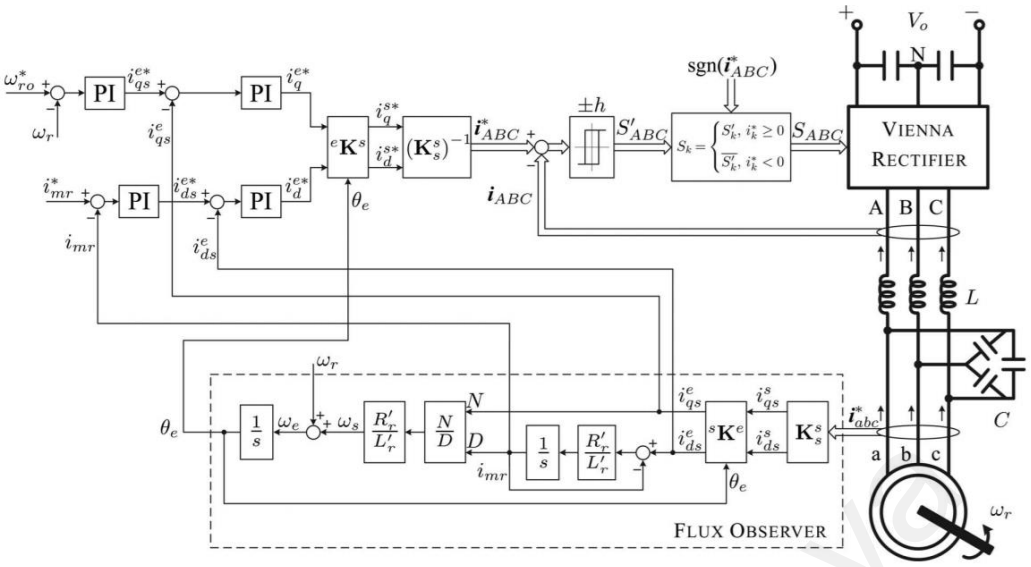

Figure 2.13: Block diagram of an induction generator with hysteresis current controller based on FOC.
(Chen & Aliprantis, 2011)

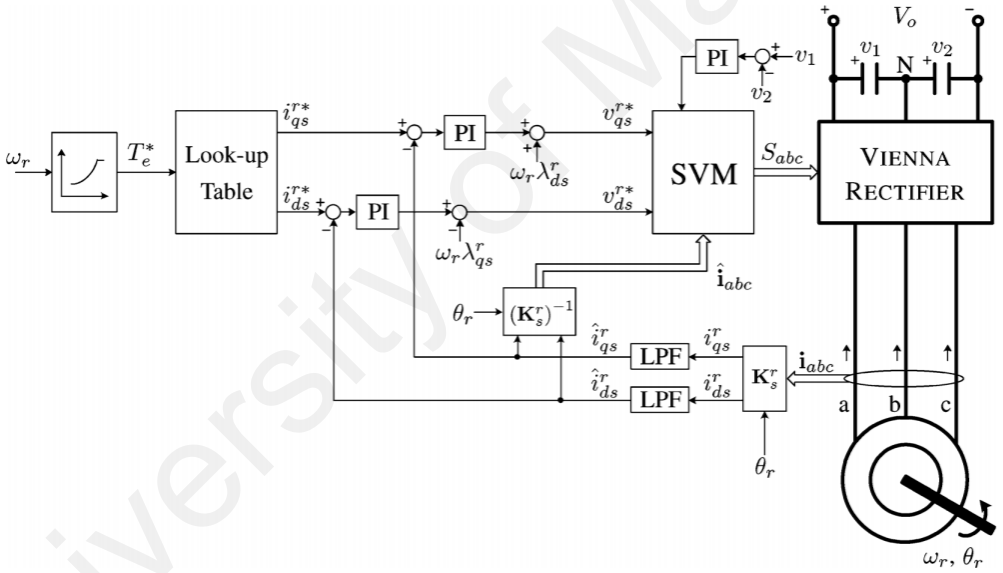

Figure 2.14: Block diagram of a PMSG with SVM based on FOC.
(Chen et al., 2013)

Limited research was conducted in terms of the employment of DTC approach with Vienna rectifier. Till date, there is just a Vienna rectifier based DTC of PMSG which was introduced by Rajaei et al. (2013). The control block diagram is presented in Figure 2.15. A DTC switching vector LUT was developed to allow torque and flux regulation whilst maintaining a balanced DC-link voltages system. Though the feasibility of DTC concept based on Vienna rectifier had been validated, the accurate and standardized model of generator voltage model is yet to be developed for the analysis of switching vectors.

University of Malaya

Meanwhile, there is no clear guideline for the switching vectors LUT development and in-depth analysis on the factors that can influence the performance of the DTC control for real-time application.

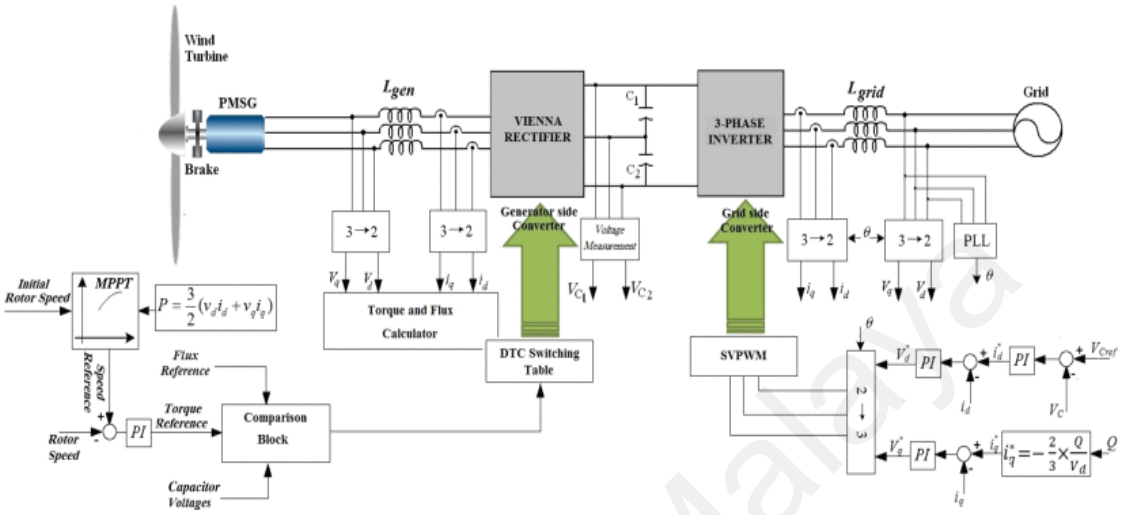

Figure 2.15: Block diagram of a PMSG with DTC. (Rajaei et al., 2013)

Recently, model predictive control (MPC) has appeared as an effective and attractive control method for power electronics converters, thanks to the advancement in microprocessor technology. The concept of MPC is intuitive and it is easy to apply to a multi-variable system (Jose Rodriguez, 2012). In addition to that, a key strength of predictive control is its ability to incorporate the constraints and nonlinearities into control law systematically (Rodriguez et al., 2013). It allows online optimization of control regardless of the state of the system. Lately, there is a MPC method based on predictive current control (PCC) applied in PMSG using Vienna rectifier where additional switching vectors are developed for the improvement of current control (Lee, Bak, Lee, & Blaabjerg, 2016). In this method, SVM was used which complicates the implementation.

To overcome this problem, finite control set model predictive control (FS-MPC) scheme can be used where fixed number of possible switching vectors are used as the control inputs. It reduces the optimal problem to an enumerated search algorithm (Vazquez, Rodriguez, Rivera, Franquelo, & Norambuena, 2017). FS-MPC of PMSG with Vienna rectifier had been proposed in (Lee & Lee, 2017; Li, Sun, Wang, Su, & Shoudao,

University of Malaya

2017) where these approaches are based on PCC concept. A MPC was synergized with a DC-link voltage PI controller as a hybrid controller for the Vienna rectifier. (Li et al., 2017). The results show good dynamic performance with wider range of operation. The outer loop was designated to control DC link voltage and input reactive power while inner loop predictive control was used to regulate the input current. The main shortcoming of the MPC is it involves a large number of computation with regards to the classic controls. The computational burden increases with the number of candidate switching vector that needs to be considered for solving the cost function. To reduce the computational burdensome for MPC, Lee and Lee (2017) used the concept of neutral point voltage bound to reduce the candidate switching vectors for MPC calculation.

Instead of PCC based MPC (as presented in (Lee et al., 2016; Lee & Lee, 2017)), predictive torque control based MPC is more advantageous in machine control, giving lower computational time and better emphasis on torque ripples rather than current ripples (Siami, Khaburi, Rivera, & Rodriguez, 2017). Table 2.4 which adopted from (Siami et al., 2017) summarized the comparative results between PCC and PTC.

Even though PTC were shown to yield satisfactory performance in machine control, its application using Vienna rectifier is not available. Hence, this work demonstrates the development of model PTC for an exhaust air turbine generator based on Vienna rectifier.

Table 2.3: Comparison between PCC and PTC.

MPC	**PCC**	**PTC**
Conceptual complexity	Low	Low
Implementation complexity	Higher	Lower
Tabulation time	Higher	Lower
Modulator requirement	No	No
Transient torque step response	Slower	Quicker
Torque ripples	Higher	Lower
Stator current THD	Lower	Higher

(Siami et al., 2017)

University of Malaya

2.6 Summary

The literature shows that there is a strong trend towards the application of variable speed systems in WECS. In terms of types of generator, PMSG is particularly favored in the small-scale direct-drive WECS. By considering the implementation cost and system efficiency, Vienna rectifier is chosen as the suitable power converter for the PMSG.

In order to implement variable speed WECS, power optimization is the main issue to be focused in order to optimize the capture power from wind energy. Based on the literature, wind power augmented devices greatly improve the performance of the VAWT. The guide-vane integration to the exhaust air turbine is implemented with a precise investigation on guide-vanes geometry, position and its distance from the turbine as suggested in the literature. Based on the surveyed literature, the application of DTC using Vienna rectifier to WECS is a relatively new concept. This situation allows the room of opportunity for WECS improvement. Therefore, MPC is suggested as a new alternative power optimization opportunity based on Vienna rectifier in this work.

University of Malaya

CHAPTER 3: PROPOSED GUIDE-VANE INTEGRATED EXHAUST AIR TURBINE GENERATOR

In this chapter, power optimization for wind power generation in terms of mechanical aspect is proposed for the exhaust air turbine generator. The mechanical improvements were made by improving the discharged airflow to the exhaust air turbine by introducing guide-vanes in between the exhaust air outlet and a vertical axis wind turbine (VAWT). A small scaled model of guide-vanes integrated exhaust air wind turbine generator was fabricated for laboratory test. The validity of the experimental results is then assessed using double multiple stream tube theory (DMST).

3.1 Theoretical background

3.1.1 Wind turbine model

The aim of this section is to describe the mechanical aspect of the wind energy conversion system (WECS). The theoretical concepts of the wind turbine for the proposed system is presented. There are two important parameters to be defined in WECS. The first parameter is the tip speed ratio, λ which it is the ratio of turbine rotational speed to the free stream wind speed. For a wind turbine with radius, R and turbine rotational speed, ω, this parameter can be expressed in terms of the free stream wind speed, V_∞ as,

$$\lambda = \frac{\text{tangential speed at blade tip}}{\text{wind speed}} = \frac{\omega R}{V_\infty} \tag{3.1}$$

The second useful parameter for the WECS is the pitch angle. Usually, the small wind turbines have fix pitch angle, β. Both parameters have their own effect on the characteristic of wind turbine that is gauged by power coefficient, C_p. The power coefficient has to be optimized to capture maximum power from a wind turbine. Theoretically, maximum C_p value can be attained is around 57% (16/27 = 0.59) according to Lanchester-Betz limit, but the good performing wind turbine can only be achieved in

University of Malaya

the value of 40%, whilst more common are in 30% range (Gitano-Briggs, 2010). This C_p does not take into account of the mechanical-into-electrical energy conversion (i.e. generator efficiency). In a typical wind turbine generator, there is an optimum tip speed ratio which denoted as λ_{opt} that yields the highest power coefficient according to different wind speed. The optimum λ value is around 5 to 7 for most of the small wind turbine (Gitano-Briggs, 2010). The total mechanical power delivered by the wind turbine is given by (Nasiri et al., 2014),

$$P = \frac{1}{2}\rho A {V_\infty}^3 C_p(\lambda, \beta) \tag{3.2}$$

where P is the wind turbine mechanical output power, A is the wind turbine's swept area, and ρ being the air density. The reference air density used at the standard sea value is 1.225 kg/m^3 at 15^o C. For a VAWT, the total swept area is,

$$A = 2Rh \tag{3.3}$$

with h being the height of the wind turbine's blade. Hence, maximum wind turbine output power, P_{max} can be attained when the VAWT is controlled to rotate at the optimized rotational speed regardless of any wind speed. It can be tabulated by,

$$P_{max} = k_{opt}{\omega_{opt}}^3 \tag{3.4}$$

The optimum constant, k_{opt} can be obtained by re-arranging equation (3.1) and (3.2) with ω_{opt} as the optimum rotational speed as follows,

$$k_{opt} = \rho h R^4 C_p(\lambda, \beta)\left(\frac{1}{\lambda_{opt}}\right)^3 \tag{3.5}$$

University of Malaya

3.1.2 General aerodynamic model for the straight-bladed VAWT

Straight-bladed Darrieus VAWT is the simplest turbine in terms of structural design (Beri & Yao, 2011; Islam, Ting, & Fartaj, 2008). Nevertheless, the magnitude and vector components of a VAWT's blade are changing continuously with the blade azimuth angle during its operation give rise to complexity in aerodynamic analysis. Blade element momentum theory is used to determine the VAWT blade performance as it allows the analytical investigation of all the forces acting on the blades as they move through the air with the consideration of the geometrical shape of the blades (Martin & Roux, 2010).

Figure 3.1 illustrates a section of a VAWT's airfoil blade with its associated forces and velocities at a specific azimuth angle. When the turbine blade is in rotating motion, giving it a tip speed, ωR in which it is tangential to the rotational axis, the turbine blade experiences a relative velocity, V_R when the wind flows through the VAWT with an induced velocity, V_a. Subscription ∞ in the figure represents the free stream condition. Meanwhile, θ denotes the blade's azimuth angle, R is the turbine's radius and ω being the rotation speed.

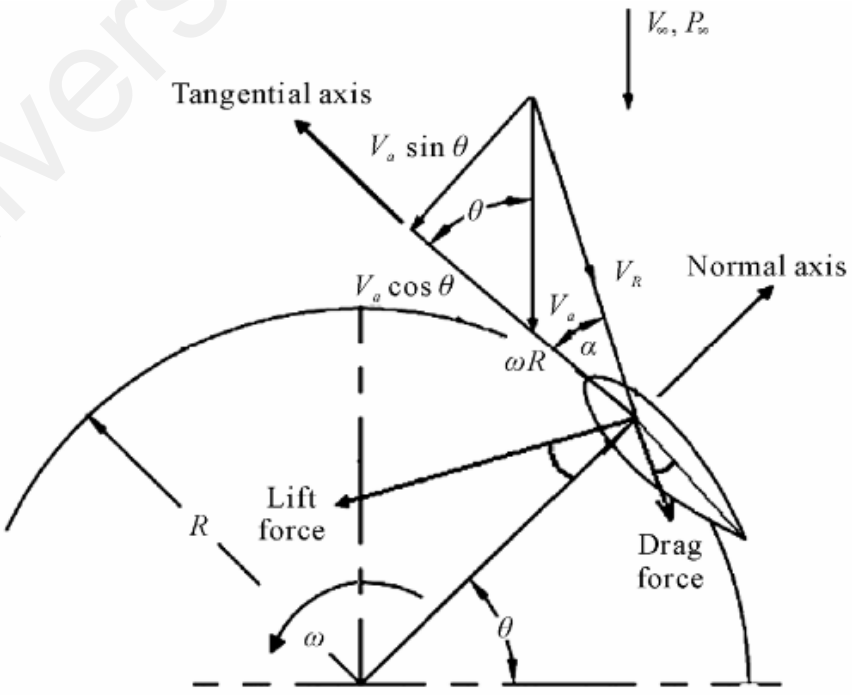

Figure 3.1: Airfoil velocity and component of the local angle of attack. (Beri & Yao, 2011)

University of Malaya

Generally, V_R can be expressed using vector velocity triangle,

$$V_R = \sqrt{(V_a \sin\theta)^2 + (\omega R + V_a \cos\theta)^2} \tag{3.6}$$

According to actuator strip theory, the deceleration of wind speed at the upstream of the rotor occurs as the wind energy is extracted by the turbine. An axial induction factor, a is used to define the fractional decrease in wind speed between the free stream and the rotor plane. The induced velocity can be calculated by,

$$V_a = V_\infty(1 - a) \tag{3.7}$$

With the consideration of induction factor, equation (3.6) can be re-written as:

$$V_R = \sqrt{(V_\infty(1 - a)\sin\theta)^2 + (\omega R + V_\infty(1 - a)\cos\theta)^2} \tag{3.8}$$

The angle of attack, α is the angle between a reference line on a lifting body (often the chord line of the blade) and it can be computed as follows,

$$\alpha = tan^{-1}\left[\frac{V_a \sin\theta}{\omega R + V_a \cos\theta}\right] \tag{3.9}$$

Figure 3.1 also shows the directions of the lift and drag forces and their normal and tangential components when the wind flows through the blades. Basically, lift coefficient, C_l weights the elevation force on the blade, and it is always perpendicular to the relative motion vector (Islam et al., 2008). On the other hand, drag coefficient, C_d is the factor that quantifies the resistance of the blade in moving against the fluid flow, and is in the direction of the relative motion vector. By resolving the C_l and C_d into the forward direction of turbine blade, tangential force and normal force coefficient (C_t and C_n respectively) can be obtained as below,

$$C_t = C_l \sin\alpha - C_d \cos\alpha \tag{3.10}$$

$$C_n = C_l \cos\alpha - C_d \sin\alpha \tag{3.11}$$

University of Malaya

From these expressions, C_t is the difference between the tangential components of lift and drag forces whilst C_n is the difference between the normal components of lift and drag forces (Beri & Yao, 2011).

From blade element analysis, lift and drag force acting over the blades are integrated over the total blade spin, incorporating the wind speed terms to obtain the shaft torque and power developed by the VAWT. Since the tangential and normal force exist for any azimuthal position, they are considered as a function of azimuth angle. Average tangential force on a blade can be described by (Islam et al., 2008):

$$F_t = \frac{1}{2\pi}\int_0^{2\pi} F_t\,(\theta)d\theta \tag{3.12}$$

The instantaneous forces acting on blade into total tangential force and normal force components at a specific azimuth angle yields,

$$F_{t_i} = \frac{1}{2}\rho {V_R}^2 (hc) C_t \tag{3.13}$$

$$F_{n_i} = \frac{1}{2}\rho {V_R}^2 (hc) C_n \tag{3.14}$$

where *h* and *c* are the blade's height and chord's length respectively.

The instantaneous torque, τ_i on a turbine's blade at an azimuth angle, θ is,

$$\tau_i = \frac{1}{2}\rho {V_R}^2 (hc) C_t R \tag{3.15}$$

The total torque, τ can be obtained with the consideration of the number of blades, *N* and VAWT's radius as:

$$\tau = N F_t R \tag{3.16}$$

Then, the total power, *P* from the VAWT can be calculated by,

$$P = \tau\omega \tag{3.17}$$

University of Malaya

3.2 Overview of the guide-vane integrated exhaust air turbine generator

The exhaust air turbine generator is an innovative idea which proposed recently to generate electricity by the means of extracting unnatural wind resources using micro WECS (Chong et al., 2013). It is an onsite energy generating system that consists of a VAWT that is connected to a PMSG which can be controlled via a power electronics converter. This system is designed to be retrofitted above the exhaust air outlets of the cooling towers to harness the wind which would otherwise be discharged to the atmosphere and hence, wasted. The discharged air is used to rotate wind turbine for energy recovery.

Shown in Figure 3.2, it is the general arrangement of the guide-vanes integrated exhaust air turbine generator. 5 blades H-rotor typed VAWT is used as the exhaust air turbine and it is mounted above the cooling tower in cross-wind orientation by a supporting frame. There are two guide-vanes hold by the supporting frame and they are fitted with their respective optimum configuration (in terms of position and angle) in between the discharged air outlet and the exhaust air turbine generator. The configuration of the VAWT with the cooling tower was optimized and the details can be found in the previous work conducted (Fazlizan, 2016).

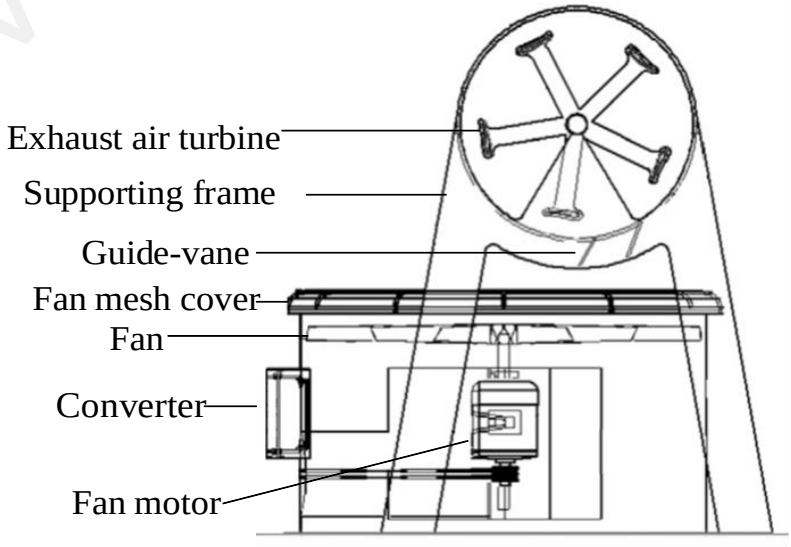

Figure 3.2: Overview of the guide-vanes integrated exhaust air turbine generator.

University of Malaya

3.3 Working principle of the guide-vanes

As a continue works for this system, power optimization approaches were applied in order to maximize the wind energy potential. There are disadvantages of the H-rotor typed VAWT, i.e. poor self-starting behavior and low power coefficient as compared to HAWT (Takao et al., 2009). As shown in equation (3.2) wind power is directly proportional to the cube of wind speed, a slight increase in wind speed approaching to wind turbine will result in significant improvement in the output power. This theory is successfully applied by the proposed guide-vanes integration exhaust air turbine.

Two guide-vanes are fitted in the middle of the VAWT and the exhaust air outlet at their respective optimum angle, dividing the discharge wind into several channels of airflow that are beneficial in terms of power efficiency. The main objective of the guide-vane is to direct and focus the wind speed to the turbine to overcome abovementioned drawbacks of the VAWT. As a result, the induced exhaust airflow characteristic improved since it is smoothened and concentrated, allowing higher wind speed interacts with the turbine. In other words, guide-vane basically acts as a nozzle in the upstream of the turbine rotor. Moreover, the integration of the guide-vanes with the exhaust air turbine generator also help in assisting the turbine's self-starting behavior. As a result, the exhaust air turbine is capable of rotating faster to the rated speed and thereby, enhancing the output power generation.

Despite to that, the maximum output power can also be obtained by matching the discharged air better towards the optimized angle of attack of the VAWT. The guide-vanes can aid in realizing this goal by achieving the correct angle of attack (AOA) of the exhaust air turbine's blade. As presented earlier, velocity triangle is deployed and it is modified with the inclusion of guide-vane angle as depicts in Figure 3.3. This figure demonstrates how the original exhaust air direction, V_∞ is affected by the installed guide-vane in the wind path to the induced wind speed, V_a.

University of Malaya

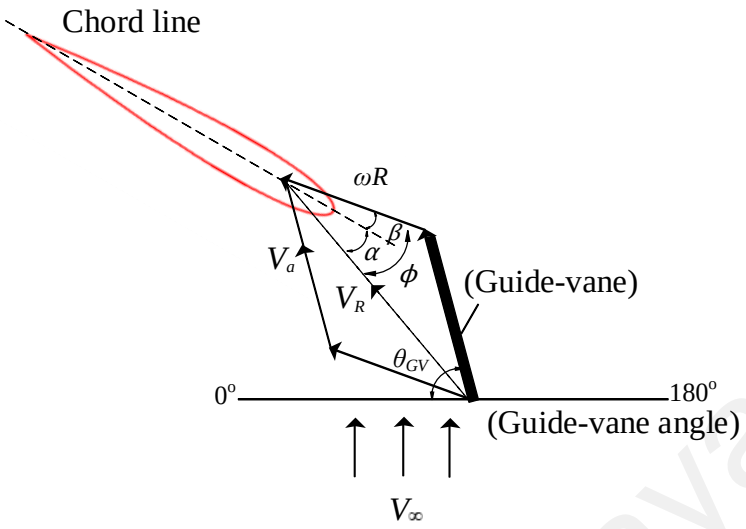

Figure 3.3: Velocity triangle with the consideration of guide-vane angle.

Guide-vane angle, θ_{GV} is defined as the induced exhaust air flow angle with respect to the horizontal axis in which it is the angle where the exhaust air is channeled to. The magnitude of guide-vane angle determines the value of AOA of fluid flow on the turbine blade. By changing the guide-vane angle, induced wind flow angle, ϕ into wind turbine is varied and thus, AOA changes. It is calculated by,

$$\alpha = \emptyset - \beta \tag{3.18}$$

The adjustment of guide-vane angle also influences the C_l experiences on the blade as it varies uniquely with the AOA. Meanwhile, it is worth to take note that the lift generated from the blade will reach maximum at a specific angle, called critical angle of attack. The increment of AOA beyond this point will create a separation of the airflow from the upper surface of the blade becomes more pronounced, leading to a reduction in the rate of increase of the C_l (Maughmer, 2003). Hence, the C_l increases up to a maximum, after which it decreases. This issue is vital to be considered during the determination of the optimum guide-vane angle for the exhaust air turbine generator. Thus, there is a suitable range of guide-vane angle to be identified for guide-vane implementation to ensure the wind flow is restricted to such wind power enhancement zone.

University of Malaya

3.4 Theoretical model development with guide-vanes angle

The mathematical expression for the AOA of the induced exhaust airflow on the turbine blade after the adjustment of guide-vane has been derived. The computation of the wind power generation with the consideration of guide-vane angle alteration uses the blade element theory and the knowledge of blade geometry as discussed previously. First, the wind turbine is divided into 4 quarters as shown in Figure 3.4 based on the blade's azimuth angle. The 4 quarters of the exhaust air turbine are determined as follows: -

1) Quarter 1: Blade azimuth angle in the range from 1^o - 90^o
2) Quarter 2: Blade azimuth angle in the range between 91^o to 180^o
3) Quarter 3: Blade azimuth angle at the range between 181^o to 270^o
4) Quarter 4: Blade azimuth angle at the range between 271^o to 360^o

In addition, there are few assumptions have to be made for the AOA determination after the adjustment of guide-vane angle, i.e.,

1) Induced wind flow angle is equivalent to the guide-vane angle after the adjustment of guide-vane angle.
2) Induced factor, a is assumed to be 1/3 such that the airflow to the rotor plane is reduced to 2/3 of its original free-stream velocity. For the case in the far wake, it further decreases to 1/3 of from its initial velocity (Ben Geurts, 2010). Thus, the wind speed for the downwind side of the exhaust air turbine, V_{a_down} (at quarter 3 and 4) is calculated by:

$$V_{a\_down} = V_{\infty}(1 - 2a) \tag{3.19}$$

University of Malaya

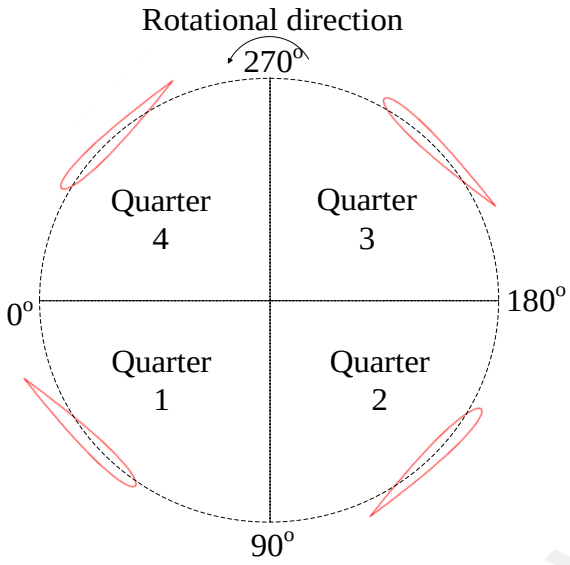

Figure 3.4: Different turbine's quarters according to blade azimuth angle.

Table 3.1: Summarized new angle calculation for each turbine's quarter.

Quarter	**Quarter 4 (271° - 360°)**	**Quarter 3 (181° - 270°)**
Velocity triangular diagram	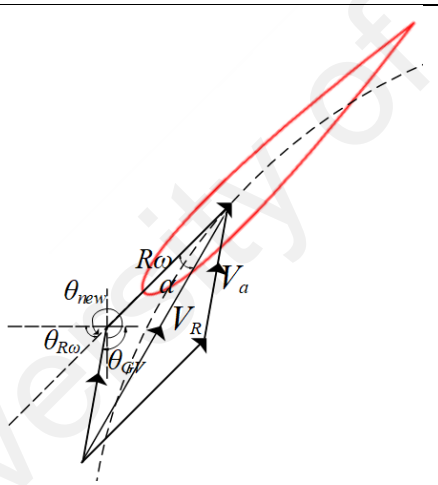	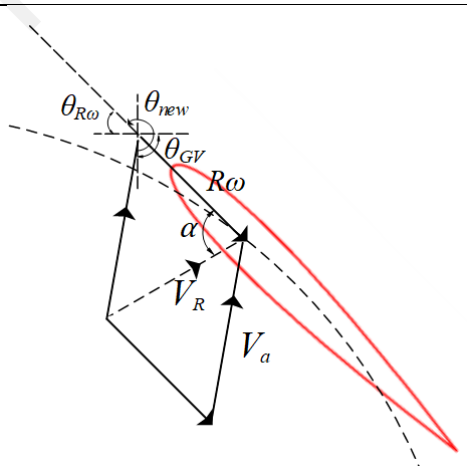
θ_{new}	$\theta_{new} = \theta_{GV} + (180^o + \theta_{R\omega})$	$\theta_{new} = \theta_{GV} + (180^o - \theta_{R\omega})$
Quarter	**Quarter 1 (1° - 90°)**	**Quarter 2 (91° - 180°)**
Velocity triangular diagram	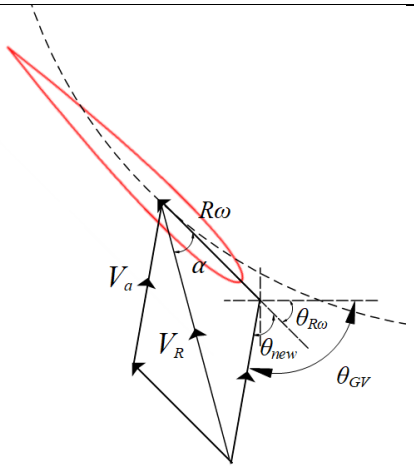	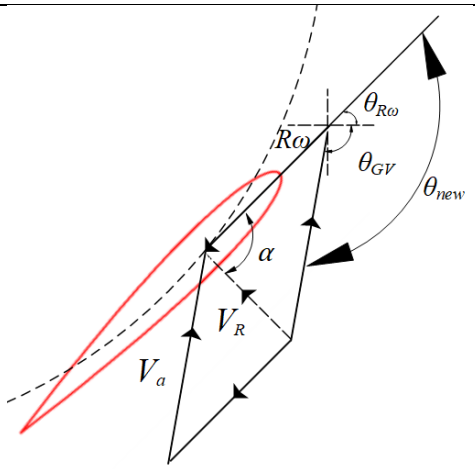
θ_{new}	$\theta_{new} = \theta_{GV} - \theta_{R\omega}$	$\theta_{new} = \theta_{R\omega} + \theta_{GV}$

University of Malaya

Table 3.1 summarized the equation for new angle calculation for each quarter together with its corresponding velocity triangular diagrams. Since guide-vane angle is determined with respect to the horizontal axis, a new angle which is known as tip speed angle, $\theta_{R\omega}$ is defined which it is the angle from blade speed, ωR (chord line) to the horizontal axis. A standardized model is developed for $\theta_{R\omega}$ tabulation which depends on the turbine's quarter, either it is even-numbered or odd-numbered quarter as follows,

$$\theta_{R\omega} = \begin{cases} \frac{q}{q_{max}} 2\pi - \theta; q \text{ is odd} - \text{numbered quarter} \\ \theta - \left(\frac{q-1}{q_{max}}\right) 2\pi; q \text{ is even} - \text{numbered quarter} \end{cases} \quad (3.20)$$

where q being the quarter number; q = {1,2,3, and 4} with q_{max} = 4.

With the inclusion of guide-vane together with the exhaust air turbine generator, the approaching wind flows to the turbine blade is no longer vertical (90^o) to the turbine's blade. Thus, the azimuth angle that used in the equation (3.9) for the AOA calculation is no longer valid and it has to be modified with the consideration of guide-vane angle, which denotes as new angle, θ_{new}. For instances, by referring the velocity triangle diagram for turbine's quarter 1 as depicted in Table 3.1, which it is located at the upwind side of the turbine, the new angle is expressed as,

$$\theta_{new} = \theta_{GV} - \theta_{R\omega} \quad (3.21)$$

Take note that the new angle is measured from the induced wind speed to the tip speed vector, ωR in counter-clockwise direction. Similarly, the new angle for quarter 2 is also created. As comparing its triangle velocity schematic to quarter 1, the tip speed angle is located above the horizontal axis. For such a case, the new angle for quarter 2 can be calculated with expression below,

$$\theta_{new} = \theta_{GV} + \theta_{R\omega} \quad (3.22)$$

The same way is used to derive the new angle for quarter 3 and quarter 4 which situated at the downwind side of the VAWT. It is worth to emphasize that the tip speed angle for

University of Malaya

quarter 3 and 4 is located on the left-hand side with respect to the vertical axis. Thus, the modified tip speed angle, $\theta'_{R\omega}$ in quarter 3 is,

$$\theta'_{R\omega} = 180^{o} - \theta_{R\omega} \tag{3.23}$$

whilst for quarter 4, it becomes expression as below since it is located below the horizontal axis,

$$\theta'_{R\omega} = 180^{o} + \theta_{R\omega} \tag{3.24}$$

Subsequently, the revised tip speed angle, $\theta'_{R\omega}$ will be added together with the guide-vane angle to compute the new angle for both quarter 3 and 4.

The calculated new angle is used to replace the blade azimuth angle in equation (3.9) to obtain the AOA produced after the adjustment of guide-vane. The expression for AOA after substituting the new angle becomes,

$$\alpha = \tan^{-1}\left[\frac{V_a \sin\theta_{new}}{\omega R + V_a \cos\theta_{new}}\right] \tag{3.25}$$

Then, the AOA is used to tabulate the tangential force using equation (3.12) as described previously. Subsequently, the generated torque and power from the exhaust air wind turbine after the guide-vane angle alteration can also be calculated using equation (3.16) and (3.17).

3.5 Experimental set-up with indoor lab-scale prototype

The effect of guide-vanes integration to the exhaust air generator was evaluated via indoor laboratory test. In conducting the study, an indoor lab-scale prototype was built as per the parameters presented in Table 3.2. A small scaled of cooling tower was made of fiber reinforced plastic, by courtesy of Truwater Cooling Tower Sdn. Bhd. There was a cooling fan which driven by a 750 W three-phase motor to discharge the exhaust air. A H-rotor typed VAWT which is commercially viable (rated at 10W with airfoil profile typed MH114 13.02%) was used as the exhaust air turbine. The specification of the

University of Malaya

VAWT can be obtained in Appendix A1. The exhaust air turbine generator was connected to a dynamometer with real-time monitoring and data logging features. The displayed outputs from the dynamometer included turbine rotational speed, torque, electrical power, and the duty cycle of the converter. These data were stored in the data logger for easy data acquisition. The sampling period for data logger was set to 1 s.

Table 3.2: Parameters of the experimental set-up used in indoor laboratory test.

Parameters	**Values**
Cooling tower's fan model	
Fan diameter	0.8 m
Stack height	0.155 m
Air inlet area	0.5329 m^2
Fan motor power	0.75 kW
Discharge air outlet duct	0.73 m
VAWT	
Diameter	0.3 m
Rated power	10 W
Rated wind speed	10 m/s
Number of blades	5
Pitch angle	10^o
Type of generator	Direct drive synchronous PMSG
Guide-vane	
Middle guide-vane length	650 mm
Side guide-vane length	200 mm
Width	100 mm

Figure 3.5 shows the fabricated guide-vanes integrated model, which will be assembled above the scaled down model of the cooling tower. The guide-vanes were fitted in a 0.73 m diameter of circular discharged air outlet duct which built using the same material as the cooling tower. The guide-vane supporting shafts were held by two ball bearings at each side and they were coupled to a servo-motor which controls by a control platform, Arduino. The servo motor was programmed to regulate the guide-vane angle after getting the desired angle from the user.

University of Malaya

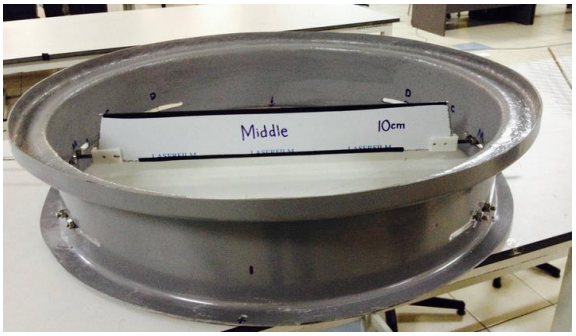

Figure 3.5: Guide-vanes model used for indoor laboratory test.

In order to implement guide-vanes together with the exhaust air turbine, it is crucial to understand the response of the exhaust air turbine to the installed guide-vanes. The position of guide-vane in the *x*-axis and its angle greatly affect the performance of VAWT especially in power coefficient (Kim & Gharib, 2013). A guide-vane panel was developed and attached on the side of the supporting frame to facilitate the guide-vanes effect investigation as depicted in Figure 3.6. The guide-vane panel was constructed with an adjustable position profile in the *x*-axis, allowing the determination of the guide-vane position in which does not gives negative impact (wind blockage) to the exhaust air wind turbine and the original cooling tower system. Two guide-vane angle scales were attached to the developed panel and hence, the adjusted angle of the guide-vane can be easily identified. The guide-vane panel with guide-vane angle scales is illustrated in Figure 3.7.

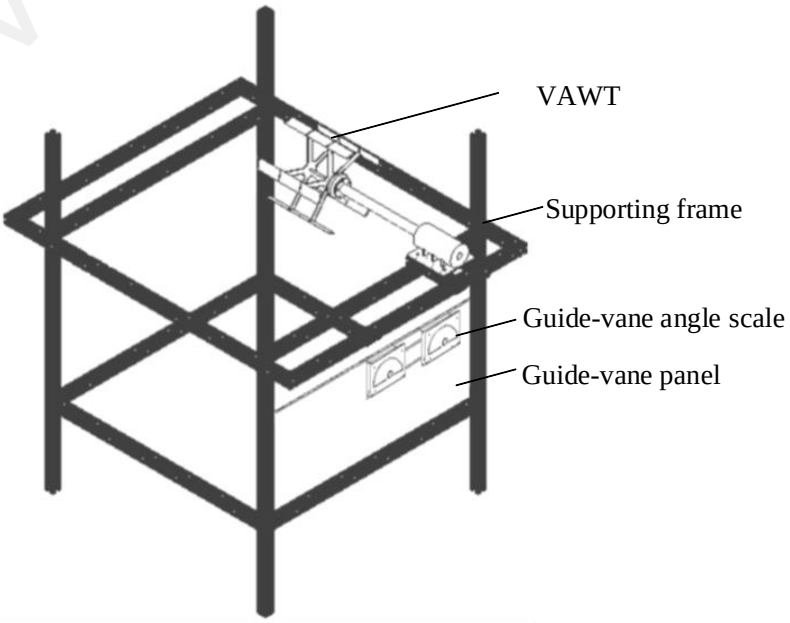

Figure 3.6: The assembled guide-vane panel with supporting structure.

University of Malaya

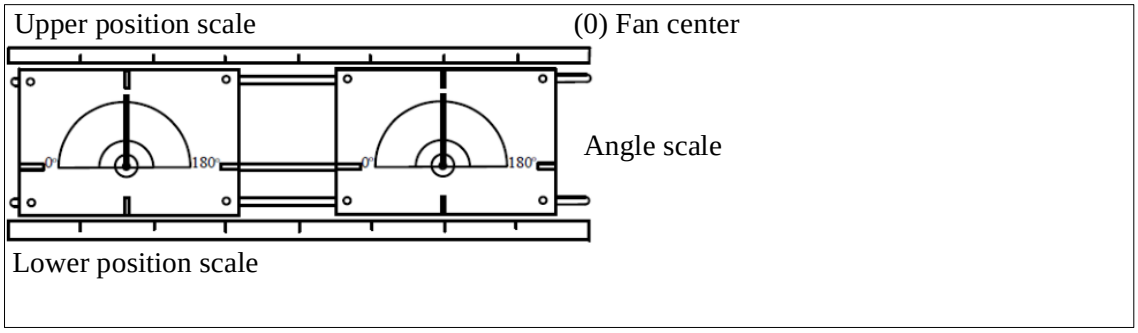

Figure 3.7: Guide-vane panel with the angle scales.

The experimental tests were carried out in two set-ups, i.e.: -

1) Cooling tower with the exhaust air turbine generator only

2) Cooling tower with the guide-vanes integrated exhaust air turbine generator

Each of the set-ups is elaborated in detail individually.

3.5.1 Set-up with exhaust air turbine generator only

The first test to be conducted will be on the exhaust air turbine generator. Based on the previous work conducted by the previous researcher (Fazlizan, 2016), the optimum exhaust air turbine's position was determined to be located at 200 mm in horizontal axis calculated from the center of VAWT to the center of fan outlet and at a height of 400 mm above the cooling fan. The height was measured from the circumference of the wind turbine to the fan outlet mesh. The obtained result of this set-up was used as the benchmark for comparison analysis as it represented the original performance of the exhaust air turbine generator without any add-on features. The experimental set-up of the exhaust air turbine with the cooling tower was depicted in Figure 3.8 and Figure 3.9.

University of Malaya

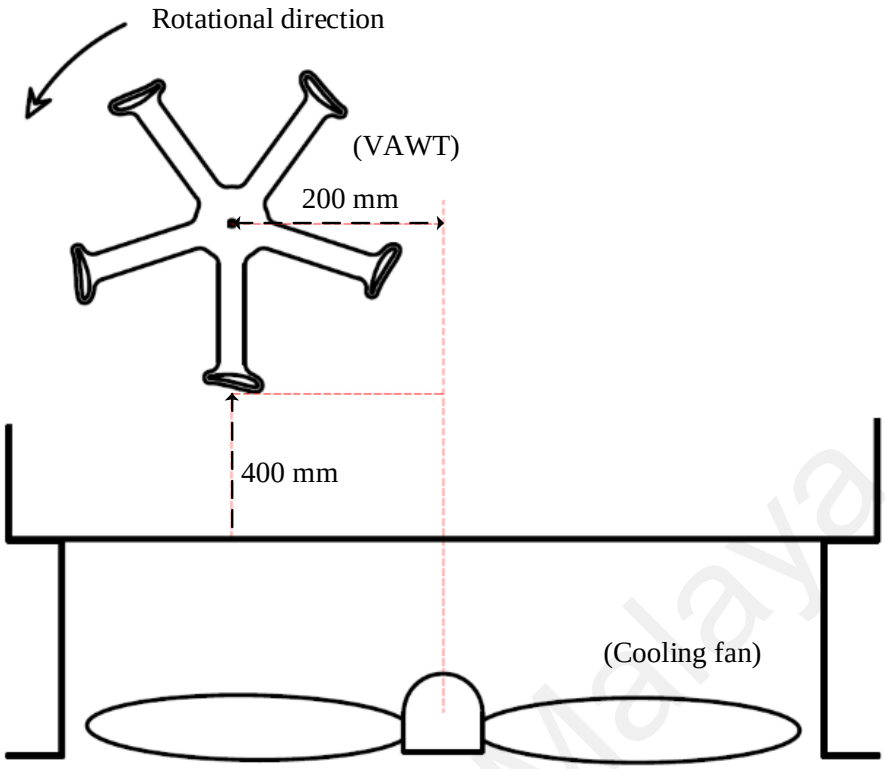

Figure 3.8: Exhaust air turbine generator's position above the cooling tower.

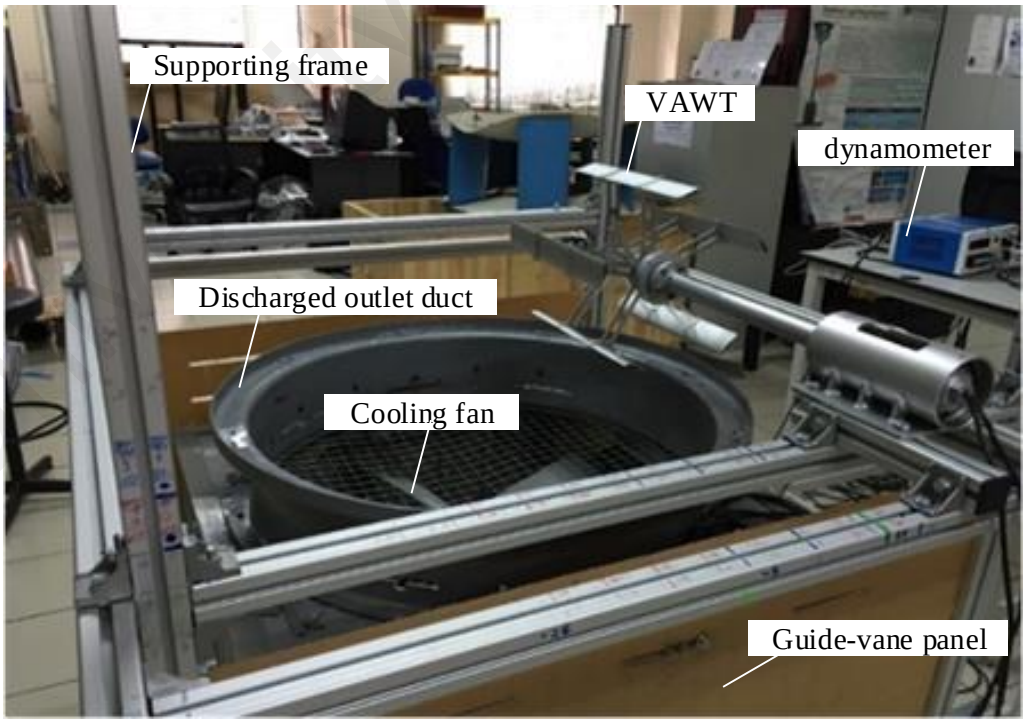

Figure 3.9: Experimental set-up for the exhaust air turbine generator.

University of Malaya

3.5.2 Set-up with the guide-vanes integrated exhaust air turbine generator

Figure 3.10 and Figure 3.11 showed the experimental set-up of the guide-vanes integrated system and the specific dimensions for guide-vane effect investigation. There were two guide-vanes fitted in the system according to the discharged air profile. One of the guide-vane which located near to the center of the fan is known as middle vane and the other is called as side vane. The guide vanes position study was only run on the middle vane as it is located away from the discharged wind-stream to the exhaust air turbine. As illustrated in Figure 3.10, there were five horizontal positions for the middle vane (in *x*-axis) to be investigated, started from 160 mm to 200 mm varies in the step of 10 mm measured from the center of VAWT to middle vane's shaft. This range of guide-vane position was decided to ensure the middle vane does not directly locate under the VAWT so that it does not become a wind blockage to the VAWT. In order to secure the accuracy of the position adjustment, the middle vane was adjusted by aligning the center of the guide-vane shaft (during the guide-vane angle set at 90^o) to match with the desired *x* position at both upper and lower position scale. The guide-vane angle was then adjusted by a servo-motor in the range from 0^o to 180^o in the interval of 10^o at a pre-set load converter's duty cycle after the position of the guide-vane was determined.

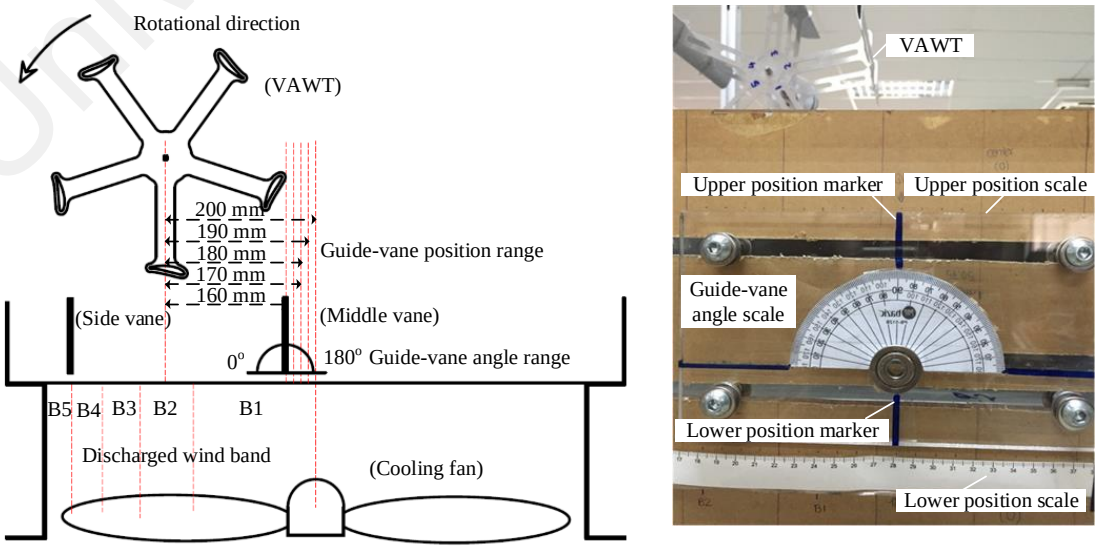

Figure 3.10: Guide vanes position and angle range for the experiment.

University of Malaya

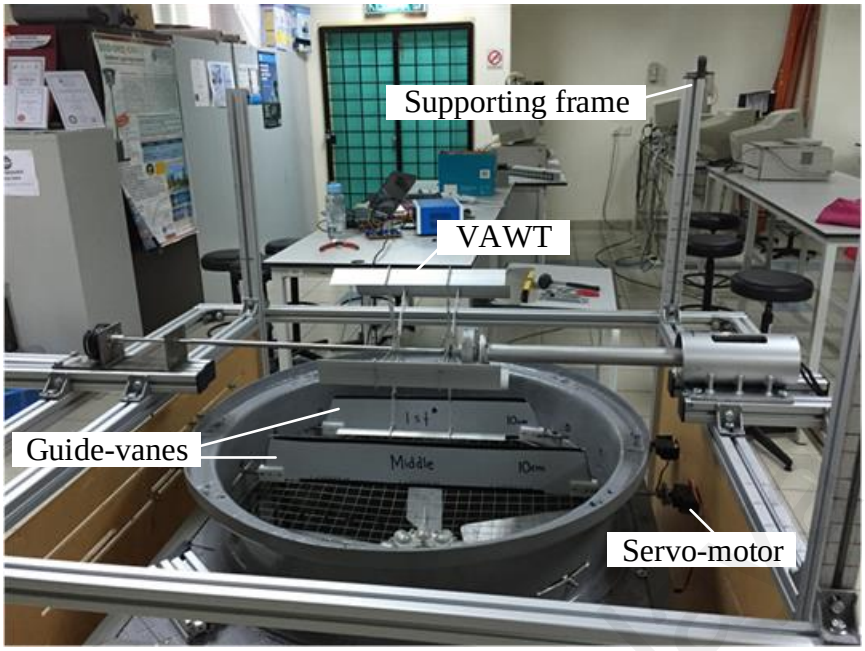

Figure 3.11: Experimental set-up of the guide-vanes integrated exhaust air turbine.

3.5.3 Turbine performance evaluation method

The experiment was carried out to clarify the effect of the guide-vanes integration with the consideration of setting angle and its installation position on the turbine's power coefficient. Power coefficient and tip speed ratio were calculated to assess the performance of the wind turbine. In order to quantify the power coefficient, the output of the wind turbine which logged using the dynamometer are used for the study. The measurement of VAWT's rotational speed was carried out by first allowing it to rotate in the discharged wind stream without any load application until it reaches its stable rotational speed. The time response of the VAWT to reach its stabilized rotational speed was also recorded.

The dynamometer was programmed with load regulation where the load applied to the generator can be adjusted by varying converter duty cycle. Different load was applied to the generator to investigate the VAWT's behavior. 100 Ohm of resistive dump load was used in this work. The load was gradually changed by 10% increment in duty cycle and its stabilized speed, torque, and power generated at each load condition were recorded.

University of Ma

3.5.4 Cooling tower performance evaluation method

In addition, the impact of the existence of the exhaust air turbine generator with and without the guide-vanes integration on cooling tower performance is also vital to be evaluated. There are three important parameters to measure, i.e. discharged air speed, inlet air speed and power consumed by the cooling fan motor. The measurement methods for each parameter are presented in the following sections.

3.5.4.1 Cooling fan power consumption measurement

A three-phase power quality analyzer was deployed to evaluate and log the fan's motor power consumption. The power measurement was made on the three-phase output on the VFD which were connected to the three-phase terminals of the cooling fan motor.

3.5.4.2 Intake air speed measurement

The inlet air speed was measured at the air entrance on each side of the cooling tower using a hot-wire anemometer. The 4 intake air measurement points of the air inlet were labeled as A, B, C, and D as shown in Figure 3.12. The mean inlet air speed was then tabulated by averaging the measured intake air speed from each measurement points.

In addition to that, the volumetric flow rate into the cooling tower was computed to evaluate the amount of wind obstruction when the exhaust air turbine with and without guide-vanes integration was positioned at the cooling tower's outlet. The volume flow rate is expressed as follows,

$$Q_{inlet} = V_{inlet} A_{inlet} \tag{3.26}$$

where Q_{inlet} being the volume flow rate; V_{inlet} is the mean intake air speed; and A_{inlet} is the air inlet area.

University of Malaya

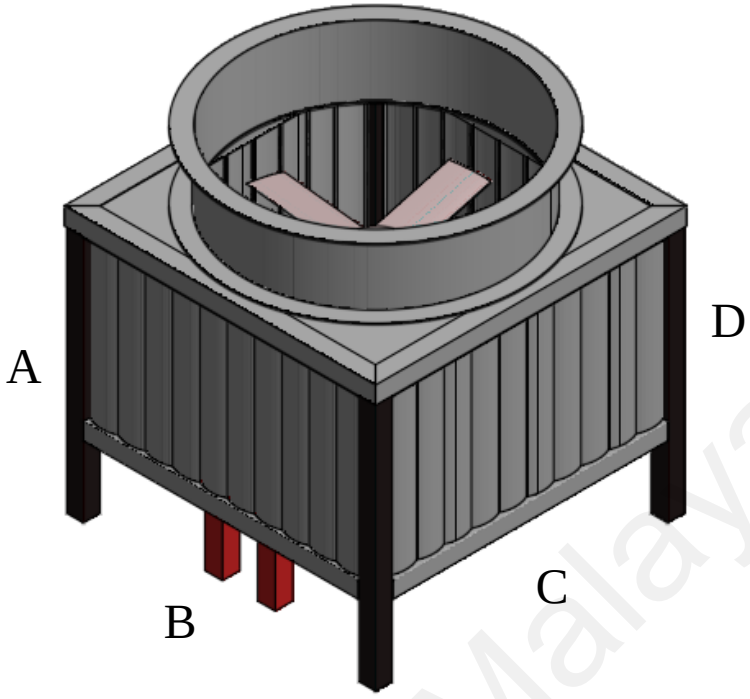

Figure 3.12: Intake air speed measuring points.

3.5.4.3 Discharged air speed measurement

In terms of discharged air speed measurement, it is more complex as the discharged air speed for each point changes over a cross-sectional area of the exhaust air cylindrical duct (Daly, 1979). Similarly, the hot-wired anemometer was used for the discharged wind speed measurement. A typical measuring method for cylindrical ducts from Cooling Tower Institute (CTI) was adopted in this test in which the discharge air area was divided into numerous circular band of identical area and the discharged air speed was computed by averaging the wind speed recorded at every quarter of the circle (Herrman, 1962). In this work, five bands of identical areas were divided for the discharged air speed measurement in four quadrants as shown in Figure 3.13. The discharged air speed's measuring point was located at the center of each band which labeled with the number in sequencing order as the distance from the fan center. The discharged air speed was then calculated by averaging the 20 readings recorded.

University of Malaya

For this scaled down model of cooling tower, the total exhaust air outlet area is 0.42 m^2 with each band of the concentric area equivalent to 0.083 m^2. Taking the center of each concentric band to the center of the outlet as the measuring points, the calculated measuring points are summarized in Table 3.3. Discharged air speed ratio was then calculated to determine the impact of discharged air flow over the guide-vanes in terms of its wind speed and guide-vane angle. With V_{outlet} being the measured discharged air speed and $V_{outlet,GV}$ being the measured discharged air speed with guide-vane integration, the discharged air speed ratio, *Ratio* is defined as,

$$Ratio = \frac{V_{outlet,GV} - V_{outlet}}{V_{outlet}} \tag{3.27}$$

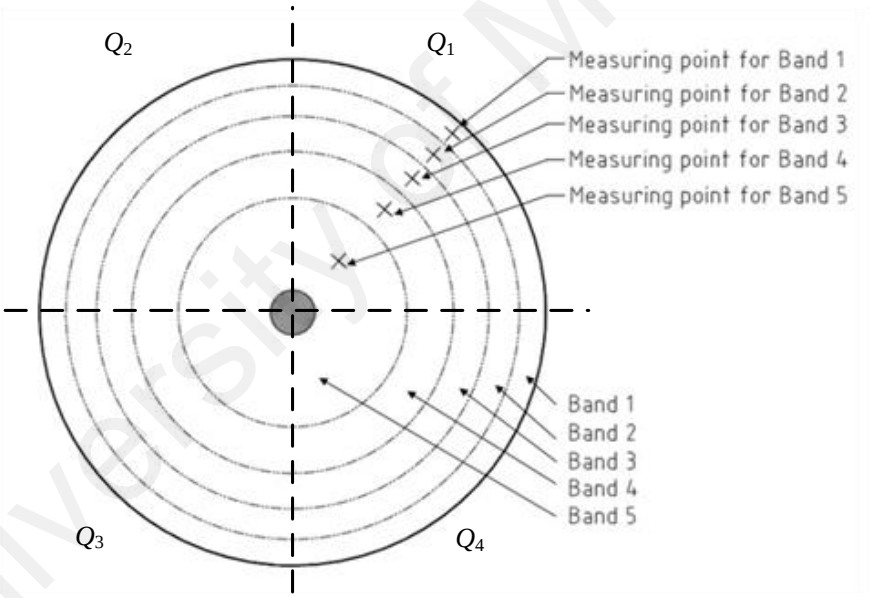

Figure 3.13: Measuring point for the discharged air flow from the circular duct.

Table 3.3: Discharge wind speed band specifications.

Band	Radius range (mm)	Measuring point for each band (mm)
1	0 – 163	82
2	163 – 231	197
3	231 – 283	257
4	283 – 326	305
5	326 - 365	346

University of Malaya

3.6 Theoretical verification using DMST theory

Due to the facts that the discharged air speed across the wind turbine is non-uniform, a well-established method, double multiple stream tube (DMST) theory was used to predict the performance of VAWT (Beri & Yao, 2011). This theory was adopted with the aim to evaluate all the forces experienced by the blade together with its generated power by using the induced velocity field of the turbine. It was conducted via a semi-empirical approach in which some of the measured parameters from the experiment, i.e. turbine's rotational speed and discharged wind speed were used together with turbine airfoil parameters for DMST-based analysis. The modified model for AOA calculation, equation (3.25) which explained in section 3.4 was included in the DMST-based analysis to study the effect of guide-vane inclusion in the wind power generation system.

The exhaust air turbine swept area was first divided into 18 aerodynamically independent parallel stream tubes with the blade's azimuth angle divided uniformly in the step of 10^o for both upstream and downstream as shown in Figure 3.14. The blade momentum balance was tabulated individually for all the 36 stream tubes, allowing arbitrary variation in airflow due to the guide-vane angle adjustment to be taken into consideration in the analysis. It was assumed that the wind speed within each stream tube is uniformed. Equation (3.6) - (3.15) were used to calculate the instantaneous torque for each stream tubes. Since the calculation of the instantaneous torque along the blade angle required the information of C_l and C_d, such data can be extracted from an online airfoil database. The airfoil's type used in this work is Martin Hepperle MH114 airfoil, Reynolds number of 25000 (Hepperle, 2008). Its data was recorded in Appendix A3.

It is important to highlight that the blade of the VAWT will undergo different wind speed as it travels along the turbine's azimuth angle since the discharge outlet circular duct gives non-uniform wind speed profile. Hence, the exhaust air turbine's diameter was divided into 5 sections according to the discharged air band (sees Figure 3.14) and each

University of Malaya

of the section has their corresponding wind speed for accurate analysis. Table 3.4 is constructed to categorize the different wind speed band for each stream tubes. Lastly, the total mean torque generated from the turbine was tabulated by summating the tangential force for one revolution with the consideration of blade numbers and turbine radius. Mean power generated from the VAWT was then obtained by multiplying rotor speed measured from the experiment. The comprehensive procedure for DMST-based analysis calculation can be found in Figure 3.15.

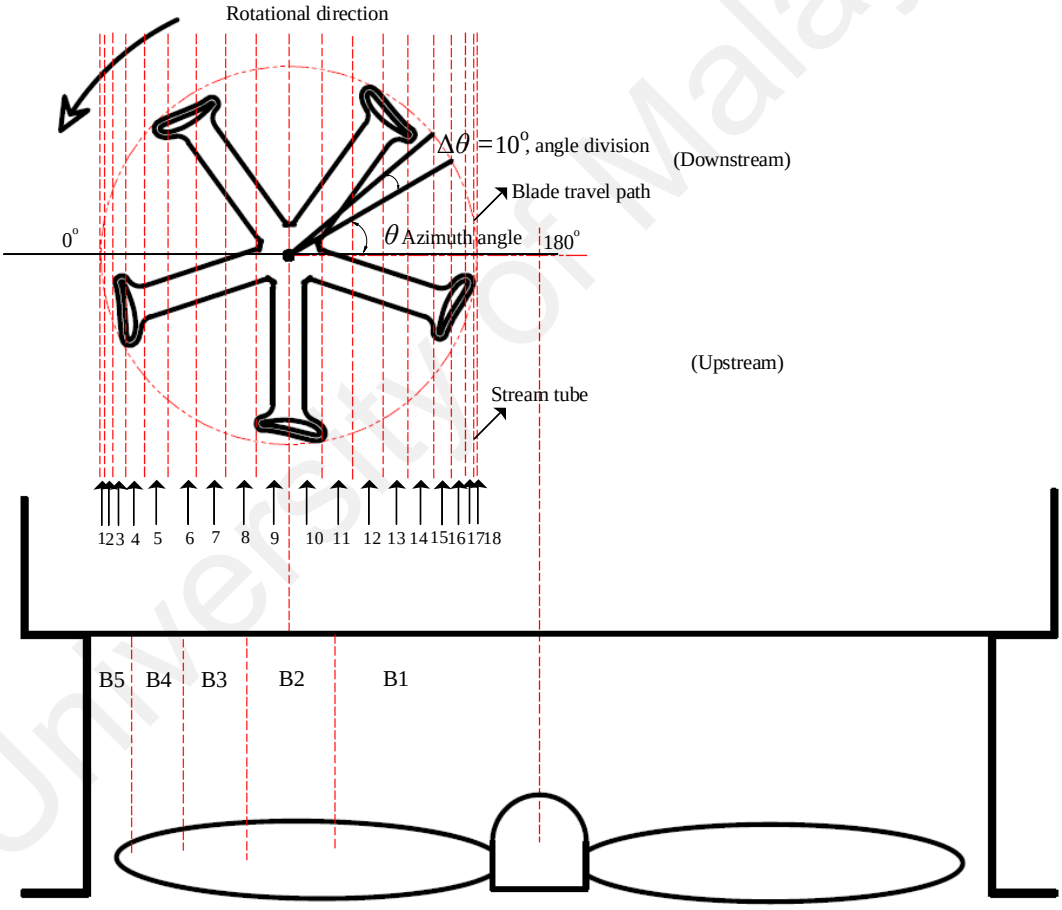

Figure 3.14: Stream tube model for the exhaust air turbine generator.

University of Malaya

Table 3.4: Different wind speed for each stream tubes.

Discharged air band	Stream tube number
1	12 - 18
2	9 - 11
3	7 - 8
4	4 - 6
5	1 - 3

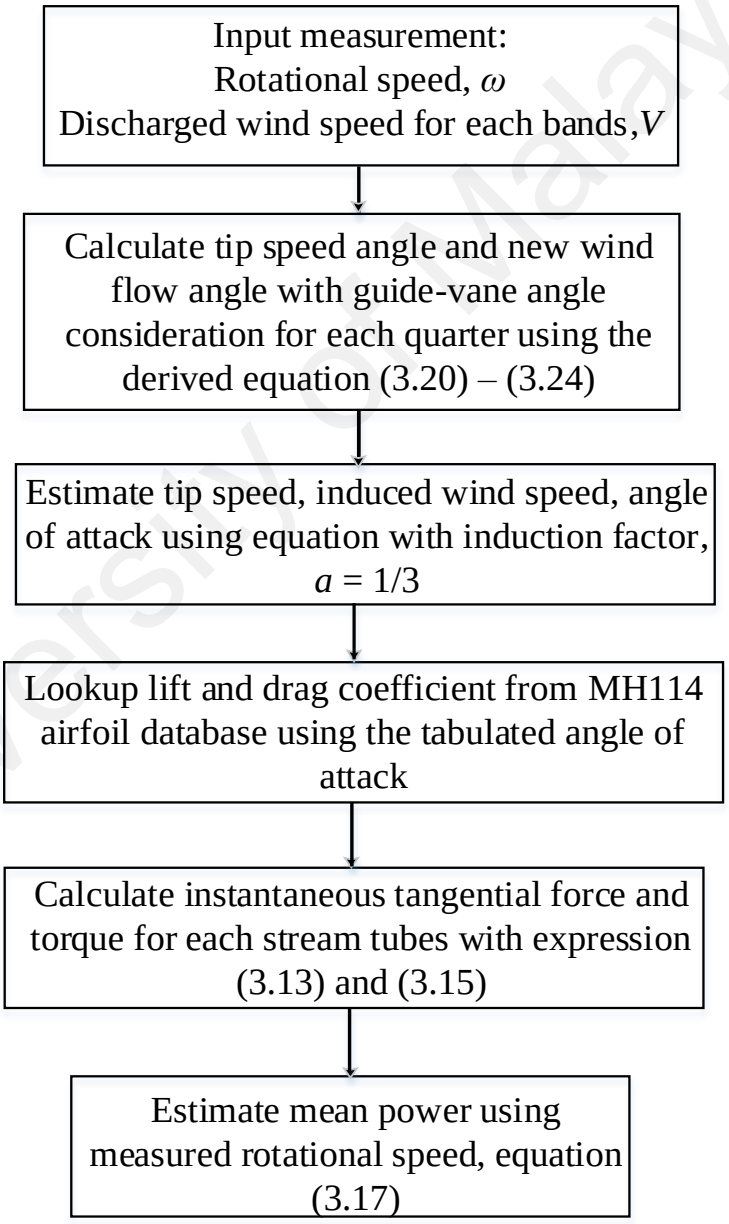

Figure 3.15: DMST-based theoretical verification procedures.

University of Malaya

3.7 Results and discussion

The 2 experimental set-up were conducted to investigate the performance of the proposed guide-vanes integrated exhaust air turbine generator. The optimum guide-vanes position and their respective optimum angle were first determined experimentally. Then, the performance of the cooling tower and the exhaust air turbine behavior were compared for the set-up before and after the integration of the guide-vanes at their optimum configuration.

3.7.1 Performance of the exhaust air turbine generator only

Table 3.5 demonstrated the experimental results of the exhaust air turbine generator. The VAWT took 14.01 s to achieve its stabilized speed at 423.45 rpm during free-running condition with the discharged wind speed of 6.0 m/s. The VAWT was able to generate its highest electrical power at 0.47 W when the application of electrical load was adjusted at 40% of its duty cycle. The further increment of the load application can be detrimental to the output power generation due to the VAWT will be rotating further away from its optimized speed. Figure 3.16 illustrated the power generated against turbine rotational speed. In the graph, the exhaust air turbine generator is best to be rotated at 31.35 rad/s for maximum power extraction. The VAWT used in this experiment was identical to the experiment which conducted by Kim and Gharib (2013). Throughout the experiment, it revealed that this turbine can only generate power less than 1 W with the approaching wind speed approximately 8.5 m/s. Thus, such low power generation from this exhaust air turbine was expected. It is worth to evaluate the VAWT's performance through power coefficient. The graph for power coefficient against tip speed ratio was plotted in Figure 3.17. The results showed that the VAWT reached its highest power coefficient at the TSR of approximately 0.83 (C_p = 0.047 at a TSR of 0.83).

University of Malaya

Table 3.5: Experimental results for the set-up with exhaust air turbine generator only.

Parameter	Value
Free running rotational speed (rpm)	423.45
Maximum electrical power generated (W)	0.47
Response time (s)	14.01
Cooling tower's average intake air speed (m/s)	4.71
Cooling tower's average discharged air speed (m/s)	6.00
Fan motor power consumption (W)	508.4

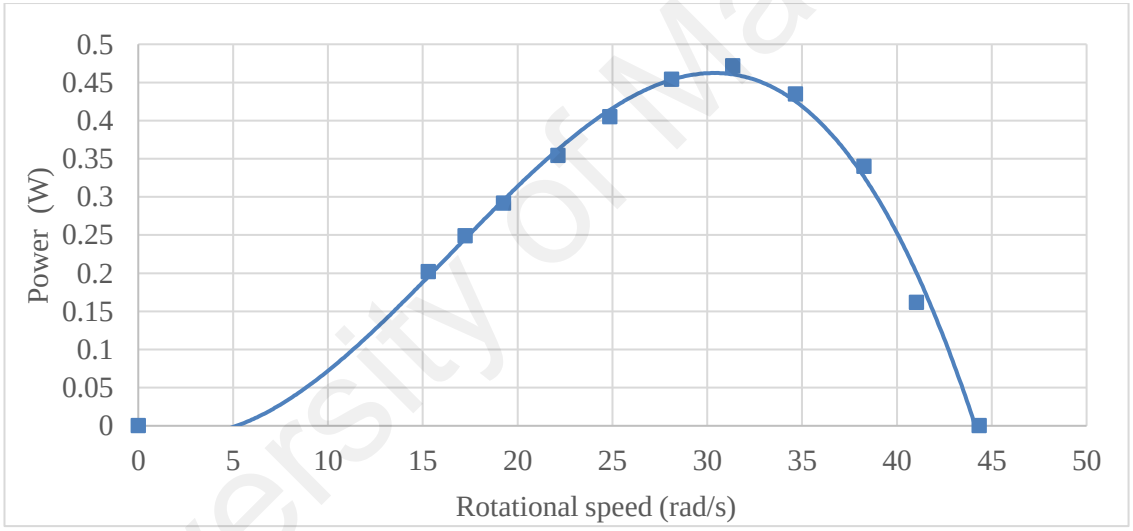

Figure 3.16: Generated power against turbine rotor speed.

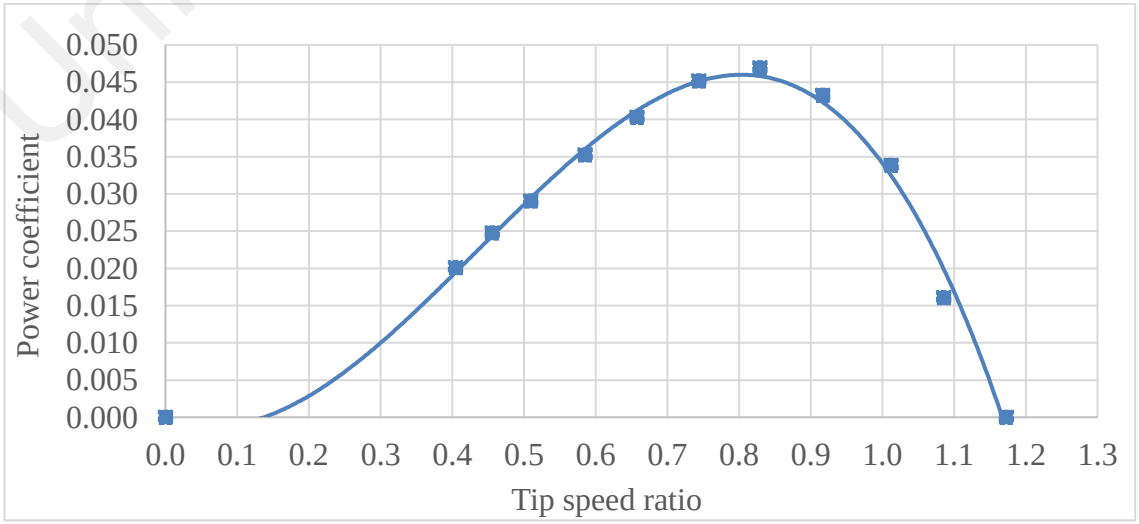

Figure 3.17: Power coefficient against tip speed ratio.

University of Malaya

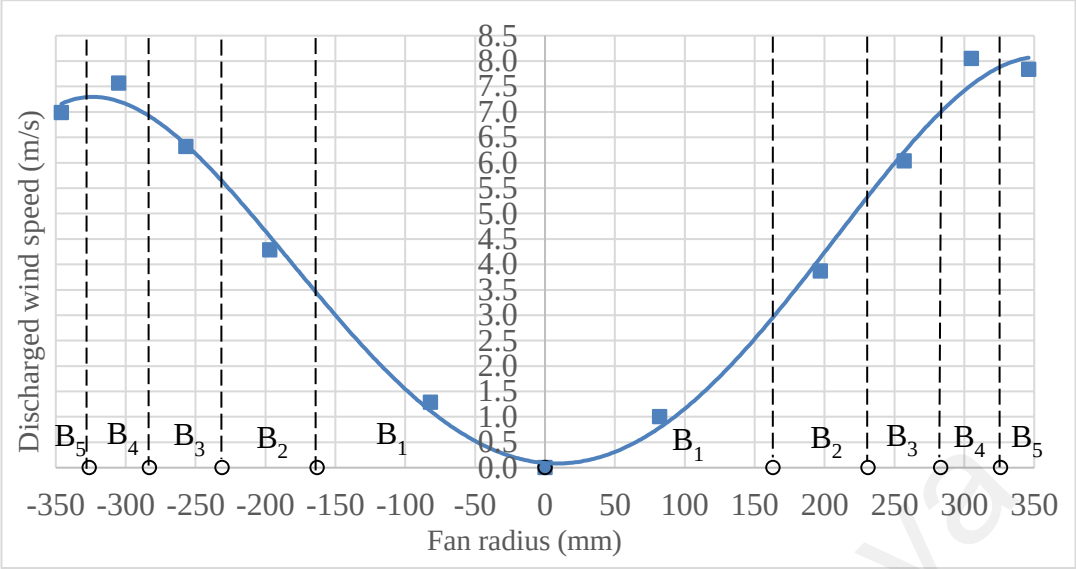

Figure 3.18: Measured discharged air speed from cooling fan's outlet.

Figure 3.18 showed the discharged air profile measured. The dotted lines divided the fan radius into its respective discharged air band. By referring to the figure, the discharged air speed along the radius was almost symmetrical. Low air speed was observed started from the middle of the fan and it progressively increased along the fan's radius until 300 mm (band 4) with the highest average discharged wind speed recorded at 8.1 m/s. The discharged wind speed started to reduce slightly when the measuring point was close to fan duct. Zero discharged wind speed was measured at radius = 0 mm due to the presence of fan hub that located at the middle of the discharged air outlet.

3.7.2 DMST analysis of the exhaust air turbine

The DMST calculated results for the exhaust air turbine was illustrated in Figure 3.19. The parameters shown in the figure included lift-to-drag coefficient ratio, AOA and instantaneous torque against the blade's azimuth angle. According to the discharged wind speed profile (sees Figure 3.14 and Figure 3.18), the highest discharged wind speed occurred at the VAWT's quarter one (band 4). Thus, the highest instantaneous torque was observed at this quarter, close to the azimuth angle of 40^{o} with 0.324 Nm. Since the blade of the VAWT was fixed at the pitch angle of 10^{o}, it was not capable of producing positive

University of Malaya

torque at small azimuth angle (Chong et al., 2017). The generated instantaneous torque started to reduce gradually from the azimuth angle of 80 ^{o} until 180^{o}. One of the reasons that the reduction of torque in quarter 2 was inevitable due to the turbine's swept area was located at the lower discharged wind speed region, which was band 1 and 2. Meanwhile, the AOA was also in reducing pattern. Negative AOA after 180^{o} blade angle (quarter 3 and 4) produced negative instantaneous torque as these quarters were positioned at the downwind side of the VAWT. By referring to the retrieved blade's profile database at Figure 3.20 (plotted using data presented in Appendix A3, focusing AOA from -20^{o} to 30^{o}), lift-to-drag coefficient ratio (blue triangle marker) will increase and start to reduce once AOA hits 5^{o}. Lift-to-drag coefficient ratio started to reduce slowly at azimuth angle of 10^{o} until 120^{o} and increased back since AOA dropped lower than 5^{o}.

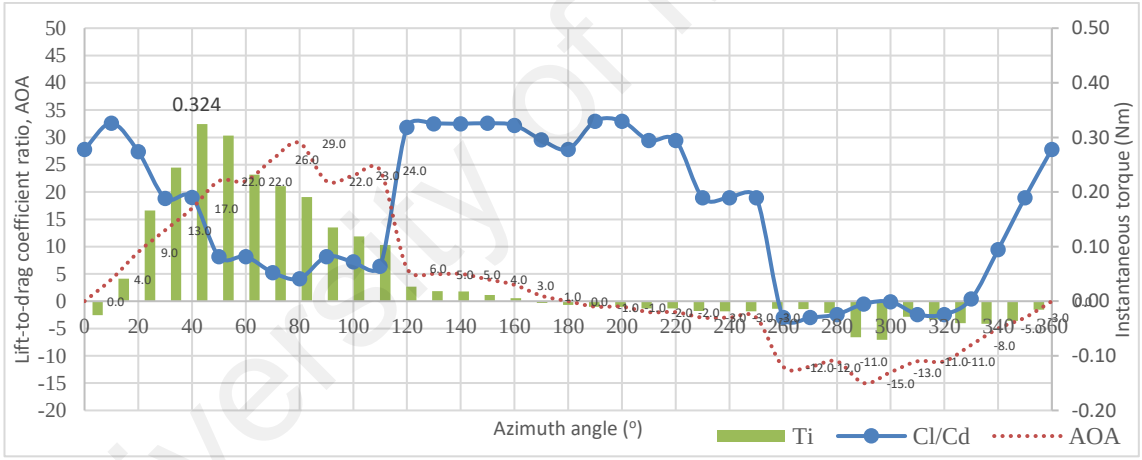

Figure 3.19: DMST calculated results for the VAWT only.

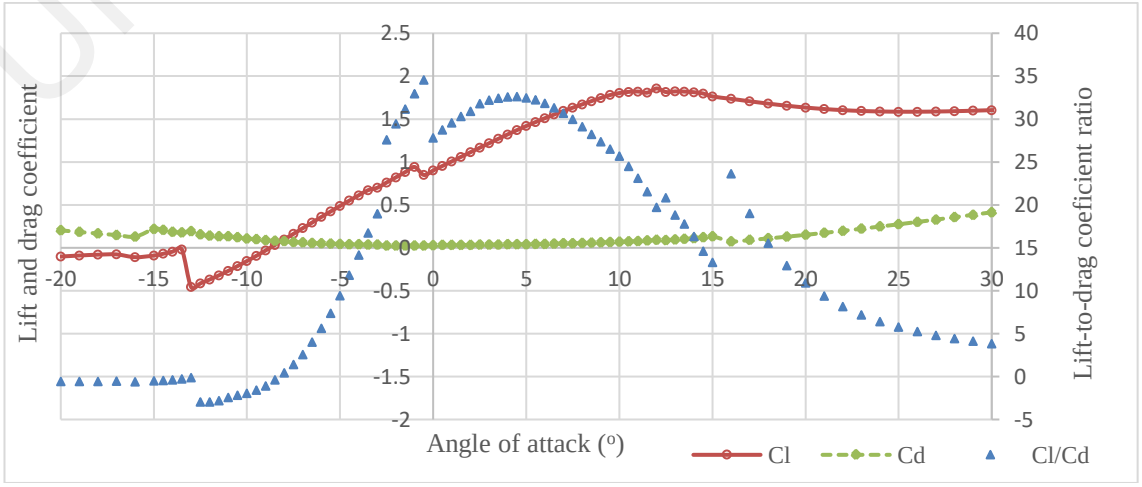

Figure 3.20: Turbine's blade profile data (MH114 Reynolds number, 25000).

University of Malaya

3.7.3 Study of the effect of the guide-vanes configuration

The investigation of the guide-vanes effect was divided into 2 sections. It will start with position study and then followed by guide-vanes angle study.

3.7.3.1 Determination of the guide-vanes position

Different configurations of the exhaust air turbine together with the guide-vanes produces different profile of outlet wind. Hence, the determination of the optimum guide-vanes position must be made according to the discharged air profile and VAWT's performance.

Based on the measured discharged air profile (Figure 3.18) and DMST-based analysis results on the VAWT discussed previously, the two guide-vanes were proposed to be located in band 4 and band 1. The turbine's blade azimuth angle in the range of $30^{o} - 50^{o}$ (stream tube numbered from 4 to 6 at the upwind side of VAWT) gave the most torque since this area was facing the wind stream from band 4 (the highest wind speed region). The side vane was proposed to be located here so it can serve as the wind directing guide to focus the highest wind speed to the VAWT. There was no angle adjustment for this guide-vane as a slight variation in angle can make it became a wind blockage for the VAWT. Such phenomena occurred due to the side vane was directly positioned at the positive torque region of the VAWT.

Figure 3.21 depicted the generated electrical power against wind turbine rotational speed at different middle guide-vane positions. The generation power showed reducing trend as summarized in Table 3.6 when the guide-vane moved further away from the exhaust air turbine's rotation circumference. The highest power generation yielded with the magnitude of 0.53 W when the middle guide-vane was adjusted to position, x = 160 mm. This position was the closest to the VAWT circumference, thereby, the approaching wind to the turbine was focused instead of spreading away. Besides, this middle guide-

University of Malaya

vane can also act as a shield to block the discharged air from re-circulating back to the center of the cooling fan. According to the experimental results, the middle guide-vane is best to be situated at the position, x = 160 mm which measured from the center of VAWT to fan center and the side vane is located at band 4 of the discharged air, which is x = 326 mm measured from the fan center.

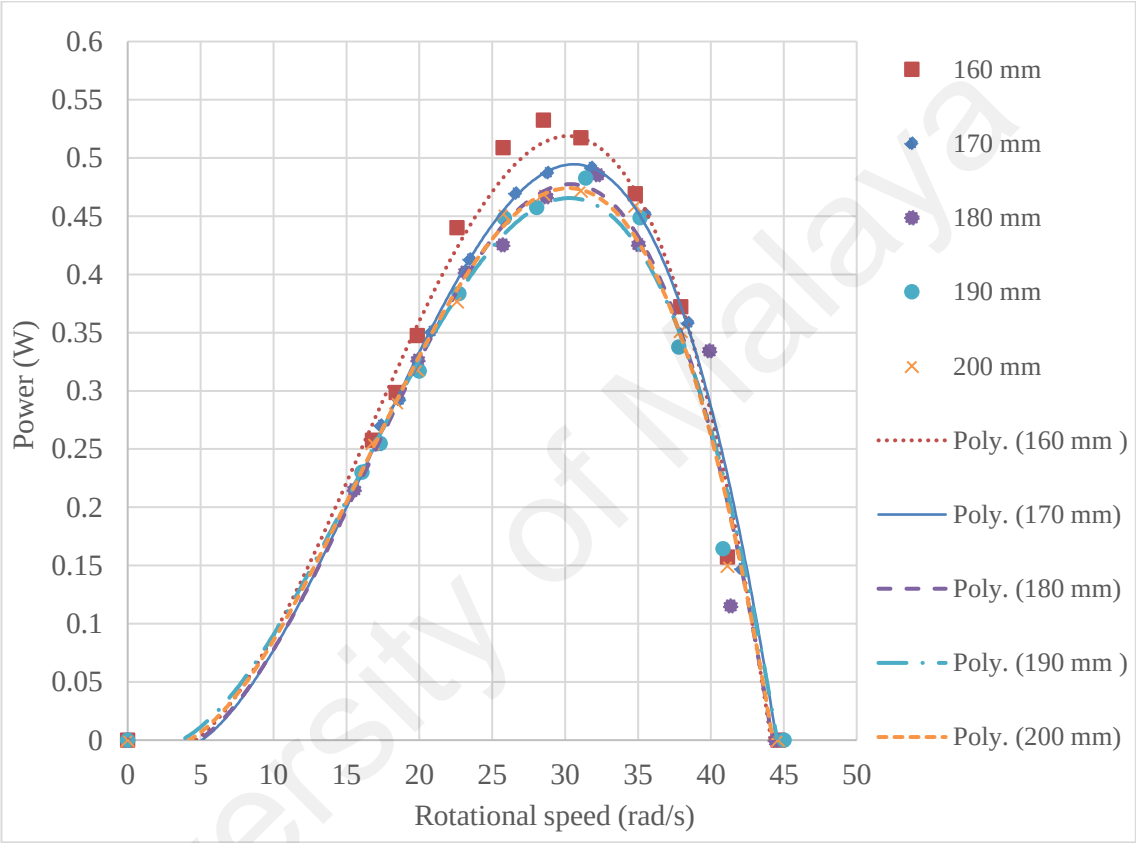

Figure 3.21: Power generated against VAWT rotational speed for 5 different middle guide-vane positions.

Table 3.6: Middle vane position study.

Middle vane position (mm)	Rotational speed (rpm)	Maximum power (W)
160	435.78	0.53
170	426.49	0.49
180	424.07	0.49
190	429.82	0.48
200	425.85	0.47

University of Malaya

3.7.3.2 Guide-vanes angle effect on the wind turbine performance

Next, the optimum angle of the middle guide-vane will be determined according to the position selected, which is at x = 160 mm. Figure 3.22 showed the performance of turbine for different guide-vane angles. There was a small range of guide-vane angle, from 60^o to 120^o which is preferable for guide-vane angle adjustment (various dotted lines) as the generated power is always higher with the set-up without guide-vane implementation as indicated with a solid blue colored line. Thus, the guide-vane angle scale can be divided into two zones, which one is called enhancement zone and the other is destructive zone (angle away from 60^o to 120^o). Adjustment of guide-vane to the destructive zone is avoided due to the guide-vane can become blockage in this region.

Figure 3.23 illustrated the power coefficient against TSR of the exhaust air wind turbine for all the guide-vane angles. Similar trend observed for the guide-vanes angles which fall at the enhancement zone where the VAWT can reach higher optimum C_p at the TSR range from 0.83 – 0.89. The highest C_p, 0.053 was observed when the middle guide-vane was fixed at 80^o. Such high C_p was observed because the torque generated was higher as compared to the set-up without guide-vane. The lift-to-drag coefficient ratio was also slightly higher with lower AOA generated and this will be further explained in the later section. In contrast, the generated C_p from the destructive zone of guide-vanes angle was relatively low. Comparatively, it was even lower over the set-up with VAWT only which shown in the same figure (solid blue line). This is due to the directed wind flow angle is not favorable to the wind turbine.

University of Malaya

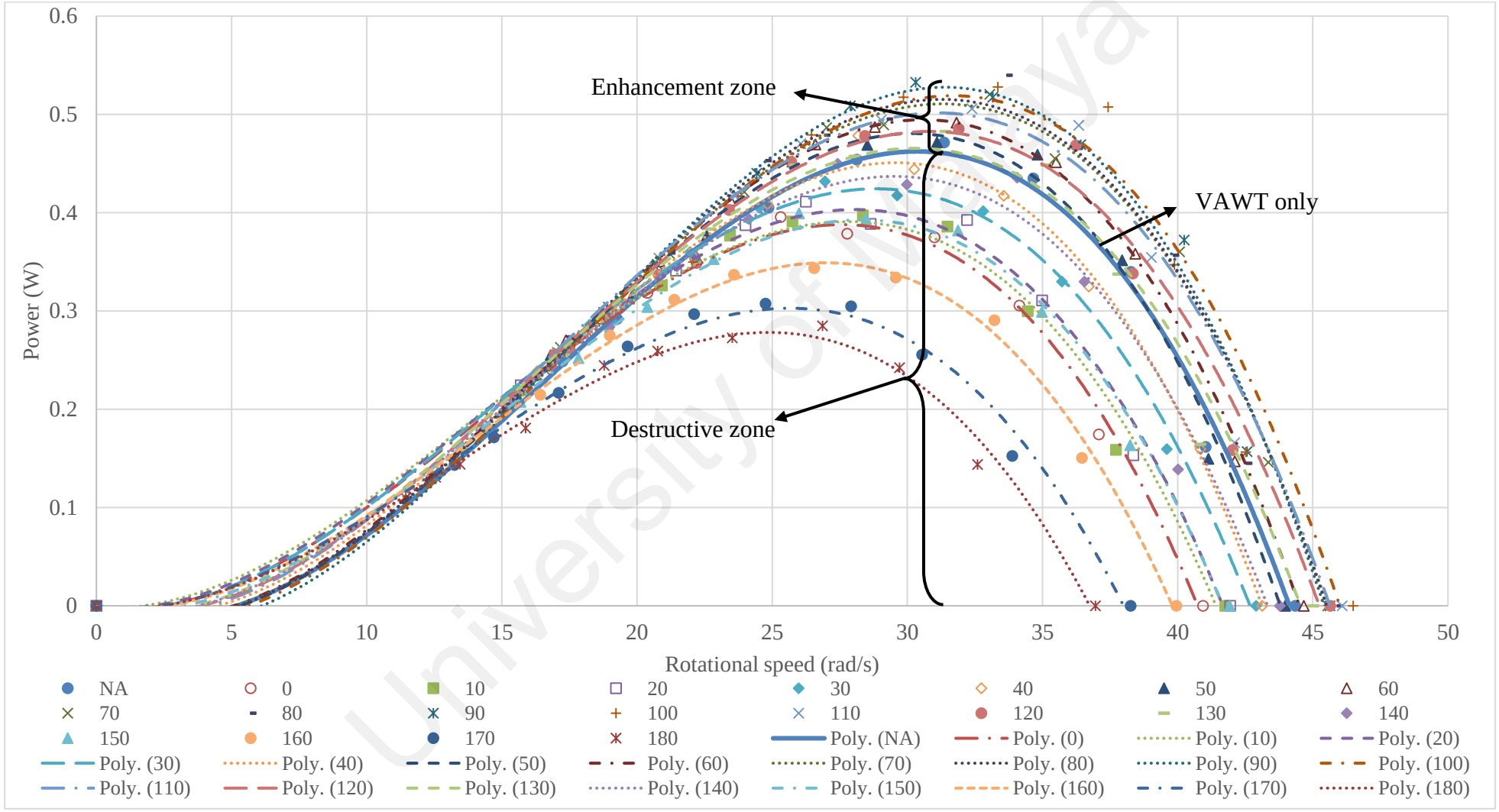

Figure 3.22: Power vs. rotational speed for the different guide-vane angle.

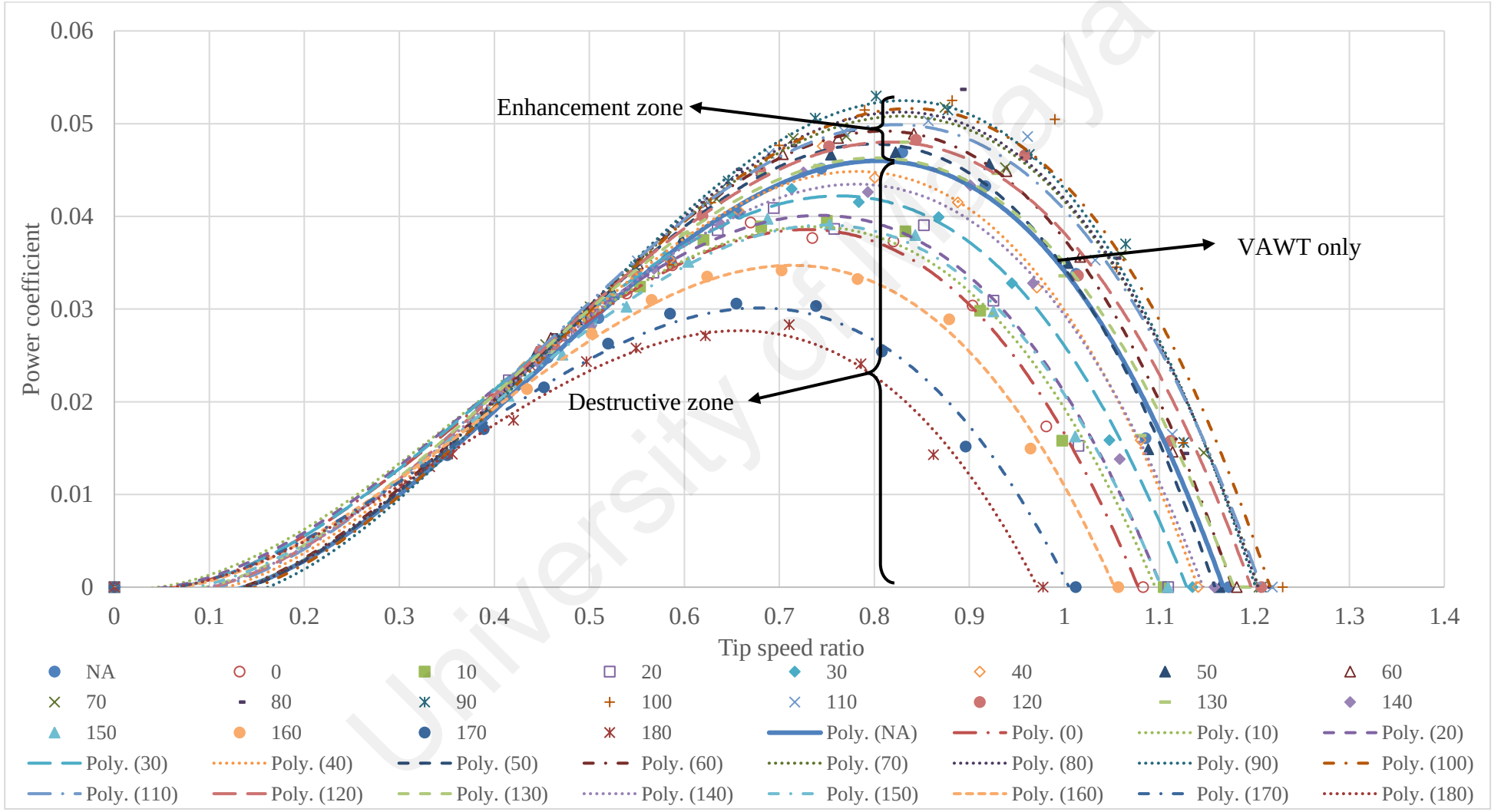

Figure 3.23: C_p against TSR curve for the different guide-vane angle.

3.7.3.3 Theoretical verification of the effect of guide-vanes angle

Adjustment of the middle guide-vane affects the wind flow at the second quarter of the wind turbine since it is directly positioned below this quarter. Hence, the wind flow angle of the other quarters remained at 90^{o} whilst only quarter 2 of the turbine was set to be equivalent to the guide-vane angle for the DMST calculation.

Figure 3.24 depicted the comparison of the experimental and DMST-based calculated output power for all the guide-vane angles. It showed good agreement of theoretical results with experiment as a similar trend was observed for all of the angle settings. It was noticeable that there was an enhancement zone of the guide-vane angle which falls from 60^{o} – 120^{o} (marked in dotted square box) was similar to what was observed in the experimental results. This zone gave higher electrical power generation as compared to the setup with exhaust air turbine generator only (indicated as the horizontal line in the figure where solid line is the DMST calculated value and the dotted line is the experiment value). The DMST-based calculated output power was slightly lower than the experimental results because of the non-uniform flow due to the blade movement contributed to the difficulty in presenting the force acting on the turbine blade accurately (Camporeale & Magi, 2000). In terms of the turbine performance, both theoretical and experiments results lead to the conclusion that the middle guide-vane angle is best to set at 80^{o} as the highest power generation can be obtained.

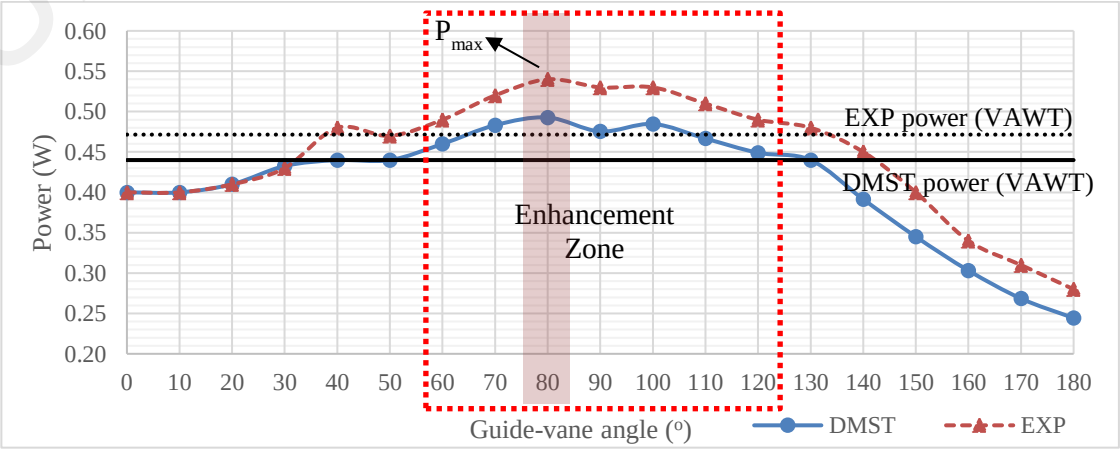

Figure 3.24: Theoretical verification results.

University of Malaya

3.7.4 Cooling tower impact analysis

Apart from that, negative effect on the cooling tower air flow performance may come from the blocking effect when an object is placed in the exhaust air stream. This effect can be detected by the reduction of flow rate and an increase in the power consumption of the fan motor. By installing the guide-vanes above the cooling tower, it can give different impact on the cooling tower performance depending on its adjusted angle.

Table 3.7 showed the summarized comparison results on the performance of the cooling tower between the set-up of the exhaust air turbine only and the guide-vanes integrated exhaust air turbine at different guide-vanes angle. As discussed previously, there were two zones can be identified depending on the guide-vane angle. The fan power consumption did not increase when the middle vane was adjusted to the enhancement zone. Instead, it aided in reducing the fan motor power consumption. On the other hand, the fan power consumption increased significantly, up to 14.1% when the adjustment of the guide-vane angle was tuned to the destructive zone.

In terms of intake air flow rate of the cooling tower, it can reduce considerably if the guide-vane angle was adjusted to the destructive zone. This showed that guide-vane can be an obstruction of the air stream when its angle was not determined appropriately. When the middle vane's angle tuned towards the enhancement region, the intake air flow rate increased as compared to the setup with VAWT only. This is because the exhaust air turbine can be rotated faster above the cooling tower and thus, the low-pressure region would be formed. Such suction effect on the top of the cooling tower might help to improve the air flow (Chong et al., 2014).

A similar trend observed in the discharged air speed. The negative ratio of discharged air was obtained when the angle was fitted to the destructive zone. The vane can exert blocking effect on the discharged air with deterioration rate up to 10% with the worse setting of guide-vane angle. This scenario is undesirable since it reduced the discharge air

University of Malaya

rate of the cooling tower. Conversely, more air can be discharged out from the cooling tower when the middle vane was adjusted to the preferable angle region. The highest increment of discharged air speed, 3% was observed when the angle was set at 70^o to 90^o.

By taking into account both impact to the cooling tower performance and turbine behavior, the middle guide-vane at x = 160 mm is best to be fixed at 80^o. The reason is due to that this angle can generate the most electrical power among all the different guide-vane angles. Meanwhile, such angle configuration also allows the cooling fan to consume lesser power with higher flow rate generated from the cooling tower.

Table 3.7: Cooling tower performance evaluation results.

Parameters	**Intake air speed (m/s)**					**Flow rate (m^3/s)**	**Discharged air speed (m/s)**		**Power consumed (W)**
	Q1	**Q2**	**Q3**	**Q4**	**Mean**		**Mean**	**Ratio**	**Mean**
VAWT only	4.9	4.5	5.0	4.4	4.71	2.51	6.00	-	508.4
0^o	4.6	4.2	4.7	4.2	4.43	2.36	5.65	-0.06	516.1 (+)
10^o	4.7	4.2	4.7	4.2	4.44	2.37	5.66	-0.06	512.0 (+)
20^o	5.1	4.3	4.8	4.2	4.58	2.44	5.84	-0.03	508.9 (+)
30^o	4.9	4.3	4.9	4.1	4.53	2.42	5.77	-0.04	509.5 (+)
40^o	5.0	4.5	5.1	4.2	4.70	2.50	5.98	0.00	508.2 (-)
50^o	5.1	4.6	4.9	4.3	4.71	2.51	6.00	0.00	506.0 (-)
60^o	5.1	4.5	5.0	4.3	4.73	2.52	6.03	0.01	507.7 (-)
70^o	5.2	4.8	5.0	4.4	4.84	2.58	6.17	0.03	507.5 (-)
80^o	**5.2**	**4.6**	**5.1**	**4.5**	**4.86**	**2.59**	**6.19**	**0.03**	**505.0** (-)
90^o	5.1	4.7	5.3	4.4	4.85	2.58	6.18	0.03	505.9 (-)
100^o	5.0	4.7	5.1	4.3	4.78	2.54	6.08	0.01	504.4 (-)
110^o	5.0	4.6	5.1	4.4	4.78	2.54	6.08	0.01	507.3 (-)
120^o	5.1	4.7	5.0	4.3	4.80	2.56	6.11	0.02	503.5 (-)
130^o	5.1	4.8	4.8	4.3	4.76	2.54	6.06	0.01	506.3 (-)
140^o	5.0	4.4	4.5	4.3	4.53	2.42	5.77	-0.04	509.1 (+)
150^o	4.8	4.4	4.3	4.1	4.42	2.35	5.62	-0.06	512.0 (+)
160^o	4.7	4.1	4.3	4.0	4.28	2.28	5.44	-0.09	508.7 (+)
170^o	4.8	4.2	4.1	3.9	4.26	2.27	5.42	-0.10	514.5 (+)
180^o	4.8	4.1	4.4	3.8	4.28	2.28	5.44	-0.09	580.0 (+)

University of Malaya

3.7.5 Overall performance comparison

Table 3.8 summarized the comparative results for both of the set-up whereby one with exhaust air turbine only and the another was integrated with the guide-vanes that configured at the selected configuration (i.e. optimum vane position at 160 mm with guide-vane angle adjusted at 80^{o}). Quantitatively, the guide-vanes integrated exhaust air turbine generator generated higher peak power than the set-up with the exhaust air turbine only with 14.9% improvement. The obtained higher power can be related to the wind speed up ratio, 3.2% which can be seen in both intake and discharged air speed. At the same time, the response time of the wind turbine to reach its stabilized speed was reduced to 12.15 s (13.3% gain of time). The improvement was observed due to the turbine can move with slightly higher average torque at the value of 0.012 Nm as compared to VAWT only at 0.011 Nm, resulting it rotated faster to its stabilized speed. With such improvement of response time, it also indicates that the introduction of the guide-vane allows better self-start of the VAWT.

In terms of the fan motor power consumption, it was reduced by 0.7 % as compared to the setup with VAWT only. The higher rotational speed of the VAWT above the cooling tower creates a low-pressure region that helps to induce more discharged air out and hence, reduction of power consumption was observed. This result shows that the presence of the guide-vane in the exhaust air stream does not exert negative impact to the system.

Table 3.8: Comparison experimental results for both of the set-up.

Configurations	**VAWT only**	**Guide-vanes integrated exhaust air turbine**	**Percentage different**
Free running rotational speed (rpm)	423.45	443.94	4.8 %
Maximum power generated (W)	0.47	0.54	14.9 %
Response time (s)	14.01	12.15	13.3 %
Average intake air speed (m/s)	4.71	4.86	3.2 %
Average discharged air speed (m/s)	6.00	6.19	3.2 %
Fan motor consumption (W)	508.4	505	0.7 %

University of Malaya

Power against rotational speed figure was plotted in Figure 3.25 which focused on the configuration of exhaust air turbine only and set-up with the optimum guide-vane configuration. The maximum power can be achieved with the turbine's rotational speed at 33.68 rad/s with the installation of guide-vane. Meanwhile. the power coefficient that can be achieved was also higher as compared to the exhaust air turbine only as shown in Figure 3.26 with the magnitude of 0.0506 (which is 10 % higher).

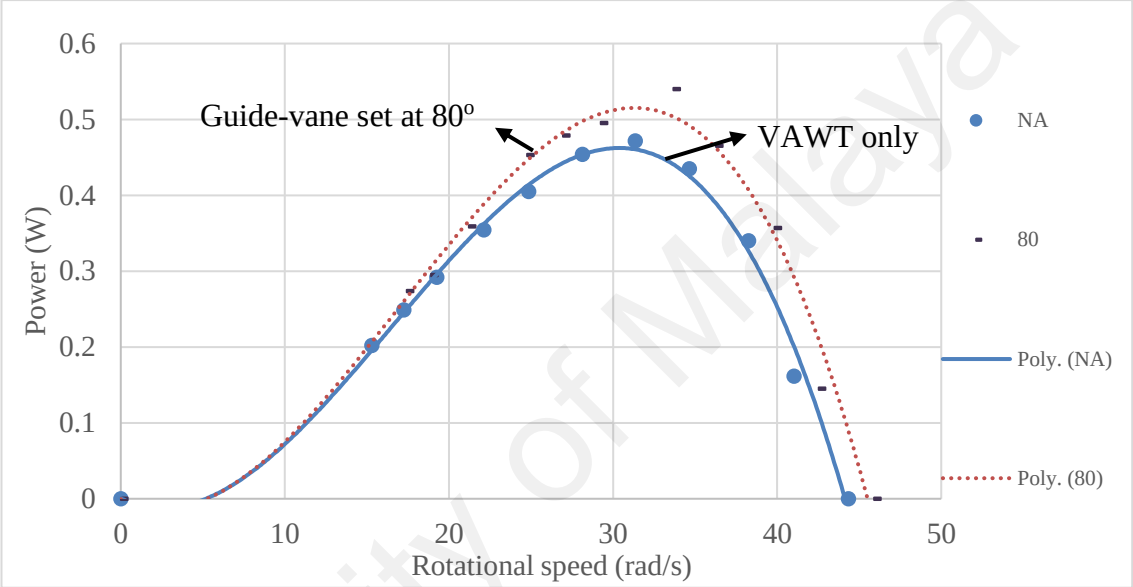

Figure 3.25: Power against rotational speed for comparison.

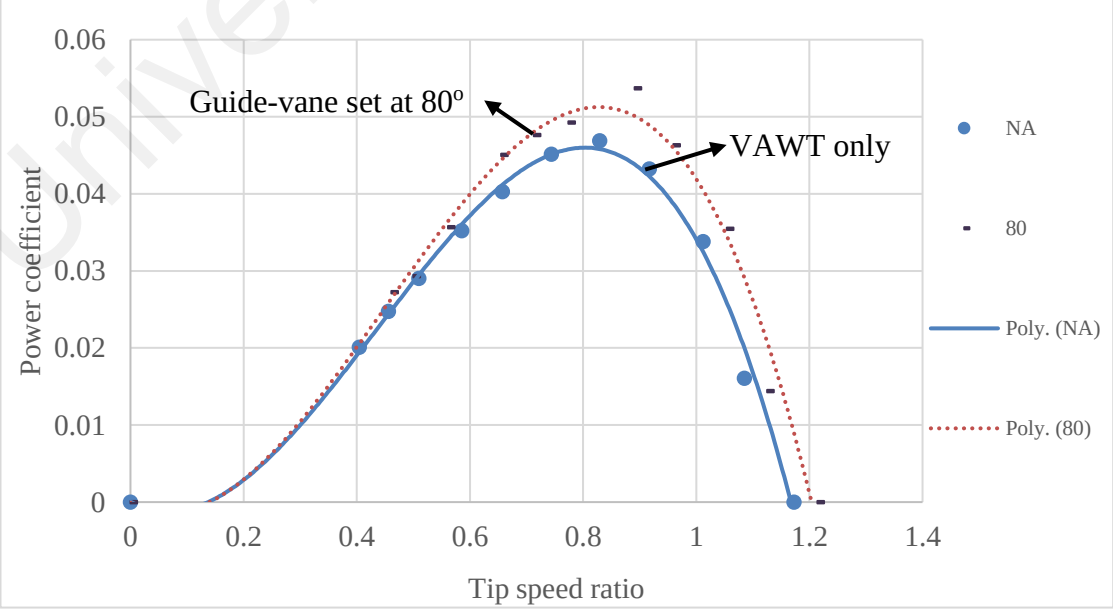

Figure 3.26: Power coefficient against tip speed ratio for comparison.

University of Malaya

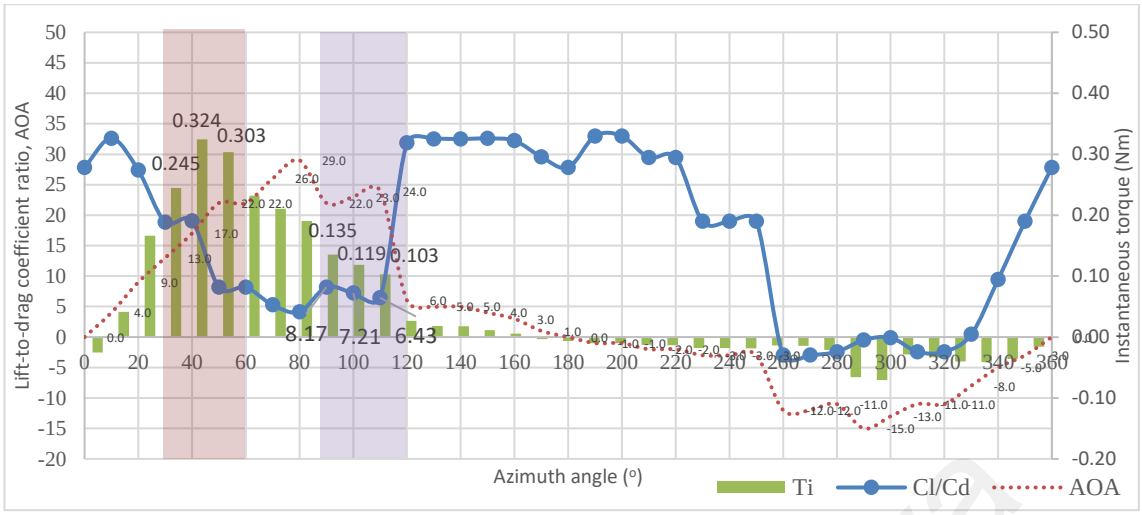

(a)

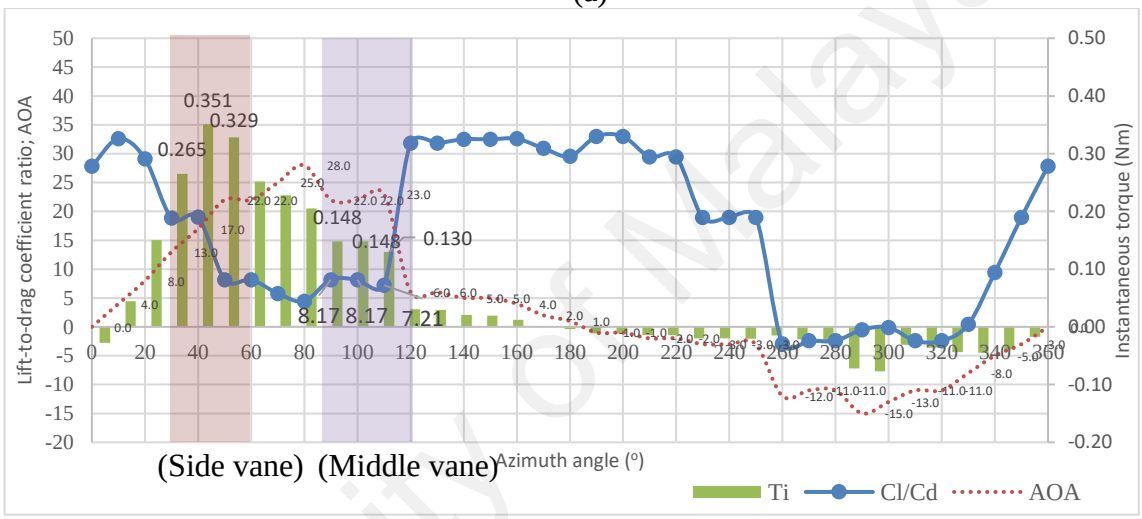

(Side vane) (Middle vane)

(b)

Figure 3.27: Comparison of the DMST calculated results. (a) VAWT only, (b) Guide-vanes integrated exhaust air turbine.

Side vane was positioned at the highest discharged wind speed region which occurs at VAWT quarter 1 (highlighted in red color in Figure 3.27). It helped in increasing the instantaneous torque and this can be clearly seen when comparing Figure 3.27(a) and (b). Middle vane (purple zone) also played its role by generating higher instantaneous torque from azimuth angle 90° - 110°. The lift-to-drag-coefficient ratio also showed slightly higher at this range of azimuth angle with smaller AOA generated (1° lower) as compared to the set-up with exhaust air turbine only. According to the extracted database of the blade profile (see Figure 3.20), the lift-to-drag coefficient ratio will increase, starting from negative value until 5°. Hence, lower AOA can give higher lift-to-drag force.

University of Malaya

3.8 Summary

Power optimization for wind power generation in terms of mechanical aspect using guide-vanes integrated exhaust air turbine generator was presented and validated. The presence of the guide-vane with the appropriate position and angle setting (horizontal position located at 160 mm with its angle set to 80^{o}) can effectively improve turbine's output power 14.9 % as compared to the original exhaust air turbine generator. This result indicated that the integration of guide-vanes with the exhaust air turbine generator contributes in harnessing additional power from the directed wind energy. Furthermore, the integration of guide-vanes allowed the cooling fan to consume lesser power with higher flow rate discharged from the cooling tower. A comprehensive theoretical verification had been carried out using DMST analysis. Both theoretical calculations and experimental data demonstrated good agreement in terms of electrical power generation.

However, improvement in power optimization only in mechanical aspect is insufficient. The exhaust air turbine has to be controlled to operate at its optimum rotational speed so that maximum power is obtained at different cooling fan speed operations. Such improvement can be achieved electrically by using power electronics with power optimization control algorithm. The details of power optimization control using a converter for the exhaust air turbine generator will be presented in the subsequent chapter.

University of Malaya

CHAPTER 4: DIRECT TORQUE CONTROL OF PMSG BASED ON VIENNA RECTIFIER

Apart from power optimization control via mechanical means, it is also important to investigate the electrical control of the PMSG in order to optimize the power extracted from the wind turbine. To do this, it is necessary to have an effective control method for the PMSG. For this project, direct torque control (DTC) of the PMSG using Vienna rectifier was investigated. The foundational concepts of PMSG were first presented in this chapter, followed by an overall discussion on the operation principles of the Vienna rectifier, highlighting the feasible switching vectors and the its operation limits. With the developed standardized stator voltage model, an in-depth analysis on the effect of the switching vectors of the Vienna rectifier on the performance of DTC was studied. Subsequently, an improved LUT was designed to improve the overall performance of the DTC approach based on Vienna rectifier, along with the investigation of the computation delay compensation for the DTC. The approach was first investigated through Matlab / Simulink before it was further validated using a lab-scale prototype. Both simulation and experimental results obtained were compared with the existing DTC method (Rajaei et al., 2013) to verify the effectiveness of the proposed LUT.

4.1 Theoretical background

4.1.1 Mathematical Model of PMSG

A PMSG with sinusoidal flux distribution (non-salient pole PMSG; $L_s = L_d = L_q$) was utilized in this project. Variables of the three-phase PMSG can be converted into various reference frames, for instance in the rotating *d-q* reference frame, stator stationary α-β reference frame, and the stator flux *x-y* reference frame as shown in Figure 4.1. In the figure, ω_r and ω_s represent the rotor speed and stator speed respectively, θ_s is the stator angle, θ_r is the rotor position of the PMSG, δ is the load angle, φ_r presents the rotor flux,

University of Malaya

and φ_s with different subscript indicates the stator flux in different reference frames (i.e. x and y for x y-axis of the rotating reference frame; and α and β for $\alpha\beta$-axis rotating frame). It is worth to take note that the d-q reference frame is rotating synchronously with rotor as shown at an angular frequency of ω_r, whilst the x-y reference frame moves in synchronization with the stator flux of the PMSG in the direction as shown with ω_s relative to the stationary $\alpha\beta$-axis rotating frame.

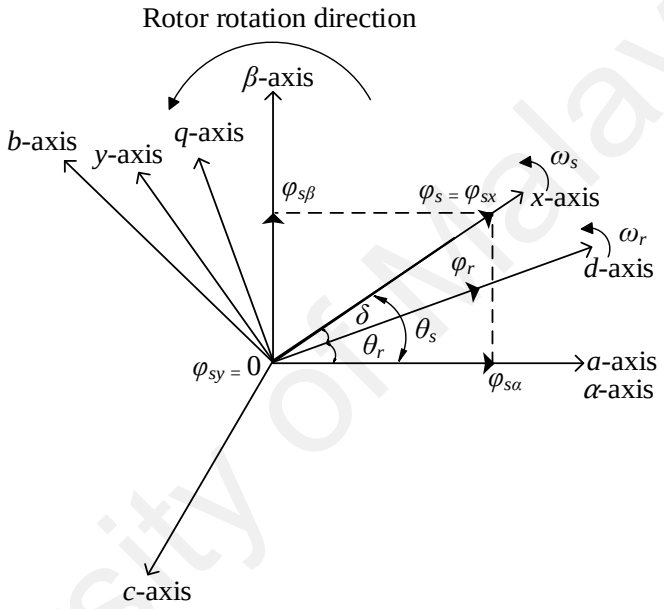

Figure 4.1: PMSG's variables in different reference frames.

The three-phase mathematical models that describing PMSG in *abc* phase variables are:

$$\begin{bmatrix} V_{sa} \\ V_{sb} \\ V_{sc} \end{bmatrix} = R_s I_s \begin{bmatrix} \cos\theta_r \\ \cos(\theta_r - \frac{2\pi}{3}) \\ \cos(\theta_r + \frac{2\pi}{3}) \end{bmatrix} + \frac{d}{dt} \begin{bmatrix} \varphi_{sa} \\ \varphi_{sb} \\ \varphi_{sc} \end{bmatrix} \tag{4.1}$$

$$\begin{bmatrix} \varphi_{sa} \\ \varphi_{sb} \\ \varphi_{sc} \end{bmatrix} = L_s I_s \begin{bmatrix} \cos\theta_r \\ \cos(\theta_r - \frac{2\pi}{3}) \\ \cos(\theta_r + \frac{2\pi}{3}) \end{bmatrix} + \varphi_r \begin{bmatrix} \cos\theta_r \\ \cos(\theta_r - \frac{2\pi}{3}) \\ \cos(\theta_r + \frac{2\pi}{3}) \end{bmatrix} \tag{4.2}$$

where V, I, φ, L, and R are the voltage, current, flux, inductance and resistance respectively; subscripts s and r denote the stator and rotor quantity respectively in three-phase components, a, b, and c.

University of Malaya

It is convenient to establish the model in stator synchronous *x-y* rotating reference frame to have direct control of stator flux and electromagnetic torque since this reference frame rotates in synchronization with the stator flux. The three-phase PMSG variables, *F* can be mathematically converted into the corresponding *x-y* reference frame by first applying Clarke transformation, $T_{\alpha\beta}$ followed by *x-y* rotational transformation, T_{xy} as follows,

$$\begin{bmatrix} F_\alpha \\ F_\beta \\ F_o \end{bmatrix} = T_{\alpha\beta} \begin{bmatrix} F_a \\ F_b \\ F_c \end{bmatrix} \tag{4.3}$$

$$\begin{bmatrix} F_x \\ F_y \end{bmatrix} = T_{xy} \begin{bmatrix} F_\alpha \\ F_\beta \end{bmatrix} \tag{4.4}$$

where:

$$T_{\alpha\beta} = \frac{2}{3} \begin{bmatrix} 1 & -\frac{1}{2} & -\frac{1}{2} \\ 0 & \frac{\sqrt{3}}{2} & -\frac{\sqrt{3}}{2} \\ \frac{1}{2} & \frac{1}{2} & \frac{1}{2} \end{bmatrix} \tag{4.5}$$

$$T_{xy} = \begin{bmatrix} \cos\theta_s & \sin\theta_s \\ -\sin\theta_s & \cos\theta_s \end{bmatrix} \tag{4.6}$$

and the variables, *F* can be voltage, current or flux of the PMSG.

In this case, the PMSG model in stationary reference frame can be written as,

$$\begin{bmatrix} V_{s\alpha} \\ V_{s\beta} \end{bmatrix} = R_s \begin{bmatrix} I_{s\alpha} \\ I_{s\beta} \end{bmatrix} + \frac{d}{dt} \begin{bmatrix} \varphi_{s\alpha} \\ \varphi_{s\beta} \end{bmatrix} \tag{4.7}$$

$$\begin{bmatrix} \varphi_{s\alpha} \\ \varphi_{s\beta} \end{bmatrix} = L_s \begin{bmatrix} I_{s\alpha} \\ I_{s\beta} \end{bmatrix} + \varphi_r \begin{bmatrix} \sin\theta_r \\ \cos\theta_r \end{bmatrix} \tag{4.8}$$

Since $\alpha\beta$ components are orthogonal to one another, the stator flux magnitude and stator angle (with respect to the α-axis) are: -

$$\varphi_s = \sqrt{\varphi_{s\alpha}^2 + \varphi_{s\beta}^2} \tag{4.9}$$

$$\theta_s = \tan^{-1} \frac{\varphi_{s\beta}}{\varphi_{s\alpha}} \tag{4.10}$$

University of Malaya

The generator torque can then be obtained as,

$$T_e = \frac{3}{2} p(\varphi_{s\alpha} I_{s\beta} - \varphi_{s\beta} I_{s\alpha}) \tag{4.11}$$

with p is the number of the generator's magnetic poles pairs.

By applying (4.6) to (4.7) and (4.8), the steady-state model for the PMSG in the *xy*-reference rotating frame is given as,

$$\begin{bmatrix} V_{sx} \\ V_{sy} \end{bmatrix} = R_s \begin{bmatrix} I_{sx} \\ I_{sy} \end{bmatrix} + \frac{d}{dt} \begin{bmatrix} \varphi_{sx} \\ \varphi_{sy} \end{bmatrix} + \omega_s \begin{bmatrix} -\varphi_{sy} \\ \varphi_{sx} \end{bmatrix} \tag{4.12}$$

$$\begin{bmatrix} \varphi_{sx} \\ \varphi_{sy} \end{bmatrix} = L_s \begin{bmatrix} I_{sx} \\ I_{sy} \end{bmatrix} + \varphi_r \begin{bmatrix} \cos\delta \\ -\sin\delta \end{bmatrix} \tag{4.13}$$

Assume that the effect of stator resistance is negligible and the stator flux is aligned along *x*-axis, such that: -

$$\varphi_{sx} = \varphi_s \tag{4.14}$$

$$\varphi_{sy} = 0 \tag{4.15}$$

the equation of the stator voltage in (4.12) can be simplified to,

$$V_{sx} = \frac{d\varphi_s}{dt} \tag{4.16}$$

$$V_{sy} = \omega_s \varphi_s \tag{4.17}$$

and the stator flux model becomes,

$$\begin{bmatrix} \varphi_s \\ 0 \end{bmatrix} = L_s \begin{bmatrix} I_{sx} \\ I_{sy} \end{bmatrix} + \varphi_r \begin{bmatrix} \cos\delta \\ -\sin\delta \end{bmatrix} \tag{4.18}$$

As can be seen in Figure 4.1, the angle between stator and rotor flux is load angle, δ. The rate of change of load angle can be defined as the difference between stator speed and rotor speed,

$$\frac{d\delta}{dt} = \frac{d}{dt}(\theta_s - \theta_r) = \omega_s - \omega_r \tag{4.19}$$

University of Malaya

During transient operation, load angle varies by the virtue of the stator flux and rotor flux are rotating at different speed. By rearranging (4.17) and substituting into (4.19), the rate of change of load angle can be obtained as a function of V_{sy} as follows,

$$\frac{d\delta}{dt} = \frac{V_{sy}}{\varphi_s} - \omega_r \tag{4.20}$$

It is known that the steady-state electromagnetic torque, T_e developed by the PMSG can be obtained as (Zhong et al., 1997),

$$T_e = \frac{3}{2L_s} p\varphi_s\varphi_r \sin\delta \tag{4.21}$$

Taking the time derivative of torque gives: -

$$\frac{dT_e}{dt} = \frac{3}{2L_s} p\varphi_r[\frac{d\varphi_s}{dt}\sin\delta + \frac{d\delta}{dt}\varphi_s\cos\delta] \tag{4.22}$$

Equation (4.22) can then be expressed in *x*-*y* reference frame as below,

$$\frac{dT_e}{dt} = \frac{3}{2L_s} p\varphi_r[\, V_{sx}\sin\delta + (V_{sy} - \varphi_s\omega_r)\cos\delta] \tag{4.23}$$

The dynamic of PMSG is characterized by electromagnetic torque and stator flux which should be controlled for optimized performance. According to (4.16) and (4.23), two conclusions can be drawn, which are: -

1) The magnitude and direction of the applied V_{sx} can directly control the magnitude of stator flux.
2) The torque can be changed by varying the load angle, δ and stator flux, φ_s which is governed by V_{sx} and V_{sy}.

Indeed, it is clear that stator flux and electromagnetic torque can be controlled by the appropriate application of stator voltage. This can be done by controlling the Vienna rectifier, as will be explained in the next subsection.

University of Malaya

4.1.2 Operation of Vienna Rectifier

With regards to the cost and performance consideration as explained in Chapter 2, Vienna rectifier was used as the power electronics converter for controlling the PMSG in this project. A detailed circuit diagram of Vienna rectifier and its equivalent circuit is depicted in Figure 4.2 and Figure 4.3. The topology of Vienna rectifier consists of 3 active bi-directional switches, a diode bridge composes of 6 diodes and 2 DC-link capacitors connected in series. Note that two resistors are connected at the other end of the DC-link as load. In real implementation, these resistors can be either replaced by DC-loads or a grid-connected inverter, depending on the application.

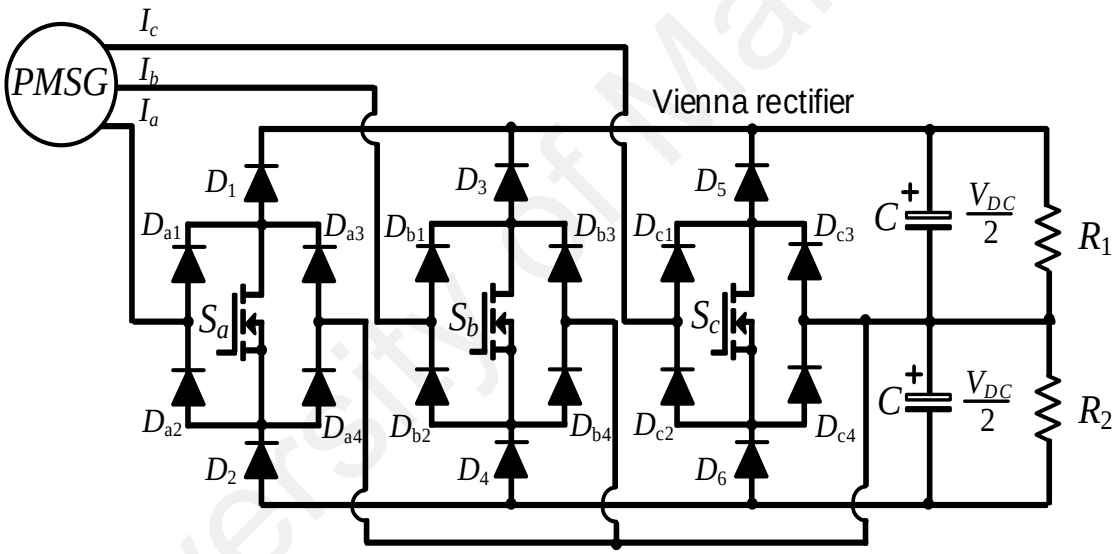

Figure 4.2: Circuit diagram of the Vienna rectifier.

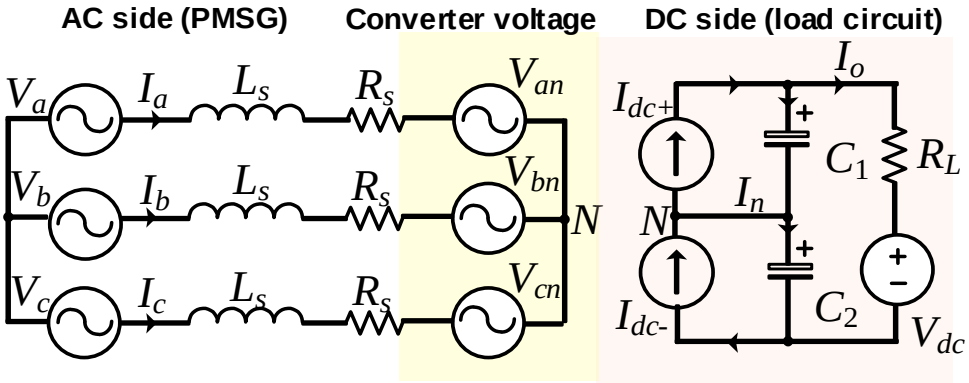

Figure 4.3: Equivalent circuit of the Vienna rectifier with PMSG.

University of Malaya

At each phase leg, Vienna rectifier can produce 3 different voltage values. Assuming the 2 capacitors are generating equal DC-link voltage with a balanced three-phase system, the rectifier input voltage can be expressed as a function of switching signals (S_a, S_b, S_c) and current polarity as (Radomski, 2007):-

$$\begin{bmatrix} V_{an} \\ V_{bn} \\ V_{cn} \end{bmatrix} = \frac{V_{dc}}{6} \begin{bmatrix} 2(1-S_a) & -(1-S_b) & -(1-S_c) \\ -(1-S_a) & 2(1-S_b) & -(1-S_c) \\ -(1-S_a) & -(1-S_b) & 2(1-S_c) \end{bmatrix} \begin{bmatrix} 2sign(I_a)-1 \\ 2sign(I_b)-1 \\ 2sign(I_c)-1 \end{bmatrix} \quad (4.24)$$

The sign function of phase-*i* current defines as,

$$sign(I_i) = \begin{cases} 1 & ; I_i \geq 0 \\ 0 & ; I_i < 0 \end{cases} \quad (4.25)$$

where V_{DC} is the DC-link voltage and *i* is the phase index which inclusive of phase *a*, *b*, and *c*. Note that the switching signals, S_i associated with the active switches of *i*-phase can be either 1 when the switch is conducting or 0 when the switch is turned off.

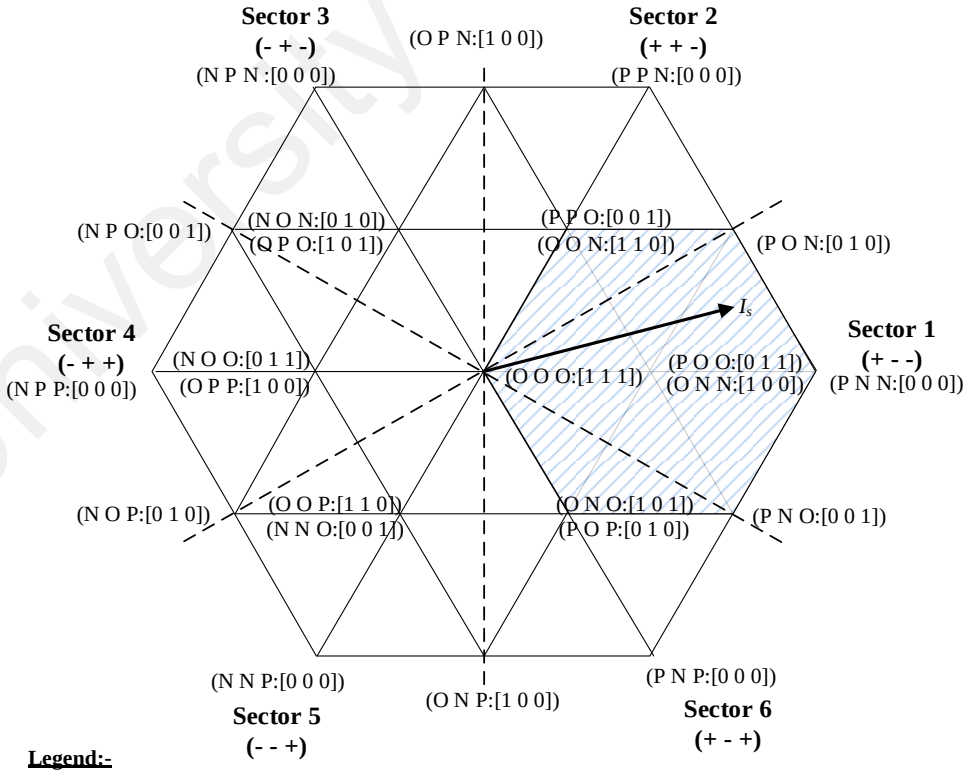

Figure 4.4: Space vector diagram of Vienna rectifier.

University of Malaya

The combination of three switching signals of Vienna rectifier leads to 27 switching vectors with space vector diagram as shown in Figure 4.4, which is similar to the conventional three-levels converter. The space vector diagram is divided into 6 zones of current sectors according to the sign of the input phase current (in the interval of 60°) as detailed in Table 4.1. Each switching vectors are labelled with its corresponding switching state together with its switching signal for each phase. However, there are only 25 switching vectors valid for Vienna rectifier since it has only one zero vector due to the input phase current's polarity, and this will be further explained in the later section. The 25 switching vectors can be categorized according to its size, i.e. 1 zero, 6 big, 6 medium and 12 small switching vectors that comprised of 6 redundant pairs. The magnitude of each size of the switching vectors is shown in Table 4.2.

Table 4.1: Current sectors based on the polarity of input phase current.

Polarity of phase current, $sign(I_i)$	**Current sector**					
	1	**2**	**3**	**4**	**5**	**6**
$sign(I_a)$	1	1	0	0	0	1
$sign(I_b)$	0	1	1	1	0	0
$sign(I_c)$	0	0	0	1	1	1

Table 4.2: Magnitude for different size of the switching vectors.

Size of switching vector	**Magnitude**
Zero	0
Small	$\frac{1}{\sqrt{6}}V_{DC}$
Medium	$\frac{1}{\sqrt{2}}V_{DC}$
Big	$\sqrt{\frac{2}{3}}V_{DC}$

University of Malaya

It is crucial to emphasize that at a given current sector, there are only 8 feasible switching vectors can be realized for system control. For instance, when the stator current vector falls in sector 1, only the 8 switching vectors in the shaded area as shown in Figure 4.4 are available at that instant of operation. Meanwhile, the sign of the phase current *a*, *b*, and *c* is positive (+), negative (-) and negative (-) respectively. Depending on the switching signal (S_i), phase *a* can produce P switching state or O switching state whilst phase *b* and *c* can generate O switching state or N switching state. By considering phase *a* as the example, O switching state generated and it connects the neutral point of the DC-link to the PMSG if the active switch is conducting. On the contrary, when the active switch is turned off, the stator of the PMSG will be connected to P switching state via diodes. In addition to that, there is only one zero switching vector for Vienna rectifier due to the fact that none of the current sectors can produces all phases with P switching state or N switching state. Thereby, only the zero switching vector which composes with O switching state for all the phases is available for Vienna rectifier.

Based on equation (4.24), the input phase voltage for each phase of the 8 different switching vectors for each current sector can be pre-tabulated and summarized as in Table 4.3, allowing an easier implementation of control later.

On the DC side of the Vienna rectifier, the dynamic of the DC-link voltages can be also expressed in terms of switching signals and current polarity as,

$$\frac{d}{dt}\begin{bmatrix}V_p\\V_n\end{bmatrix} = \frac{1}{C}\begin{bmatrix}(1-S_a) & (1-S_b) & (1-S_c)\\ -(1-S_a) & -(1-S_b) & -(1-S_c)\end{bmatrix}\begin{bmatrix}sign(I_a)I_a\\sign(I_b)I_b\\sign(I_c)I_c\end{bmatrix} - I_o \qquad (4.26)$$

with V_p and V_n being the voltage of the upper and lower DC-link capacitors respectively, *C* being the capacitance of the DC-link capacitor and I_o being the load current.

University of Malaya

Table 4.3: Rectifier input phase voltage for all current sectors.

Phase	Switching signals	Current sector					
		1	**2**	**3**	**4**	**5**	**6**
a	[0 0 1]	$\frac{V_{dc}}{2}$	$\frac{V_{dc}}{6}$	$\frac{-V_{dc}}{2}$	$\frac{-V_{dc}}{2}$	$\frac{-V_{dc}}{6}$	$\frac{V_{dc}}{2}$
	[0 1 0]	$\frac{V_{dc}}{2}$	$\frac{V_{dc}}{2}$	$\frac{-V_{dc}}{6}$	$\frac{-V_{dc}}{2}$	$\frac{-V_{dc}}{2}$	$\frac{V_{dc}}{6}$
	[0 1 1]	$\frac{V_{dc}}{3}$	$\frac{V_{dc}}{3}$	$\frac{-V_{dc}}{3}$	$\frac{-V_{dc}}{3}$	$\frac{-V_{dc}}{3}$	$\frac{V_{dc}}{3}$
	[1 0 0]	$\frac{V_{dc}}{3}$	0	0	$\frac{-V_{dc}}{3}$	0	0
	[1 0 1]	$\frac{V_{dc}}{6}$	$\frac{-V_{dc}}{6}$	$\frac{-V_{dc}}{6}$	$\frac{-V_{dc}}{6}$	$\frac{V_{dc}}{6}$	$\frac{V_{dc}}{6}$
	[1 1 0]	$\frac{V_{dc}}{6}$	$\frac{V_{dc}}{6}$	$\frac{V_{dc}}{6}$	$\frac{-V_{dc}}{6}$	$\frac{-V_{dc}}{6}$	$\frac{-V_{dc}}{6}$
	[1 1 1]	0	0	0	0	0	0
	[0 0 0]	$\frac{2V_{dc}}{3}$	$\frac{V_{dc}}{3}$	$\frac{-V_{dc}}{3}$	$\frac{-2V_{dc}}{3}$	$\frac{-V_{dc}}{3}$	$\frac{V_{dc}}{3}$
b	[0 0 1]	$\frac{-V_{dc}}{2}$	$\frac{V_{dc}}{6}$	$\frac{V_{dc}}{2}$	$\frac{V_{dc}}{2}$	$\frac{-V_{dc}}{6}$	$\frac{-V_{dc}}{2}$
	[0 1 0]	0	0	$\frac{V_{dc}}{3}$	0	0	$\frac{-V_{dc}}{3}$
	[0 1 1]	$\frac{-V_{dc}}{6}$	$\frac{-V_{dc}}{6}$	$\frac{V_{dc}}{6}$	$\frac{V_{dc}}{6}$	$\frac{V_{dc}}{6}$	$\frac{-V_{dc}}{6}$
	[1 0 0]	$\frac{-V_{dc}}{6}$	$\frac{V_{dc}}{2}$	$\frac{V_{dc}}{2}$	$\frac{V_{dc}}{6}$	$\frac{-V_{dc}}{2}$	$\frac{-V_{dc}}{2}$
	[1 0 1]	$\frac{-V_{dc}}{3}$	$\frac{V_{dc}}{3}$	$\frac{V_{dc}}{3}$	$\frac{V_{dc}}{3}$	$\frac{-V_{dc}}{3}$	$\frac{-V_{dc}}{3}$
	[1 1 0]	$\frac{V_{dc}}{6}$	$\frac{V_{dc}}{6}$	$\frac{V_{dc}}{6}$	$\frac{-V_{dc}}{6}$	$\frac{-V_{dc}}{6}$	$\frac{-V_{dc}}{6}$
	[1 1 1]	0	0	0	0	0	0
	[0 0 0]	$\frac{-V_{dc}}{3}$	$\frac{V_{dc}}{3}$	$\frac{2V_{dc}}{3}$	$\frac{V_{dc}}{3}$	$\frac{-V_{dc}}{3}$	$\frac{-2V_{dc}}{3}$
c	[0 0 1]	0	$\frac{-V_{dc}}{3}$	0	0	$\frac{V_{dc}}{3}$	0
	[0 1 0]	$\frac{-V_{dc}}{2}$	$\frac{-V_{dc}}{2}$	$\frac{-V_{dc}}{6}$	$\frac{V_{dc}}{2}$	$\frac{V_{dc}}{2}$	$\frac{V_{dc}}{6}$
	[0 1 1]	$\frac{-V_{dc}}{6}$	$\frac{-V_{dc}}{6}$	$\frac{V_{dc}}{6}$	$\frac{V_{dc}}{6}$	$\frac{V_{dc}}{6}$	$\frac{-V_{dc}}{6}$
	[1 0 0]	$\frac{-V_{dc}}{6}$	$\frac{-V_{dc}}{2}$	$\frac{-V_{dc}}{2}$	$\frac{V_{dc}}{6}$	$\frac{V_{dc}}{2}$	$\frac{V_{dc}}{2}$
	[1 0 1]	$\frac{V_{dc}}{6}$	$\frac{-V_{dc}}{6}$	$\frac{-V_{dc}}{6}$	$\frac{-V_{dc}}{6}$	$\frac{V_{dc}}{6}$	$\frac{V_{dc}}{6}$
	[1 1 0]	$\frac{-V_{dc}}{3}$	$\frac{-V_{dc}}{3}$	$\frac{-V_{dc}}{3}$	$\frac{V_{dc}}{3}$	$\frac{V_{dc}}{3}$	$\frac{V_{dc}}{3}$
	[1 1 1]	0	0	0	0	0	0
	[0 0 0]	$\frac{-V_{dc}}{3}$	$\frac{-2V_{dc}}{3}$	$\frac{-V_{dc}}{3}$	$\frac{V_{dc}}{3}$	$\frac{2V_{dc}}{3}$	$\frac{V_{dc}}{3}$

University of Malaya

4.1.2.1 Feasible operation region of Vienna rectifier

It is vital to consider the feasible operating region of Vienna rectifier due to its limitation on power factor variation. It is essential to ensure that the phase current does not lead or lag the phase voltage by more than 30°. The lowest allowable power factor for Vienna rectifier is 0.866. The phase angle, γ range can be defined as:

$$-30^{\circ} < \gamma < 30^{\circ} \tag{4.27}$$

Thus, it is preferable to control the PMSG to be operated in the unity power factor operation. In such a case, it is important to compute the sector difference between the stator current and stator flux, Δ_{sec} to identify the available switching vectors for control application. Based on equation (4.10), stator flux sector, $\varphi_{s\,sec}$ can be identified. Similar as the current sector, the stator flux is split into 6 sectors and each of them are spaced equally of 60°. The sector difference is either 1 or 2 due to the feasible operation region of Vienna rectifier as described with equation (4.27). Since the stator flux of the PMSG always lagged behind stator voltage by 90°, the allowable lag angle of stator flux with stator current ranges from 60° to 120° as clearly shown in Figure 4.5.

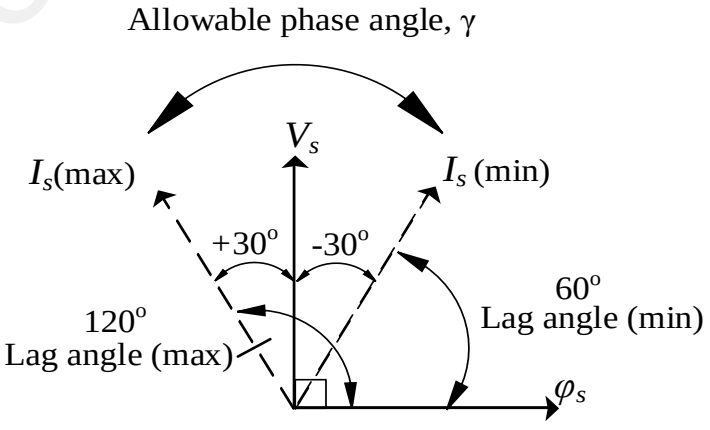

Figure 4.5: Displacement angle between PMSG's variables.

University of Malaya

4.2 Direct torque control (DTC) based on Vienna rectifier

While there are different ways of implementing DTC, the classical approach is based on a switching vector look-up table (LUT). Hence, the discussion here will be referring to the concept of the LUT-DTC based on Vienna rectifier adapted from (Rajaei et al., 2013), and the control block diagram is as depicted in Figure 4.6. The parameters to be controlled are the rotor speed, stator flux, torque, and neutral point voltage, V_{pn}.

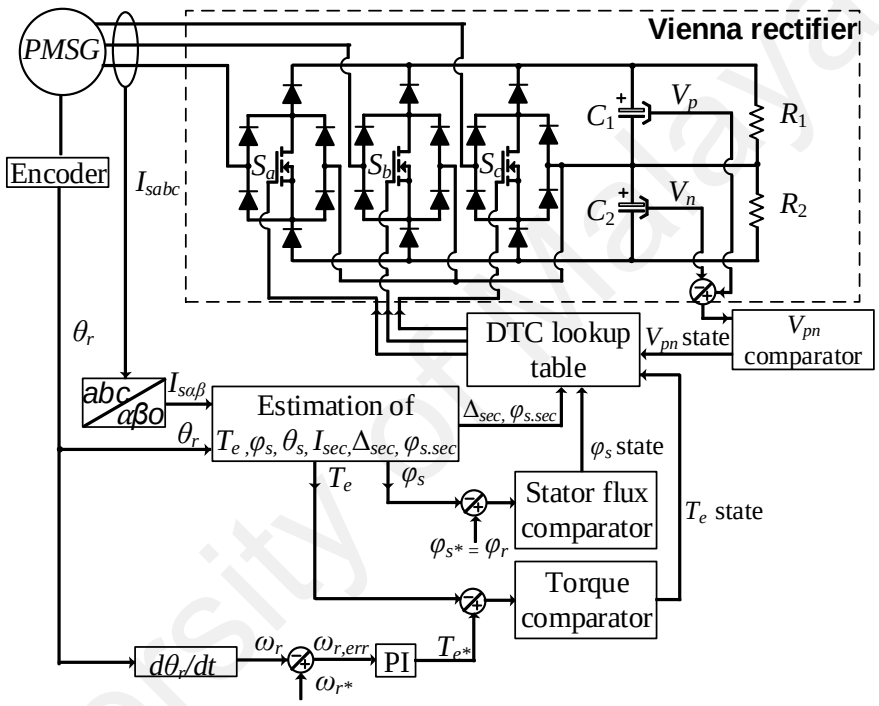

Figure 4.6: Block diagram of the DTC based on Vienna rectifier.

First, three-phase current are measured and transformed into the corresponding α-β components, $I_{s\alpha\beta}$. Rotor speed, ω_r and rotor position, θ_r of the PMSG are measured from the encoder and they are used together with the stator current to estimate the torque and stator flux using models described previously ((4.9) to (4.11)). In order to determine the feasible switching vectors of the Vienna rectifier from a LUT, the sector difference, Δ_{sec} between stator current sector, I_{sec} and stator flux sector, $\varphi_{s\,sec}$ is also calculated. There is a proportional integrator (PI) speed controller produces a reference torque, T_e^* based on the rotor speed error, $\omega_{r\,err.}$ Since unity power factor is desired, the reference stator flux, φ_s^* is set to be same as to the rotor flux, φ_r.

University of Malaya

There are three comparators for the control variables, i.e. DC-link voltages, torque and stator flux. Based on the output of the comparators, $\Delta_{sec,}$ and $\varphi_{s\,sec}$, an optimum switching vector is selected according to the LUT to achieve the desired rotor speed, ω_r^*.

As explained in the previous section, the sector difference is either 1 or 2 due to the limited operation region of Vienna rectifier. In such a case, the development of DTC lookup table has to be built for both conditions, which depends on the sector differences (Δ_{sec} is 1 or 2) as the selection of switching vectors for the DTC will be different.

4.3 Proposed PMSG voltage model for DTC based on Vienna rectifier

It is beneficial to develop a standard PMSG model that relates with the switching vector which will help in the analysis and the design of the DTC lookup table. In the previous section, it had been explained that the desired change of PMSG's torque and stator flux can be achieved by selecting the optimum voltage vector. Hence, a standard model for stator voltage in the *x-y* reference frame is developed. A new labelling system is designed for the switching vectors of the Vienna rectifier to facilitate the stator voltage model development. First, the voltage space vector diagram is divided into 12 uniform sectors identifiable with sector index, *k; k* = {1,2,3,4,5,6,7,8,9,10,11, and 12}, each with an angle of 30^o. The switching vector of the Vienna rectifier is then labeled as V_n (*r*, *k*), sees Figure 4.7 in which its coordinate is created based on its length from the origin, *r* and sector index, *k.* The vector index, *n* is derived from the binary representation of the switching signals in the phase sequence of *a*, *b*, and *c* (J. Hu & Zhu, 2011). Take note that *r* is the radius of switching vector from origin, *r* = {0, 1,$\sqrt{3}$, and 2} that depends on the size of the switching vectors, as indicated in Table 4.2. As compared to the existing labelling system in (Rajaei et al., 2013), coordinate, size, and switching signals of the switching vectors can be easily identified with this proposed vector labeling method as can be clearly seen in Figure 4.7.

University of Malaya

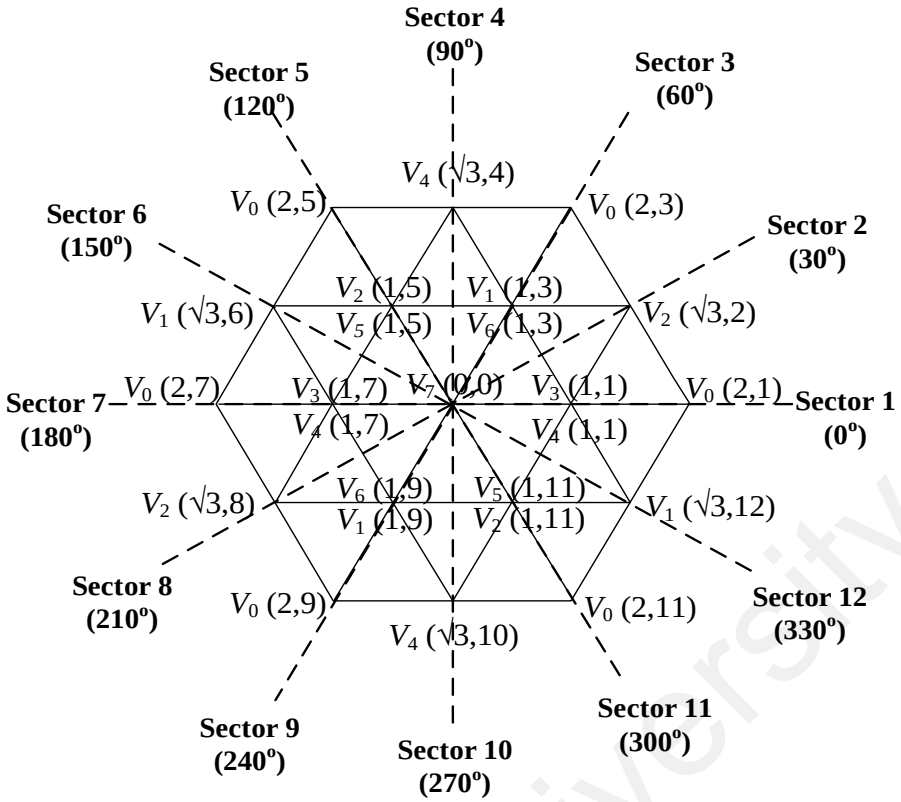

(a)

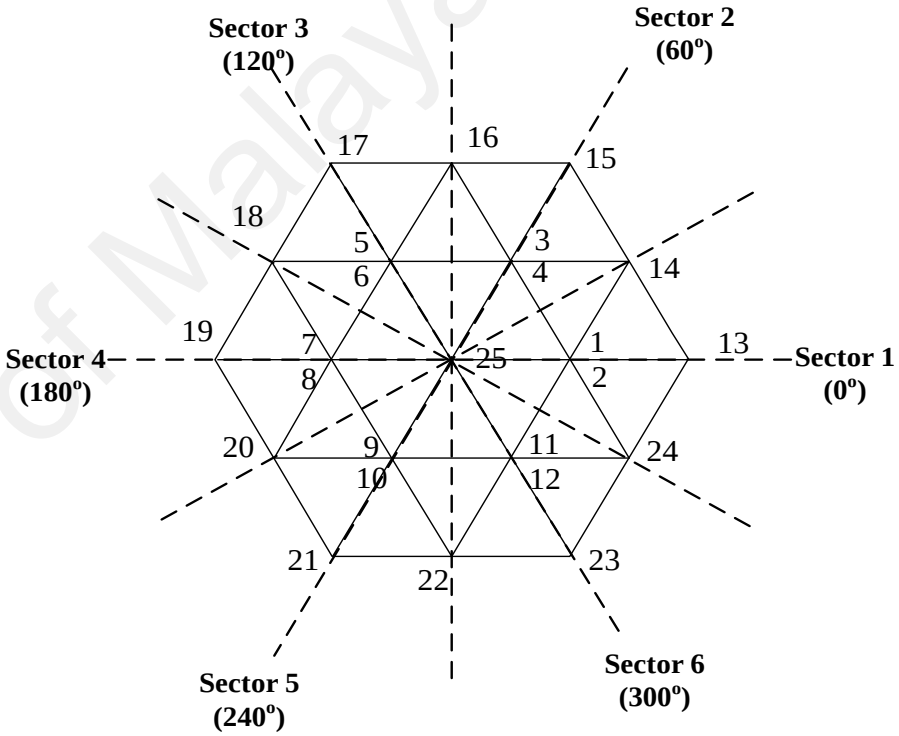

(b)

Legend:
V_n (r,k)
where,
n is the switching vector's index, n={0,1,2,...7};
r is switching vector's radius, r ={0, 1,√3 ,2};
k sector index, r ={1,2,3...12}.

Figure 4.7: Labelling system of each switching vectors for Vienna rectifier. (a) Proposed labeling system, (b) Existing labeling system.

University of Malaya

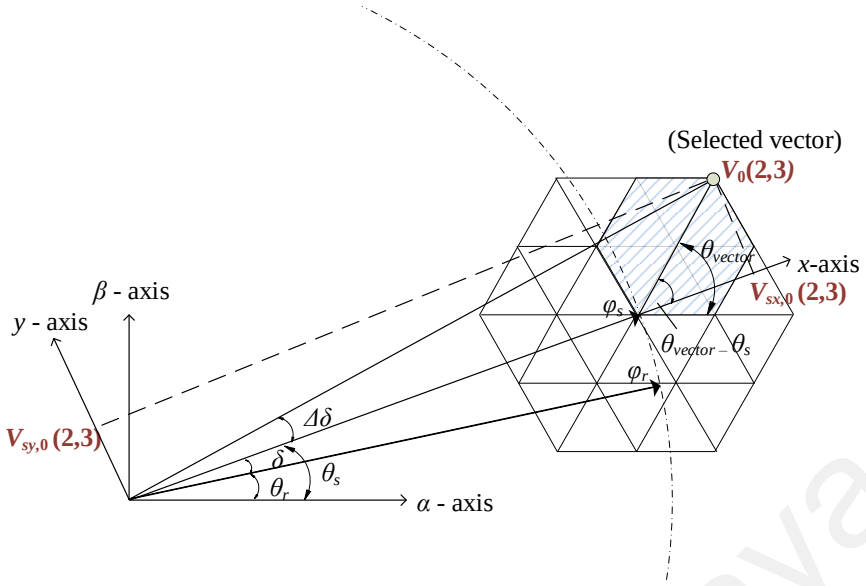

Figure 4.8: Generalized stator voltage development.

Figure 4.8 shows the projection of the selected applied voltage vector, V_0 (2,3) in both *x*- and *y*-axis. The switching vectors at the shaded area are obtained when Δ_{sec} is 1 with the stator flux positioned at sector 1. The generalized mathematical model of the stator voltage can be created using trigonometry as follows;

$$V_{sxy,n}(r,k) = |V_s| e^{j(\theta_{vector} - \theta_s)} \tag{4.28}$$

with θ_{vector} and $|V_s|$ is the angle and magnitude of the selected vector respectively which defined as: -

$$\theta_{vector} = \frac{(k-1)2\pi}{k_{max}} \tag{4.29}$$

$$|V_s| = \sqrt{\frac{2}{3}} V_{DC} \left(\frac{r}{r_{max}}\right) \tag{4.30}$$

Take note that they can be easily tabulated using vector's coordinate, (*r*, *k*) with r_{max} and k_{max} are 2 and 12 respectively. By substituting (4.29) and (4.30) into (4.28), it becomes,

$$V_{sxy,n}(r,k) = \sqrt{\frac{2}{3}} V_{DC} \left(\frac{r}{r_{max}}\right) e^{j\left(\frac{(k-1)2\pi}{k_{max}} - \theta_s\right)} \tag{4.31}$$

By expanding the stator voltage model into *x* and *y* components,

$$V_{sx.n}(r,k) = \sqrt{\frac{2}{3}} V_{DC} \frac{r}{r_{max}} \cos\left(\frac{k-1}{k_{max}} 2\pi - \theta_s\right) \tag{4.32}$$

$$V_{sy,n}(r,k) = \sqrt{\frac{2}{3}} V_{DC} \frac{r}{r_{max}} \sin\left(\frac{k-1}{k_{max}} 2\pi - \theta_s\right) \tag{4.33}$$

University of Malaya

This standardized model can be used for the effect analysis of all the 25 switching vectors of the Vienna rectifier. By substituting the derived stator voltage model (4.32) and (4.33) for each switching vectors into PMSG's dynamic model ((4.16) and (4.23)), the rate of change of the torque and stator flux can be examined. Comparatively, the derivation of both stator flux and the change of load angle for each switching vectors as found in (Rajaei et al., 2013) is no longer required. Such derived stator voltage model could help in the reduction of wrong model derivation possibility since it can be merely calculated based on the vector's coordinate. Furthermore, it simplifies the analysis as well as the development of the LUT for DTC compared to the method in (Rajaei et al., 2013).

4.4 Theoretical analysis on switching vectors selection

The detailed analysis on the effect of each switching vectors was conducted so that the appropriate switching vectors were selected for the DTC LUT. The PMSG properties which used in the analysis are shown in Table 4.4. There are three important variables of the PMSG will be affected by the selected voltage vector, i.e. torque, stator flux and DC-link voltage. The analysis of each variable was carried out by assuming stator flux is equal to the rotor flux, i.e. 0.06 Wb with load angle of 15º.

Table 4.4: PMSG and Vienna Rectifier parameters used.

Parameters	**Values**
PMSG	
Stator resistance, R_s	2.2 Ohm
Stator inductance, L_s	8.721 mH
Pole pairs, p	4
Inertia, J	0.031 mkg/m^2
Rotor flux, φ_r	0.06 Wb
Rated torque	-1.27 Nm
Rated rotor speed	3000 rpm
Vienna rectifier	
DC-link voltage	300 V
DC-link capacitance	470 µF
Load resistance	40 Ohm

University of Malaya

4.4.1 Effect study of electromagnetic torque and stator flux

Figure 4.9 and Figure 4.10 are plotted to investigate the effect of the switching vectors on the rate of change of torque and stator flux for the full cycle of stator flux respectively. The stator flux angle is divided into 6 sectors of 60^o interval. Take note that there are 4 vectors are shared between the stator flux sectors depending on the Δ_{sec}, and they can be identified through the legend in the figure with Δ_{sec}, i.e. 1 or 2. As can be seen in both figures, the torque and stator flux variation trajectories repeat themselves in each stator flux sector. The suitable switching vectors for the other sectors can be easily decided by analyzing the effect of switching vectors on torque and stator flux variation for a sector. Therefore, Table 4.5 can be built to summarize the torque and stator flux variation when the stator flux positioned in sector 1 for DTC at both conditions of Δ_{sec}.

If the stator flux is positioned in sector 1 with Δ_{sec} is 1, most of the available switching vectors (which represent in terms of the vector index), i.e. 0, 1, 2, 3, 4, 5, and 6 can cause positive torque variation. On the contrary, only switching vector, 7 can be employed if negative change in torque is desired. Similarly, the stator flux variation will be positive when switching vectors, 0, 1, 2, 3, and 6 are applied. Switching vectors 4 and 5 will give negative stator flux variation while switching vector, 7 does not give any changes on the stator flux since its magnitude is zero. Similar conclusions can be drawn on the switching vectors when Δ_{sec} is 2 as given in Table 4.5.

Table 4.5: Summarized switching table for direct torque control.

<table>
<tr><th rowspan="2">Δ_{sec}</th><th rowspan="2">$\frac{d\tau}{dt}$</th><th rowspan="2">$\frac{d\varphi_s}{dt}$</th><th colspan="4">Stator flux angle (sector 1)</th></tr>
<tr><th>$-30^o < \theta_s < -15^o$</th><th>$-15^o < \theta_s < 0^o$</th><th>$0^o < \theta_s < 15^o$</th><th>$15^o < \theta_s < 30^o$</th></tr>
<tr><td rowspan="4">1</td><td rowspan="2">+</td><td>+</td><td colspan="3">0, 1, 2, 3, 6</td><td>0, 1,2, 4, 6</td></tr>
<tr><td>−</td><td colspan="2">4, 5</td><td colspan="2">5</td></tr>
<tr><td rowspan="2">−</td><td>+</td><td colspan="3" rowspan="2">7</td><td>3, 7</td></tr>
<tr><td>−</td><td>7</td></tr>
<tr><td rowspan="4">2</td><td rowspan="2">+</td><td>+</td><td colspan="2">6</td><td colspan="2">4, 6</td></tr>
<tr><td>−</td><td>0, 2, 4, 5</td><td>0, 1, 2, 4, 5</td><td>0, 1, 2, 5</td><td>0, 2, 3, 4, 5</td></tr>
<tr><td rowspan="2">−</td><td>+</td><td colspan="4">7</td></tr>
<tr><td>−</td><td>1, 3, 7</td><td colspan="2">3, 7</td><td>7</td></tr>
</table>

University of Malaya

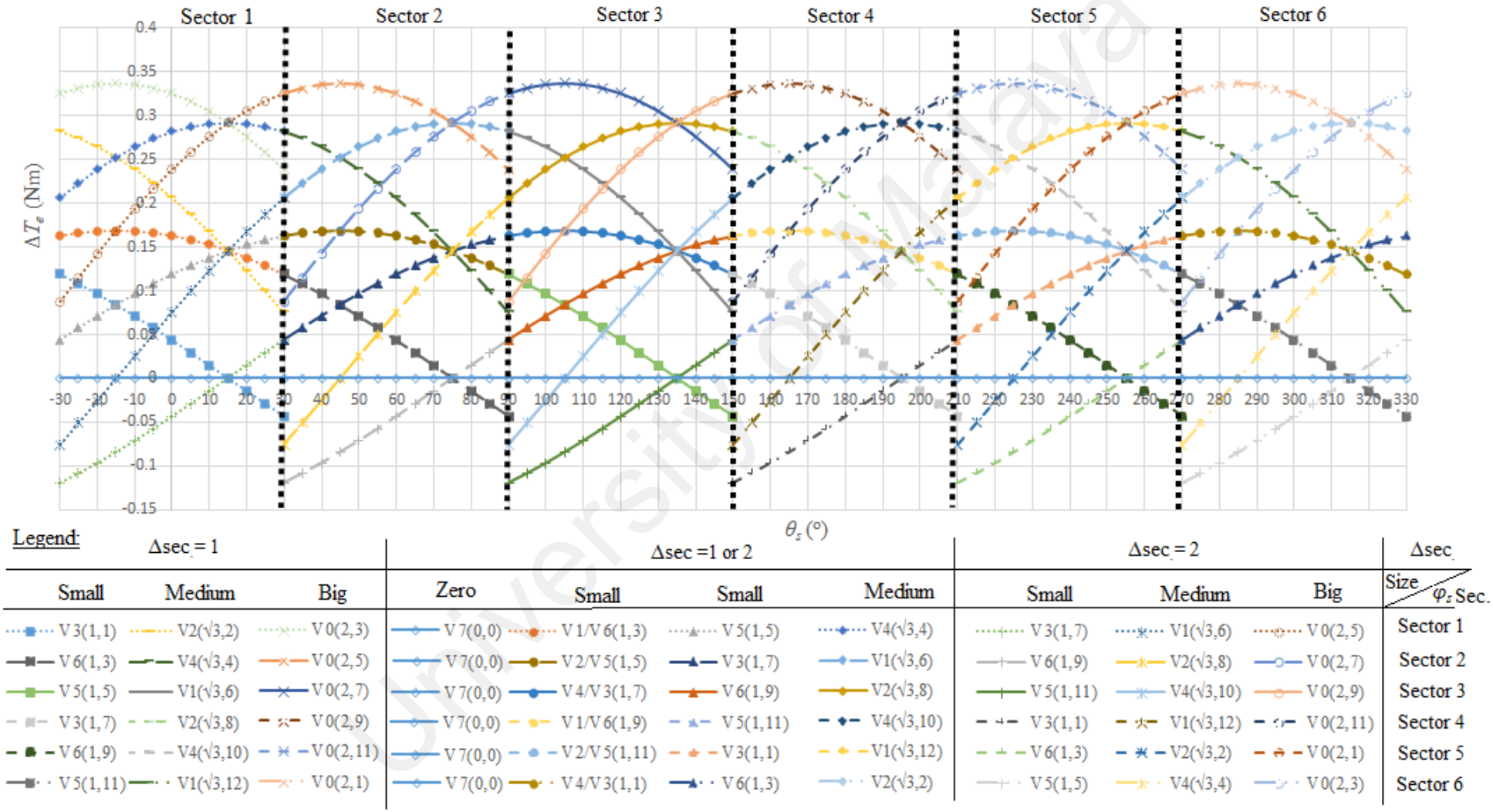

Figure 4.9: Effect of the switching vector on electromagnetic torque.

University of Malaya

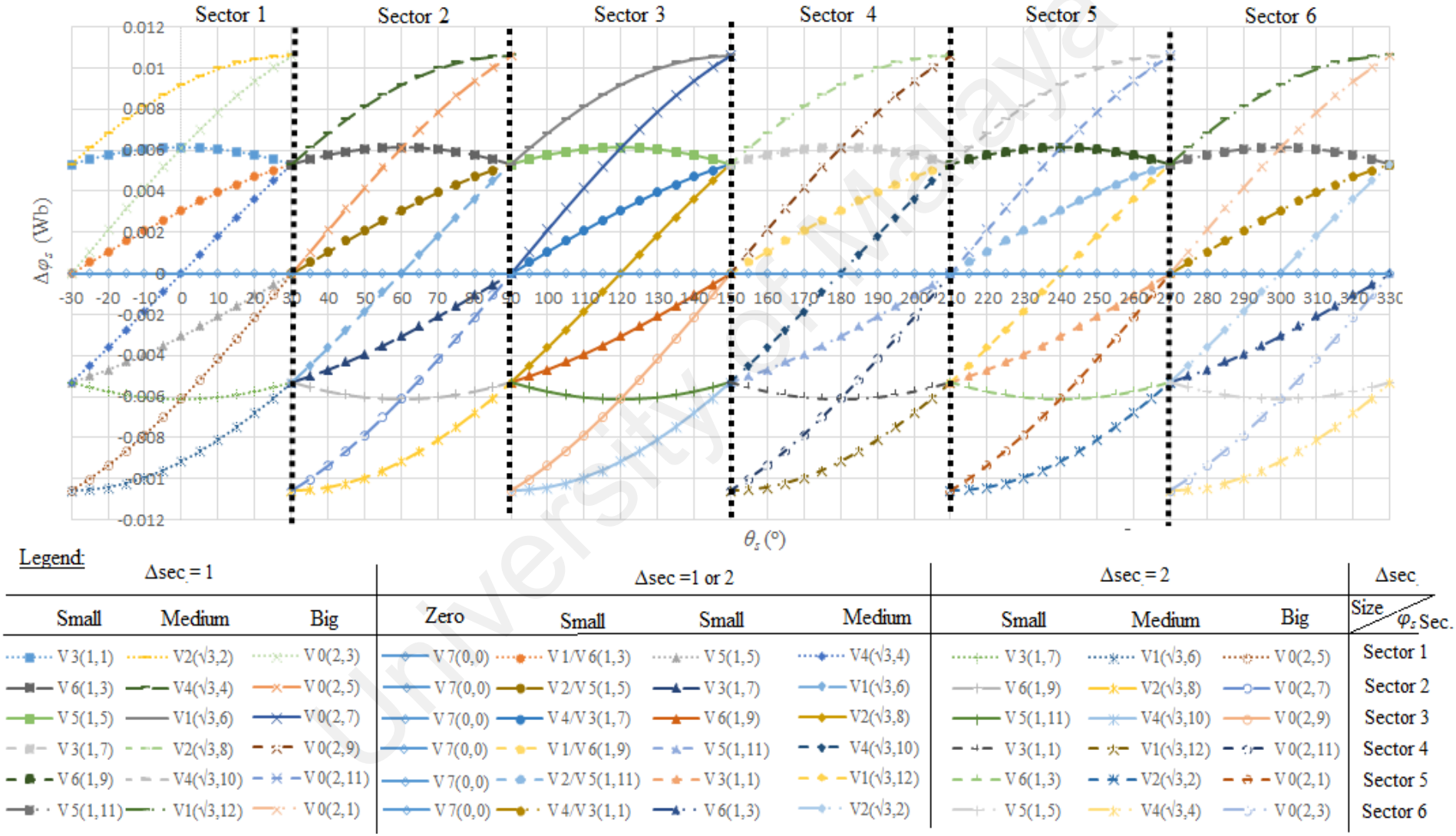

Figure 4.10: Effect of the switching vector on the stator flux.

University of Malaya

Additionally, it is worth noting that each switching vector produces different magnitude of torque variation and stator flux within the sectors. Table 4.6 and Table 4.7 show the switching vectors which are producing electromagnetic torque variation and stator flux variation in decreasing order for both of the Δ_{sec}.

Table 4.6: Variation rate of electromagnetic torque.

$\Delta_{sec} = 1$		
Stator flux sector	$\frac{d\tau}{dt} > 0$	$\frac{d\tau}{dt} < 0$
$-30^o < \theta_s < -15^o$	0>2>4>1 or 6>3>5	7
$-15^o < \theta_s < 0^o$	0>4>2>1 or 6>5>3	
$0^o < \theta_s < 15^o$		
$15^o < \theta_s < 30^o$	4>0>5>1 or 6>2	7>3
$\Delta_{sec} = 2$		
$-30^o < \theta_s < -15^o$	4>6>0>2 or 5	7>1>3
$-15^o < \theta_s < 0^o$	4>0>6>2 or 5>1	7>3
$0^o < \theta_s < 15^o$		
$15^o < \theta_s < 30^o$	0>4>1>2 or 5>6>3	7

Table 4.7: Variation rate of stator flux.

$\Delta_{sec} = 1$			
Stator flux sector	$\frac{d\varphi_s}{dt} > 0$	$\frac{d\varphi_s}{dt} = 0$	$\frac{d\varphi_s}{dt} < 0$
$-30^o < \theta_s < -15^o$	2>3>0>1 or 6	7	4>5
$-15^o < \theta_s < 0^o$			
$0^o < \theta_s < 15^o$	2>0>3>1 or 6>4		5
$15^o < \theta_s < 30^o$			
$\Delta_{sec} = 2$			
$-30^o < \theta_s < -15^o$	6	7	4>2 or 5>3>1
$-15^o < \theta_s < 0^o$			
$0^o < \theta_s < 15^o$	6>4		2 or 5 >0>3>1
$15^o < \theta_s < 30^o$			

These tables can be served as the guideline for the switching vectors LUT development.

University of Malaya

It is important to highlight that the rate of change of torque can be affected by the operating point of the machine. By referring to equation (4.23), it is obvious that the rate of change of torque is influenced by the operating rotor speed. The torque variation for a sector is plotted (Figure 4.11 (a) and (b)) for both extreme scenarios when the PMSG is operating at 0 rpm and at its rated condition, 3000 rpm when stator flux located in sector 1. The overall effect of all the feasible switching vectors is shifted downward during high speed operation with lower torque variation magnitude. It is important to take note of those switching vectors near to the zero crossing (switching vectors that are close to the horizontal dotted line) during LUT development. The selected vectors near this area might no longer give the desired torque change direction when the PMSG is operating at different speed.

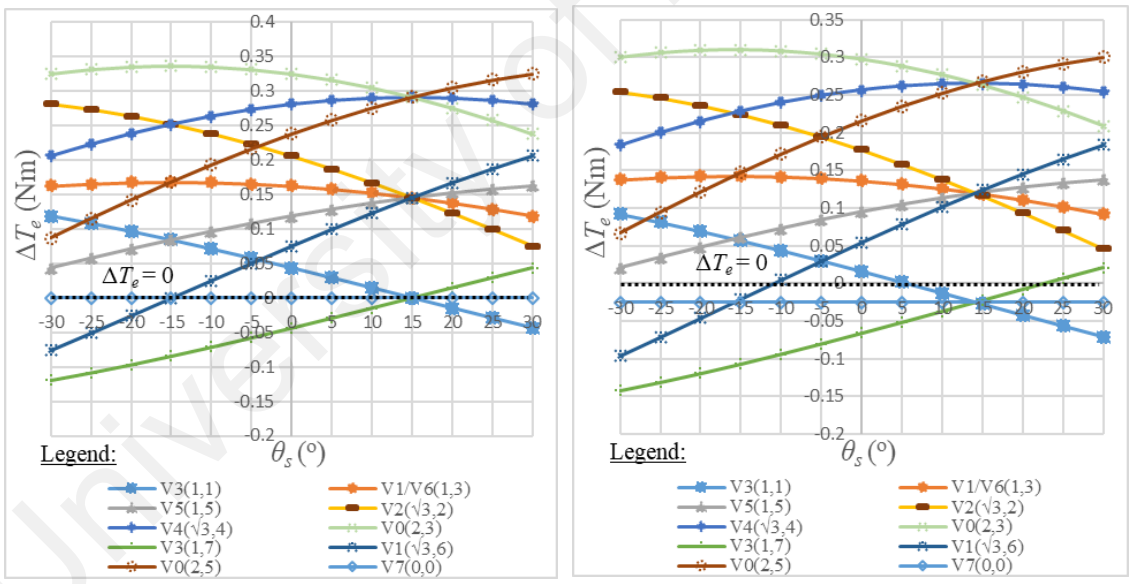

(a) (b)

Figure 4.11: Torque variation at different rotor speeds for both Δ_{sec} of 1 and 2. (a) 0 rpm, (b) 3000 rpm.

University of Malaya

4.4.2 Effect of the upper and lower DC-link voltage variation

The balanced three-phase stator current of the PMSG can be defined as: -

$$I_{sa} = I_s \cos \theta_r \tag{4.34}$$

$$I_{sb} = I_s \cos(\theta_r - \frac{2\pi}{3}) \tag{4.35}$$

$$I_{sc} = I_s \cos(\theta_r + \frac{2\pi}{3}) \tag{4.36}$$

The effect of the switching vector on the upper and lower DC-link voltage variation is calculated using equation (4.26) and (4.34) to (4.36). The neutral point voltage variation, ΔV_{pn} which is the difference between the upper and lower DC-link voltage variation is then computed to identify the variation in terms of polarity for switching vectors in each current stator as follows,

$$\Delta V_{pn} = \Delta V_p - \Delta V_n \tag{4.37}$$

where ΔV_{pn}, ΔV_p, and ΔV_n are the neutral point voltage variation, upper DC-link voltage variation, and lower DC-link voltage variation respectively.

The DC-link voltage variation of each vector is plotted with respect to the rotor position and it is depicted in Figure 4.12. Furthermore, their respective variation is also summarized in term of polarity for each current sector in Table 4.8. The time interval, ΔT and the capacitance magnitude of the upper and lower capacitors are assumed to be one for the simpler analysis purpose.

University of Malaya

Table 4.8: Summarized of neutral point voltage variation in terms of polarity for each current sector.

Switching signals	Index	ΔV_{pn}	Current sector					
			1	**2**	**3**	**4**	**5**	**6**
[0 0 1]	1	$-\frac{1}{C}I_c\Delta t$	+	+	+	−	−	−
[0 1 0]	2	$-\frac{1}{C}I_b\Delta t$	+	−	−	−	+	+
[0 1 1]	3	$+\frac{1}{C}I_a\Delta t$	+	+	−	−	−	+
[1 0 0]	4	$-\frac{1}{C}I_a\Delta t$	−	−	+	+	+	−
[1 0 1]	5	$+\frac{1}{C}I_b\Delta t$	−	+	+	+	−	−
[1 1 0]	6	$+\frac{1}{C}I_c\Delta t$	−	−	−	+	+	+
[1 1 1]	7	0	0	0	0	0	0	0
[0 0 0]	0	0	0	0	0	0	0	0

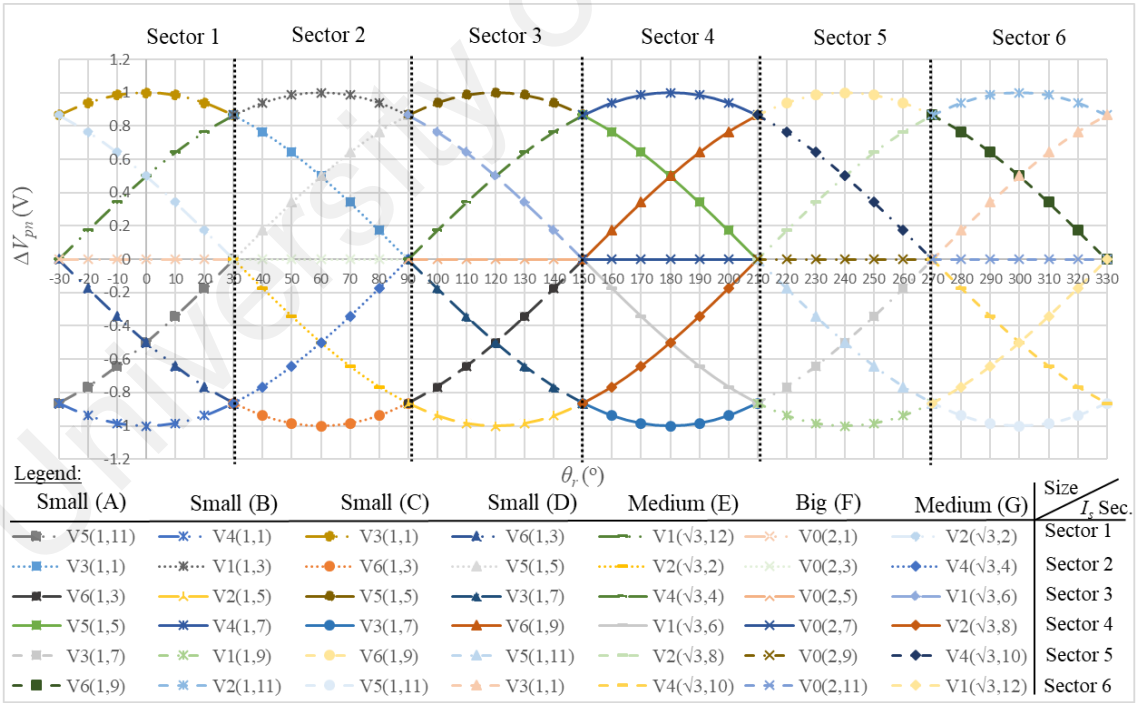

Figure 4.12: The effect of the switching vector on DC-link voltage.

University of Malaya

Figure 4.13 shows the transition of the stator current from current sector one to two. Take note that the alphabets denote the positions of each switching vector of a current sector. For instances, A is the small switching vector, 5 when the stator current is located in sector one whilst it is 3 in sector two. The position of the switching vectors available for each current sector is labeled accordingly as shown in the legend in Figure 4.12.

As can be seen in Figure 4.12, there is an important remark to be outlined in which the effect of a switching vector from the same position on the neutral point will be alternated every sector. For example, by using the case of current sector one in Figure 4.13, the same small switching vector "A" (with square marker in Figure 4.12) which denoted as switching vector with index of 5 will give negative change of ΔV_{pn}. On the contrary, the small switching vector "A", switching vector 3 will produce positive change in ΔV_{pn} instead when stator current transits to sector two. Thereby, by applying the similar analysis to the rest of the current sectors, it can be observed that the effect of small switching vector "A" on the ΔV_{pn} will alternate as shown in Figure 4.12. For odd-numbered sector, vector "A" reduces ΔV_{pn} while for even-numbered sector, ΔV_{pn} will be increased. The effect of switching vectors on the ΔV_{pn} at the same position can be identified, depending on the stator flux sector. As a result, the switching vector LUT should be developed up to sector two of the stator flux when the DC-link voltage variation on the neutral point is considered.

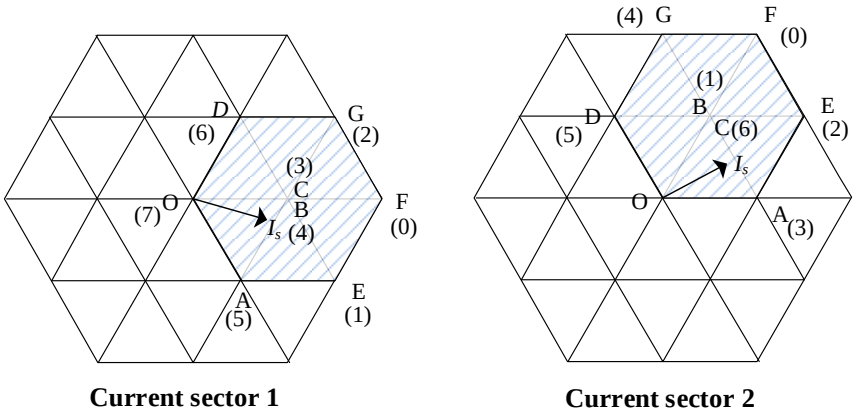

Figure 4.13: Applicable vectors when stator current transits from sector 1 to 2.

University of Malaya

4.5 Improved DTC lookup table development

In this section, the proposed DTC lookup table was discussed. The target for the LUT development is to minimize in PMSG's torque and stator flux ripples as well as to reduce DC-link voltage balancing error. To facilitate the description on the development of the proposed DTC LUT, the torque and stator flux variation was plotted for sector one of the stator flux as shown in Figure 4.14 and Figure 4.15.

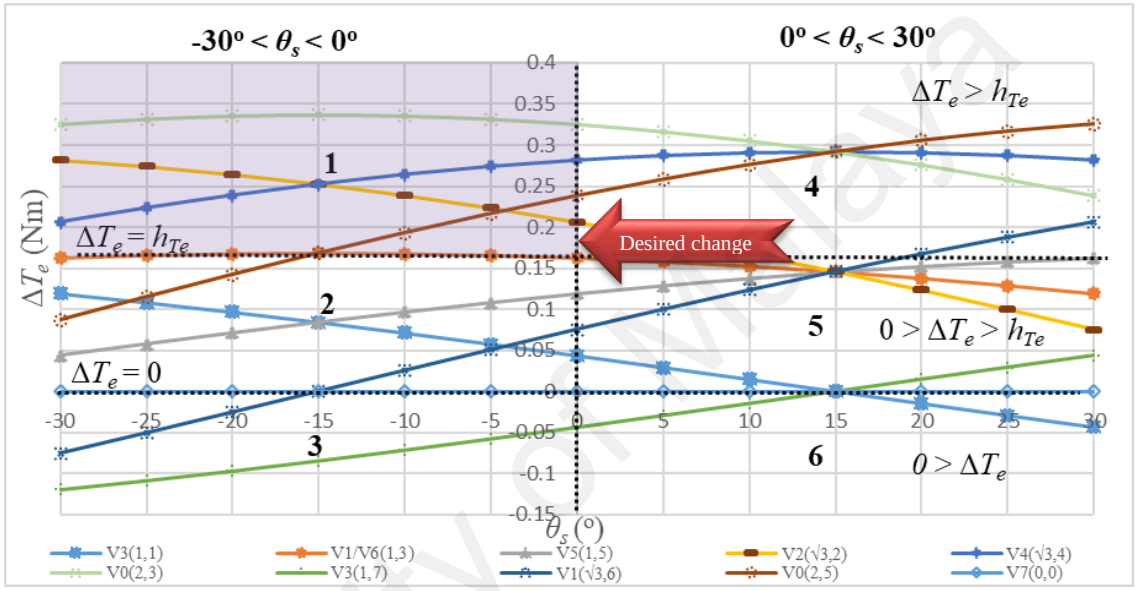

(a)

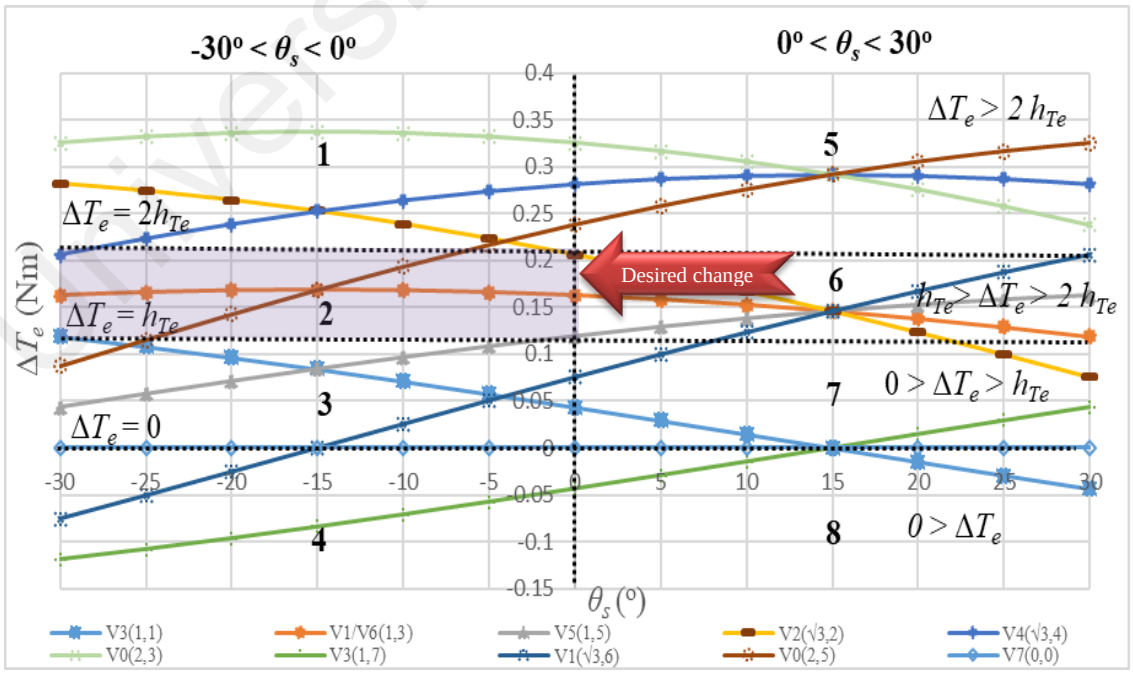

(b)

Figure 4.14: Variation of torque at stator flux sector one for both Δ_{sec} of 1 and 2. (a) The existing method with 6 comparison zones. (b) Proposed approach with 8 comparison zones.

University of Malaya

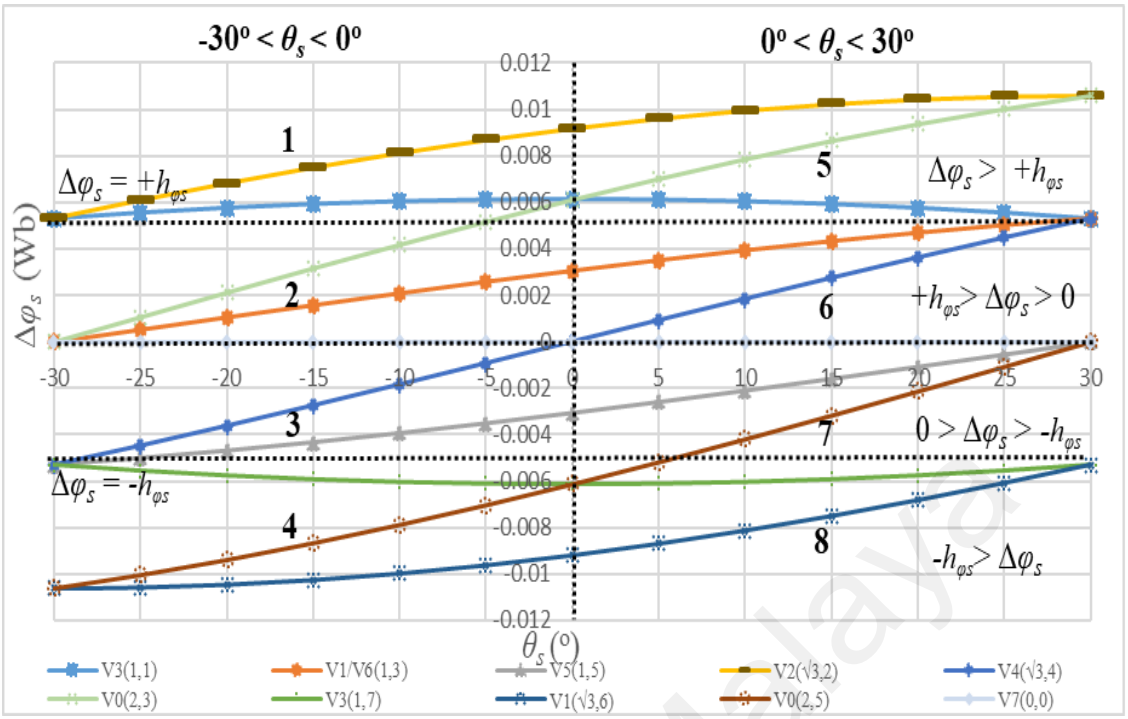

Figure 4.15: Variation of stator flux at stator flux sector one.

Apart from ensuring the selected switching vector creates the desired change in torque and stator flux, the magnitude of the switching vector also play an important role in governing the control performance. By choosing the switching vector that produces small rate of change in both torque and stator flux, the steady-state torque and stator flux ripples can be reduced but the control dynamics during transient will deteriorate. In (Rajaei et al., 2013), comparators are used to cater for torque and stator flux regulation. In terms of torque, 6 comparison zones are established from a 3-level comparator as can be seen in Figure 4.14 (a). In the graph, the horizontal dotted lines indicate the pre-set comparator's band. When the desired change of torque is negative, the switching vectors that fall in zone 3 and 6 are selected. If the desired change of torque is above hT_e, the switching vectors in both zone 1 and 4 are suitable for control. For the case when the desired torque change is fall within 0 and hT_e, switching vectors that belong to zone 2 and 5 are selected. However, with lesser number of comparator's limit set for torque regulation, higher ripples may be results due to bigger variation magnitude of the switching vectors can be selected for the LUT development.

University of Malaya

One of the ways to improve the DTC performance is by increasing the torque comparator's level. As can be seen in Figure 4.14(b), the variation of torque can be divided into 8 zones of comparison conditions by using a 4-level comparator. As compared to the existing method (Rajaei et al., 2013), there are two additional comparing conditions for the torque comparator, i.e. for the case of torque change between h_{Te} and $2h_{Te}$ and the other when the torque change is more than $2h_{Te}$. For instances, if the desired torque change during the stator flux angle at -15^o is 0.18 Nm, those switching vectors that are belonging to zone 2 in Figure 4.14(b) are more appropriate to be chosen for the LUT development as compared to the switching vectors that fall in zone 1 in Figure 4.14(a), since the variation produced is closer to the required change. The possibility of choosing the switching vectors that produce larger change, such as switching vector 0, 2, and 4 can be eliminated. Same way can be applied to choose the suitable switching vectors for stator flux variations with $h_{\varphi s}$ as the pre-set stator flux's comparator band. With such LUT development method, switching vectors that produce smaller change in variation are chosen and hence, smaller ripples in both torque and stator flux during the steady-state can be expected.

Since the DC-link voltage balancing is essential for Vienna rectifier, the DC-link voltage error ($V_{pn} = V_p - V_n$) is subjected to a DC-link voltage comparator which defined with an error band of $\pm h_v$. As presented earlier on the switching vector's effect on the DC-link voltage variation, the switching vectors for LUT development can be selected based on the DC-link voltage error, V_{pn} , error band ($\pm h_v$), and the current sector. For instances, if the V_{pn} is larger than the upper error band ($+h_v$), switching vectors that give either negative or zero change in ΔV_{pn} can be chosen. This corresponds to switching vectors 4, 5, 6, 0 or 7 based on Table 4.8. When V_{pn} is within the error band, small switching vectors and two other switching vectors which consist of a zero and a medium switching vector

University of Malaya

should be selected, such that switching vectors 2, and 3 are classified as producing positive change in DC-link voltage whilst 5, and 6 give the opposite effect.

The redundant small switching vector is eliminated by removing those switching vectors that are not shared between two current sectors to solve the erroneous voltage generated when phase current is near to the zero crossing. These switching vectors can cause the potential change of phase voltage when there is a change in phase current polarity if the switch is in the off state (Johnson & Aliprantis, 2014). In Figure 4.4, switching vectors 3 and 4 are the small switching vectors in sector one, which are POO and ONN respectively. POO will be chosen for LUT development as the state in *b* and *c* phase are composed with O state (which is neutral to the current polarity). This is due to the fact that phase *c* current will turn to negative when the current changes from sector 6 to 1. Similarly, the current polarity of phase *b* will alter when current vector changes from sector 1 to 2.

Table 4.9 and Table 4.10 are the proposed LUT with extra torque comparison conditions for both Δ_{sec} of 1 and 2. The developed LUT is simplified to stator flux at sector 2 and it is a bitwise-operated switching table. The binary search algorithm reduces the memory requires to store the LUT and its details can be found in Appendix B1.

University of Malaya

Table 4.9: Proposed DTC lookup table when the sector difference = 1.

$\Delta_{sec} = 1$			Stator flux sector			
			$-30^o<\theta_s<0^o$	$0^o<\theta_s<30^o$	$30^o<\theta_s<60^o$	$60^o<\theta_s<120^o$
$V_{pn}>+h_v$	$\Delta T_e>2h_{Te}$	$\Delta\varphi_s>+h_{\varphi s}$	4	4*	3	3
		$+h_{\varphi s}>\Delta\varphi_s>0$	4	4*	3	3
		$0>\Delta\varphi_s>-h_{\varphi s}$	0	4	0	0
		$-h_{\varphi s}>\Delta\varphi_s$	2	0	0	0
	$h_{Te}>\Delta T_e>2h_{Te}$	$\Delta\varphi_s>+h_{\varphi s}$	4	4*	3	3
		$+h_{\varphi s}>\Delta\varphi_s>0$	4	4*	3	3
		$0>\Delta\varphi_s>-h_{\varphi s}$	6	6	2	2
		$-h_{\varphi s}>\Delta\varphi_s$	6	6	2	2
	$0>\Delta T_e>h_{Te}$	$\Delta\varphi_s>+h_{\varphi s}$	4	4*	3	3
		$+h_{\varphi s}>\Delta\varphi_s>0$	4	4*	3	3
		$0>\Delta\varphi_s>-h_{\varphi s}$	6	6	2	2
		$-h_{\varphi s}>\Delta\varphi_s$	6	2	2	2
	$0>\Delta T_e$; any φ_s conditions		7	7	7	7
$+h_v>V_{pn}>-h_v$	$\Delta T_e>2h_{Te}$	$\Delta\varphi_s>+h_{\varphi s}$	4	5	1	3
		$+h_{\varphi s}>\Delta\varphi_s>0$	4	5	1	3
		$0>\Delta\varphi_s>-h_{\varphi s}$	0	4	0	1
		$-h_{\varphi s}>\Delta\varphi_s$	2	0	4	0
	$h_{Te}>\Delta T_e>2h_{Te}$	$\Delta\varphi_s>+h_{\varphi s}$	4	5	1	3
		$+h_{\varphi s}>\Delta\varphi_s>0$	5	5	3	3
		$0>\Delta\varphi_s>-h_{\varphi s}$	1	1	2	2
		$-h_{\varphi s}>\Delta\varphi_s$	1	1	2	2
	$0>\Delta T_e>h_{Te}$	$\Delta\varphi_s>+h_{\varphi s}$	4	5	1	3
		$+h_{\varphi s}>\Delta\varphi_s>0$	4	5	1	3
		$0>\Delta\varphi_s>-h_{\varphi s}$	0	4	0	1
		$-h_{\varphi s}>\Delta\varphi_s$	2	0	4	0
	$0>\Delta T_e$; any φ_s conditions		7	7	7	7
$V_{pn}<-h_v$	$\Delta T_e>2h_{Te}$	$\Delta\varphi_s>+h_{\varphi s}$	5	5	1	1*
		$+h_{\varphi s}>\Delta\varphi_s>0$	5	5	1	1*
		$0>\Delta\varphi_s>-h_{\varphi s}$	0	0	0	1
		$-h_{\varphi s}>\Delta\varphi_s$	0	0	4	0
	$h_{Te}>\Delta T_e>2h_{Te}$	$\Delta\varphi_s>+h_{\varphi s}$	5	5	1	1*
		$+h_{\varphi s}>\Delta\varphi_s>0$	5	5	1	1*
		$0>\Delta\varphi_s>-h_{\varphi s}$	1	1	5	5
		$-h_{\varphi s}>\Delta\varphi_s$	1	1	5	5
	$0>\Delta T_e>h_{Te}$	$\Delta\varphi_s>+h_{\varphi s}$	5	5	1	1*
		$+h_{\varphi s}>\Delta\varphi_s>0$	5	5	1	1*
		$0>\Delta\varphi_s>-h_{\varphi s}$	1	1	5	5
		$-h_{\varphi s}>\Delta\varphi_s$	1	1	5	4
	$0>\Delta T_e$; any φ_s conditions		7	7	7	7

University of Malaya

Table 4.10: Proposed DTC lookup table when the sector difference = 2.

$\Delta_{sec} = 2$			Stator flux sector			
			$-30^o<\theta_s<0^o$	$0^o<\theta_s<30^o$	$30^o<\theta_s<60^o$	$60^o<\theta_s<120^o$
$V_{pn} > +h_v$	$\Delta T_e > 2h_{Te}$	$\Delta\varphi_s > +h_{\varphi s}$	0	0	1	0
		$+h_{\varphi s} > \Delta\varphi_s > 0$	0	0	0	0
		$0 > \Delta\varphi_s > -h_{\varphi s}$	6	6	1*	1
		$-h_{\varphi s} > \Delta\varphi_s$	6	6	1*	1
	$h_{Te} > \Delta T_e > 2h_{Te}$	$\Delta\varphi_s > +h_{\varphi s}$	0	0	1	0
		$+h_{\varphi s} > \Delta\varphi_s > 0$	0	0	0	2
		$0 > \Delta\varphi_s > -h_{\varphi s}$	6	6	1*	1
		$-h_{\varphi s} > \Delta\varphi_s$	6	6	1*	1
	$0 > \Delta T_e > h_{Te}$	$\Delta\varphi_s > +h_{\varphi s}$	2	2	3	3
		$+h_{\varphi s} > \Delta\varphi_s > 0$	2	2	3	3
		$0 > \Delta\varphi_s > -h_{\varphi s}$	6	6	1*	1
		$-h_{\varphi s} > \Delta\varphi_s$	6	6	1*	1
	$0 > \Delta T_e$; any φ_s conditions		7	7	7	7
$+h_v > V_{pn} > -h_v$	$\Delta T_e > 2h_{Te}$	$\Delta\varphi_s > +h_{\varphi s}$	4	0	1	0
		$+h_{\varphi s} > \Delta\varphi_s > 0$	0	0	0	0
		$0 > \Delta\varphi_s > -h_{\varphi s}$	6	4	5	1
		$-h_{\varphi s} > \Delta\varphi_s$	6	4	5	1
	$h_{Te} > \Delta T_e > 2h_{Te}$	$\Delta\varphi_s > +h_{\varphi s}$	4	0	1	0
		$+h_{\varphi s} > \Delta\varphi_s > 0$	0	0	0	0
		$0 > \Delta\varphi_s > -h_{\varphi s}$	6	4	5	1
		$-h_{\varphi s} > \Delta\varphi_s$	6	4	5	1
	$0 > \Delta T_e > h_{Te}$	$\Delta\varphi_s > +h_{\varphi s}$	5	5	3	3
		$+h_{\varphi s} > \Delta\varphi_s > 0$	5	5	3	3
		$0 > \Delta\varphi_s > -h_{\varphi s}$	6	6	5	5
		$-h_{\varphi s} > \Delta\varphi_s$	6	6	5	5
	$0 > \Delta T_e$; any φ_s conditions		7	7	7	7
$V_{pn} < -h_v$	$\Delta T_e > 2h_{Te}$	$\Delta\varphi_s > +h_{\varphi s}$	4	0	0	0
		$+h_{\varphi s} > \Delta\varphi_s > 0$	0	0	0	0
		$0 > \Delta\varphi_s > -h_{\varphi s}$	4*	4	5	5
		$-h_{\varphi s} > \Delta\varphi_s$	4*	4	5	5
	$h_{Te} > \Delta T_e > 2h_{Te}$	$\Delta\varphi_s > +h_{\varphi s}$	4	0	0	0
		$+h_{\varphi s} > \Delta\varphi_s > 0$	0	1	0	0
		$0 > \Delta\varphi_s > -h_{\varphi s}$	4*	4	5	5
		$-h_{\varphi s} > \Delta\varphi_s$	4*	4	5	5
	$0 > \Delta T_e > h_{Te}$	$\Delta\varphi_s > +h_{\varphi s}$	5	5	4	4
		$+h_{\varphi s} > \Delta\varphi_s > 0$	5	5	4	4
		$0 > \Delta\varphi_s > -h_{\varphi s}$	4*	4	5	5
		$-h_{\varphi s} > \Delta\varphi_s$	4*	4	5	5
	$0 > \Delta T_e$; any φ_s conditions		7	7	7	7

University of Malaya

4.6 Proposed compensation delay for digital implementation of DTC

Compensation of the calculation delay was considered when the DTC was implemented experimentally using a digital signal processor (DSP). The estimation block of the torque and stator flux at sampling instant, (*t*) involves most of the computation. This delay can deteriorate the performance of the DTC if it is not taken into consideration during the control. In order to ensure the DTC realization behaves approximated to the continuous time system, a simple remedy was proposed using a model-based computation delay compensation approach. The estimated change of the selected switching vector for both torque and stator flux from the previous cycle ($\Delta T_{e,n_{opt}}{}^{*}(t-1)$ and $\Delta \varphi_{s,n_{opt}}{}^{*}(t-1)$) were applied in the estimation models. In this way, the torque and stator flux of the PMSG at the current instant time, (*t*) can be shifted one step forward in time as follows,

$$\varphi_s{}'(t) = \sqrt{\varphi_{s\alpha}{}^2(t) + \varphi_{s\beta}{}^2(t)} + \Delta \varphi_{s,n_{opt}}{}^{*}(t-1) \tag{4.38}$$

$$T_e{}'(t) = \frac{3}{2} p \left(\varphi_{s\alpha}(t) I_{s\beta}(t) - \varphi_{s\beta}(t) I_{s\alpha}(t) \right) + \Delta T_{e,n_{opt}}{}^{*}(t-1) \tag{4.39}$$

Where $n_{opt}{}^{*}$ being the index of the selected optimal switching vector, $\varphi_s{}'(t)$ and $T_e{}'(t)$ are the estimated stator flux and torque with computation delay compensation. The revised control block diagram and its corresponding algorithm is shown in Figure 4.16(a) and Figure 4.16(b). As compared to the conventional DTC, an additional model of variable at (*t*-1) is added into the torque and stator flux estimation model. Note that this additional model can increase the computation time but it is only marginally because the calculation for the selected switching vector is only calculated once.

University of Malaya

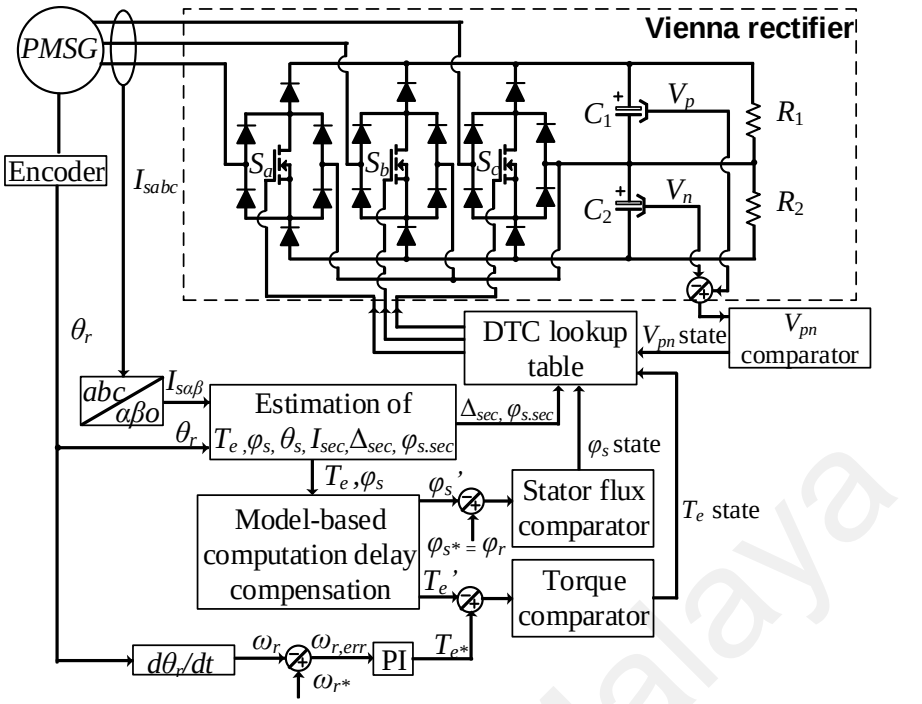

(a)

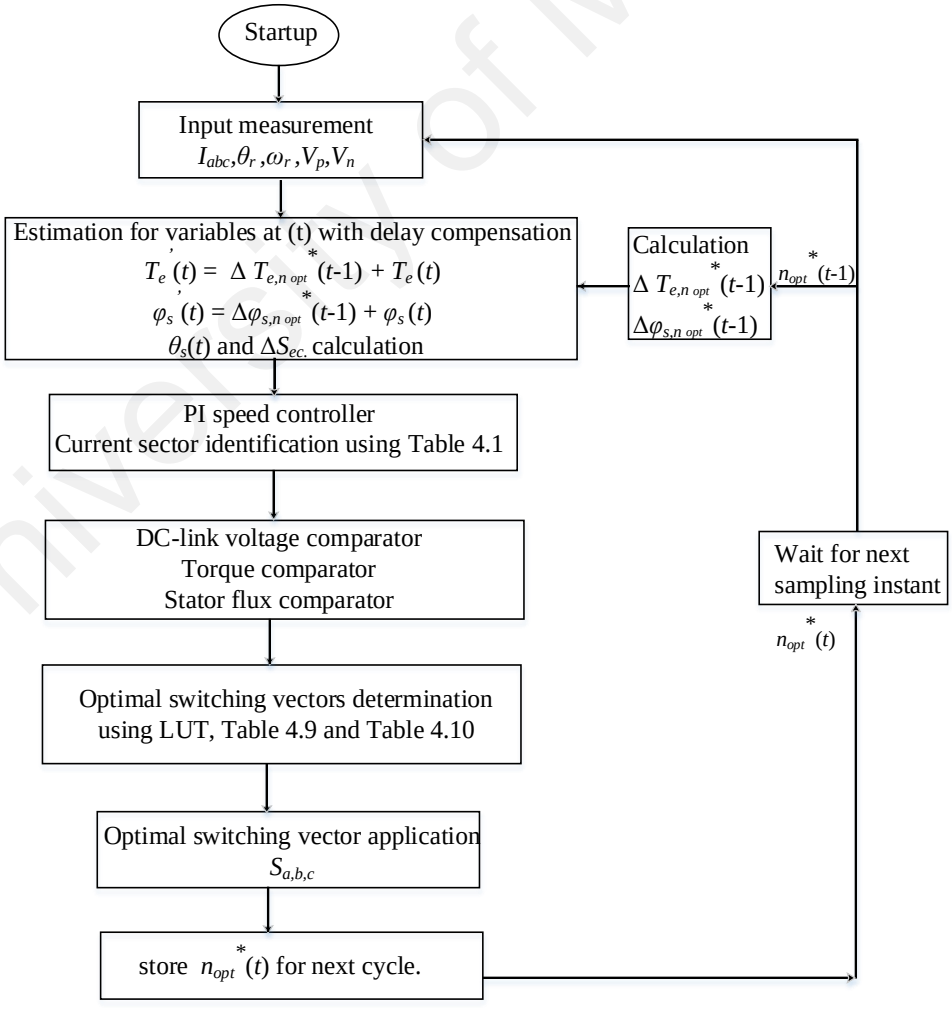

(b)

Figure 4.16: DTC with computation delay compensation. (a) Control block diagram, (b) Flow chart.

University of Malaya

4.7 Matlab simulation

The control of the PMSG based on Vienna rectifier was simulated in Matlab / Simulink using parameters in Table 4.4 to investigate the operation and performance of the DTC method. The Matlab simulation models can be found in the Appendix C1. The output DC-link voltage was simulated using a DC voltage source with the magnitude of 300 V. A wye-resistor was connected to the PMSG with neutral point to obtain the phase voltage measurement. The wye resistor was made up with 220 kOhm of resistance at each phase. The comparator band was fixed at -0.1 Nm and 0.005 Wb for electromagnetic torque and stator flux respectively. The simulations had been carried out using following scenarios to investigate the performance of the DTC with the improved LUT: -

1) Scenario one: Steady-state operation at constant PMSG's speed, 1500 rpm.
2) Scenario two: Transient response during torque step change. The PMSG was initially controlled to be operated at torque, -1 Nm and then a sudden step change of torque was applied at the time, t = 1.1 s to -0.5 Nm.
3) Scenario three: Operation under unbalance DC load condition. This scenario was run to demonstrate the ability of the control to balance the neutral point of the DC link voltage. A resistor (330 Ohms) was connected in parallel to the lower side of the DC link capacitor, C_2. This will result in an unbalanced load for the capacitor with approximately 10% difference in resistance value between the upper and lower load.

In addition, there are factors that can directly affect the overall performance of the proposed LUT-DTC approach. These factors include sampling time, comparator band width, DC-link voltage, and rotor speed. Investigation on how the factors can impact the behavior of the DTC was also studied during the steady-state operation.

University of Malaya

4.7.1 Validation of the stator voltage model in *-xy* reference frame

The simulation was first started with the validation of the developed stator voltage model. Figure 4.17 depicted the comparison results of the torque and stator flux generated from the developed model and simulated output obtained from the PMSG model in Simulink. The simulation results (orange solid line) appeared in good accordance with the developed model output (blue dotted line). This result indicated that the developed stator voltage model was precise and hence, the effect of the switching vectors can be quantified accurately.

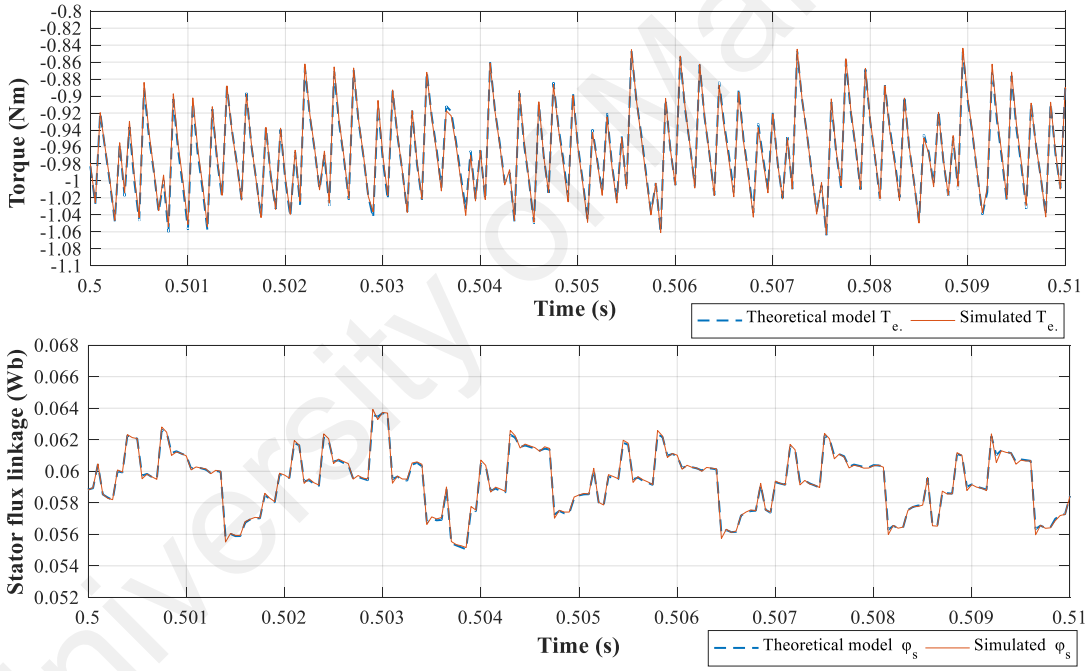

Figure 4.17: Developed theoretical model validation results on electromagnetic torque and stator flux.

University of Malaya

4.7.2 Simulation results of the DTC performance

The improved LUT based DTC were tested with the 3 scenarios described previously and the generated simulation results were compared to the existing DTC as proposed in (Rajaei et al., 2013).

4.7.2.1 Assessment of the proposed DTC's steady-state response

The performance of the DTC for both existing and improved DTC approaches during the operation of constant speed rotor speed at 1500 rpm was shown in Figure 4.18(a) to Figure 4.18(f). The left figure in Figure 4.18 shows the simulation results for the existing DTC approach whilst the right figure presented the results of the proposed LUT-DTC approach. It was clear that the generated three-phase current for both of the approaches were balanced and sinusoidal. The displacement angle between the stator current and phase voltage was in phase since the system was desired to be operated with unity power factor. Besides, the upper and lower DC-link voltages were also restricted within the predefined error band of ±2 V in the range from 148 V to 152 V. The speed, torque and stator flux were well regulated around their corresponding references. Nevertheless, there were spikes presented at the generated torque for the existing DTC approach. The stator flux was also somewhat offset downward from the desired stator flux as compared to the improved LUT of the DTC approach.

For a detailed analysis on the torque ripples section, simulation results for the existing DTC were enlarged and focused in the time interval of 0.005s with the switching vector labelled according to (Rajaei et al., 2013) as depicted in Figure 4.18 (g). In the figure, switching vector was shown at the top-most subfigure, followed by the rate of change of torque, ΔT_e and torque at the bottom. The ΔT_e was calculated using (4.23) by substituting the selected switching vector. The big switching vector, 17 was selected which gives a huge positive variation in torque. Since the torque was desired to track the reference

University of Malaya

magnitude (indicated by dotted line), zero state, 25 was selected after a big variation applied in torque. Thereby, the stator flux exhibited an offset pattern as zero state gives zero or minimum change in stator flux. Such simulation results showed that the proposed LUT can choose more optimized switching vectors that track closer to the reference of the control parameters.

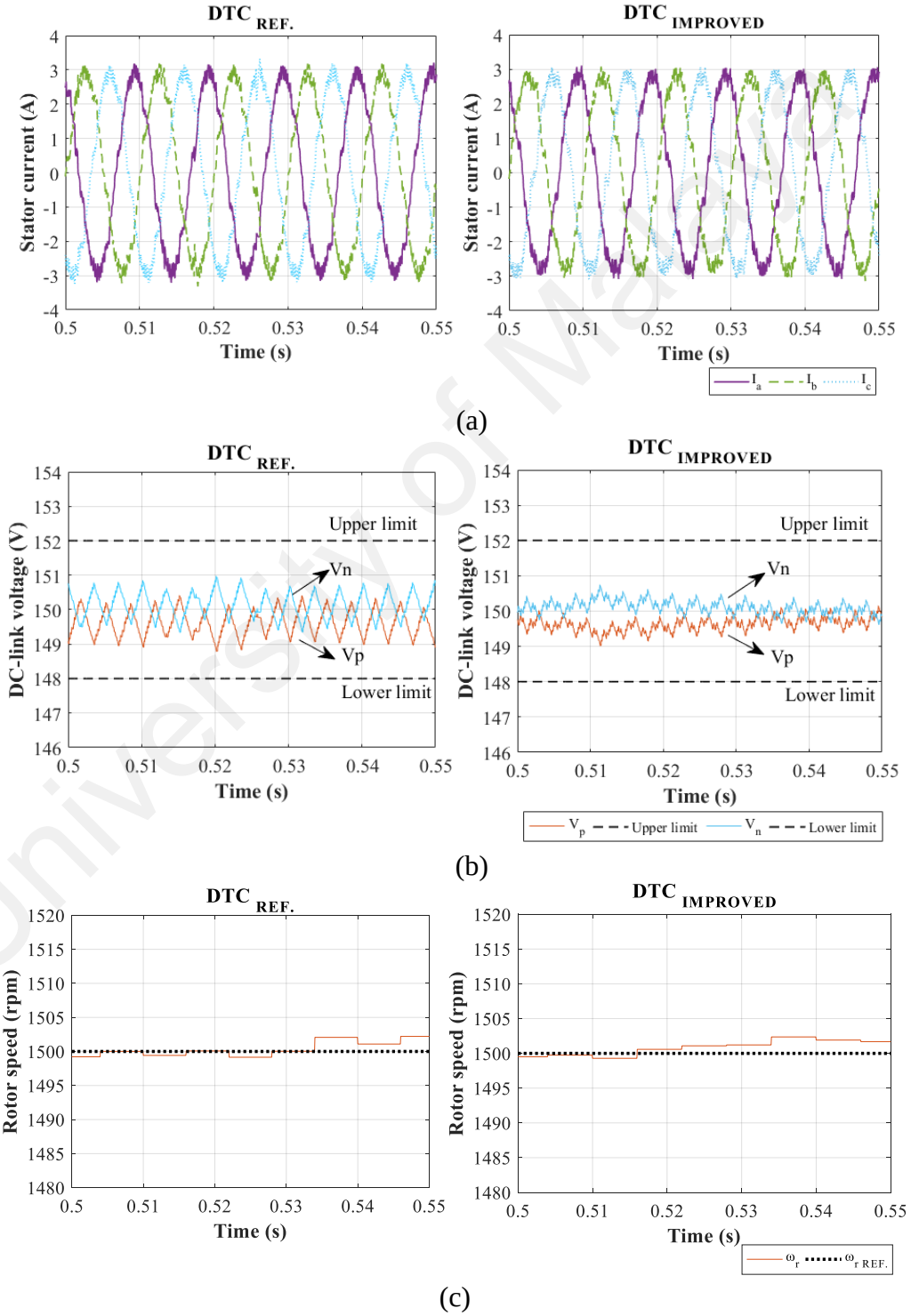

Figure 4.18: Comparison results of the existing DTC and improved DTC during steady-state condition. (a) Stator current, (b) DC-link voltage, (c) rotor speed.

University of Malaya

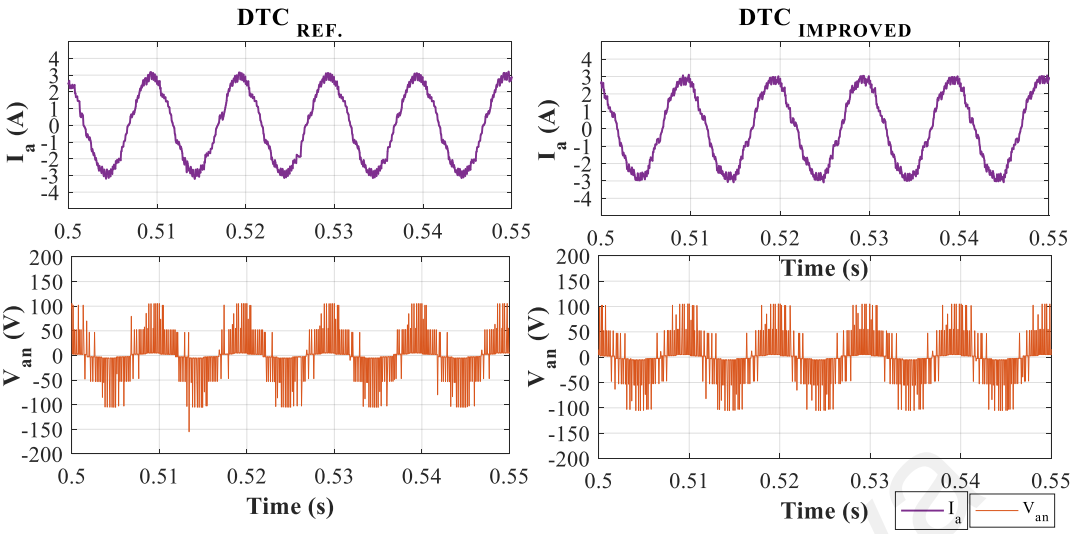

(d)

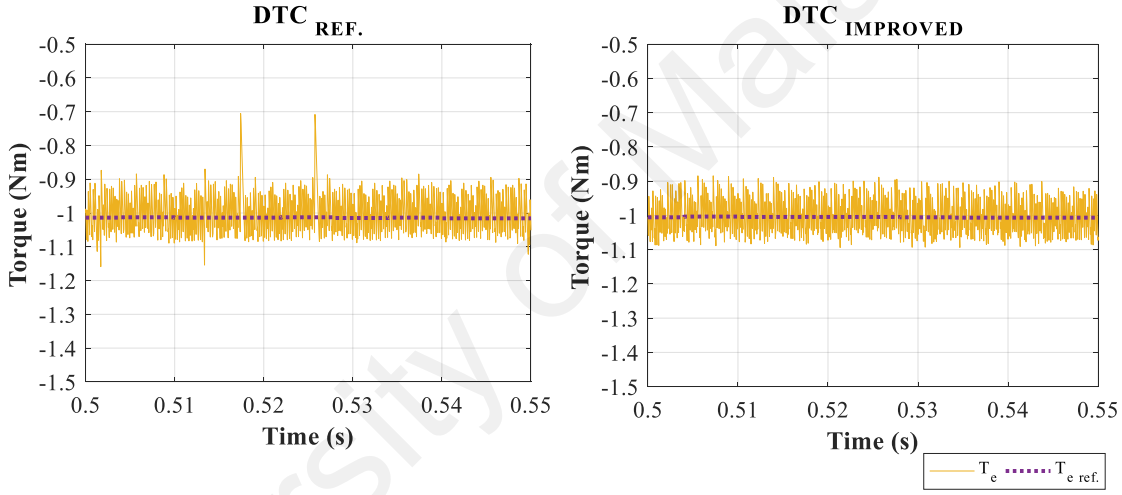

(e)

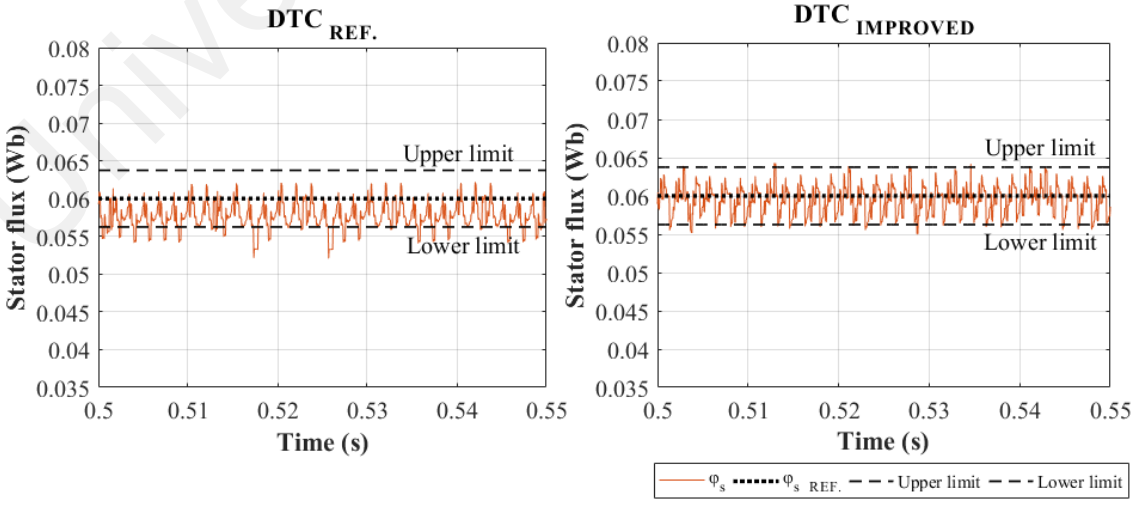

(f)

Figure 4.18, continued: Comparison results of the existing DTC and improved DTC during steady-state condition.
(d) Phase current and phase voltage, (e) Torque, (f) Stator flux.

University of Malaya

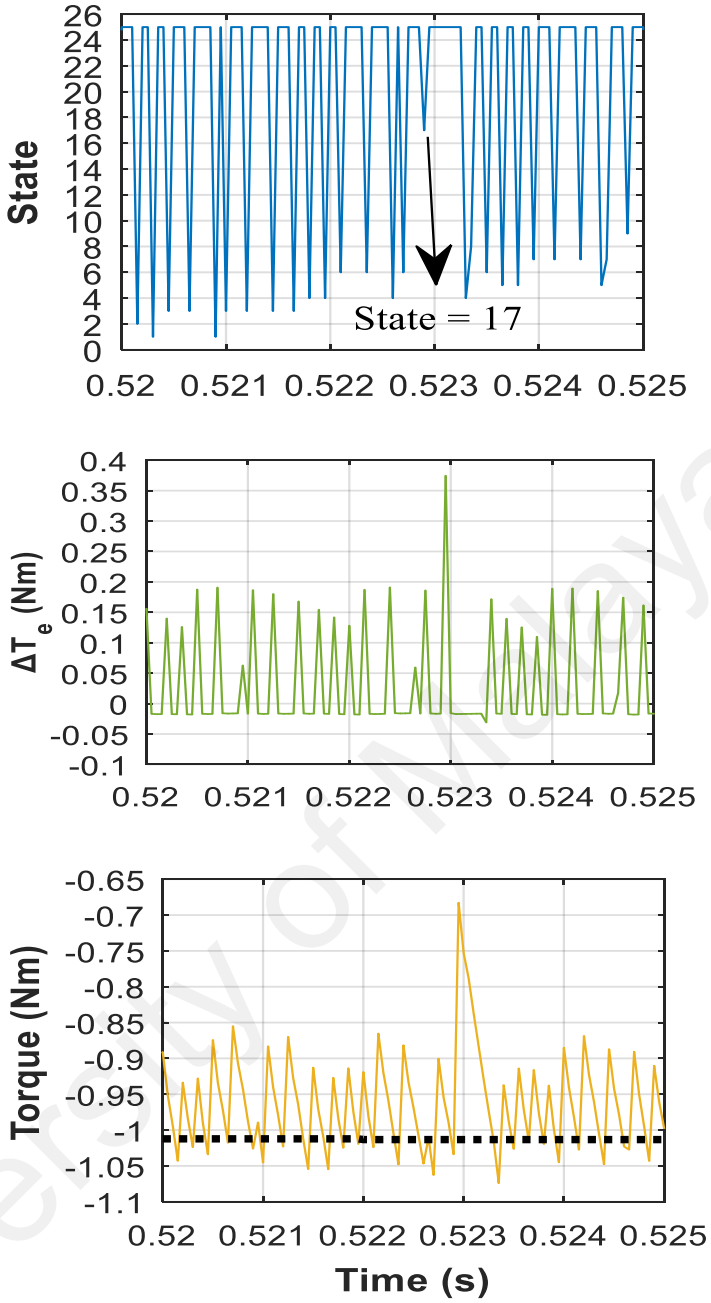

Figure 4.18, continued: Comparison results of the existing DTC and improved DTC during steady-state condition. (g) Enlarged torque distortion section for analysis.

University of Malaya

4.7.2.2 Transient response investigation

Next, Figure 4.19 showed the comparative simulation results for the torque transient response performance. It was found that both approaches can achieve a fast dynamic by tracking the torque trajectory accurately as shown in Figure 4.19(c). Throughout the step change in torque, the stator current remained balanced and sinusoidal, whilst the DC-link voltages stayed within the error band, sees Figure 4.19(a) and (b). By referring to Figure 4.19(d), the same trend as the steady-state can be observed for the stator flux where it was slightly offset downward from the reference value. There was no delay observed for both torque and stator flux to reach its steady-state condition for the improved LUT-based DTC approach even though the smaller variation of switching vectors was deployed for the LUT development. In the meantime, it helped to improve the steady response with no sudden spike observed in torque during its operation at -1 Nm.

4.7.2.3 Evaluation of the DTC's unbalance load response

Finally, the performance of both of the DTC approaches was investigated under Scenario three. In this case, both approaches were capable of producing upper and lower DC-link voltage close to 150 V at 1500 rpm (Figure 4.20(b) and (c)). It can be seen in Figure 4.20(a) that the stator current generated from the existing DTC method was distorted, and even more severe ripples were observed in stator flux (Figure 4.20(e)). To be more specific, the stator flux results on the distorted section was enlarged as presented in Figure 4.20(f) with switching vectors selected, rate of change of the stator flux and stator flux displayed from top to bottom. Similar to the torque ripples analysis, (4.16) was used to compute the stator flux variation using the selected switching vector. The switching vector selected, 18 in stator flux sector 1 was incorrect, leading to negative change of stator flux which was opposing to the desired value (dotted line at 0.06 Wb). Henceforth, the stator flux showed higher ripples. This phenomenon happened due to

University of Malaya

incorrect development of stator flux variation model and consequently, the selection of switching vectors for LUT was inaccurate. As such, it can be concluded that the proposed LUT-based DTC outperformed the existing DTC under unbalance load condition.

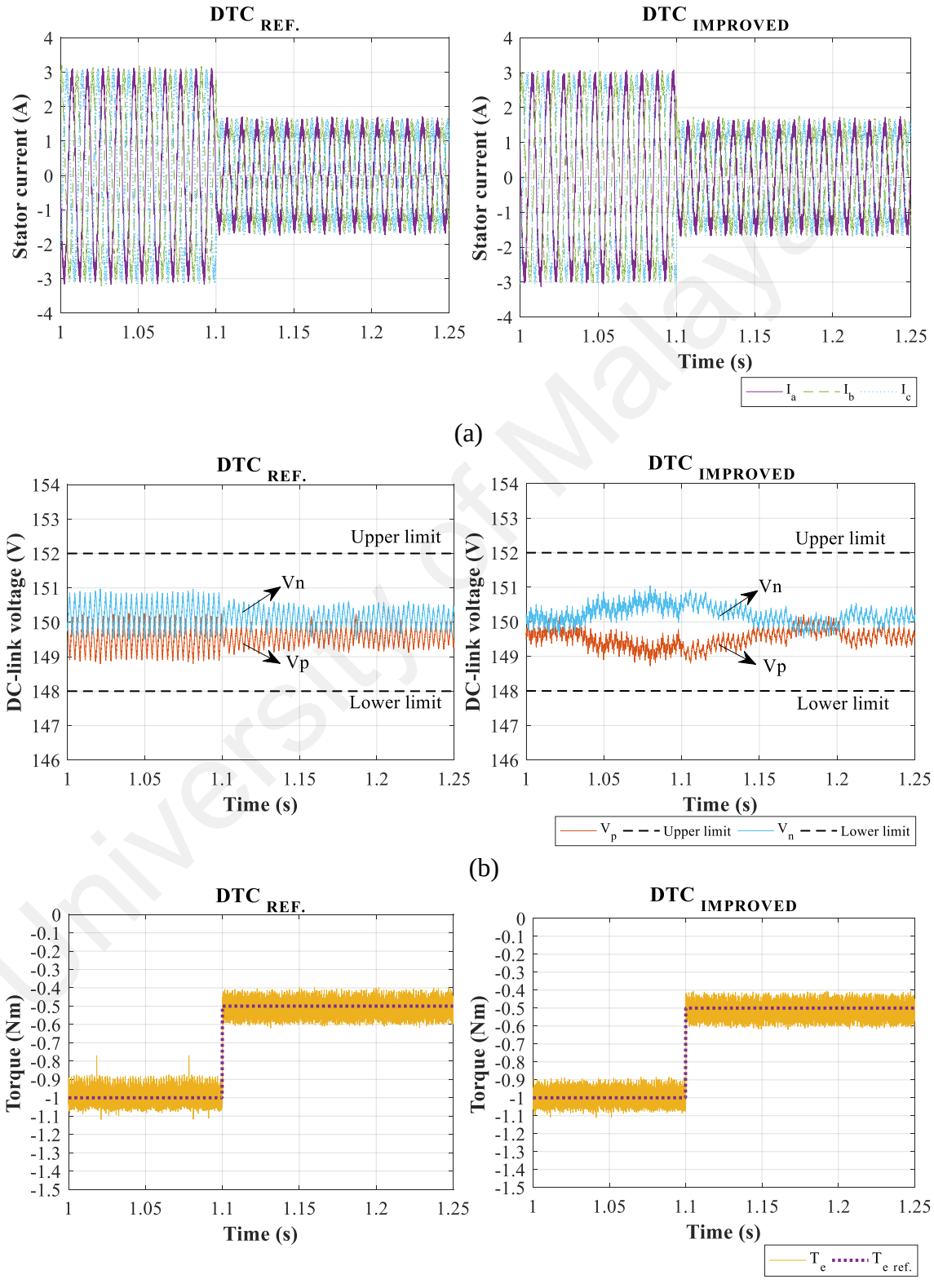

Figure 4.19: Comparison results between the existing DTC and improved DTC when step change applied. (a) Torque, (b) Stator flux, (c) Stator current.

University of Malaya

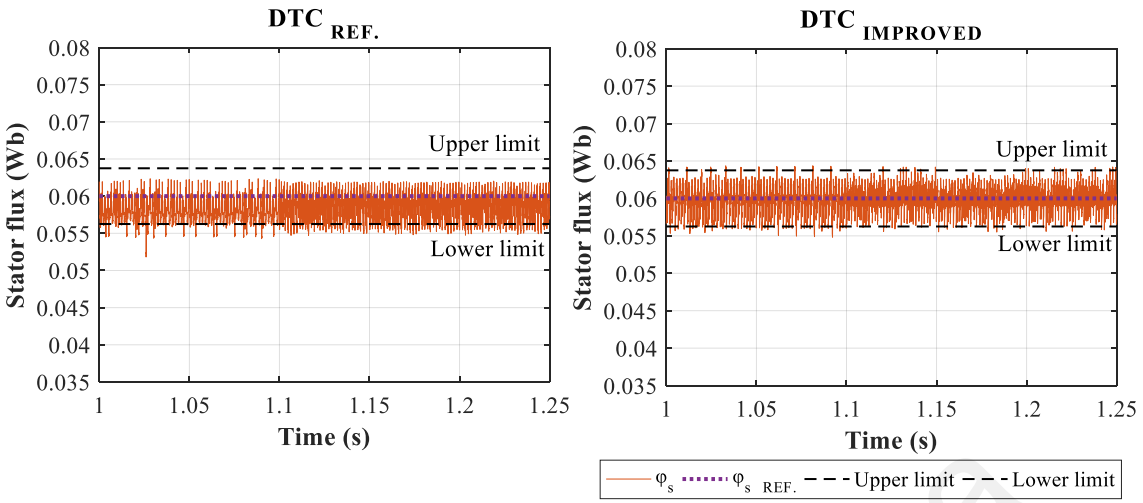

(d)

Figure 4.19, continued: Comparison results between the existing DTC and improved DTC when step change applied. (d) DC-link voltage.

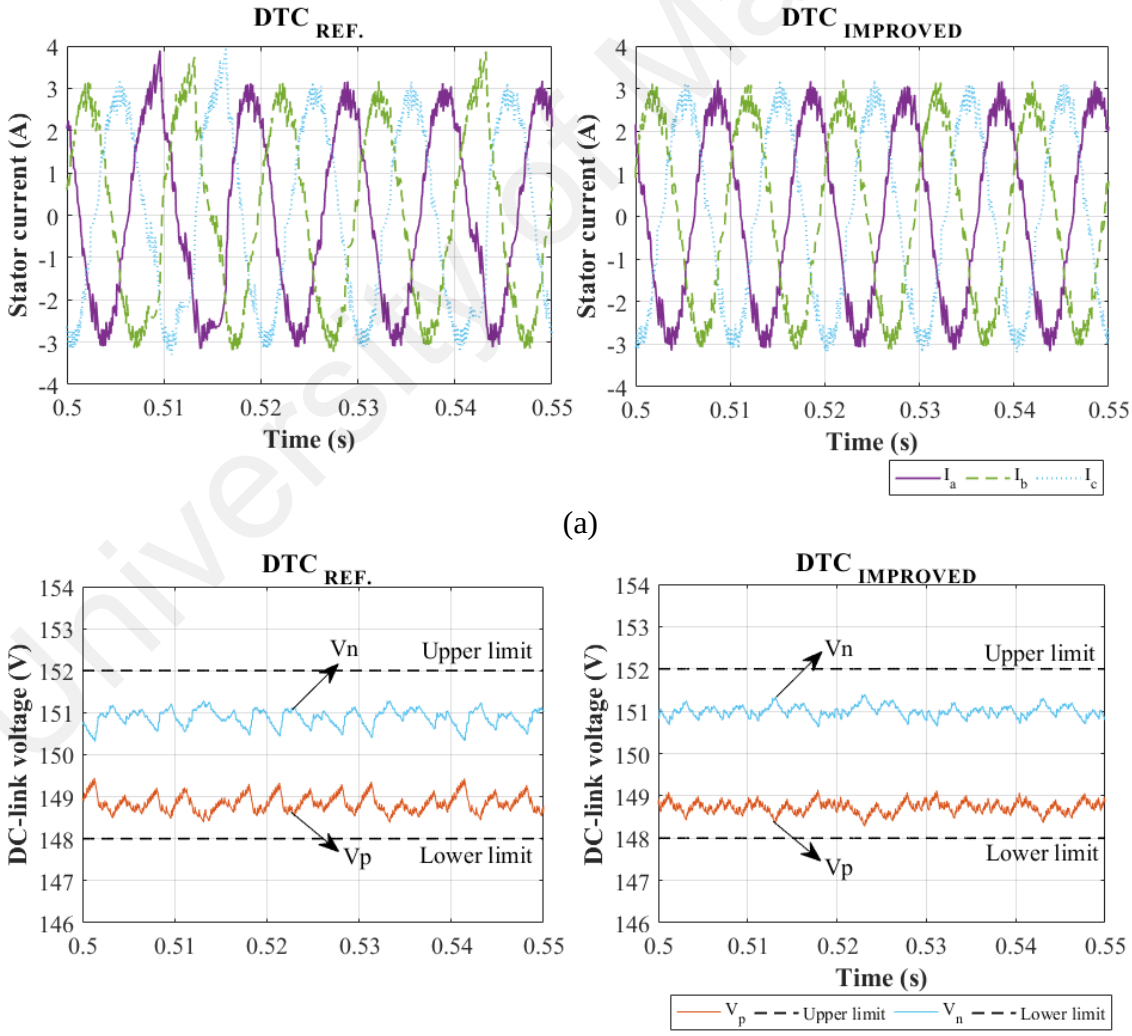

(a)

(b)

Figure 4.20: Comparison results between the existing DTC and improved DTC during unbalance load condition. (a) Stator current, (b) DC-link voltage

University of Malaya

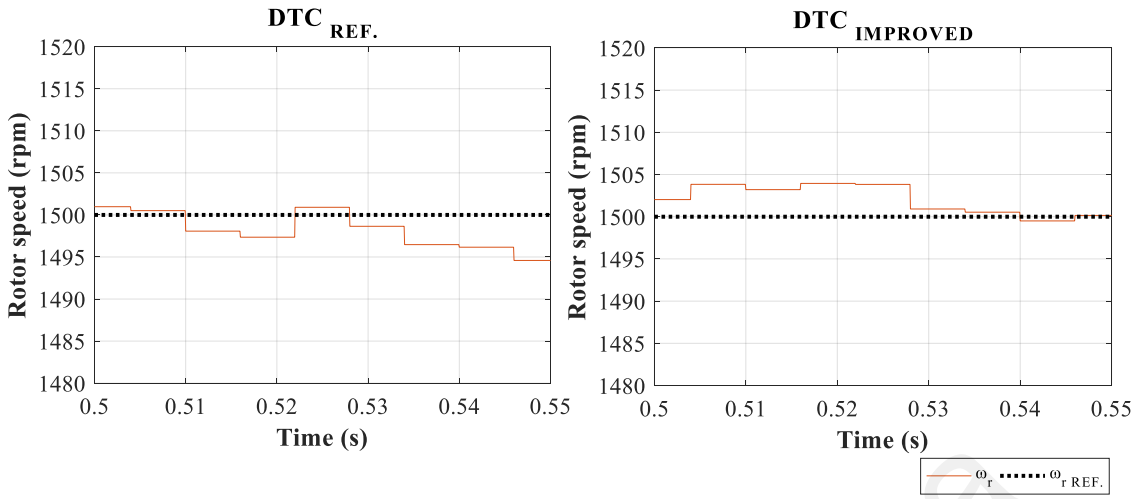

(c)

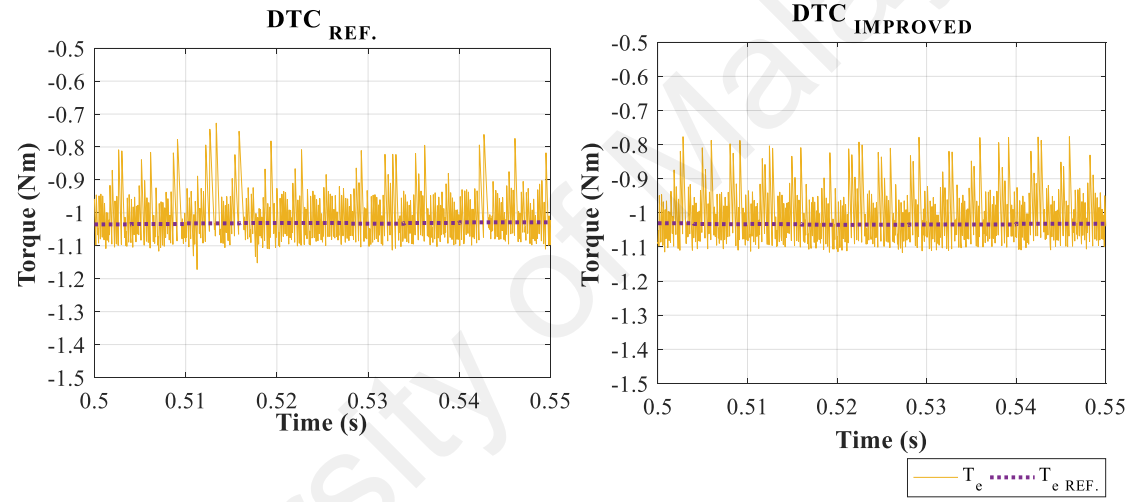

(d)

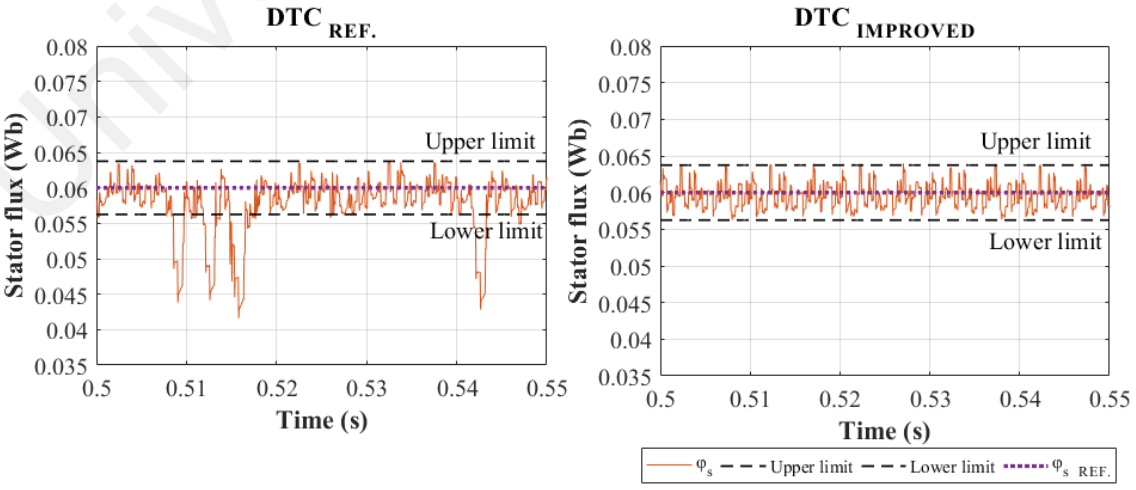

(e)

Figure 4.20, continued: Comparison results between the existing and improved DTC during unbalance load condition. (c) Rotor speed, (d) Torque, (e) Stator flux.

University of Malaya

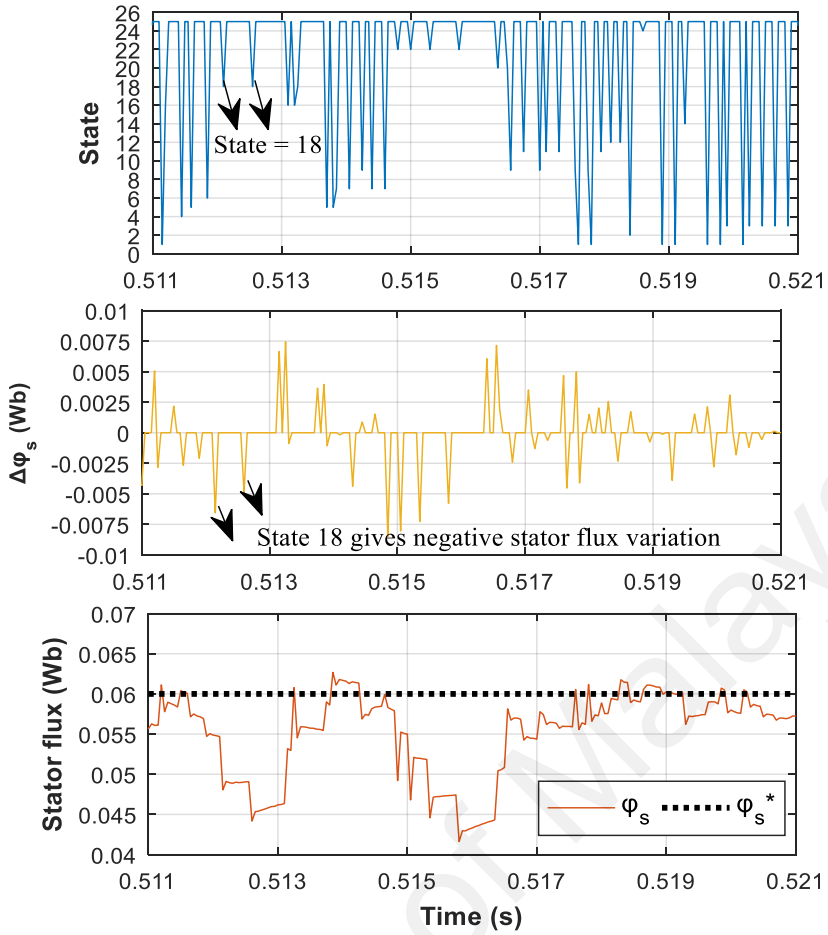

(f)

Figure 4.20, continued: Comparison results between the existing DTC and improved DTC during unbalance load condition. (f) Zoom in stator flux results.

4.7.3 Investigation of the factors on the performance of LUT-based DTC

In this section, the influence of the aforementioned factors on the torque, stator flux, and stator current were analyzed. Quantitative evaluation of the control performance was conducted based on the standard deviation for torque and stator flux as well as THD for the stator current. The torque and stator flux ripples generated for different factors study was quantified by the standard deviation as expressed (Ren & Zhu, 2015):

$$\sigma_x = \sqrt{\frac{1}{N-1}\sum_{i=1}^{N}(x_i + \bar{x})^2} \tag{4.40}$$

where N is the number of samples, x_i is the instant value of variable and $\bar{x}$ is the mean value of the collected samples. Meanwhile, total harmonics distortion (THD) of the stator current was obtained using Matlab FFT tools.

University of Malaya

4.7.3.1 Sampling time and comparator band

The behavior of the DTC is highly sensitive to the system's operating sampling time. There were three sampling times to study here, i.e. 0.0002 s, 0.0001 s, and 0.00005 s. Before different sampling time was applied, the comparator band for the torque and stator flux must be altered accordingly. The switching frequency is a function of both torque and stator flux band (Mathapati & Bocker, 2013). Thus, the influence of both sampling frequency and comparator band were analyzed together in this section. The band setting for both torque and stator flux for each sampling time can be found in Table 4.11.

The simulation results for the DTC with the variation in sampling time and comparator band was shown in Figure 4.21(a) to (c). In comparison, the system with the lowest sampling time exhibited the best for all of the parameters. Table 4.11 also summarized the tabulated standard deviation and THD obtained from the Matlab FFT tools for each setting. As the table shown, the standard deviation for torque and stator flux increased by approximately two times when the sampling time was double. This can be translated that the ripples are directly proportional to the system's sampling time. In terms of stator current, the lowest THD (less than 10 %) was observed when the control system was set at 20 kHz. It can be concluded that the performance of the DTC can be improved significantly with the reduction of sampling time.

Table 4.11: Comparison results at the different sampling time.

Sampling time	Comparator band		Standard deviation		THD
	Torque	Stator flux	Torque	Stator flux	Current
0.0002 s	-0.4 Nm	0.02 Wb	0.215	0.007	29.08 %
0.0001 s	-0.2 Nm	0.01 Wb	0.104	0.004	19.25 %
0.00005 s	-0.1 Nm	0.005 Wb	0.051	0.002	8.43 %

University of Malaya

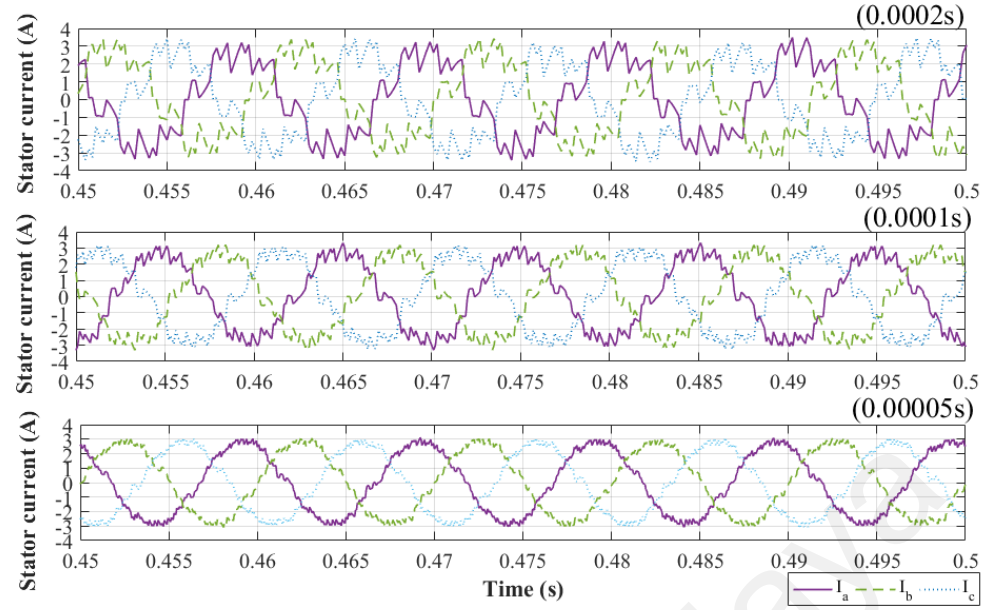

(a)

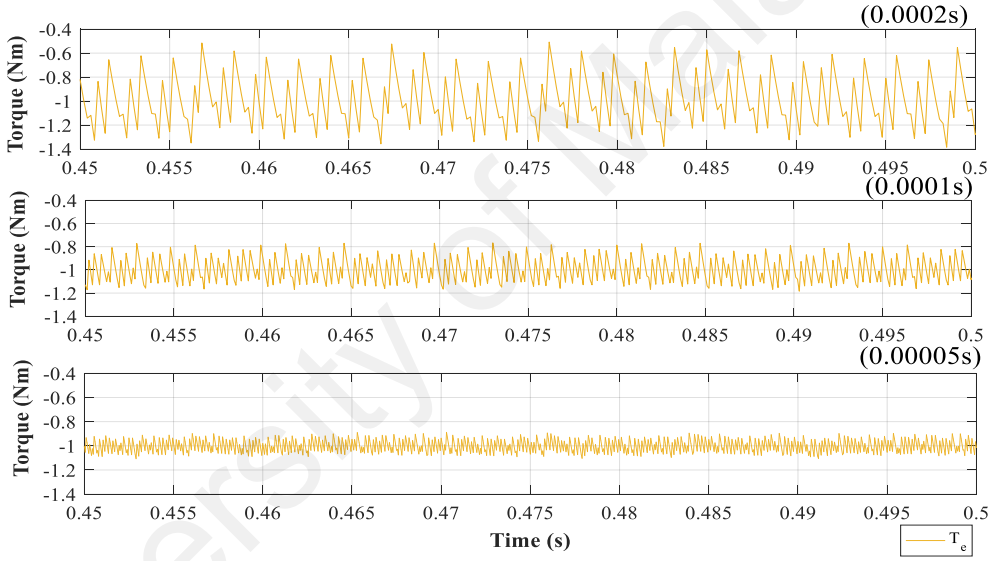

(b)

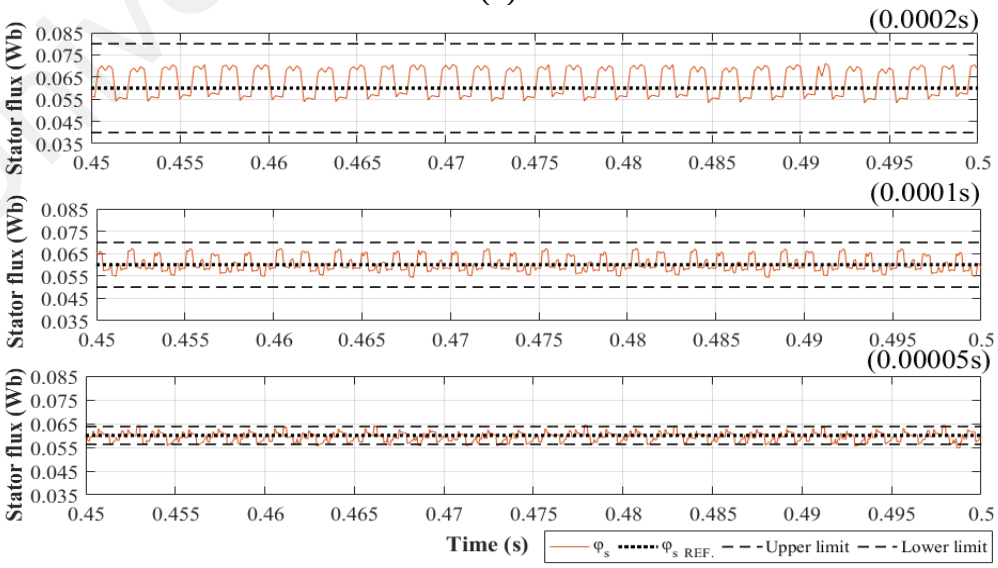

(c)

Figure 4.21: Simulation comparison results at the different sampling time. (a) Stator current, (b) Torque, (c) Stator flux.

University of Malaya

(0.0002s)

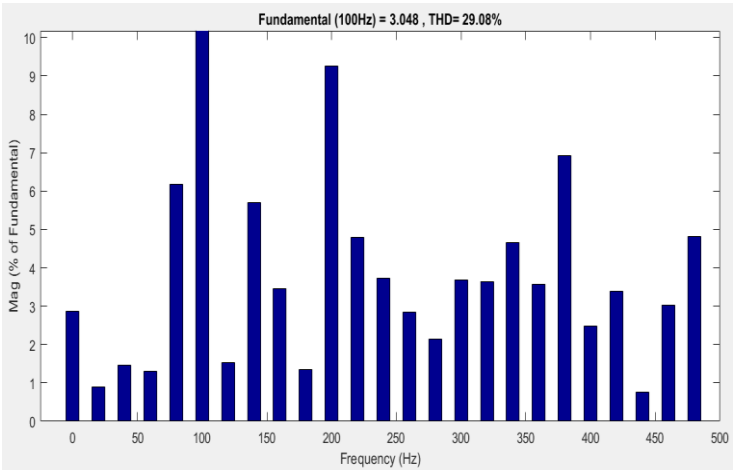


```
Sampling time      = 0.0002 s
Samples per cycle = 50
DC component       = 0.0871
Fundamental        = 3.048 peak (2.155 rms)
THD                = 29.08%

     0 Hz   (DC):          2.86%    90.0°
    20 Hz                  0.90%   242.9°
    40 Hz                  1.45%   176.3°
    60 Hz                  1.30%   193.9°
    80 Hz                  6.19%    93.8°
   100 Hz   (Fnd):       100.00%   -48.7°
   120 Hz                  1.52%   124.9°
   140 Hz                  5.70%   217.3°
   160 Hz                  3.47%   263.4°
   180 Hz                  1.36%    86.0°
   200 Hz   (h2):          9.25%   -68.1°
   220 Hz                  4.79%   -78.4°
   240 Hz                  3.73%   -28.1°
   260 Hz                  2.85%    28.8°
   280 Hz                  2.15%    22.4°
   300 Hz   (h3):          3.69%   254.4°
   320 Hz                  3.65%    54.7°
   340 Hz                  4.66%   112.5°
   360 Hz                  3.57%   204.3°
   380 Hz                  6.92%   -73.8°
   400 Hz   (h4):          2.47%    68.3°
   420 Hz                  3.40%    34.2°
   440 Hz                  0.76%    25.7°
   460 Hz                  3.04%   -84.8°
   480 Hz                  4.82%   -74.9°
```

(0.0001s)

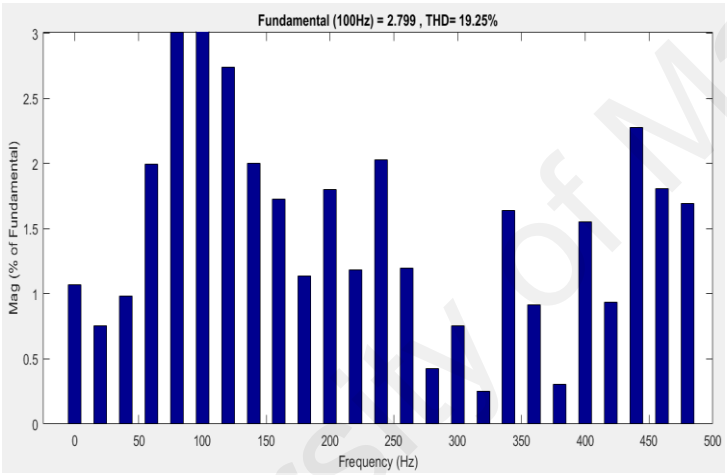


```
Sampling time      = 0.0001 s
Samples per cycle = 100
DC component       = 0.02994
Fundamental        = 2.799 peak (1.979 rms)
THD                = 19.25%

     0 Hz   (DC):          1.07%    90.0°
    20 Hz                  0.76%    79.8°
    40 Hz                  0.98%    40.3°
    60 Hz                  1.99%   106.2°
    80 Hz                  3.01%    93.7°
   100 Hz   (Fnd):       100.00%   -86.5°
   120 Hz                  2.74%   -77.2°
   140 Hz                  2.00%   -34.1°
   160 Hz                  1.73%   212.5°
   180 Hz                  1.14%   218.4°
   200 Hz   (h2):          1.80%   246.0°
   220 Hz                  1.19%   252.4°
   240 Hz                  2.03%   252.8°
   260 Hz                  1.19%    97.3°
   280 Hz                  0.42%   180.6°
   300 Hz   (h3):          0.75%   -63.5°
   320 Hz                  0.25%   231.1°
   340 Hz                  1.64%   213.2°
   360 Hz                  0.91%    61.6°
   380 Hz                  0.30%   -22.3°
   400 Hz   (h4):          1.55%   101.0°
   420 Hz                  0.94%    95.7°
   440 Hz                  2.27%   130.5°
   460 Hz                  1.81%   -67.8°
   480 Hz                  1.70%   -57.4°
```

(0.00005s)

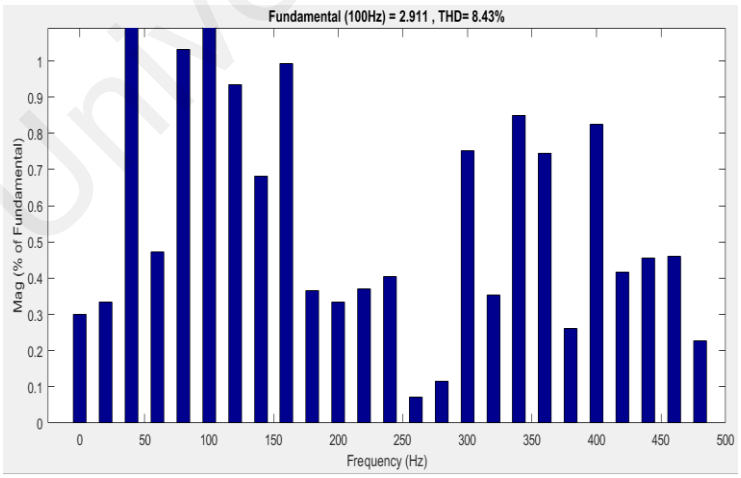


```
Sampling time      = 5e-05 s
Samples per cycle = 200
DC component       = 0.008755
Fundamental        = 2.911 peak (2.058 rms)
THD                = 8.43%

     0 Hz   (DC):          0.30%    90.0°
    20 Hz                  0.33%   159.3°
    40 Hz                  1.11%   -40.3°
    60 Hz                  0.47%   259.1°
    80 Hz                  1.03%   -41.9°
   100 Hz   (Fnd):       100.00%   120.5°
   120 Hz                  0.94%   103.3°
   140 Hz                  0.68%   189.4°
   160 Hz                  0.99%   164.1°
   180 Hz                  0.37%    10.8°
   200 Hz   (h2):          0.33%    20.8°
   220 Hz                  0.37%    56.5°
   240 Hz                  0.40%   247.9°
   260 Hz                  0.07%    24.0°
   280 Hz                  0.12%   231.2°
   300 Hz   (h3):          0.75%   -72.4°
   320 Hz                  0.35%   269.7°
   340 Hz                  0.85%   109.4°
   360 Hz                  0.75%   146.0°
   380 Hz                  0.26%    34.5°
   400 Hz   (h4):          0.82%    -7.1°
   420 Hz                  0.42%    74.8°
   440 Hz                  0.46%   256.1°
   460 Hz                  0.46%   187.3°
   480 Hz                  0.23%    38.6°
```

(d)

Figure 4.21, continued: Simulation comparison results at different sampling time. (d) THD of the stator current.

University of Malaya

4.7.3.2 Magnitude of the DC- link voltage

Similarity, the comparator band for both torque and stator flux were required to be changed when the DC-link voltage at the output of the Vienna rectifier was varied. The variation of DC link voltage was achieved by adjusting the magnitude of the DC voltage supply to three different values (i.e. 100 V, 150 V, and 300 V) with the same system's operating sampling frequency at 20 kHz. Figure 4.22(a) to (c) were the output waveforms of the PMSG at the different DC-link output voltage. As expected, the performance of the system with the lowest DC-link voltage had far better performance in terms of smaller pulsation in stator current, torque and stator flux than the higher DC-link voltage. This also can be seen in terms of standard deviation as well as THD for the stator current as recorded in Table 4.12 which its magnitude increased with the increment in the DC-link voltage.

Table 4.12: Comparison results at different output DC-link voltage.

DC-link voltage	Comparator band		Standard deviation		THD
	Torque	Stator flux	Torque	Stator flux	Current
100 V	-0.04 Nm	0.002 Wb	0.023	0.0009	5.26 %
150 V	-0.05 Nm	0.0025 Wb	0.029	0.0012	6.29 %
300 V	-0.1 Nm	0.005 Wb	0.051	0.0020	8.43 %

University of Malaya

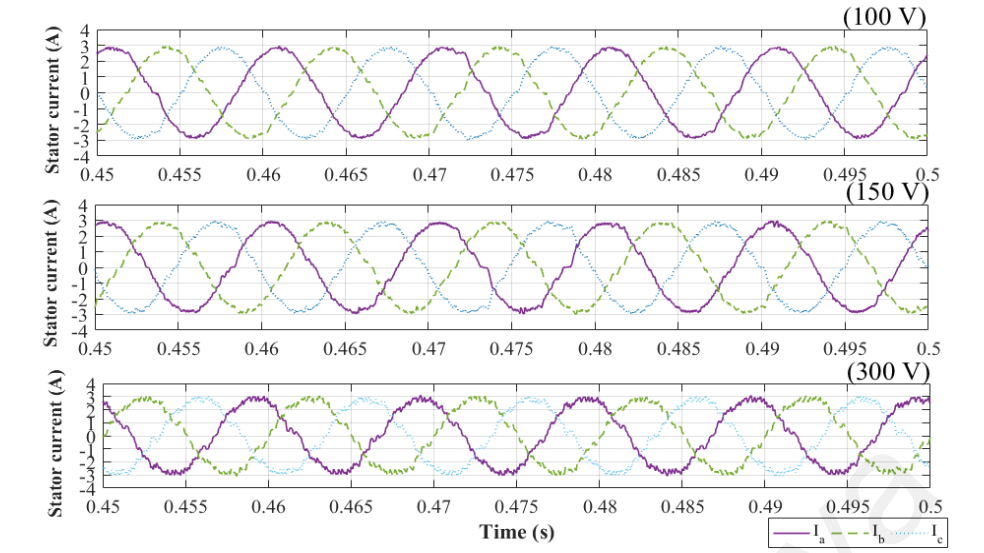

(a)

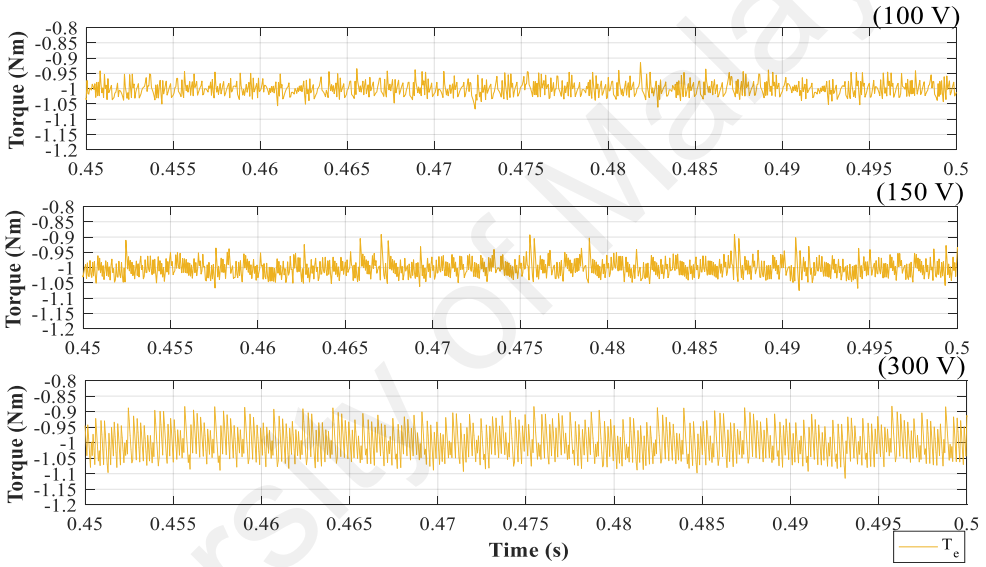

(b)

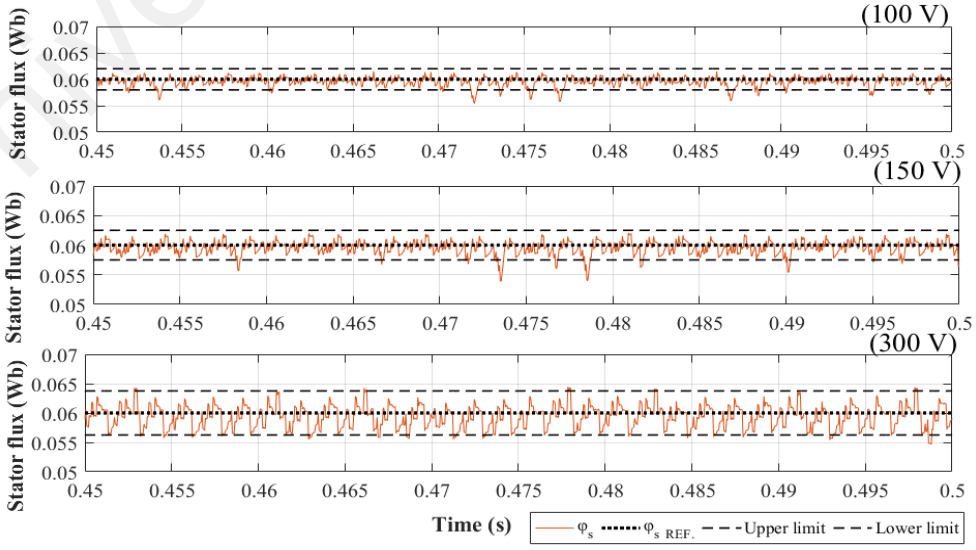

(c)

Figure 4.22: Generated results at DC-link voltage variation. (a) Stator current, (b) Torque, (c) Stator flux.

University of Malaya

(100 V)

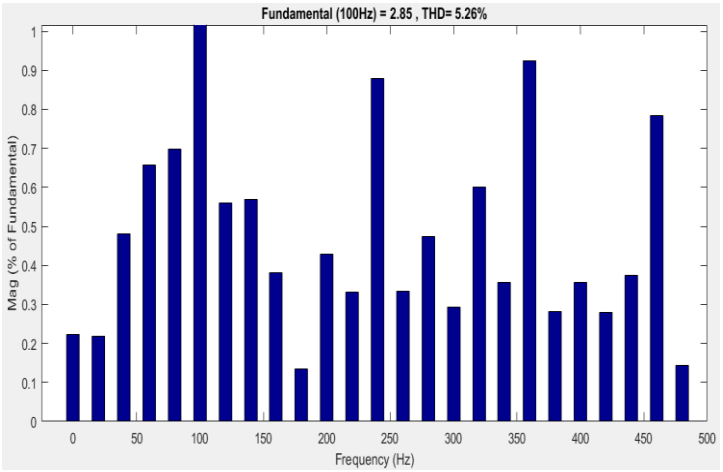


```
Sampling time      = 5e-05 s
Samples per cycle  = 200
DC component       = 0.006384
Fundamental        = 2.85 peak (2.016 rms)
THD                = 5.26%

     0 Hz   (DC):          0.22%    270.0°
    20 Hz                  0.22%    -81.1°
    40 Hz                  0.48%    -65.1°
    60 Hz                  0.66%    -77.8°
    80 Hz                  0.70%    262.4°
   100 Hz   (Fnd):       100.00%     53.4°
   120 Hz                  0.56%     33.5°
   140 Hz                  0.57%      6.1°
   160 Hz                  0.38%    199.5°
   180 Hz                  0.13%     13.9°
   200 Hz   (h2):          0.43%     60.2°
   220 Hz                  0.33%     29.9°
   240 Hz                  0.88%     70.9°
   260 Hz                  0.33%    -18.8°
   280 Hz                  0.47%     48.4°
   300 Hz   (h3):          0.29%     13.7°
   320 Hz                  0.60%     10.0°
   340 Hz                  0.36%     91.3°
   360 Hz                  0.92%    -20.1°
   380 Hz                  0.28%     74.7°
   400 Hz   (h4):          0.36%     -4.3°
   420 Hz                  0.28%    137.5°
   440 Hz                  0.38%    205.8°
   460 Hz                  0.78%     79.3°
   480 Hz                  0.14%    131.8°
```

(150 V)

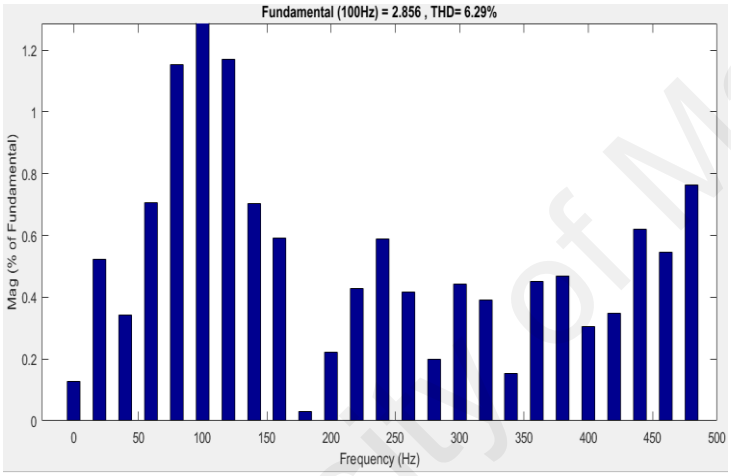


```
Sampling time      = 5e-05 s
Samples per cycle  = 200
DC component       = 0.003636
Fundamental        = 2.856 peak (2.02 rms)
THD                = 6.29%

     0 Hz   (DC):          0.13%    270.0°
    20 Hz                  0.52%    -57.3°
    40 Hz                  0.34%    147.8°
    60 Hz                  0.71%    -27.4°
    80 Hz                  1.15%    218.2°
   100 Hz   (Fnd):       100.00%     66.2°
   120 Hz                  1.17%     87.5°
   140 Hz                  0.70%    -20.9°
   160 Hz                  0.59%    102.1°
   180 Hz                  0.03%     46.6°
   200 Hz   (h2):          0.22%     70.1°
   220 Hz                  0.43%     22.7°
   240 Hz                  0.59%    252.2°
   260 Hz                  0.42%    130.0°
   280 Hz                  0.20%    195.4°
   300 Hz   (h3):          0.44%     95.2°
   320 Hz                  0.39%    -74.9°
   340 Hz                  0.15%     54.1°
   360 Hz                  0.45%    228.7°
   380 Hz                  0.47%     47.2°
   400 Hz   (h4):          0.30%     39.1°
   420 Hz                  0.35%    157.5°
   440 Hz                  0.62%     25.9°
   460 Hz                  0.55%    207.3°
   480 Hz                  0.76%    -33.6°
```

(300 V)

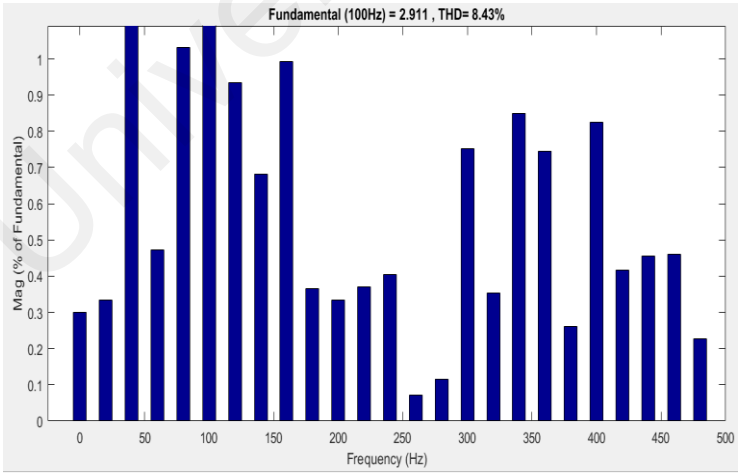


```
Sampling time      = 5e-05 s
Samples per cycle  = 200
DC component       = 0.008755
Fundamental        = 2.911 peak (2.058 rms)
THD                = 8.43%

     0 Hz   (DC):          0.30%     90.0°
    20 Hz                  0.33%    159.3°
    40 Hz                  1.11%    -40.3°
    60 Hz                  0.47%    259.1°
    80 Hz                  1.03%    -41.9°
   100 Hz   (Fnd):       100.00%    120.5°
   120 Hz                  0.94%    103.3°
   140 Hz                  0.68%    189.4°
   160 Hz                  0.99%    164.1°
   180 Hz                  0.37%     10.8°
   200 Hz   (h2):          0.33%     20.8°
   220 Hz                  0.37%     56.5°
   240 Hz                  0.40%    247.9°
   260 Hz                  0.07%     24.0°
   280 Hz                  0.12%    231.2°
   300 Hz   (h3):          0.75%    -72.4°
   320 Hz                  0.35%    269.7°
   340 Hz                  0.85%    109.4°
   360 Hz                  0.75%    146.0°
   380 Hz                  0.26%     34.5°
   400 Hz   (h4):          0.82%     -7.1°
   420 Hz                  0.42%     74.8°
   440 Hz                  0.46%    256.1°
   460 Hz                  0.46%    187.3°
   480 Hz                  0.23%     38.6°
```

(d)

Figure 4.22, continued: Generated results at DC-link voltage variation. (d) THD of the stator current.

University of Malaya

4.8 Experimental results

In order to verify the performance of the improved LUT-based DTC using Vienna rectifier, a laboratory prototype had been built with the parameters same as the simulation as listed in Table 4.4. The control algorithm was programmed in a Texas Instrument's TMS320F28335 DSP using Matlab Embedded Coder. The details of the hardware development included control algorithm and the PCB schematic can be found in Appendix C and D respectively. Power modules IXYS VUM25-05E (Kolar et al., 1996) was used to build the Vienna rectifier. The PMSG was connected to a DC motor fed with a controllable DC power supply to emulate the wind turbine. Figure 4.23 (a) and (b) showed the experimental set-up with its corresponding schematic diagram for the DTC based Vienna rectifier. The DC-link voltage on the Vienna rectifier was practically kept at a constant value of 300 V. Since the power supply was only able to operate in single quadrant mode, the resistive loads were connected in parallel with the DC-link capacitor to absorb the generated power from the Vienna rectifier. The generated torque and stator flux from the PMSG were evaluated indirectly via the measured stator current and rotor position using the estimation model with Matlab. The studies were conducted by considering the same three scenarios as in the simulation.

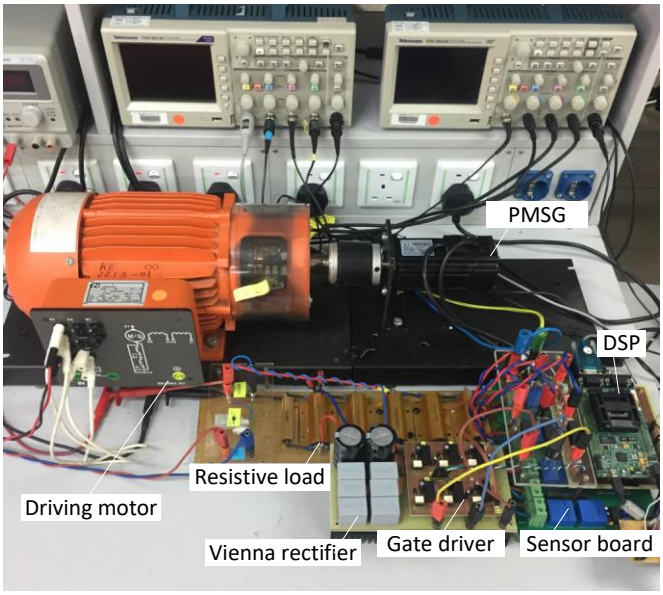

Figure 4.23: Experimental setup for the DTC based on Vienna rectifier. (a) Physical set-up

University of Malaya

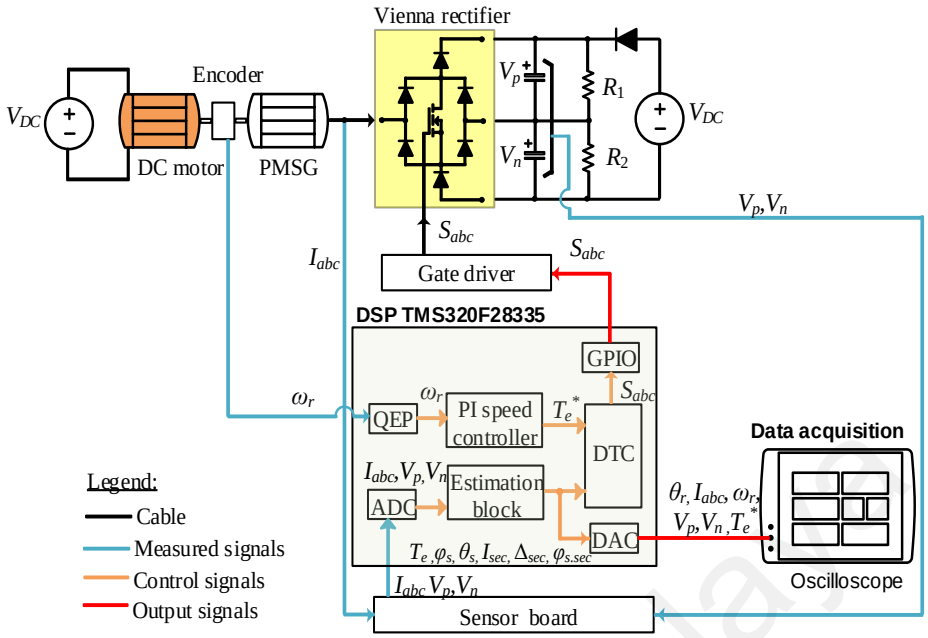

Figure 4.23, continued: Experimental setup for the DTC based on Vienna rectifier. (b) Schematic diagram.

4.8.1.1 Delay compensation analysis

The computation delay analysis was first performed for the proposed LUT-based DTC approach. The implementation of the delay compensation based on model-based approach mitigated the ripples effectively as observed in Figure 4.24(a) to (c). It means that one-step delay in digital DTC is one of the key reasons for high ripples generation. The distortion in stator current was significant when the delay was not compensated as can be seen from the results in Figure 4.24(a). Rotor position, θ_r was recorded to ensure it is aligned with phase A of the stator current. Meanwhile, the torque pulsation (Figure 4.24 (b)) was considerable with the range from -1.27 Nm to -0.67 Nm. This delay gave the standard deviation of 1.299 from the generated torque which was approximated 19.5 more as compared with the algorithm implemented with delay compensation. On the other hands, the produced stator flux also had higher ripples when the control did not consider the computation delay as shown in Figure 4.24(c). It was experimentally proven that it is important to include the computation compensation delay in order to achieve smoother

University of Malaya

control output, making a better use of Vienna rectifier. As the results, the DTC operation is possible to be operated similarly to the simulation results.

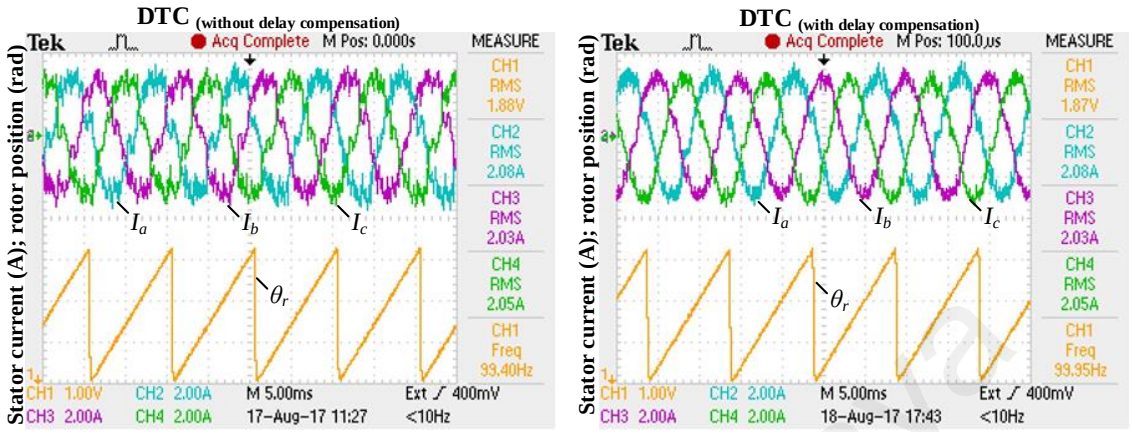

(a)

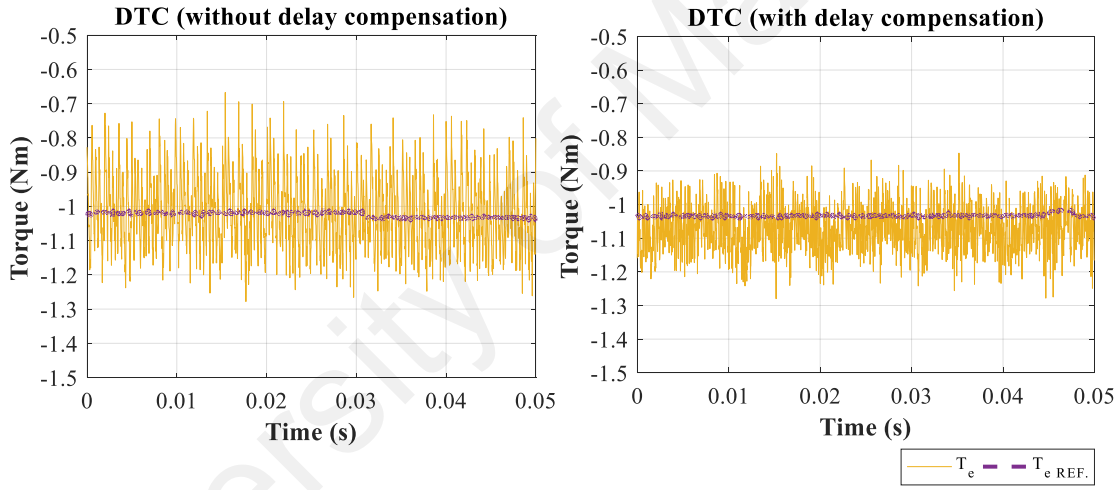

(b)

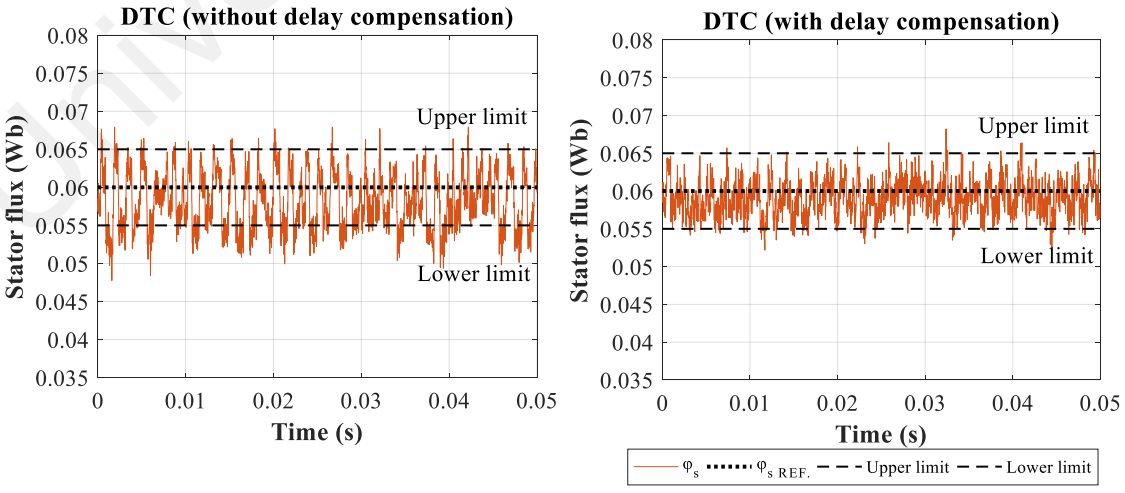

(c)

Figure 4.24: With and without delay compensation experimental results. (a) Stator current, (b) Torque, (c) Stator flux.

University of Malaya

4.8.1.2 Steady-state performance comparison

Similar to the simulation study, the steady-state performance of the proposed LUT-based DTC system, running at a constant speed of 1500 rpm was first evaluated and compared to the existing DTC approach. By referring to Figure 4.25(a), the stator currents generated from both of the approaches were balanced and sinusoidal. Accurate tracking of rotor speed, stator flux and torque were achieved with the upper and lower DC-link voltages were well confined within the designated band value as depicted in the Figure 4.25 (b) to (d) respectively. Nevertheless, stator flux from the improved LUT-based DTC controlled closer to its reference value over the existing method as can be seen from the graph in Figure 4.25(e). Overall, the experiment results showed the same trend observed from the simulation results, confirming that the control had been implemented correctly.

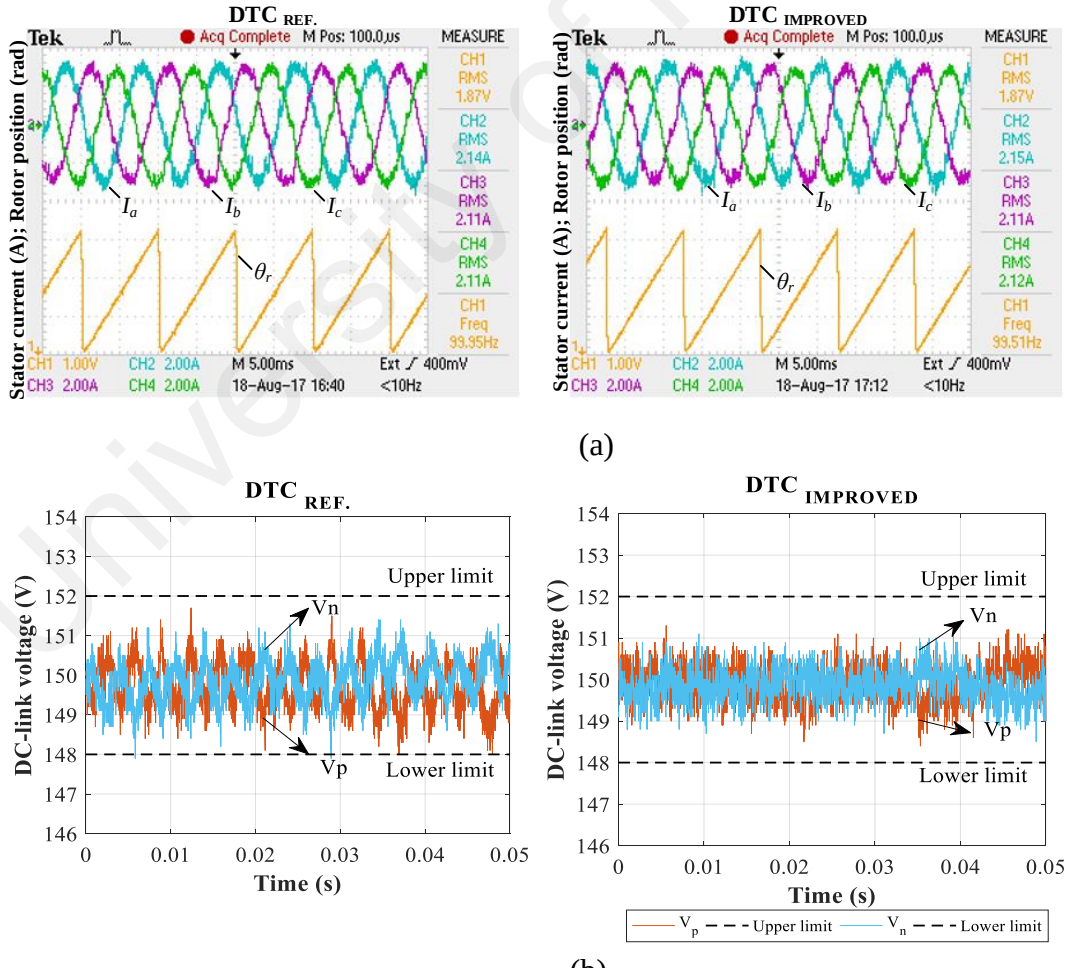

Figure 4.25: Experiment results when speed was controlled to 1500 rpm. (a) Stator current, (b) DC-link voltage.

University of Malaya

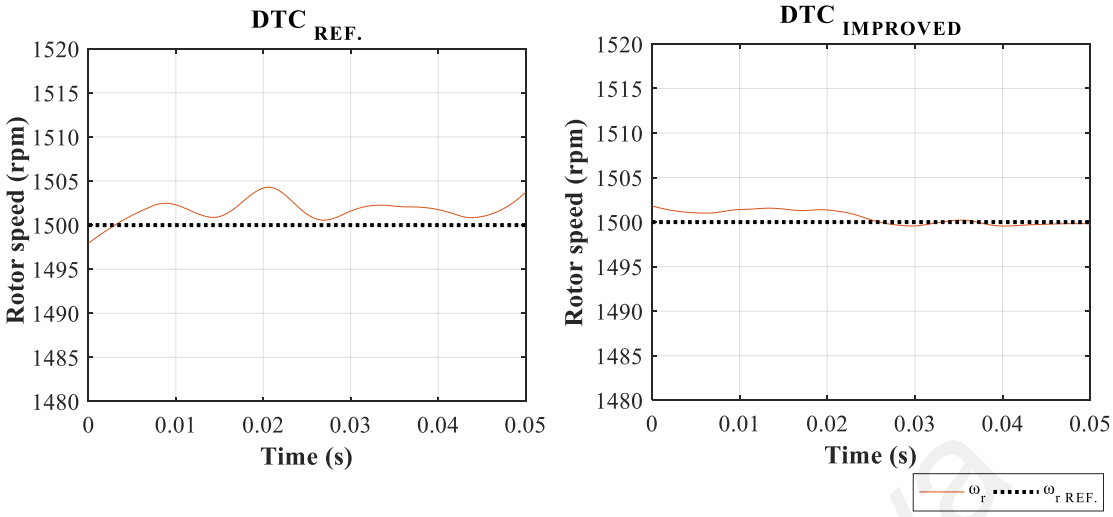

(c)

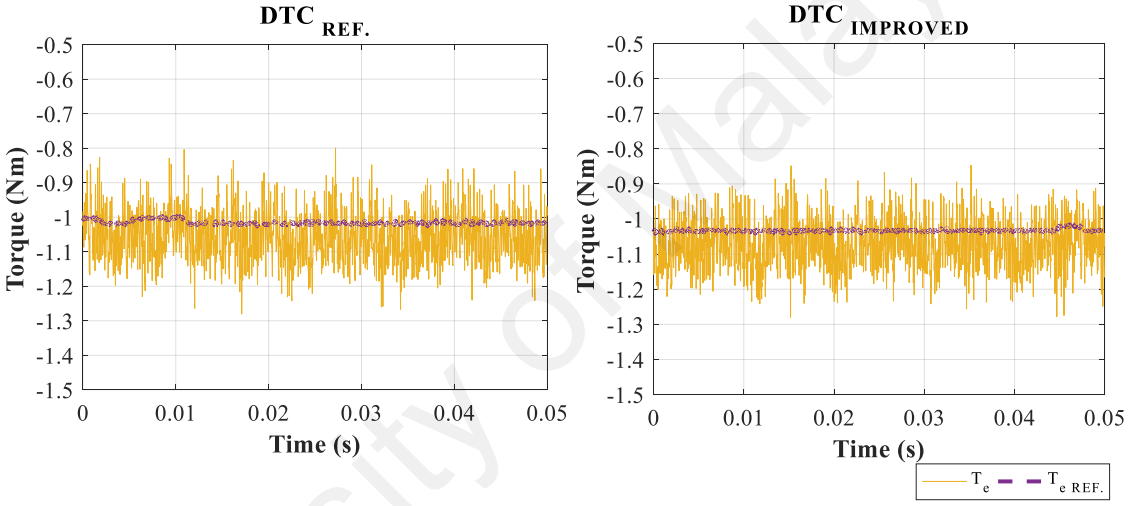

(d)

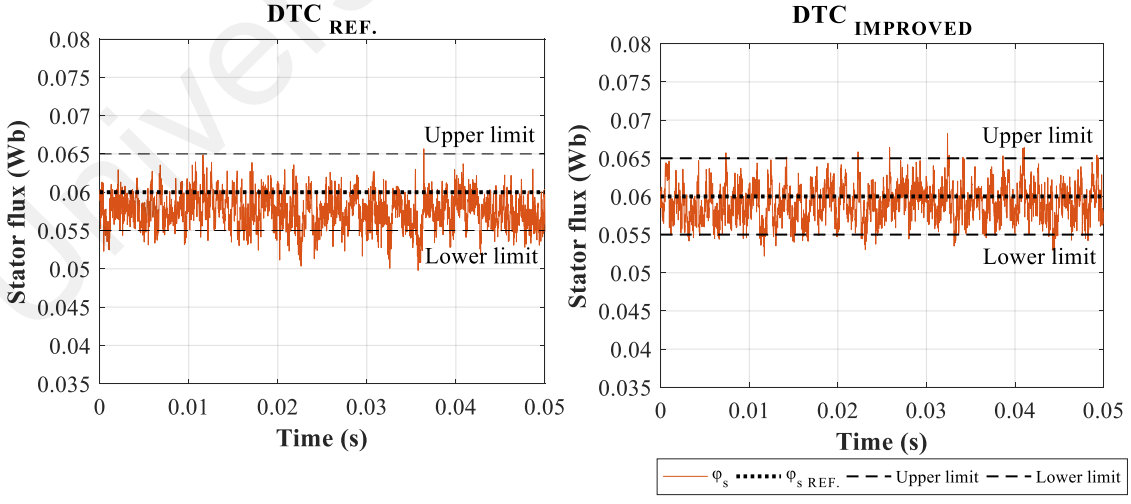

(e)

Figure 4.25, continued: Experiment results when speed was controlled to 1500 rpm. (c) Rotor speed, (d) Torque, (e) Stator flux.

University of Malaya

4.8.1.3 Step change response comparison

The proposed system performance had also been tested experimentally to study its transient behavior, by the means of reference torque step varied from -1 Nm to -0.5 Nm at the time, t = 0.04. The dynamic behavior of the PMSG was shown in Figure 4.26(a) to (d). It can be noted that the generated torque followed closely the reference value with low ripples generation for the improved LUT-based DTC. Meanwhile, it can also regulate the stator flux and the DC-link voltages closer to the desired value.

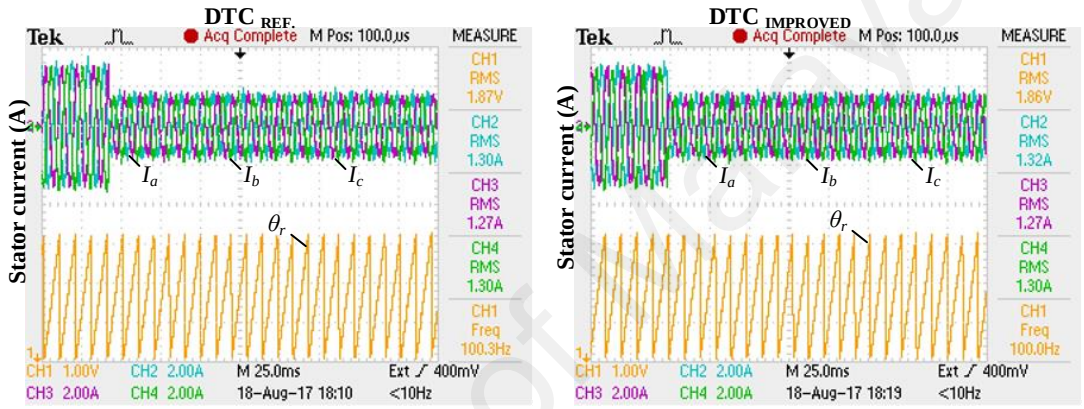

(a)

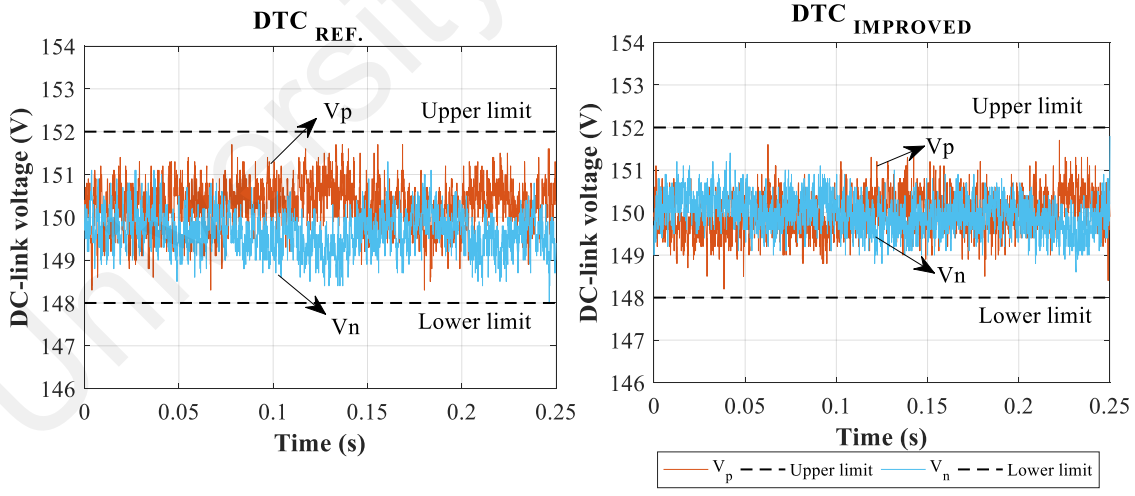

(b)

Figure 4.26: Experimental results for abrupt step change of torque. (a) Stator current, (b) DC-link voltage.

University of Malaya

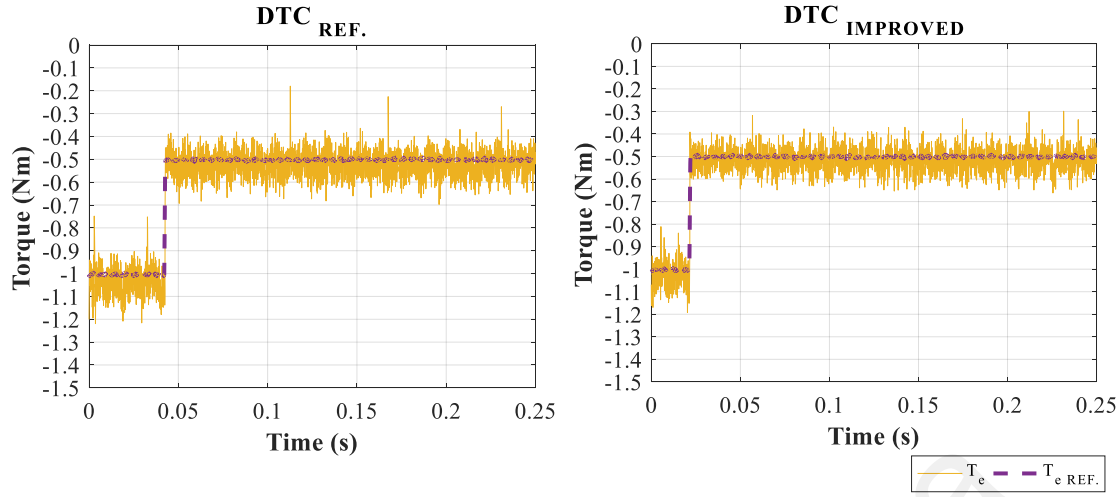

(c)

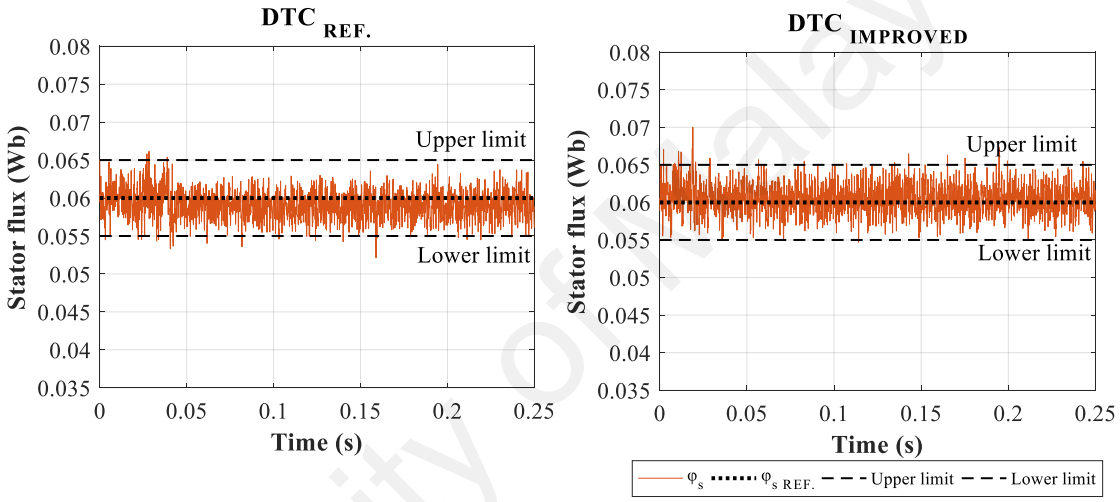

(d)

Figure 4.26, continued: Experimental results for abrupt step change of torque. (c) Torque, (d) Stator flux.

4.8.1.4 Unbalance load response

Similar to the simulation observation, the generated stator current of the existing DTC method was distorted when the control system was operated under unbalance load condition. The obtained waveforms were shown in Figure 4.27(a). By referring to Figure 4.27(b), both control approaches were still capable of maintaining a balanced DC-link voltage output. Nevertheless, the torque and stator flux obtained from the reference's LUT-DTC method (Figure 4.27(d) and (e)) exhibited higher ripples as compared to the improved LUT-based DTC approach. Such phenomena agreed with what was observed

University of Malaya

in the simulation i.e. the improved LUT-based DTC can perform better when there is an unbalance load at the Vienna rectifier's DC output.

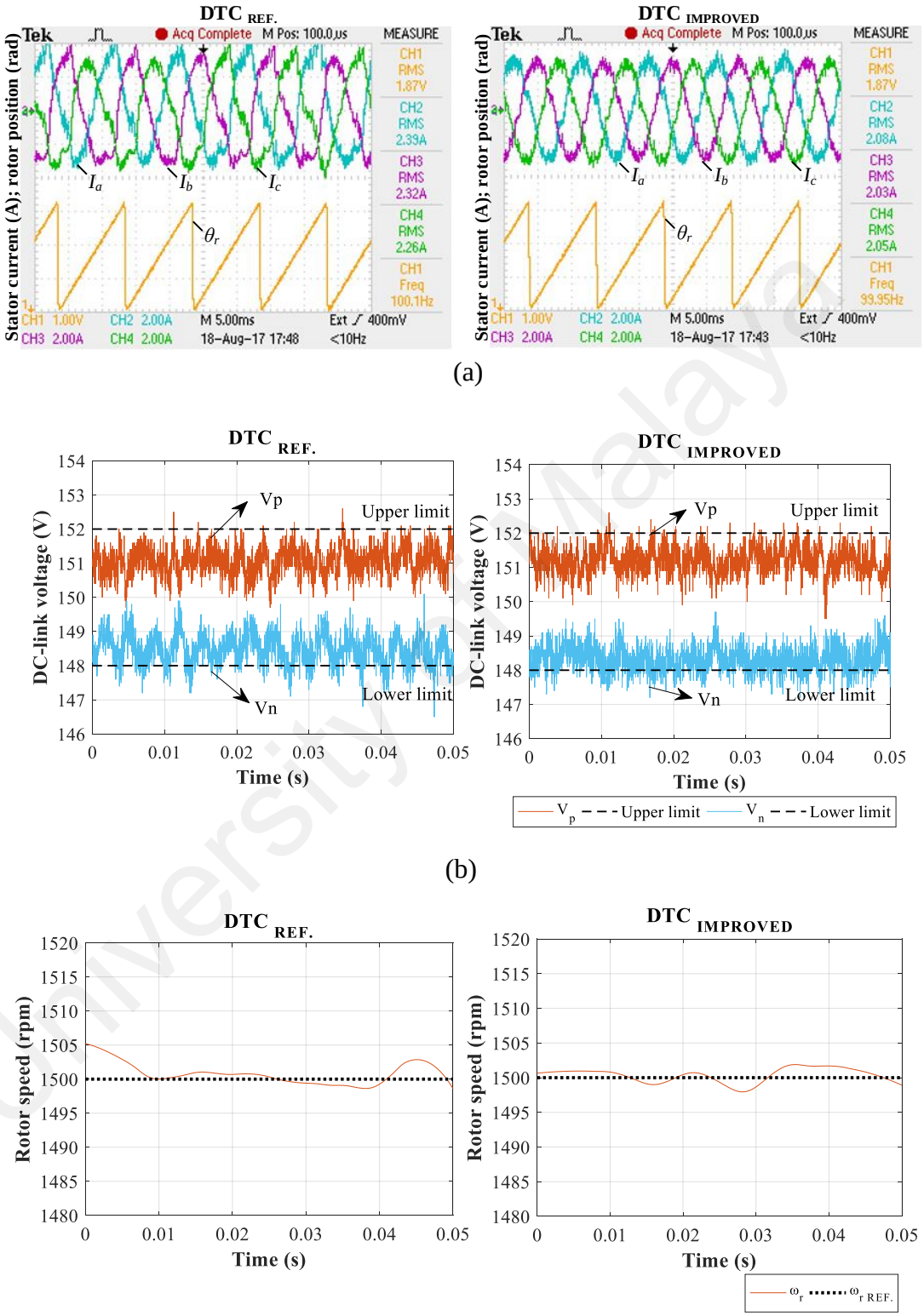

Figure 4.27: Experimental results for unbalance load setup. (a) Stator current, (b) DC-link voltage, (c) Rotor speed.

University of Malaya

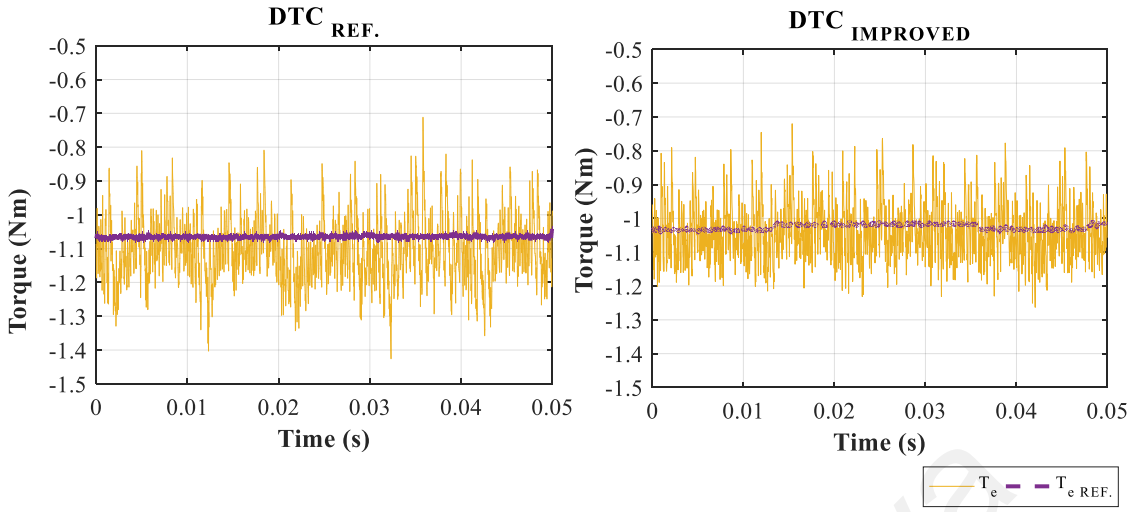

(d)

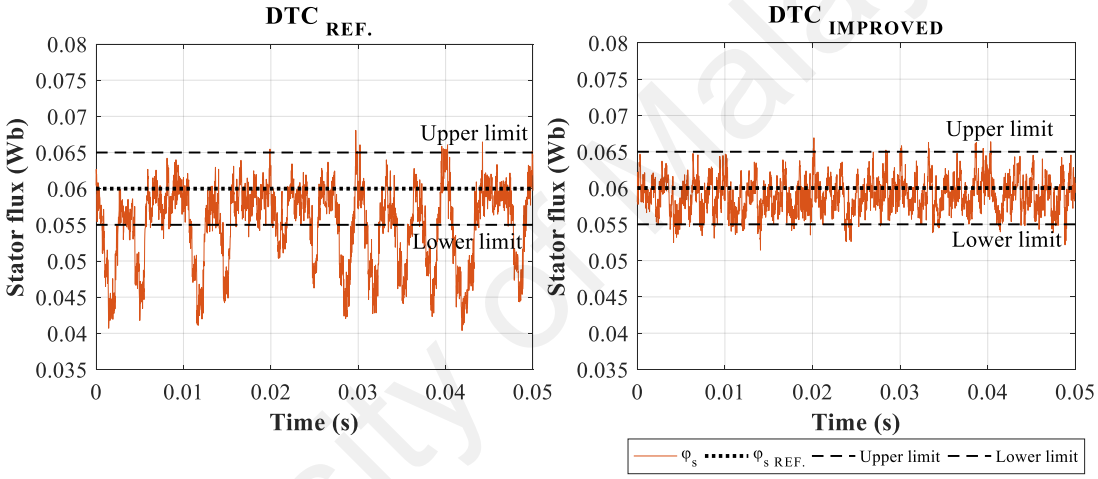

(e)

Figure 4.27, continued: Experimental results for unbalance load setup (d) Torque, (e) Stator flux.

University of Malaya

4.9 Overall performance comparison between the two approaches

For a fair comparison, both control methods were compared under the same operating conditions, where the reference torque is -1 Nm and stator flux is 0.06 Wb. In this section, the discussed results from the experiment were summarized. The comparison had been focused to study on the torque and stator flux and they were quantified in terms of mean and standard deviation as reported in Table 4.13.

The proposed LUT gave better control outputs with lower standard deviation on both torque and flux ripples. The stator flux was well confined within the comparator band limit with the generated magnitude closer to the desired stator flux, instead of shifting downwards as compared to the existing DTC approach. The discrepancy percentage of the stator flux to its reference value was 1.45 % which smaller as compared to the existing approach with the value of 4.04 %. The reasons behind is due to the more suitable switching vectors were selected with the smaller variation rate for the LUT development.

Unlike the existing DTC approach, the desired changed of stator flux can be achieved when there was an unbalanced condition by using the improved LUT-based DTC method. The standardized stator voltage model helped in choosing the accurate switching vector for LUT since error-free of switching vector's effect analysis can be conducted.

Table 4.13: Comparison results for the existing and improved LUT-based DTC.

Parameter	Set-up	DTC		LUT	
		Standard deviation	Mean	Standard deviation	Mean
Torque	Steady-state	0.069	-1.056	0.067	-1.070
	Unbalance load	0.094	-1.104	0.082	-1.041
Stator flux	Steady-state	0.002	0.0576	0.002	0.0591
	Unbalance load	0.006	0.0587	0.002	0.0590

Table 4.14: Discrepancy percentage to its reference

Set-up	DTC		LUT	
	Torque	Stator flux	Torque	Stator flux
Steady-state	6.00 %	4.04 %	6.00 %	1.45 %
Unbalance load	10.43 %	2.11 %	4.08 %	1.64 %

University of Malaya

4.10 Summary

The operation principles of the DTC based Vienna rectifier had been explained in details in this chapter. It can be concluded that the performance of the DTC method is highly dependent on the design of the LUT. By studying the effect of switching vector using the developed stator voltage model, an improved LUT had been developed for the DTC of the PMSG based on Vienna rectifier. As compared to the existing DTC method, more comparing conditions for the torque comparator were designed and hence, more suitable switching vectors that give smaller variation rate in torque are chosen for the LUT. Furthermore, the effectiveness of the developed LUT with computational delay compensation was evaluated with both simulation and experiments and compared to the existing DTC approach. Both results showed the improved LUT capable of generating better performance especially during unbalance DC-link condition.

However, the performance of the DTC operation heavily dependent on the operation condition. In particular, the rotor speed is the most difficult factors to be considered for LUT development as it is always changing based on the desired operation requirement. As an alternative to dynamically build lookup table as an optimal switching vector selector, model predictive direct torque control (MPDTC) was proposed as an adaptive DTC control method. This control method can extend the rotor speed operating condition, and it will be explained in the subsequent chapter.

University of Malaya

CHAPTER 5: LOOKUP TABLE BASED MODEL PREDICTIVE DIRECT TORQUE CONTROL

This chapter presents a model predictive control (MPC) based DTC method to solve the limitations of the conventional direct torque control as described in Chapter 4. In particular, a finite-set model predictive control (MPC) scheme was used to enhance the DTC based on Vienna rectifier. As compared to the classic LUT-DTC, the proposed model predictive direct torque control (MPDTC) permitted online optimization of the switching vector selection, allowing better control performance regardless of the PMSG operating conditions. To reduce computation burden, a LUT was used in conjunction with a neutral point voltage comparator to directly reduced the candidates of the switching vector based on neutral point voltage errors. The effectiveness of the proposed MPDTC method was verified and compared with the improved LUT-DTC method developed in Chapter 4 using simulations and experiments. In the experimental evaluation, a wind turbine emulator was developed with the consideration of guide-vanes integration to demonstrate the feasibility of the proposed control for the exhaust air turbine generator. A perturbed-and-observed (P&O) maximum power point tracker (MPPT) method was implemented together with the developed turbine emulator. Hence, the optimized power yielded from the guide-vanes integrated exhaust air turbine generator can be assured.

University of Malaya

5.1 Direct torque control for Vienna rectifier using model predictive control

The overall control scheme for the MPDTC of the PMSG using Vienna rectifier is shown in Figure 5.1. The controller consists of an inner finite set model predictive torque controller and an outer PI speed controller. Similar to the classic DTC approach, the phase currents of the PMSG are measured and transformed into the corresponding α-β components during each control cycle. By measuring the output from the encoder, rotor speed, ω_r and θ_r is calculated. Torque and stator flux are estimated based on the PMSG's model described in Chapter 4, using equation (4.8) to (4.11). Model-based computation delay compensation (4.38) and (4.39) are then applied on the estimated variables to get T_e', φ_s' before they are used as the control input variables for the prediction model. Such models that relate to the delay compensation will be explained in details in the later section. Here, a speed PI controller is deployed to give the reference torque based on the rotor speed error. The reference stator flux is considered to be a constant, which is fixed to be equivalent to the rotor flux for unity power factor operation. The reference torque is the only variable that is varying based on the speed PI controller output.

The main difference between the classic DTC and MPDTC approach is the inner control loop where the latter uses a MPDTC controller to replace the comparators for both torque and stator flux together with the switching vector LUT. Based on the information presented in Chapter 4, it is clear that the selection of the switching vector and polarity of stator current will affect the torque and stator flux variation as well as the DC-link voltage variation. The MPDTC will predict the achievable torque, stator flux, upper and lower DC-link capacitor voltage for all the possible candidate switching vectors of the Vienna Rectifier. According to equation (4.26), the polarity of the three-phase currents is required to predict the change in DC-link voltage. The best switching vector that minimizes a cost function is then selected by penalizing those switching vectors that produce prediction of control parameters which distant from the reference value. These are the fundamental

University of Malaya

concepts of the MPDTC method. Overall, the system is controlled to achieve following objectives: -

1) To minimize the electromagnetic torque error.
2) To minimize the stator flux error.
3) To maintain the neutral point voltage balance.

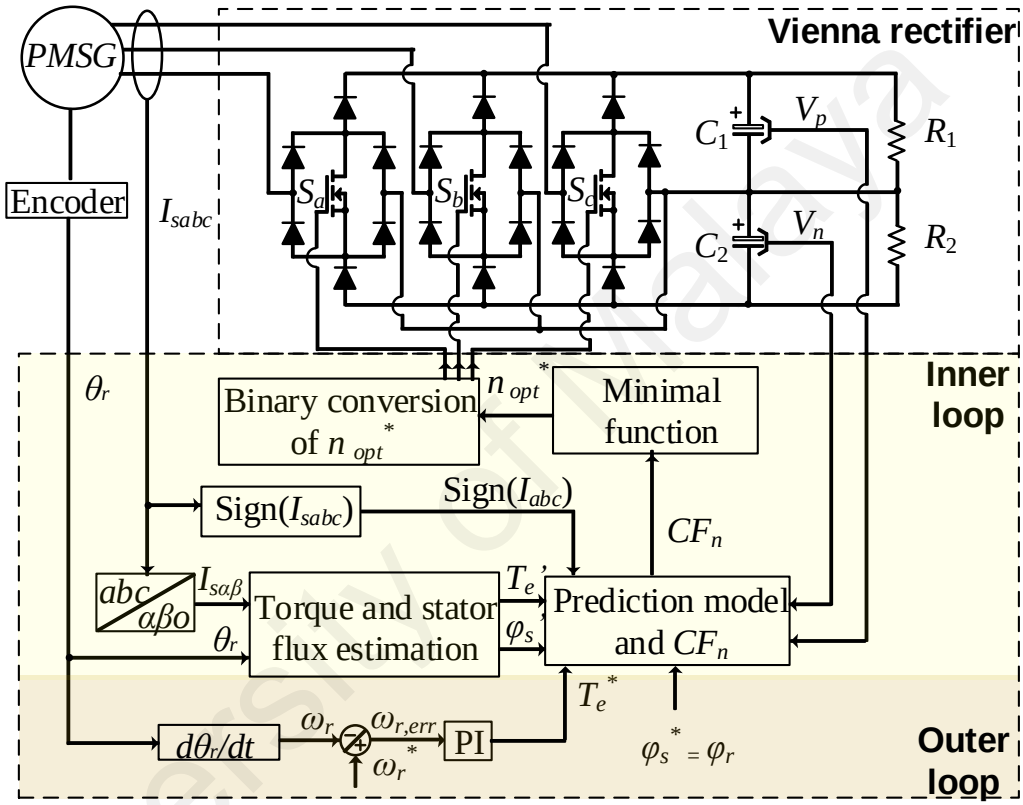

Figure 5.1: The block diagram of the model predictive direct torque control.

5.2 MPDTC design requirements and issues

A key strength of the MPDTC is its ability to perform online optimization control that effectively uses all of the feasible switching vector candidates of the Vienna rectifier regardless of the PMSG's operating conditions. However, there are some prominent setbacks that have to be highlighted, especially the higher computation burden as compared to the classic DTC. Besides, the quality of the PMSG's parameters also possesses a direct impact on the performance of the MPDTC. These design's requirements and issues will be discussed in the following sub-sections.

University of Malaya

5.2.1 Discrete-time model of PMSG and Vienna rectifier

Building a discrete-time model of the PMSG and Vienna rectifier is the first step towards the design and implementation of the MPDTC. These models are required to predict the torque, stator flux and DC-link voltage generated at the next control cycle.

The discrete-time model of the PMSG can be obtained by the means of the forward Euler discretization as follows: -

$$\frac{dT_e}{dt} = \frac{T_e(t+1)-T_e(t)}{T_s} \tag{5.1}$$

$$\frac{d\varphi_s}{dt} = \frac{\varphi_s(t+1)-\varphi_s(t)}{T_s} \tag{5.2}$$

with T_s being the sampling period, (t) and (t+1) denote the variables at current and the next iteration respectively. According to the dynamic equations of the PMSG as presented in Chapter 4 (equation (4.23) and (4.16) in *x-y* reference frame), (5.1) and (5.2) can be re-arranged with switching vector of the Vienna rectifier, *n* as: -

$$T_e(t+1)_n = T_e(t) + \frac{3T_s}{2L_s}\rho\varphi_r[V_{sx,n}\sin\delta(t) - (V_{sy,n} - \varphi_s(t+1)\omega_r)\cos\delta(t)] \tag{5.3}$$

$$\varphi_s(t+1)_n = \varphi_s(t) + V_{sx,n}T_s \tag{5.4}$$

It is worthwhile to emphasize that the rotor speed does not change rapidly for the small sampling period, therefore, ω_r (t+1) is approximately equal to ω_r (t) and it is treated as a constant in the model prediction horizon (Geyer, Papafotiou, & Morari, 2009; Jose Rodriguez, 2012; Lee & Lee, 2017).

Similarly, the upper and lower capacitor DC-link voltage of the Vienna rectifier can be obtained in discrete-time model as,

$$\frac{dV_p}{dt} = \frac{V_p(t+1)-V_p(t)}{T_s} \tag{5.5}$$

$$\frac{dV_n}{dt} = \frac{V_n(t+1)-V_n(t)}{T_s} \tag{5.6}$$

University of Malaya

After re-arranging, the expressions used to predict the future value of the upper and lower DC-link capacitor voltage are: -

$$V_p(t+1)_n = V_p(t) + \frac{T_s}{C}[(1-S_{a,n})sign(I_a)I_a + (1-S_{b,n})sign(I_b)I_b + (1-S_{c,n})sign(I_c)I_c - I_o] \tag{5.7}$$

$$V_n(t+1)_n = V_n(t) + \frac{T_s}{C}[-(1-S_{a,n})sign(I_a)I_a - (1-S_{b,n})sign(I_b)I_b - (1-S_{c,n})sign(I_c)I_c - I_o] \tag{5.8}$$

The output load current at the DC-side of Vienna rectifier can be defined using Ohm's law as,

$$I_o = \frac{V_{dc}}{R} \tag{5.9}$$

where *R* being the total load resistance at the DC-side of the Vienna rectifier.

Take note that all the eight candidate switching vectors labeled as *n* where *n* = 0,1,2…7, together with the current polarity are deployed in these discrete-time models to obtain the next instant value of the control variables.

5.2.2 Cost function for MPDTC

A cost function, *CF* of the MPC represents the objectives or the desired behaviors of the control system. It can be defined using the absolute error on the control variables depending on the candidate switching vectors. As mentioned previously, there are three main objectives for the MPDTC, such that the *CF* can be expressed as follows:

$$CF = |T_e^* - T_e(t+1)_n| + k_1 |\varphi_s^* - \varphi_s(t+1)_n| + k_2 |V_p(t+1)_n - V_n(t+1)_n| \tag{5.10}$$

where the first term represents the torque's absolute error, the second term is the tracking error of the reference stator flux, and lastly, the third term defines the variation of the upper and lower DC-link capacitor voltages. Constant k_1 and k_2 denote the weighting factors that can be adjusted in order to modify the importance of each term since it is a multi inputs cost function (Kazmierkowski, 2012; Rodriguez et al., 2013). Besides, these

University of Malaya

weighing factors are used to compensate the difference in magnitude for the control variables. By minimizing (5.10), the torque, stator flux and DC-link voltage balancing error can be minimized.

The optimal actuation is obtained by minimizing the cost function. Hence, the optimal switching vectors, $n_{opt}{}^{*}$ which gives the minimal cost are selected. This is defined by: -

$$n_{opt}{}^{*} = \min_{n=0,1,\dots 7}(CF_n) \tag{5.11}$$

There are a total of eight feasible switching vectors, $n = 0, 1, 2, \dots 7$ for the MPDTC's calculation dependent on the stator current position and operation characteristic of the Vienna rectifier. The selected optimal switching vector will be applied to the Vienna rectifier during a whole sampling interval at time, $(t+1)$.

5.2.3 Delay compensation for the real-time MPDTC implementation

When the MPDTC is implemented experimentally, a huge amount of computation is involved, introducing a time delay depending on the speed of microprocessor used. This delay can lead to a significant deterioration in control performance especially in torque and stator flux ripples when the time between the input parameters measurement and the application of the new instant of switching vectors is considerable (Wenxiang, Shengkang, Xiaoxin, & Yi, 2017).

In Figure 5.2, the diagram shows the trajectory of torque generated together with the computation time required when different switching vectors are applied. In this case, V_1, V_2 and V_3 are the switching vectors that use for the prediction of torque trajectory. The black solid line represents the actual trajectory with the application of the optimal switching vector, T_e, red solid line is the torque reference, $T_e{}^{*}$ and the dashed lines indicate the predictions for torque, T_e $(t+1)_n$ for switching vector n = 1, 2, and 3. The ideal condition is shown in the first schematic diagram in Figure 5.2 where the computational time of the microprocessor is assumed to be negligible. The selected optimal switching

University of Malaya

vector at the time, (t), V_{opt} (t) is applied instantly after the calculation, and the actual torque follows the reference torque with minimal error. Nevertheless, this assumption leads to an error in the prediction control during real-time implementation. As shown in the second diagram of Figure 5.2, due to the computation time, the calculated optimal switching vector at time (t) will only applied at the time (t+1), giving rise to a computational delay of approximately a sampling period. Meanwhile, the estimated variables are going to change to (t+1) in practical application. The decision for the optimal switching vector is also different, where the ideal case select V_1, V_2, and V_2 by considering the system's control from the instant time of (t) to (t+3) whilst V_3, V_1 and V_1 are selected in the event of computation delay.

Hence, it is crucial to include the computational delay in the MPDTC. As can be clearly seen in the lowest diagram in Figure 5.2, the operation of the MPDTC becomes similar to the ideal condition after the time delay compensation is considered. A model-based delay compensation approach, which is similar to what had proposed in Chapter 4 for classic DTC is used to address such issue for the real-time application. It is done by considering the previous selected optimal variation in both torque and stator flux in the estimation model. Thus, the variables at a current instant time, (t) is moved one step forward in time. The revised estimation for both torque and stator flux with the computation delay compensation can be obtained using equation (4.38) and (4.39).

University of Malaya

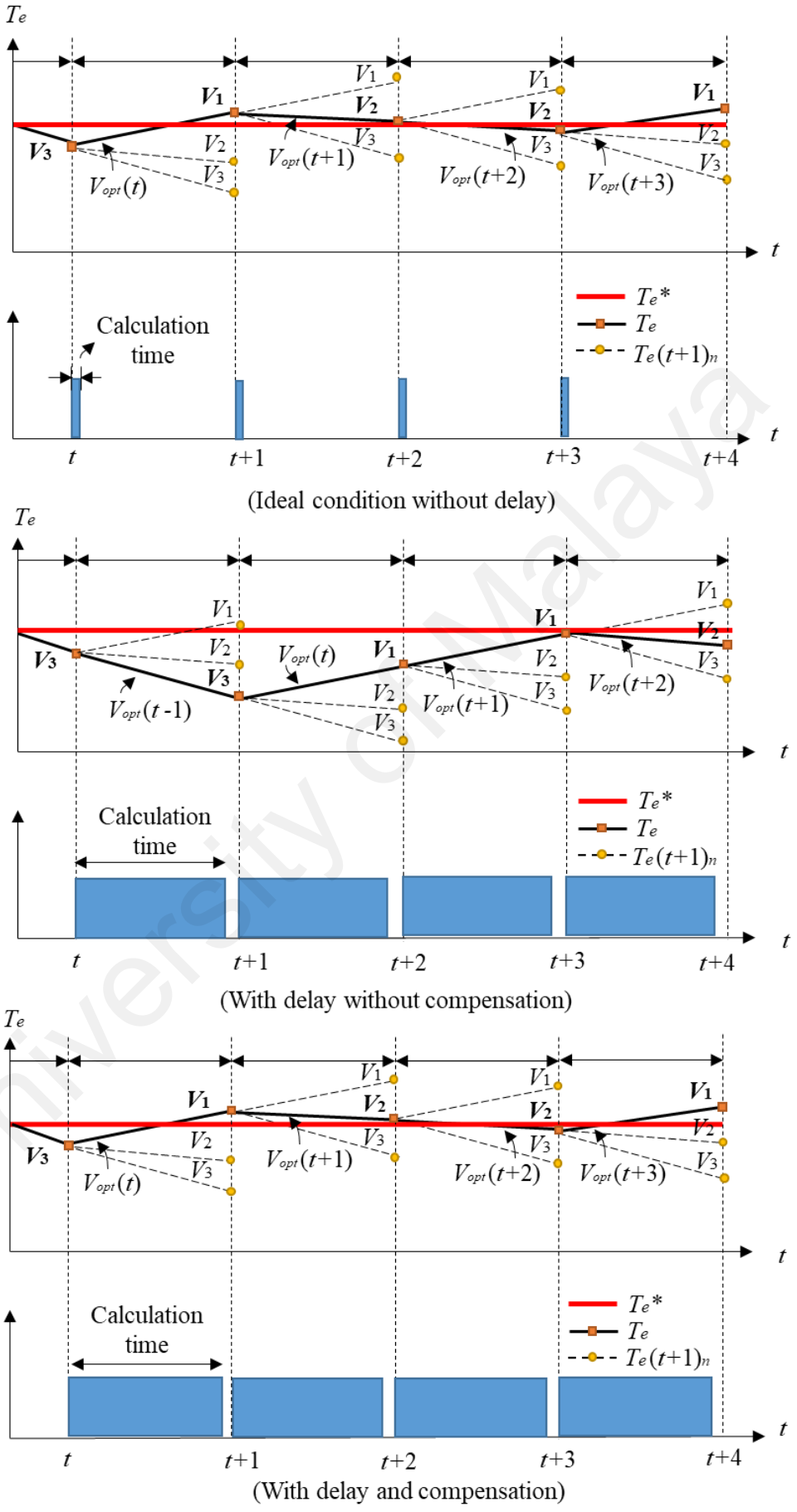

Figure 5.2: Operation of the MPDTC with and without compensation delay.

University of Malaya

5.2.4 Model parameter error

An important characteristic of the MPDTC is the explicit use of the PMSG model for predicting the future behavior of torque and stator flux to select the optimal switching vector according to the cost function. There are two main parameters used in both estimation and prediction model for the MPDTC, i.e. the stator inductances, L_s and rotor flux, φ_r. Considering that PMSG's parameters might change due to the temperature or a precise measurement of the parameters are difficult to obtain due to the nonlinear nature of the PMSG, it is important to consider the robustness of the MPDTC against the errors in machine parameters. This will be investigated in the simulation and experimental test.

5.3 Hybrid lookup table for computation delay improvement

As mentioned earlier, the key challenge of the MPC implementation is its high computational burden. In this case, the computation depends on two main factors, i.e.: -

1) Number of candidate switching vectors to be evaluated.
2) The complexity of the MPC algorithm.

To reduce computation burden for the MPDTC method, a hybrid lookup table MPDTC approach is proposed here in this project, with its control block diagram as shown in Figure 5.3. The reduction of the computation burden is made possible by using a simple LUT with a neutral point voltage comparator at the outer loop control. By considering the effect of switching vectors on DC-link voltage balancing in terms of variation's polarity, the suggested LUT table (sees Table 5.1 in Figure 5.3) reduces the number of candidate switching vectors from 8 to 5, which ease the computational burden of the MPDTC. Stator current sector, $I_{s\,sec}$ is used to identify the suitable candidates of switching vectors, n for MPDTC from the LUT according to the neutral point voltage comparator's output (V_{pn} state). Since the LUT inherently ensures a balanced DC-link voltage, the number of the prediction model is greatly reduced because the anticipation for both upper and lower

University of Malaya

DC-link capacitor voltage at next instant cycle can be eliminated. Furthermore, the cost function can also be simplified by excluding the effect of DC-link voltage balancing. Thereby, a simpler algorithm of MPDTC can be obtained. As compared to the conventional MPDTC approach, the proposed MPDTC method has lesser computation burden since it has a LUT that helps in reducing the number of candidate switching vectors and simplifying the complexity of the control algorithm.

Although the proposed MPDTC has a switching vector LUT which is similar as the classic LUT-DTC method, the development of the LUT is much simpler. This is due to the detailed analysis of switching vectors on both torque and stator flux as what had investigated in Chapter 4 can be omitted. The selection of the switching vectors for LUT is merely based on the neutral point voltage variation's direction (ΔV_{pn}) and the evaluation of the control variables' magnitude variation are not required.

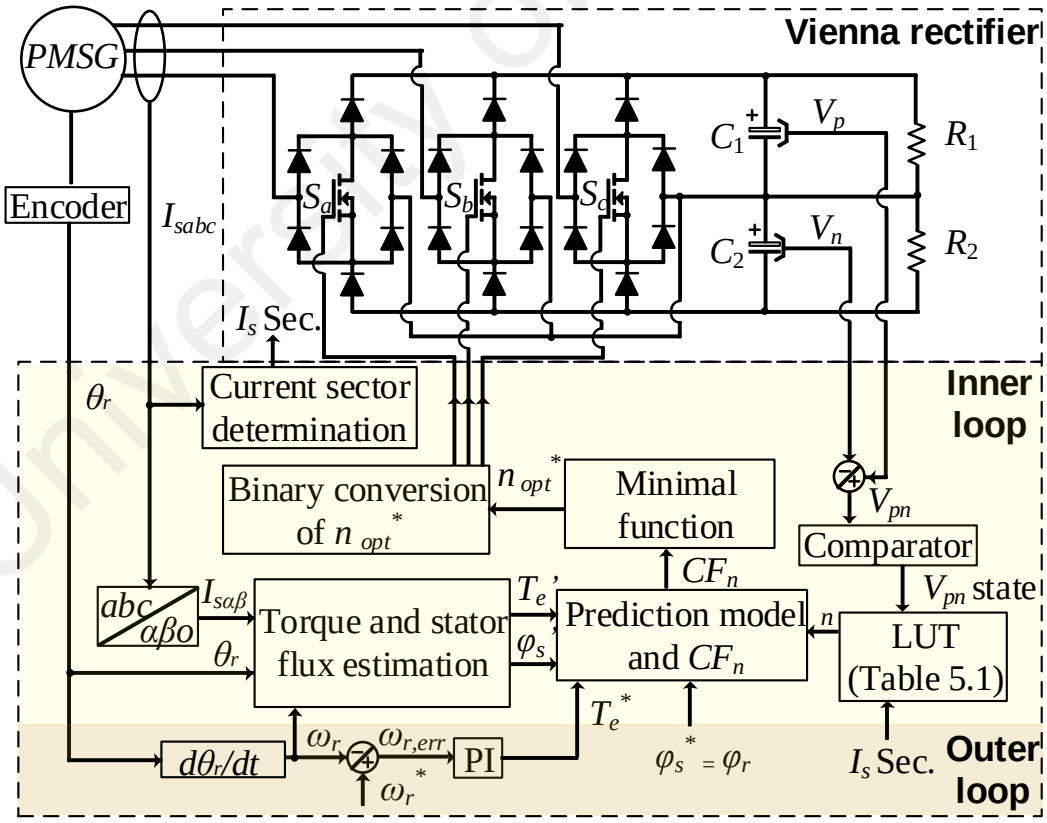

Figure 5.3: Block diagram of the hybrid LUT-MPDTC with MPPT.

University of Malaya

Table 5.1: LUT developed for MPDTC computational burden reduction.

DC-link voltage comparator output	Current sector					
	Sector 1	**Sector 2**	**Sector 3**	**Sector 4**	**Sector 5**	**Sector 6**
$V_{pn} > +h$	4	2	2	1	1	1
	5	4	3	2	3	4
	6	6	6	3	5	5
	7	7	7	7	7	7
	0	0	0	0	0	0
$+h > V_{pn} > -h$	2	3	1	2	3	1
	3	4	3	3	4	3
	5	5	5	5	5	5
	6	6	6	6	6	6
	7	7	7	7	7	7
$V_{pn} < -h$	1	1	1	4	2	2
	2	3	4	5	4	3
	3	5	5	6	6	6
	7	7	7	7	7	7
	0	0	0	0	0	0

The concept and development of this LUT are elaborated here. The available switching vectors of Vienna rectifier from each current sector are first categorized in terms of the polarity of the neutral point voltage variation as previously discussed in Chapter 4 (Table 4.8). By referring to the table, it is clear that switching vector 0 and 7 do not have any impact on the neutral point since the current flowing into the neutral point is zero. Meanwhile, switching vectors 1 to 6 can adjust the DC-link voltages by either increase or decrease the neutral point voltage, V_{pn} depending on the current sector. At any time, there are always 3 switching vectors that increase V_{pn} and another 3 vectors that decrease V_{pn}. Hence, given knowledge of the current sector and the DC-link voltage error, the 3 switching vectors that increase V_{pn} can be excluded from selection, leaving only 5 possible switching vectors. Based on this concept, the LUT, i.e. Table 5.1 is developed.

The DC-link voltage error is subjected to a comparator defined with a V_{pn} error band ($\pm h$). If the error is higher than $+h$, only switching vectors that give either negative or zero

University of Malaya

change in ΔV_{pn} are chosen; if the error is lower than -*h*, the three vectors that give negative change of ΔV_{pn} are excluded. For instance, let's assume the current is in sector one. If the V_{pn} is larger than the upper error band (+*h*), switching vectors 4, 5, 6, 0 or 7 is selected based on Table 4.8. On the contrary, switching vectors 1, 2, 3, 7 and 0 are chosen if V_{pn} is smaller than the lower error band (-*h*). When V_{pn} is within the error band, switching vectors to be selected for LUT can be either give positive or negative change in the neutral point voltage. Smaller switching vector is preferable since it can produce smaller variation in torque and stator flux which is beneficial in terms of ripples reduction especially during steady-state condition. In such a case, a big and a medium switching vector which are located further away from the origin (or zero state) are not considered. Meanwhile, there are 2 small switching vectors that are located at the same position and will give the same variation rate for both torque and stator flux. For instance, switching vector 3 and 4 (see Figure 4.4) formed such pair of small switching vectors when stator current is positioned in sector 1. As a result, one of them will become the redundant and it is eliminated by removing the switching vector that is not shared between the current sectors. As explained in Chapter 4, the operation of Vienna rectifier is highly dependent on the stator current's polarity. Choosing the switching vector with switching state that is common between the two current sectors can solve the erroneous voltage generated when the current transits from one sector to the subsequent sector. Such erroneous voltage occurs due to the change of polarity of any phase of current if the switching signal is in the off state (i.e. switching state P or N depends on the current sector). Thereby, there will be a possibly that the vector cannot be realized for the control and as a result, erroneous voltage arises.

The use of the LUT table hence allows the selection of the best switching vector without the exhaustive exploration of all the feasible switching vectors at any instances. Since the LUT inherently reduces the DC-link voltage error, the cost function can be

University of Malaya

simplified by re-formulating it to consider only the torque and flux absolute errors as follows: -

$$CF = |T_e^* - T_e(t+1)_n| + k|\varphi_s^* - \varphi_s(t+1)_n| \quad (5.12)$$

In this case, k is fixed as the ratio between the magnitude of the nominal electromagnetic torque and nominal stator flux in which both of them are controlled simultaneously with the same weight (Justo et al., 2017). According to (5.12), there is only a weighing factor is used and hence, the less tuning effort is required for the cost function.

In addition to that, the tabulation of minimal function for the optimal switching vector, n_{opt}^* selection can also be simplified with only 5 candidates of switching vector as:

$$n_{opt}^* = \min_{n=0,1,\ldots 4}(CF_n) \quad (5.13)$$

In short, the proposed LUT-MPDTC is expected to have similar control performance as the MPDTC, but lower algorithm complexity and computation burden. Table 5.2 summarizes the differences among the control approaches that had discussed for the PMSG's speed control using Vienna rectifier. In terms of implementation procedures, Figure 5.4 depicts the flowchart for both of the proposed LUT-DTC and LUT-MPDTC with the consideration of computation delay compensation.

Table 5.2: Comparison among the control methods.

Comparison parameters	**LUT-DTC**	**MPDTC**	**LUT-MPDTC**
Algorithm complexity	Low	High	Medium
Implementation complexity	Indirect	Direct	Direct
Performance (ripples reduction)	Low	High	High
Complexity of the LUT development	Complex	NA	Simple
Optimization method	Offline	Online	Online
Computation burdens	Low	High	Medium

University of Malaya

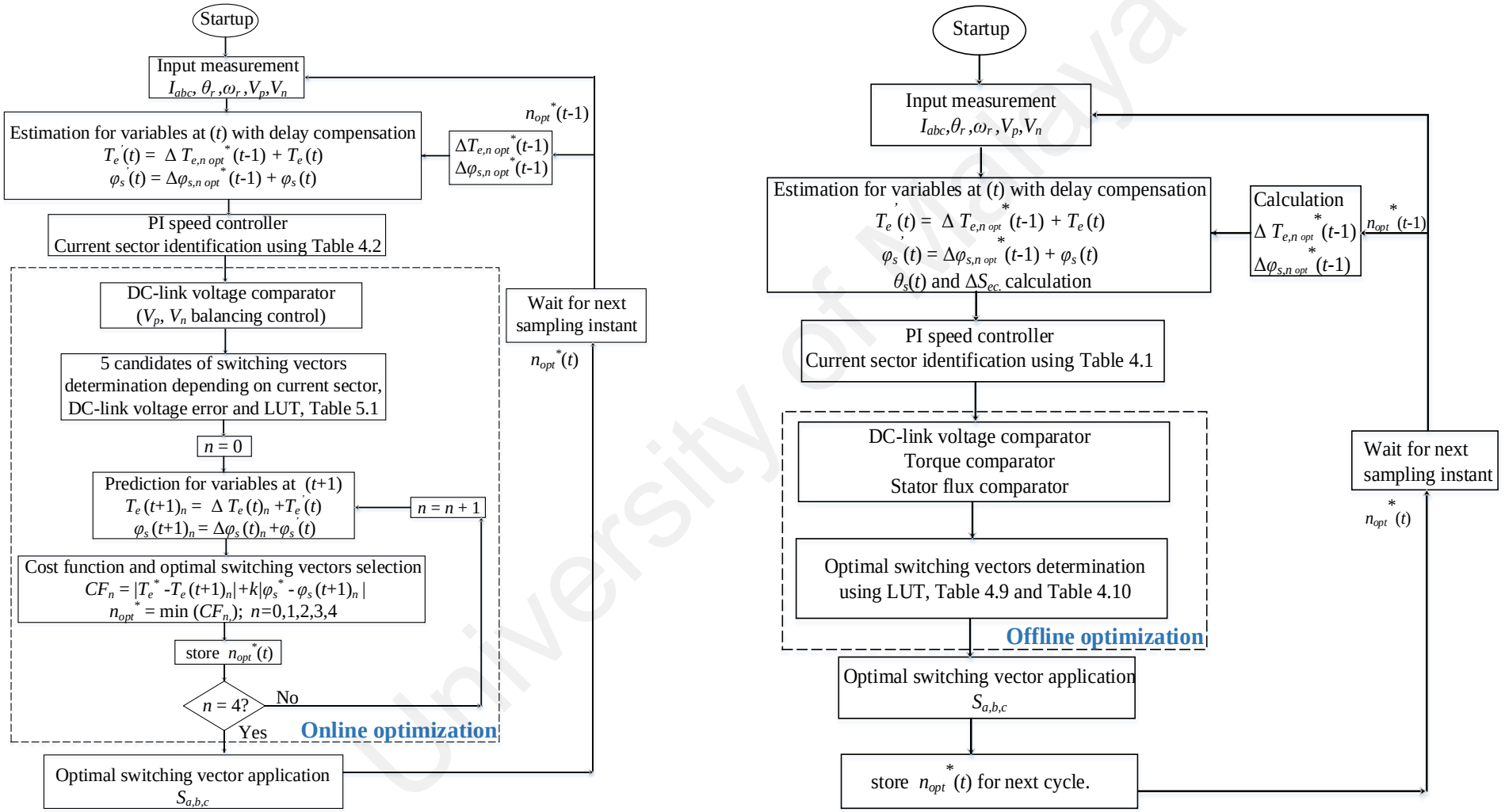

Figure 5.4: Comparison of the flowchart. (a) LUT-MPDTC, (b) LUT-DTC.

University of Malaya

5.4 Matlab simulation results

Numerical simulation was first conducted using Matlab Simulink to validate the performance of the developed hybrid LUT-MPDTC. There were three scenarios to be conducted which are similar to what had been presented in Chapter 4 for the LUT-DTC approach. The steady-state response and the unbalance load response were carried out for both low and high rotational speed, with the values of 700 rpm and 1500 rpm respectively. The comparator band of the DC-link voltage was set to be ±2 V. The remaining parameters used in the simulation can be obtained in Table 4.4.

5.4.1 Overall response of the proposed hybrid LUT-MPDTC approach

The performance of the hybrid LUT-MPDTC during constant speed at both high and low speed was shown in Figure 5.5(a) to (f). The left figure showed the simulation result for high rotor speed operation and the graph on the right was for low rotor speed operation. By referring to Figure 5.5(d) to (f), the rotor speed, torque and stator flux were well regulated around their respective references regardless of high or low speed operations of the PMSG. Furthermore, the generated stator current and stator voltage are also in phase as depicted in Figure 5.5 (b) guaranteed the operation of Vienna rectifier.

As can be seen in Figure 5.5(f), the stator flux generated was controlled closely to the magnitude of rotor flux, 0.06 Wb which is beneficial as the system can be assured to operate closely to the unity power factor. Meanwhile, the neutral point voltage balancing was well maintained within the predefined error band of ±2 V, around 150 V, as depicted in Figure 5.5 (c). This confirmed the effectiveness of the proposed LUT in balancing the DC-link voltages without the need of using the cost function.

University of Malaya

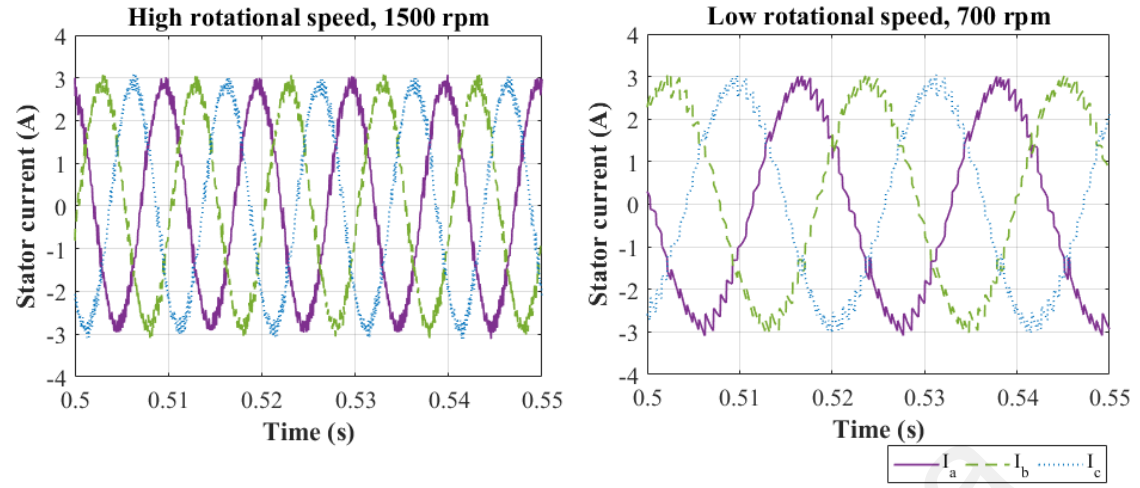

(a)

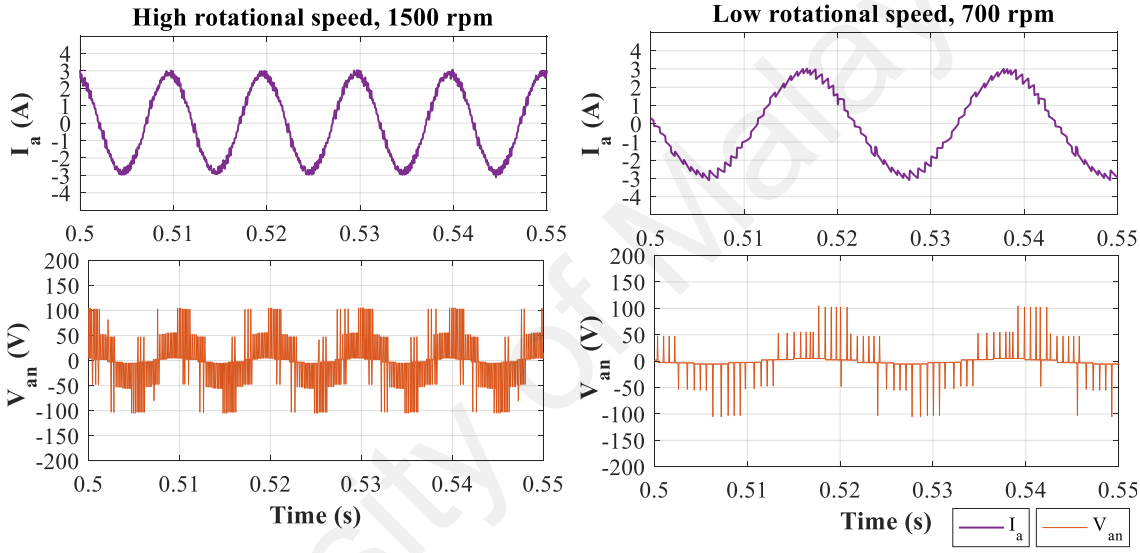

(b)

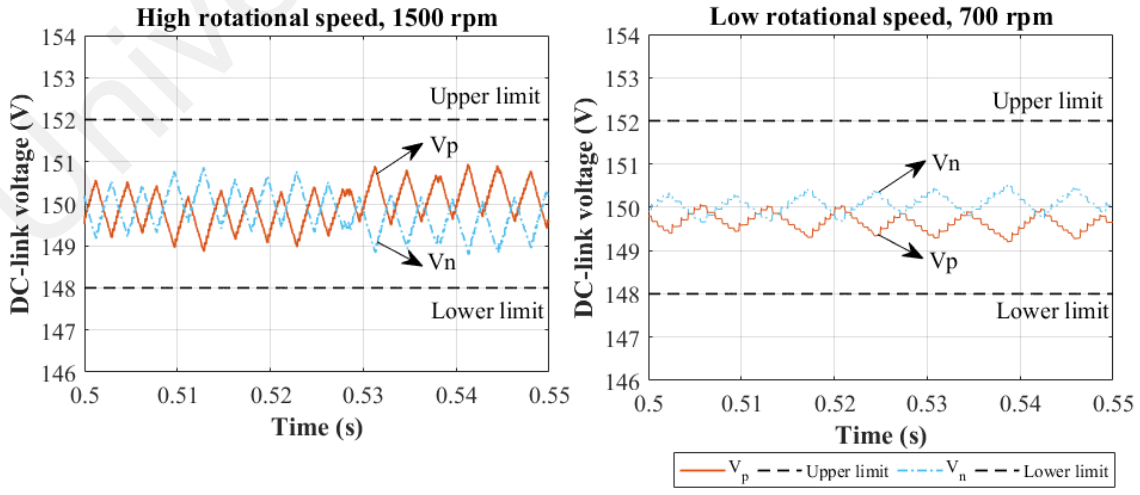

(c)

Figure 5.5: Simulation results of LUT-MPDTC for both high and low rotational speed. (a) Stator current, (b) Phase voltage and phase current, (c) DC-link voltage.

University of Malaya

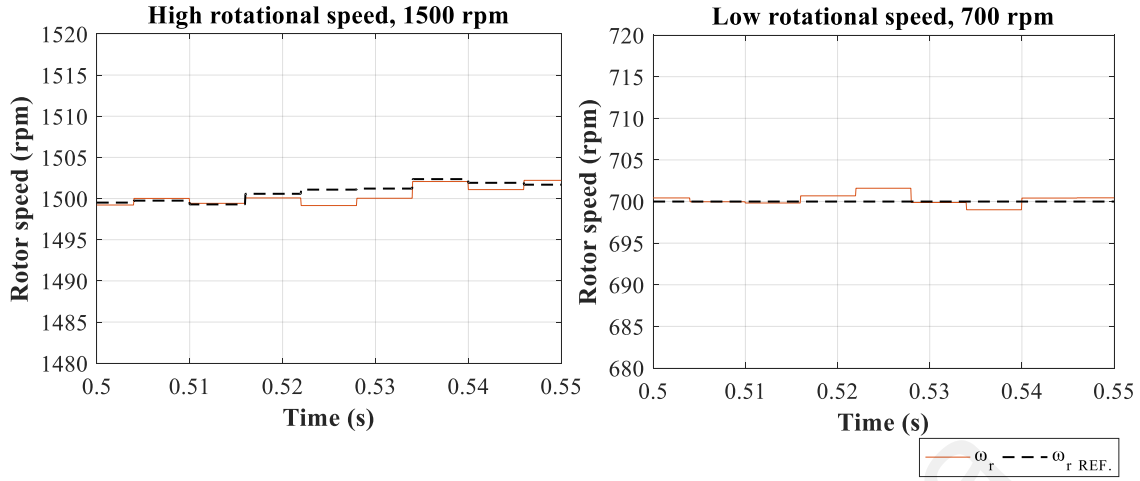

(d)

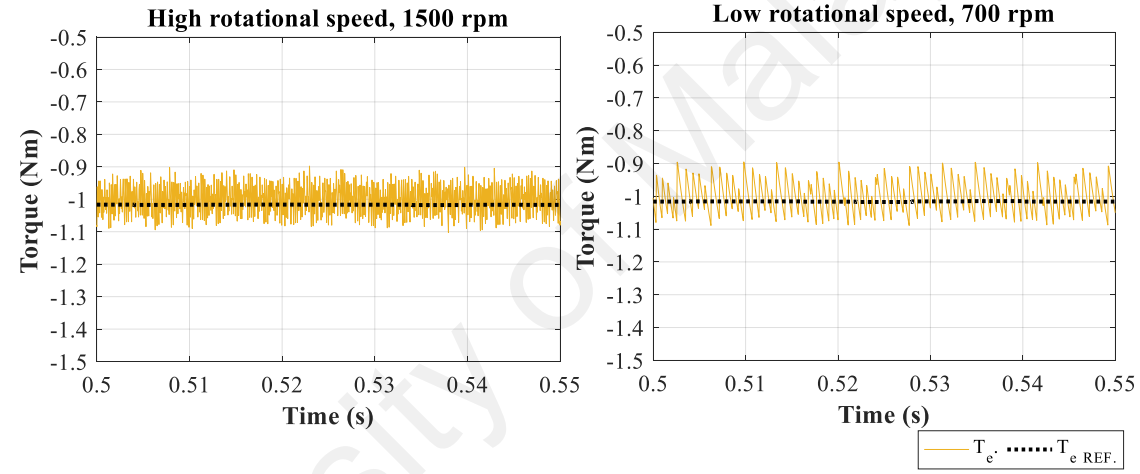

(e)

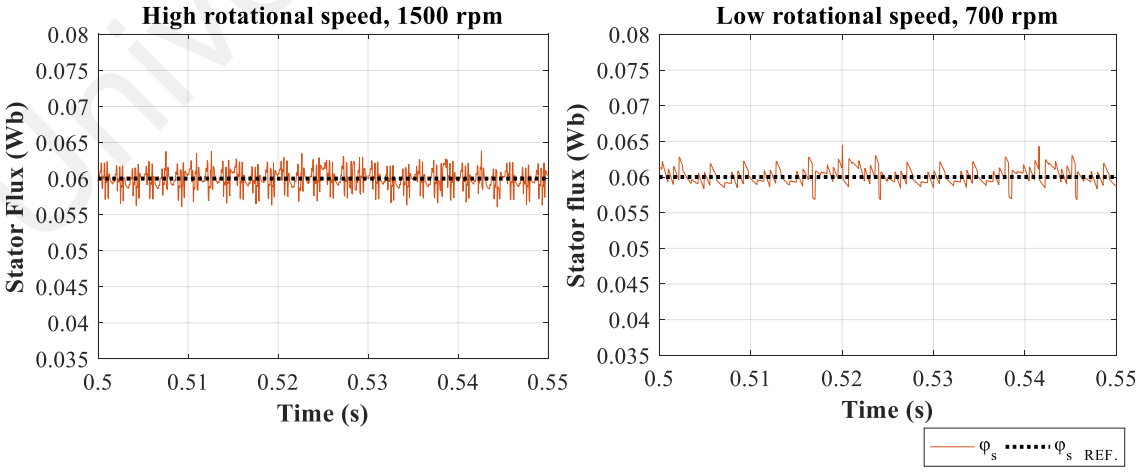

(f)

Figure 5.5, continued: Simulation results of LUT-MPDTC for both high and low rotational speed. (d) Rotor speed, (e) Torque, (f) Stator flux.

University of Malaya

5.4.2 Transient response of LUT-MPDTC

To demonstrate the dynamic performance of the proposed hybrid LUT-MPDTC, the same way was applied as the classic DTC, where the PI speed controller was bypassed and the reference torque was changed at a time, t = 1.1 s from -1 Nm to -0.5 Nm. It was observed that prediction torque control achieved a fast and accurate tracking performance of torque as shown in Figure 5.6(c). In Figure 5.6(d), there were no ripples seen in the stator flux at the instance of torque change. Throughout the step change in torque, the stator current remained balanced and sinusoidal, whilst the DC-link voltages were still well regulated within the error band as can be observed in Figure 5.6(a) and (b) respectively. This meant that the proposed LUT-MPDTC worked well when the reference torque was changed suddenly.

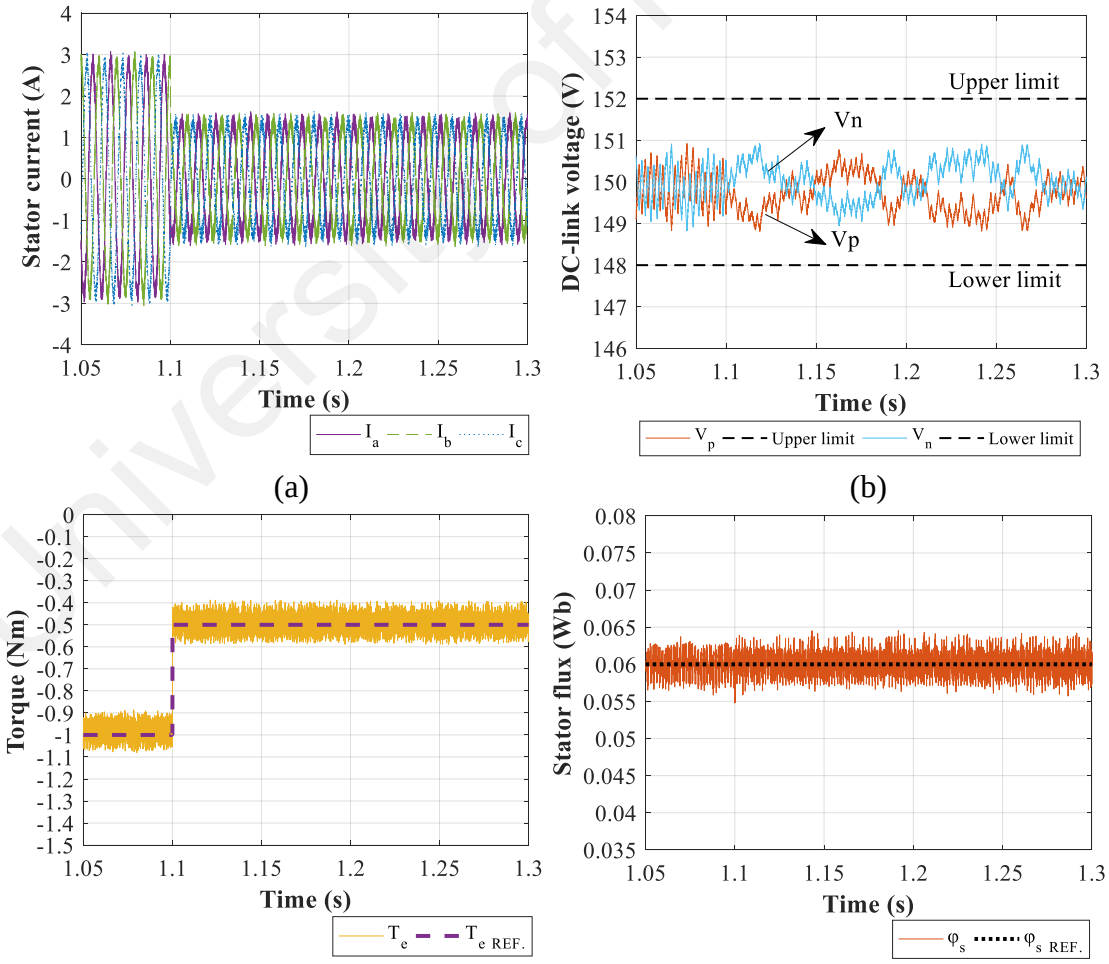

Figure 5.6: Transient response of LUT-MPDTC.
(a) Stator current, (b) DC-link voltage. (c) Torque, (d) Stator flux.

University of Malaya

5.4.3 Unbalance load study

This section presented the ability of LUT-MPDTC to balance neutral point of DC link voltage in the event of unbalanced load. The total DC-link voltage was kept close to 300V while implementing the LUT-MPDTC. Figure 5.7(a) presents the generated 3 phase stator current from control approach and they are in phase with the stator voltage, sees Figure 5.7(c). As shown in Figure 5.7(b), it was observed that the upper and lower capacitor DC-link voltage were confined within the range from 148 V to 152 V. By referring to Figure 5.7(e) and (f), there were no anomalies observed in the output torque and stator flux. They were still controlled closely to their respective reference value with rotor speed regulated at 1500 rpm (Figure 5.7(d)). This result showed the effectiveness of the hybrid LUT with MPDTC on balancing the capacitor voltage even under unbalanced load.

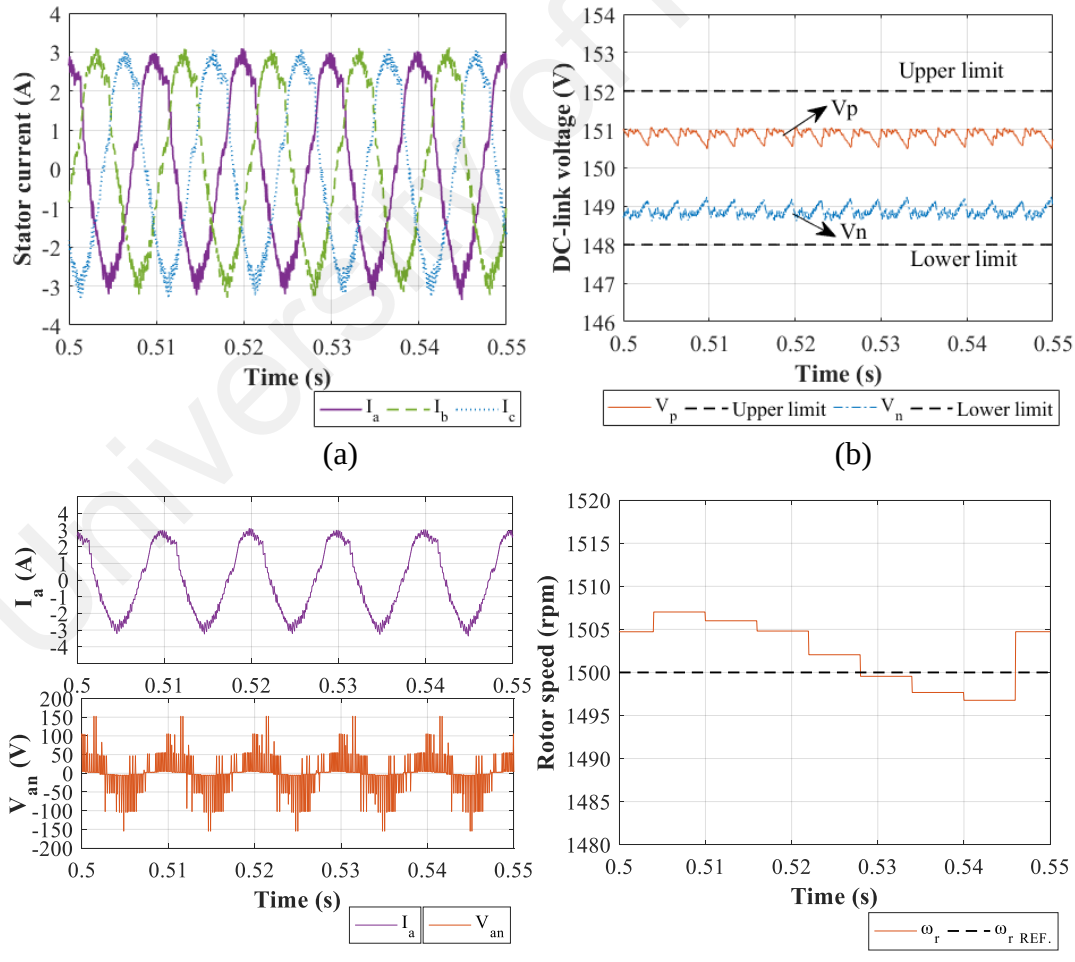

Figure 5.7: Capability of balancing neutral point voltage simulation results. (a) Stator current, (b) DC-link voltage, (c) Phase voltage and phase current, (d) Rotor speed.

University of Malaya

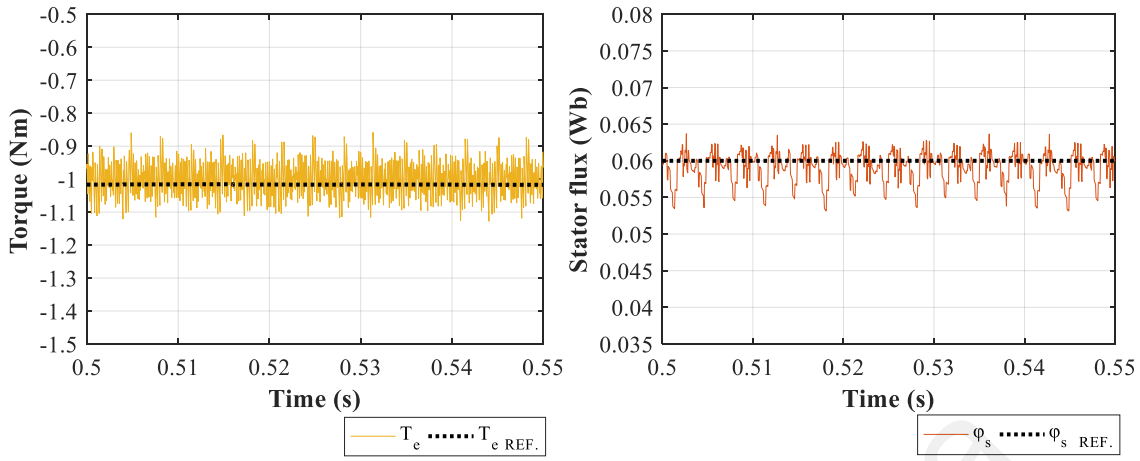

(e) (f)

Figure 5.7, continued: Capability of balancing neutral point voltage simulation results. (e) Torque, (f) Stator flux.

5.5 Experimental evaluation of the developed LUT-MPDTC

In order to evaluate the proposed hybrid LUT-MPDTC experimentally, the same lab-scaled prototype which developed for the LUT-DTC approach was used. The test conditions were set to be identical to the simulation. With the same operating frequency (20 kHz) and PI speed controller, it allowed a fair comparison between the generated experimental results with the LUT-DTC approach.

5.5.1 Experimental results – with and without delay compensation

Computation delay effect on the LUT-MPDTC was evaluated in this section. It can be seen in the Figure 5.8(a) that there were higher ripples generated at the waveform of the stator current at the left when the delay compensation approach was not applied to the LUT-MPDTC. The same pattern can also be observed in both torque and stator flux as shown in Figure 5.8(b) to (c). The torque pulsations were considerable, oscillating from -1.18 Nm to -0.6 Nm. This delay gave the standard deviation of 0.09 in generated torque, which was approximately 61 % more as compared with the algorithm implemented with the computation delay compensation. Through this result, it should be emphasized that the effect of the one-step delay was significant on both torque and stator flux ripples. This

University of Malaya

issue can be addressed effectively by using the proposed compensation approach in the LUT-MPDTC.

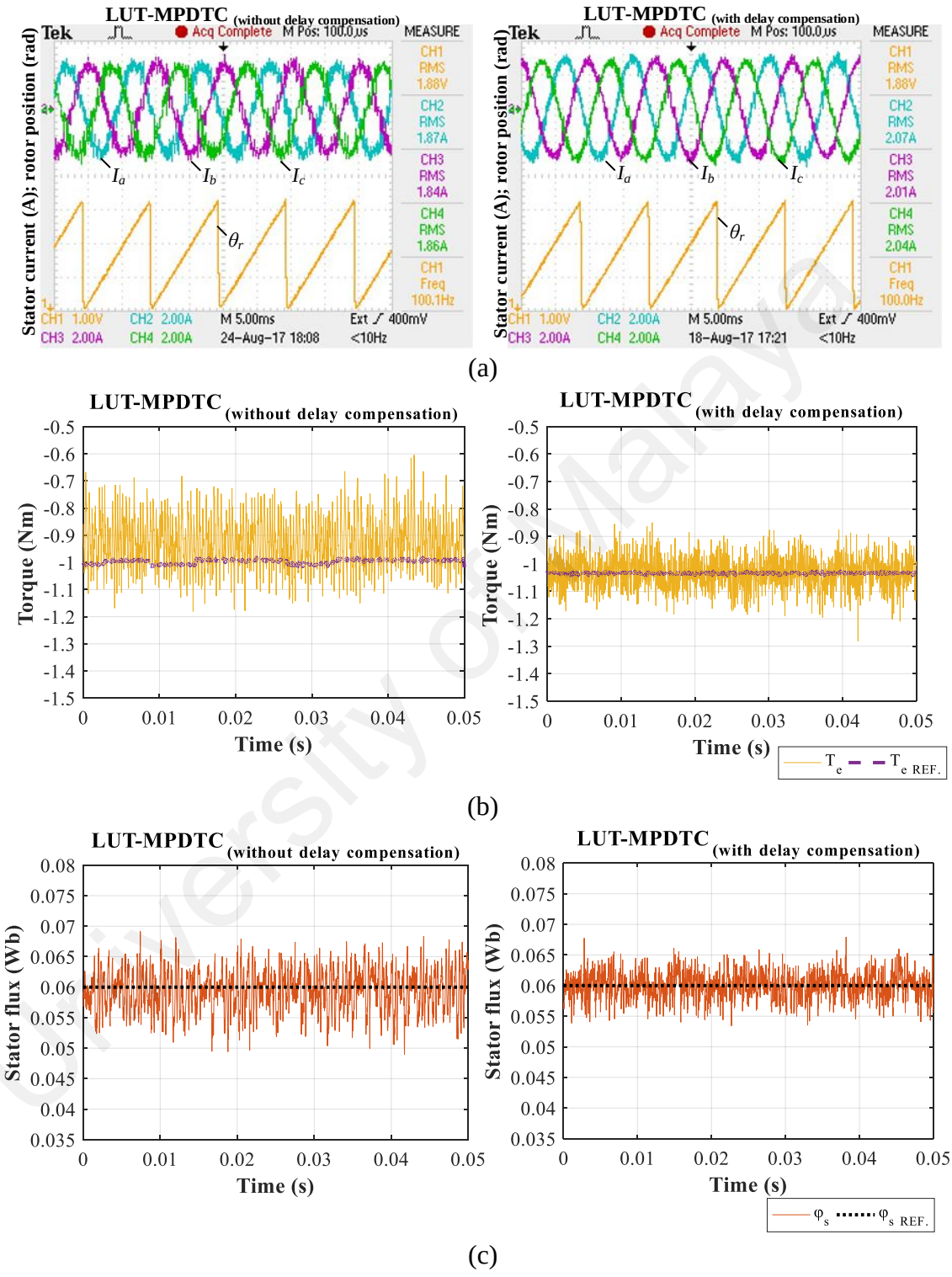

Figure 5.8: Generated results for LUT-MPDTC with and without delay compensation. (a) Stator current (b) Torque, (c) Stator flux

University of Malaya

5.5.2 Experimental results for steady-state response

The performances of the system under constant speed operation of 700 rpm and 1500 rpm with load controlled at -1 Nm were evaluated. As seen in Figure 5.9(a) and (b), the stator currents were balanced and sinusoidal, while being kept in phase with the stator voltage. Accurate tracking of the rotor speed and torque was achieved with the upper and lower DC-link voltages were confined within the designated band value, referring to Figure 5.9(c) to (f). The experiment results showed consistent pattern as observed from the simulation results.

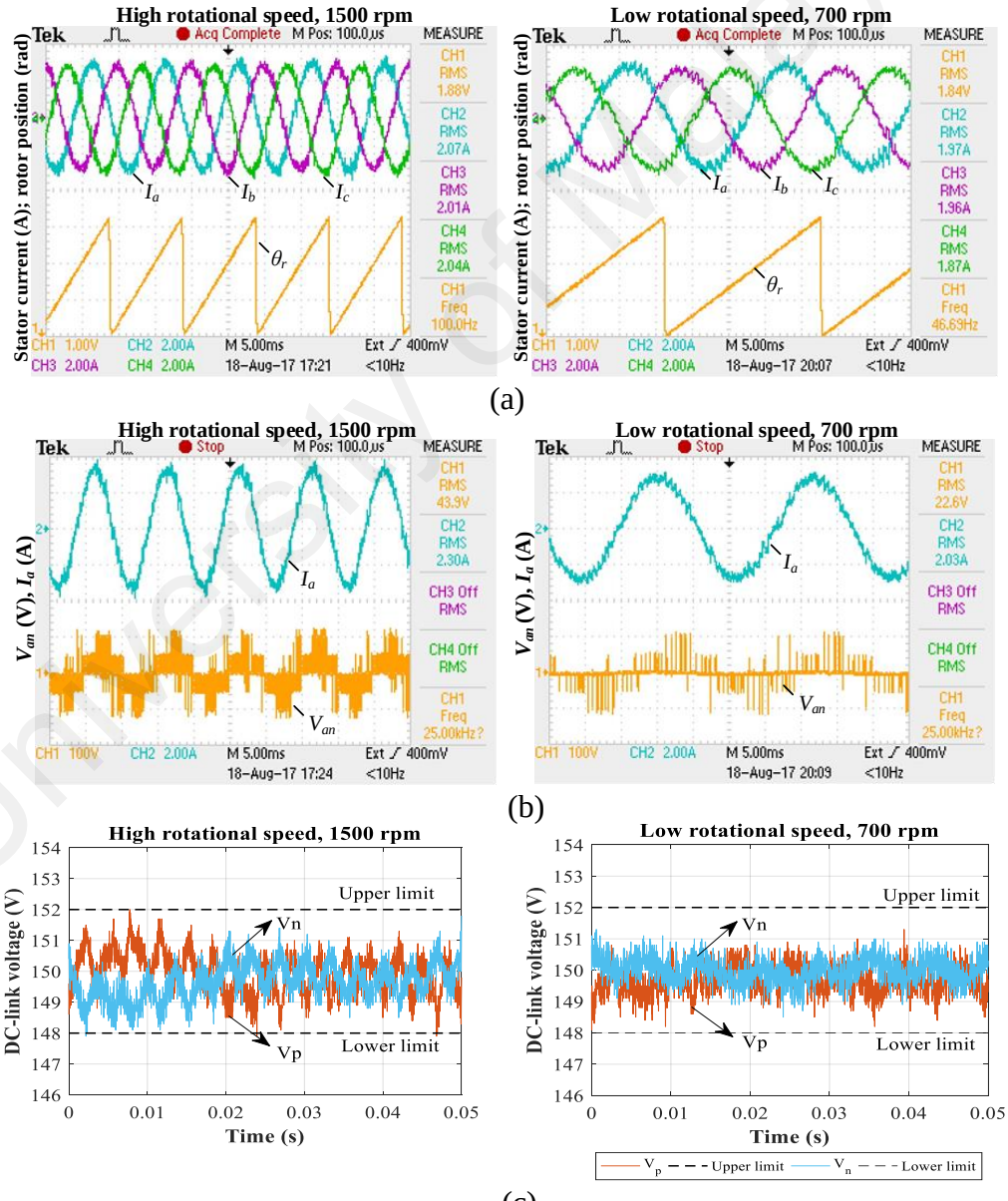

Figure 5.9: Experimental results of the LUT-MPDTC at both low and high rotational speed. (a) Stator current, (b) Phase current and phase voltage. (c) DC-link voltage,

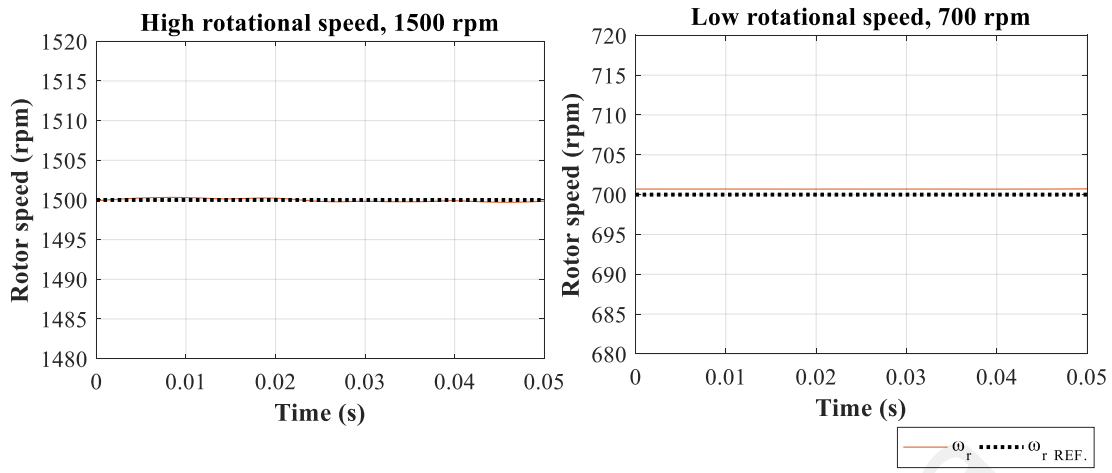

(d)

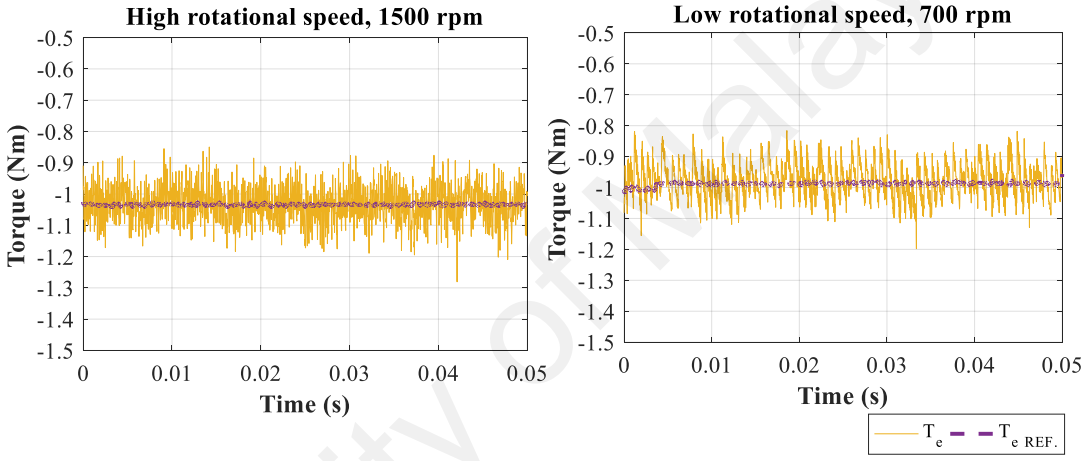

(e)

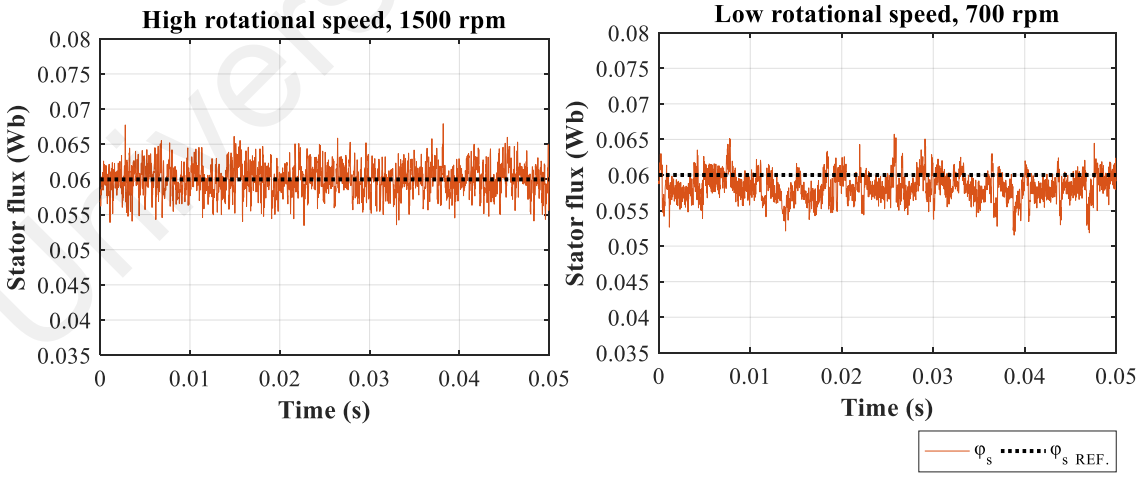

(f)

Figure 5.9, continued: Experimental results of LUT-MPDTC at both low and high rotational speed. (d) Rotor speed, (e) Torque. (f) Stator flux.

University of Malaya

5.5.3 Experimental results on dynamic response

A step change in torque was applied when t = 0.05 s, and the dynamic behavior of the PMSG was recorded and displayed in Figure 5.10. According to Figure 5.10(c), it was observed that the generated torque changed quickly to the new reference value at -0.5 Nm. At the same time, the abrupt change did not affect the LUT-MPDTC in regulating the stator flux (Figure 5.10(d)). The generated upper and lower DC-link voltages were coinciding to each other within the upper and lower limit as shown in Figure 5.10(b).

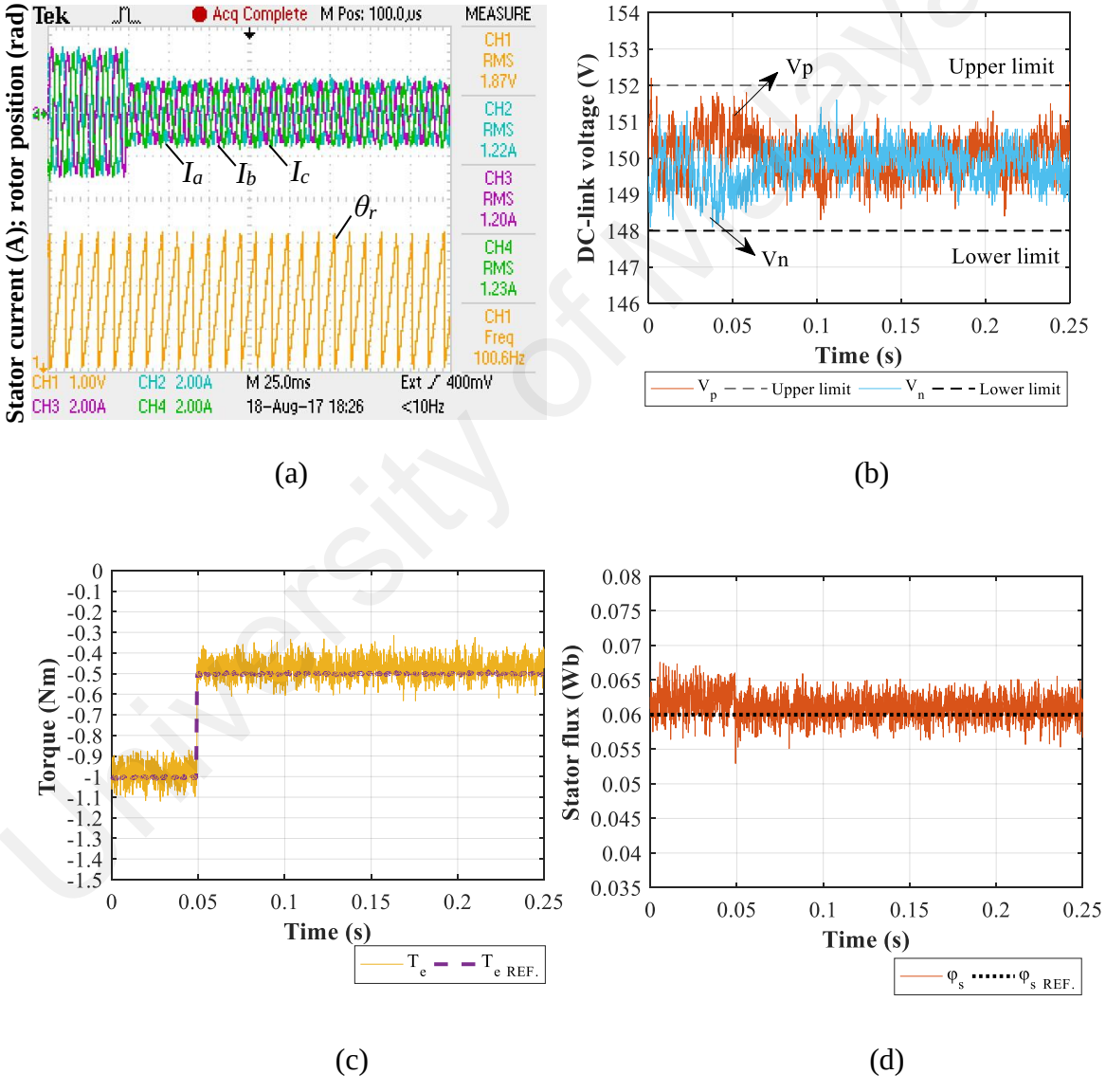

Figure 5.10: Experimental results on dynamic response. (a) Stator current, (b) DC-link voltage, (c) Torque, (d) Stator flux.

University of Malaya

5.5.4 Experimental results on unbalance load response

Another important behavior of the LUT-MPDTC was its ability to maintain a proper control under the presence of unbalance load of 10% at the DC output. As shown in Figure 5.11(a), the upper and lower DC capacitance voltage were confined within the predefined error band, whilst implementing the LUT-MPDTC. Other control variables, i.e. output torque and stator flux were still controlled closely to their respective reference value with rotor speed of 1500 rpm (see Figure 5.11(b) to (d)). The unbalance load did not have obvious impacts on the control.

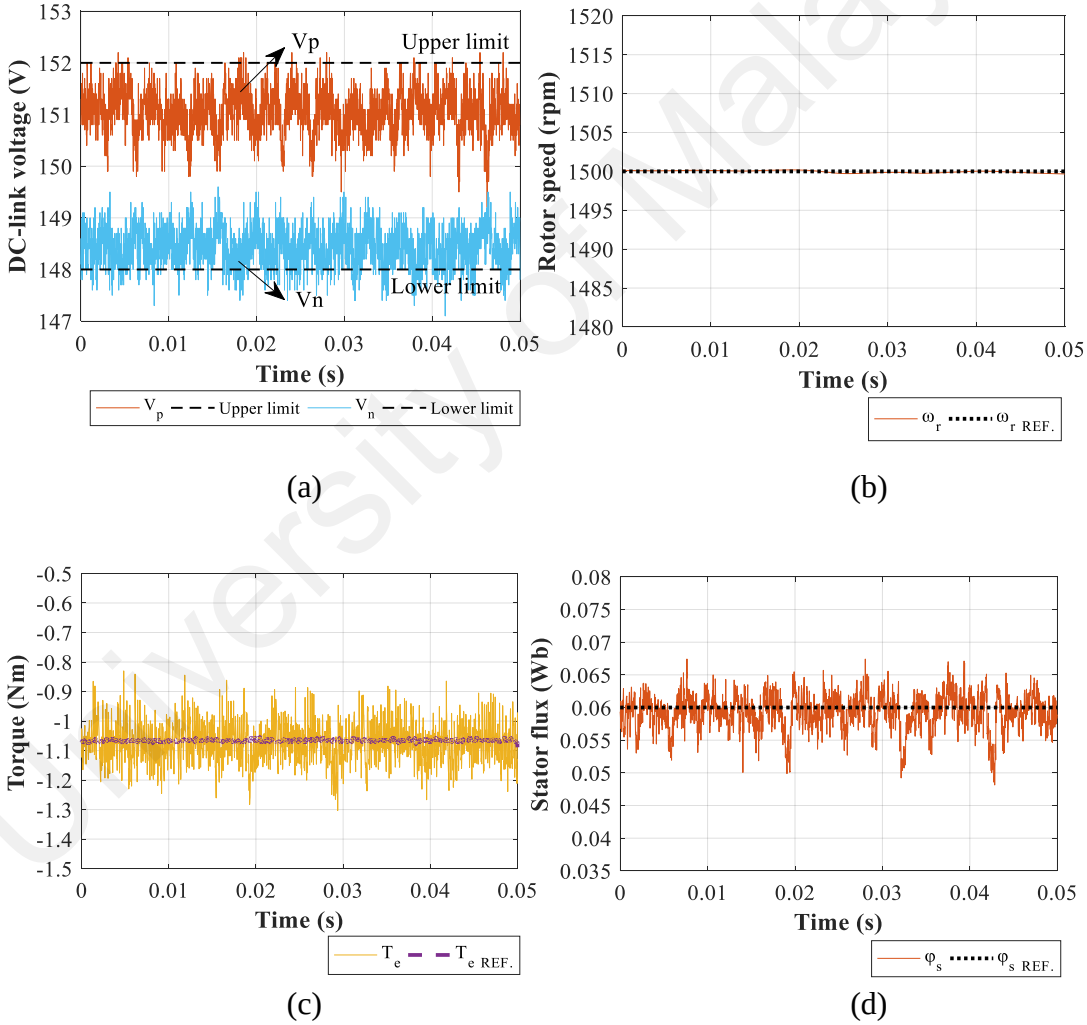

Figure 5.11: Generated results during unbalance DC load application. (a) DC-link voltage, (b) Rotor speed, (c) Torque, (d) Stator flux.

University of Malaya

5.5.5 Experimental results on parameter detuning

The parameter detuning in the prediction control can greatly affect the performance of the proposed LUT-MPDTC. Two extra scenarios with the incorporation of different L_s and φ_r were investigated for the implementation of the MPDTC, i.e. 50% and 200% shifted of their corresponding nominal magnitude. Figure 5.12 and Figure 5.13 displayed the effect of stator inductance and rotor flux variation respectively when the rotor speed was controlled to 1500 rpm. As seen in Figure 5.12(a), very little ripples can be observed on the generated torque when stator inductance was reduced to 50 % of its original magnitude. The ripples appeared in the torque became slightly higher when the variation was increased to 200%. In terms of stator flux, it was slightly drifted away from its nominal value of 0.06 Wb as indicated by the dotted line in Figure 5.12(b). The ripples generated on the stator flux was higher especially during 50 % variation in stator inductance. For the case with rotor flux variation, the produced torque as depicted in Figure 5.13(a) did not exhibit significant ripples, but a small offset was detected in stator flux. Slightly higher ripples appeared in stator flux when 200 % of rotor flux difference applied, as seen in Figure 5.13(b). From the obtained experimental results, it can be concluded that these variations of parameters had minimal effect on the performance of the proposed LUT-MPDTC. Furthermore, the proposed LUT-MPDTC was quite robust against parameter detuning and it was expected to be able to perform reasonably well even with the presence of parameters uncertainties.

University of Malaya

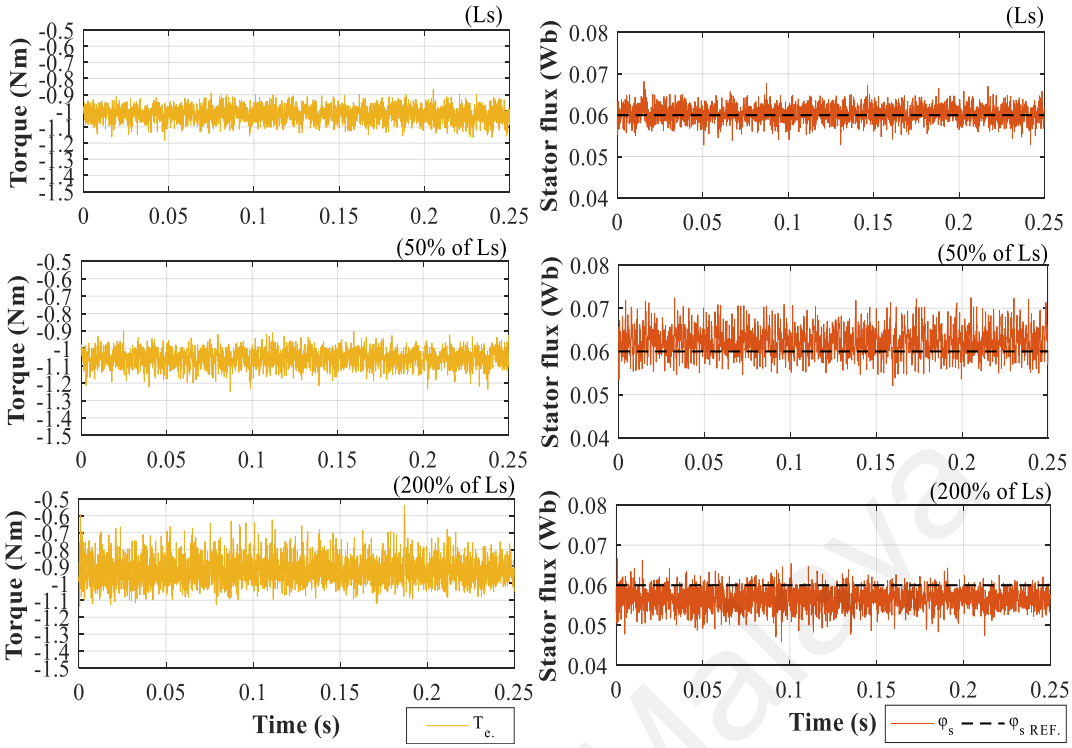

(a) (b)

Figure 5.12: Generated results when stator inductance varies at 0 %, 50 % and 200 %. (a) Torque, (b) Stator flux.

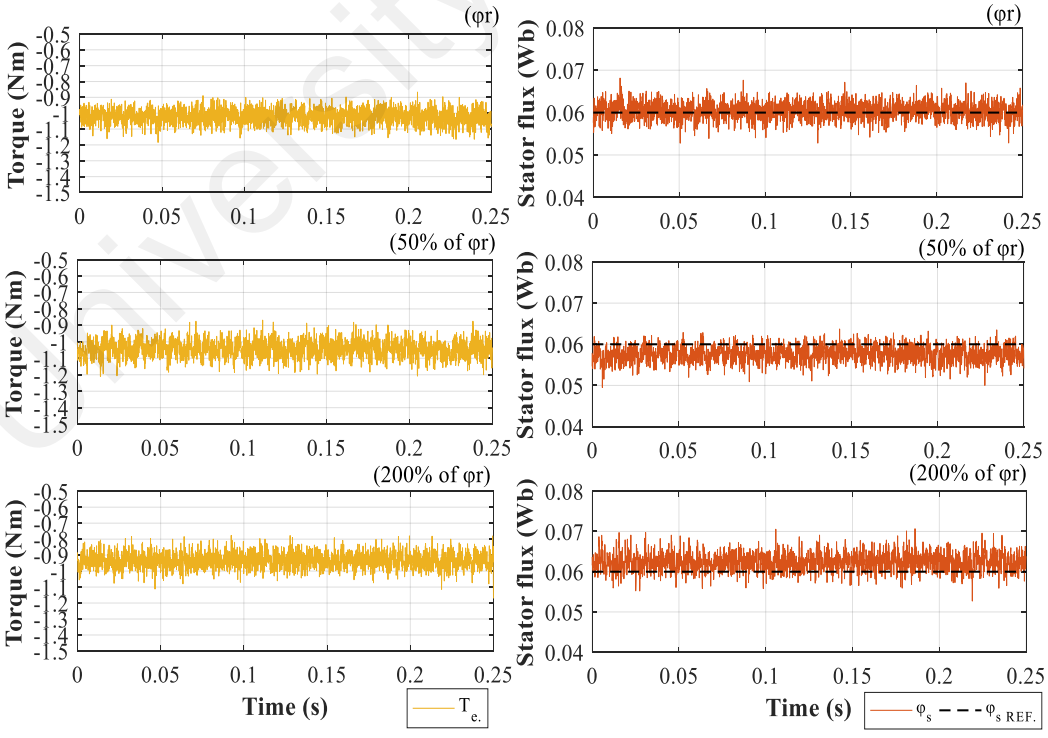

(a) (b)

Figure 5.13: Experimental results at the presence of rotor flux variation. (a) Torque, (b) Stator flux.

University of Malaya

5.5.6 Comparison results of conventional DTC and proposed LUT-MPDTC

The obtained experimental results in terms of torque and stator flux for the conventional LUT-DTC approach with the improved LUT proposed in Chapter 4 and the hybrid LUT-MPDTC were compared under 4 operating conditions, i.e.:

1) Low rotational speed at 700 rpm with driving torque of -1 Nm.
2) High rotational speed at 1500 rpm with driving torque -1Nm.
3) Low rotational speed at 700 rpm with driving torque of -0.6 Nm.
4) High rotational speed at 1500 rpm with driving torque -0.6 Nm.

The standard deviation explained in Chapter 4 for the torque and stator flux was used to identify the performance difference between the control approaches. Meanwhile, the discrepancy in percentage value was also evaluated by comparing the mean value of the torque generated to its reference value. The main attractive feature of the MPDTC is its capability to achieve an optimal control performance over a wide range of PMSG speed operation. The tabulated standard deviation for the corresponding control approaches was recorded in Table 5.3. It was observed that the standard deviation for both torque and stator flux of the proposed LUT-MPDTC was always smaller than the conventional LUT-DTC for all the PMSG's operational conditions. This is due to the fact that the ripples generated for the control variables from the LUT-MPDTC is always lower. With regards to the control accuracy, Table 5.4 gives the percentage difference of different control approaches in terms of torque ripples. The generated torque from LUT-MPDTC was closer to its reference value with the percentage difference lower than 4 % for all of the conditions. The percentage discrepancy from the LUT-DTC was severe, especially during low speed operation. The same pattern can be observed for the stator flux in which the standard deviation is smaller for LUT-MPDTC. This comparison showed that LUT-MPDTC was more superior in terms of torque and stator flux control as compared to the conventional LUT-DTC approach.

University of Malaya

Table 5.3: Comparison of standard deviation for LUT-DTC and MPDTC

Operational conditions	LUT-DTC		LUT-MPDTC	
	Torque	Stator flux	Torque	Stator flux
700 rpm; -1 Nm	0.066	0.0021	0.056	0.0019
1500 rpm; -1 Nm	0.067	0.0023	0.056	0.0021
700 rpm; -0.6 Nm	0.063	0.0019	0.051	0.0019
1500 rpm; -0.6 Nm	0.064	0.0021	0.051	0.0018

Table 5.4: Comparison of the percentage difference of the torque ripples to its reference for LUT-DTC and MPDTC

Operational conditions	LUT-DTC			LUT-MPDTC		
	Range (Nm)	Mean	%	Range (Nm)	Mean	%
700 rpm; -1 Nm	-1.12 ~ -0.65	-0.94	6	-1.12 ~ -0.82	-0.98	2
1500 rpm; -1 Nm	-1.28 ~ -0.85	-1.07	7	-1.28 ~ -0.85	-1.03	3
700 rpm; -0.6 Nm	-0.75~ -0.3	-0.54	10	-0.76 ~ - 0.41	-0.58	3.33
1500 rpm; -0.6 Nm	-0.85 ~ -0.29	-0.62	3.33	-0.78 ~ -0.43	-0.58	3.33

5.6 Verification of the LUT-MPDTC with turbine emulator

So far, a LUT-DTC and a hybrid LUT-MPDTC had been developed for the control of PMSG using Vienna rectifier. Both simulation and experimental results had been used to confirm the effectiveness of both methods in controlling the torque and flux (as well as speed, through a PI speed controller) of the PMSG to their desired references, with the LUT-MPDTC being more superior in terms of control performance. In order to achieve power optimization on the guide-vanes integrated wind turbine system, an additional MPPT controller should be utilized on top of the DTC control method to provide a suitable speed reference that will ensure the wind turbine runs at its optimal point regardless of wind speed variation. This will be explained in this subsection.

University of Malaya

5.6.1 Perturbed-and-observed (P&O) based maximum power point tracker

Due to the size constrains of the available prototype guide-vanes integrated wind turbine, a wind turbine emulator was developed and used for the evaluation of the MPPT control here instead of the actual system. Details on the wind turbine emulator development can be found in Appendix B2. In this work, perturbed-and-observed (P&O) MPPT method is adopted. It is the most common and simplest MPPT method that allows the rotor speed of the wind turbine to operate at the optimal operational point regardless of the oncoming wind speed. It is worthy to mention that the wind speed measurement through anemometer is not required for this MPPT, making it is easy and lower in cost.

Basically, the P&O based MPPT just monitor the generated electrical power of PMSG and identified the suitable change of rotor speed to be applied for the PMSG according to the turbine's power against rotor speed curve as shown in Figure 5.14. This power curve will be used as the baseline to verify the performance of the MPPT at different wind speeds.

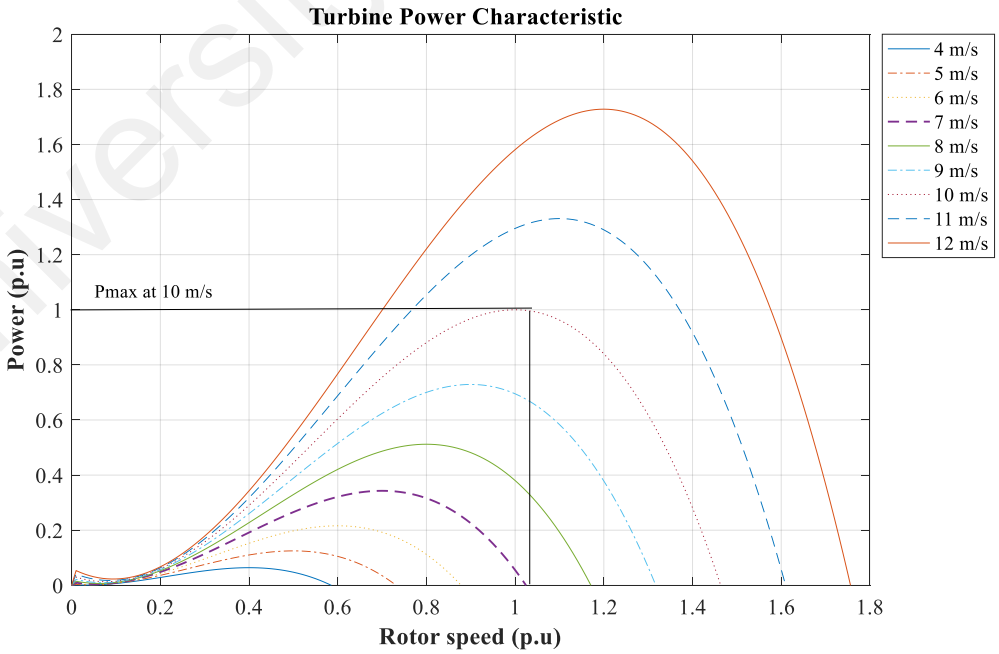

Figure 5.14: Guide-vanes integrated exhaust air turbine 's power characteristic curve.

University of Malaya

The applied change of the rotor speed, *C* is decided based on 4 criteria, i.e.,

$$C = +\Delta_{\omega r}\ ; \begin{cases} P(t) - P(t-1) > 0 \text{ and } \omega_r(t) - \omega_r(t-1) > 0 \\ P(t) - P(t-1) < 0 \text{ and } \omega_r(t) - \omega_r(t-1) < 0 \end{cases}$$

$$C = -\Delta_{\omega r}\ ; \begin{cases} P(t) - P(t-1) < 0 \text{ and } \omega_r(t) - \omega_r(t-1) > 0 \\ P(t) - P(t-1) > 0 \text{ and } \omega_r(t) - \omega_r(t-1) < 0 \end{cases} \quad (5.14)$$

where $\Delta_{\omega r}$ is the step-size of rotor speed change. For instances, when MPPT induces a positive step change, $+\Delta_{\omega r}$ in rotor speed, the direction of the rotor speed change is correct if the generated electrical power is increased. Thus, the same $+\Delta_{\omega r}$ change is applied during the next control instant. In contrast, the opposite change in speed will be applied ($-\Delta_{\omega r}$ is applied) if the reduction of the electrical power is observed. Expression (5.14) can be simplified become one model using signum function as follows,

$$C = \Delta_{\omega r} * sign(\big(P(t) - P(t-1)\big) * sign(\omega_r(t) - \omega_r(t-1)) \quad (5.15)$$

The main setback of the P&O-based MPPT is that its operating point always oscillate during steady-state. Reducing the step-size can reduce the steady-state oscillation but can cause slower response for the MPPT to converge to the maximum power point, MPP more slowly especially if there is a large transient. Here, two step-sizes are used in such a way that smaller step-size is used to reduce the oscillation during steady-state whilst bigger step-size is used to improve the transient response of the MPPT. Step-size to be applied for the P&O based MPPT is decided based on the speed error, $\Delta_{\omega r}$ as follows,

$$\Delta_{\omega r} = \begin{cases} 0.1 & ; \text{when } P(t) - P(t-1) < 0.5 \\ 1.0 & ; \text{when } P(t) - P(t-1) \geq 0.5 \end{cases} \quad (5.16)$$

Two step-sizes of rotor speed change, $\Delta_{\omega r}$ are established, which are 0.1 rad/s (0.95 rpm) and 1.0 rad/s (about 9.55 rpm) depending on the magnitude of electrical power difference. The resultant rotor speed from the P&O based MPPT determines the reference speed that will be applied to the PI speed controller.

University of Malaya

5.6.2 Experimental results with wind turbine emulator

The WT emulator was first analyzed at different operation curve of the WT based on different wind speed. The wind speed inserted into the Graphic user interface (GUI) through the dSPACE DS1104 ControlDesk will be varied in both increasing (from 7 m/s to 10 m/s) and reducing wind conditions (from 10 m/s to 6 m/s), which covered the whole range of wind speed.

To further verify the transient and steady-state operation of the hybrid LUT-MPDTC approach with the MPPT, a sudden change of wind speed was applied. It is done by applying a step change of wind speed from 5 m/s to 10 m/s.

The experimental waveforms of the hybrid LUT-MPDTC with the emulator were presented to demonstrate the functionality of WT emulator together with the adapted P&O based MPPT. Figure 5.15 shows the experimental set-up of wind turbine emulator wind with the hybrid LUT-MPDTC based on Vienna rectifier.

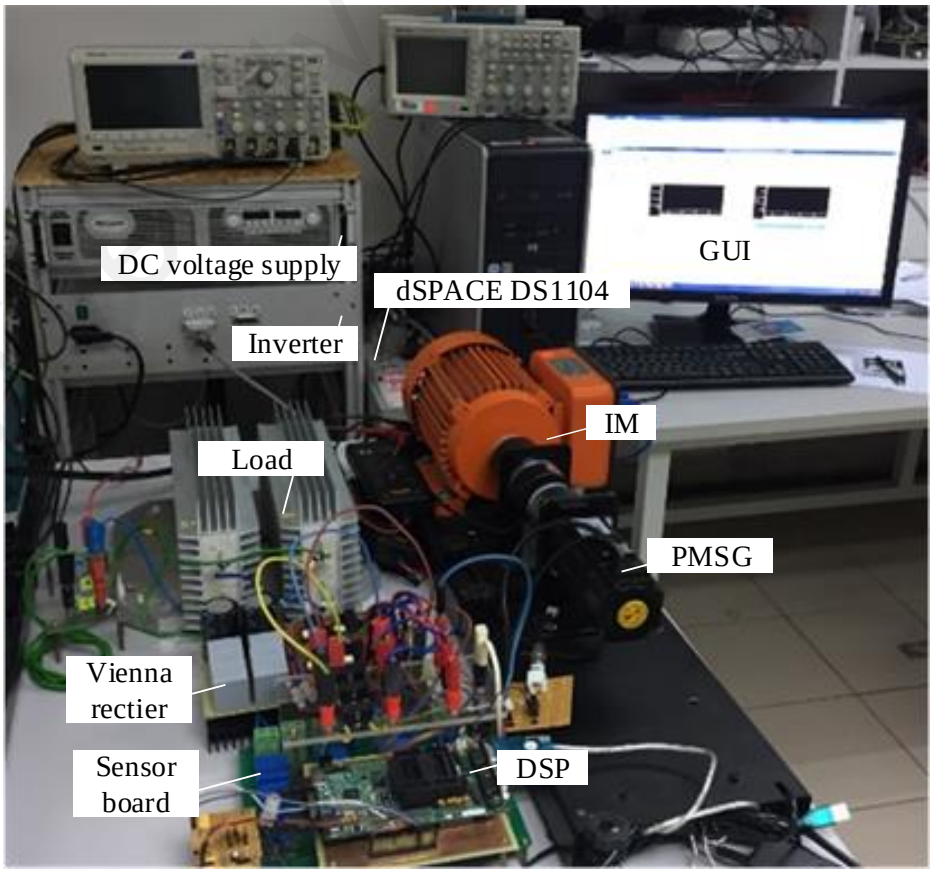

Figure 5.15: The experimental set-up of the wind turbine emulator.

University of Malaya

Figure 5.16 showed the results generated when different wind speeds were applied in step to the wind turbine emulator. By referring to the Figure 5.16(b), it was observed that the optimum power point was achievable for every wind speeds in terms of mechanical aspect as the generated power coefficient magnitude was close to its peak value, 0.0506 as indicated by the red dotted line during its steady-state.

Figure 5.17 showed the tracking of the optimum point obtained from the two steps P&O based MPPT algorithm when the wind speed was altered. In the figure, the purple solid line indicates for the case of decreasing wind speed from 10 m/s, 8 m/s and lastly, at 6 m/s while brown-colored solid line is for the wind speed changes from 7 m/s, 9m/s and then at 10 m/s. The different color dotted lines for different wind speeds were obtained from the turbine power characteristic curve as plotted in Figure 5.14. It was observed that the MPPT was able to track the maximum power point for each wind speed regardless of the wind speed was increasing or decreasing. This can be also observed through the recorded average maximum power for all the wind speeds by comparing to its expected power generation as shown in Table 5.5. The expected power for each wind speeds was extracted from the turbine power characteristic curve. The percentage discrepancy was small, which was less than 2 % for all of the wind speed applied. Meanwhile, the PMSG was also rotated closely to its optimum rotational speed and it can be seen in Table 5.6.

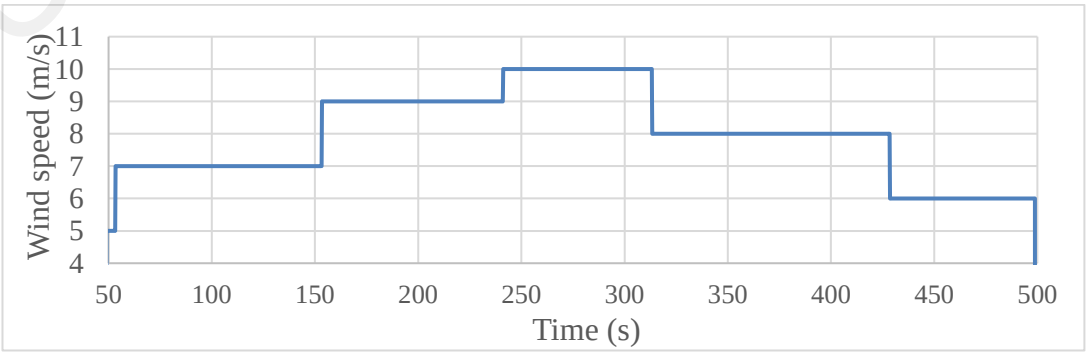

(a)

Figure 5.16: Results generated when different wind speeds are applied in step. (a) Applied wind speed.

University of Malaya

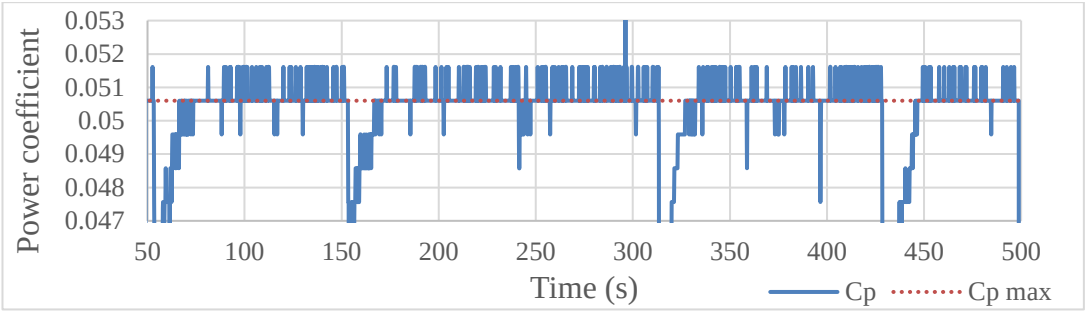

(b)

Figure 5.16, continued: Results generated when different wind speeds are applied in step. (b) Power coefficient.

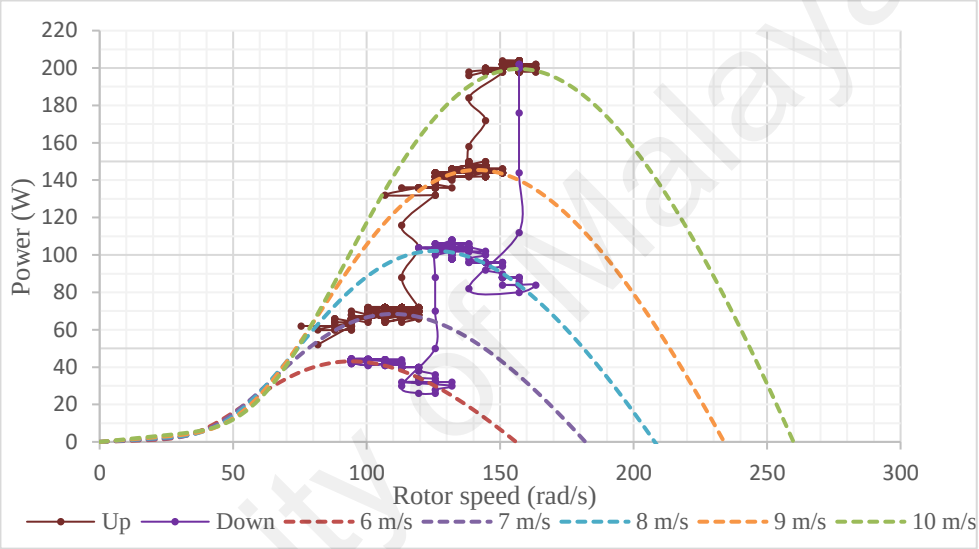

Figure 5.17: Experimental result of the P&O based method MPPT.

Table 5.5: PMSG's power for different wind speed.

Wind speed (m/s)	Expected power (W)	Power (W)	% difference
6	43.2	42.7	1.16
7	68.6	69.7	-1.60
8	102.4	102.7	-0.29
9	145.8	144.3	1.02
10	200.0	200.5	-0.25

Table 5.6: PMSG's speed for different wind speed.

Wind speed (m/s)	Expected speed (rad/s)	Speed (rad/s)	% difference
6	94.248	98.341	-4.34
7	109.956	111.919	-1.78
8	125.664	131.006	-4.25
9	141.372	141.607	-0.17
10	157.080	155.633	0.92

University of Malaya

A drastic change of wind speed was also applied to further examine the MPPT and LUT-MPDTC response. There was a sudden change of the control variables can be clearly seen in Figure 5.18(a) to (c) during the instant change of the wind speed. Nevertheless, the P&O based MPPT was able to cause them to converge back to their corresponding reference value. The tracking of the optimum operation was fast as the time took approximated 43 s during the abrupt change of wind speed applied at the time, t = 177 s.

Throughout the electrical test with the wind turbine emulator, it confirmed that the proposed hybrid LUT-MPDTC worked well at both increasing and reducing wind speeds. The adopted P&O based MPPT guaranteed the guide-vanes integrated exhaust air turbine always operates close to its optimum point for maximum power generation.

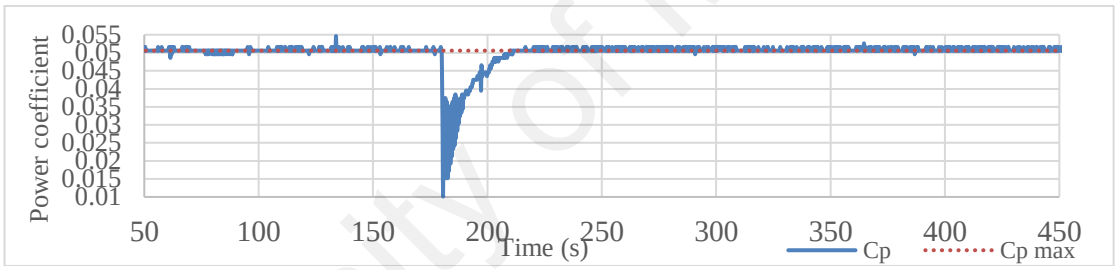

(a)

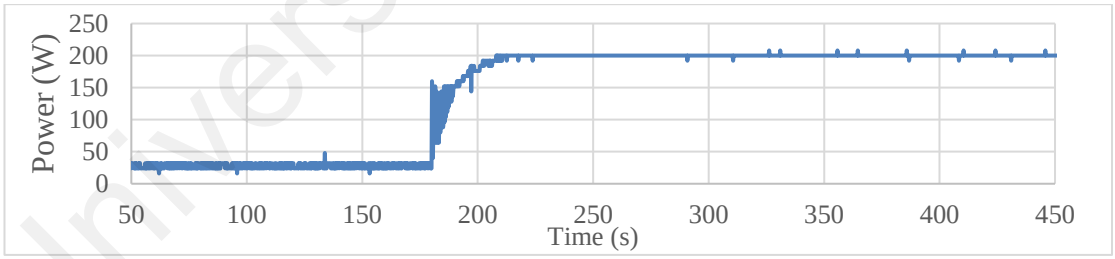

(b)

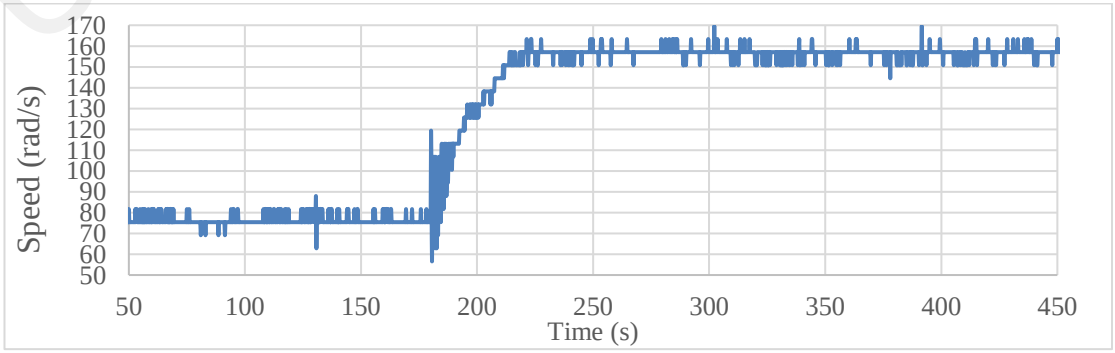

(c)

Figure 5.18: Generated speed when abrupt wind speed change from 5 m/s to 10 m/s. (a) Power coefficient, (b) Power, (c) Speed.

University of Malaya

5.7 Summary

This chapter presented the hybrid LUT-MPDTC of a PMSG based on Vienna rectifier. Simulation and experimental results proved that the proposed control scheme allowed online optimization and fast control of the torque and stator flux for the PMSG while maintaining a balanced DC-link voltage. The use of the LUT reduced the computational burden of the MPDTC, but preserved the effectiveness of the control method. By comparing with the existing LUT-DTC, the hybrid LUT-MPDTC method was found to be more superior.

Furthermore, a lab scale wind turbine emulator, developed based on the model of the guide-vanes integrated exhaust air turbine studied in Chapter 3 was used to optimize the power extraction from the WECS using the developed DTC controller. By using a P&O based MPPT method, maximum power was generated from the wind turbine, as shown by the experimental result. The utilization of P&O based MPPT method with the LUT-MPDTC demonstrated the feasibility and the effectiveness of power optimization using electrical approach.

University of Malaya

CHAPTER 6: CONCLUSION

6.1 Conclusion

In this thesis, the power optimization control of an exhaust air turbine generator using both mechanical and electrical approaches had been explored. In Chapter 3, the power optimization by the means of mechanical approach was detailed. A small-scale model of the guide-vanes integrated exhaust air wind turbine generator was fabricated and used for the experimental verification. Through the experimental results and DMST analysis, it was found that the best configurations for the middle guide-vane is located at 160 mm at 80^{o} and the side guide-vane has to be fixed at 90^{o}. With the presence of guide-vanes, the intake air speed of the cooling tower was found to have improved with lesser fan power consumption. In terms of wind turbine performance, the guide-vanes integration can be effectively improved the turbine's output power as compared to the original exhaust air turbine generator. Both theoretical calculations and experimental data demonstrated good agreement in terms of the trend of electrical power generation.

For the power optimization with electrical approach, DTC of the PMSG using Vienna rectifier was presented. By analyzing the effect of the switching vectors on the control variables based on stator voltage model in *x-y* frame, an improved LUT was proposed. The proposed LUT-DTC gave better control with lower standard deviation on torque and flux ripples as compared to the existing LUT-DTC method. Computation delay compensation using a model-based approach had also been successfully suppressing the ripples generated in both torque and stator flux. In addition to that, the DTC with the improved LUT also outperformed the existing DTC method when there was an unbalanced at the DC-link.

Although the improved LUT-DTC method is more superior than the existing DTC method, its performance is still dependent on the operating conditions due to the rigid vector selection rules governed by the LUT. In order to achieve online optimization

University of Malaya

control of the torque and stator flux for the PMSG regardless of the operating conditions, a hybrid LUT-MPDTC was proposed in Chapter 5. The proposed control scheme allowed fast-tracking of reference torque and stator flux with a balanced DC-link voltage and it was evidenced by the simulation and experimental results. The hybrid utilization of LUT and MPDTC made it less computationally burdensome than a full MPDTC but better than the classical LUT-DTC. With the implementation of the proposed LUT-MPDTC, better PMSG control can be achieved without the development of dynamic lookup table or sophisticated control technique requires.

Finally, to complete the power optimization control, a P&O MPPT controller was implemented together with the developed LUT-MPDTC method. Electrical tests were conducted on the developed turbine emulator to validate the performance of the overall power optimization mechanism using the proposed LUT-MPDTC method. It is found that the LUT-MPDTC was able to extract maximum power from the wind turbine under the varying wind speed condition by using the P&O based MPPT.

In a nutshell, it can be concluded that this thesis has contributed the knowledge on power optimization method for an exhaust air turbine generator system, taking into account both mechanical and electrical approaches. The studies presented in the thesis can provide some foundations towards the actual implementation the exhaust air turbine generator as a sustainable energy and green technology to harvest exhaust air energy that would be otherwise wasted.

University of Malaya

6.2 Future works

There are some potential relates to the guide-vanes integrated wind turbine generator which are yet to be explored. The suggested future works are listed here as below: -

1) Fault tolerance control

   Include a fault tolerance LUT for MPDTC to maintain the controllability and reliability of overall performance. LUT can be built with different failure modes of PMSG for instances, in an event of open circuit or short circuit for one of the phase terminal.

2) Adjustable guide-vane

   To build an adjustable guide-vanes based upon different operation modes of wind turbine, i.e. self-start, optimization, and over-spinning. The guide-vanes angle can be varied depends on the operation mode to assist the operation of the wind turbine.

3) Aero-foil shaped guide-vane

   The guide-vane can be constructed in airfoil shaped as it might be useful in reducing friction of the airflow, therefore further maximizing the wind energy potential. Meanwhile, a more detailed analysis on the effect of guide-vane configuration can be carried out by using Computational Fluid dynamic (CFD) on the variation of the guided airflow with the different guide-vane configuration. The optimum configuration of guide-vane in terms of guide-vane's geometrical shape (width and length of the vane) and its vertical distance from the wind turbine and the cooling tower can be identified by analyzing the simulation of the guided flow field.

4) Power optimization control with a backup energy storage

   Since there may be an interruption of the cooling tower operation, the proposed system may not be capable of sustaining the desired power demand. The overall

University of Malaya

system is suggested to include an energy storage unit with a power management scheme.

5) Energy-saving cooling tower

   A new type of cooling tower which is embedded with the power optimization and energy saving feature could be introduced by the cooling tower manufacturer.

University of Malaya

REFERENCES

Abdullah, M. A., Yatim, A. H. M., Tan, C. W., & Saidur, R. (2012). A review of maximum power point tracking algorithms for wind energy systems. *Renewable and Sustainable Energy Reviews, 16*(5), 3220-3227.

After deadly floods, engineers urge focus on climate change. (2017, November 27). *Malay Mail Online.* . Retrieved from http://www.themalaymailonline.com/malaysia/article/after-deadly-floods-engineers-urge-focus-on-climate-change#CSx4pSwRmbVvzvjp.97

Ahmad, S., Kadir, M. Z. A. A., & Shafie, S. (2011). Current perspective of the renewable energy development in Malaysia. *Renewable and Sustainable Energy Reviews, 15*(2), 897-904.

Akwa, J. V., Vielmo, H. A., & Petry, A. P. (2012). A review on the performance of Savonius wind turbines. *Renewable and Sustainable Energy Reviews, 16*(5), 3054-3064.

Alahuhtala, J., Virtakoivu, J., Viitanen, T., Routimo, M., & Tuusa, H. (2007). *Space Vector Modulated and Vector Controlled Vienna I Rectifier with Active Filter Function.* Paper presented at the 2007 Power Conversion Conference - Nagoya.

Alexander A.J., Holownia. B. P. (1978). Wind tunnel tests on a Savonius rotor. *Journal of Industrial Aerodynamics, 3*, 343-351.

Ali, R., Daut, I., & Taib, S. (2012). A review on existing and future energy sources for electrical power generation in Malaysia. *Renewable and Sustainable Energy Reviews, 16*(6), 4047-4055.

Altan, B. D., Atılgan, M., & Özdamar, A. (2008). An experimental study on improvement of a Savonius rotor performance with curtaining. *Experimental Thermal and Fluid Science, 32*(8), 1673-1678.

Arifujjaman, M., Iqbal, M. T., & Quaicoe, J. E. (2008). Energy capture by a small wind-energy conversion system. *Applied Energy, 85*(1), 41-51.

University of Malaya

Aslam Bhutta, M. M., Hayat, N., Farooq, A. U., Ali, Z., Jamil, S. R., & Hussain, Z. (2012). Vertical axis wind turbine – A review of various configurations and design techniques. *Renewable and Sustainable Energy Reviews, 16*(4), 1926-1939.

Bahaj, A. S., Myers, L., & James, P. A. B. (2007). Urban energy generation: Influence of micro-wind turbine output on electricity consumption in buildings. *Energy and Buildings, 39*(2), 154-165.

Barakati, S. M., Kazerani, M., & Aplevich, J. D. (2009). Maximum Power Tracking Control for a Wind Turbine System Including a Matrix Converter. *IEEE Transactions on Energy Conversion, 24*(3), 705-713.

Beri, H., & Yao, Y. (2011). Double Multiple Streamtube Model and Numerical Analysis of Vertical Axis Wind Turbine. *Energy and Power Engineering, 3*(03), 262.

Burgos, R., Lai, R., Pei, Y., Wang, F., Boroyevich, D., & Pou, J. (2007). *Space Vector Modulation for Vienna-Type Rectifiers Based on the Equivalence between Two- and Three-Level Converters: A Carrier-Based Implementation.* Paper presented at the 2007 IEEE Power Electronics Specialists Conference.

Burlando, M., Ricci, A., Freda, A., & Repetto, M. P. (2015). Numerical and experimental methods to investigate the behaviour of vertical-axis wind turbines with stators. *Journal of Wind Engineering and Industrial Aerodynamics, 144* (Supplement C), 125-133.

Camporeale, S. M., & Magi, V. (2000). Streamtube model for analysis of vertical axis variable pitch turbine for marine currents energy conversion. *Energy Conversion and Management, 41*(16), 1811-1827.

Carrasco, J. M., Franquelo, L. G., Bialasiewicz, J. T., Galvan, E., Portillo-Guisado, R. C., Prats, M. A. M., . . . Moreno-Alfonso, N. (2006). Power-Electronic Systems for the Grid Integration of Renewable Energy Sources: A Survey. *IEEE Transactions on Industrial Electronics, 53*(4), 1002-1016.

University of Malaya

Chen, H., & Aliprantis, D. C. (2011). Analysis of Squirrel-Cage Induction Generator With Vienna Rectifier for Wind Energy Conversion System. *IEEE Transactions on Energy Conversion, 26*(3), 967-975.

Chen, H., David, N., & Aliprantis, D. C. (2013). Analysis of Permanent-Magnet Synchronous Generator With Vienna Rectifier for Wind Energy Conversion System. *IEEE Transactions on Sustainable Energy, 4*(1), 154-163.

Cheng, M., & Zhu, Y. (2014). The state of the art of wind energy conversion systems and technologies: A review. *Energy Conversion and Management, 88* (Supplement C), 332-347.

Chong, W. T., Fazlizan, A., Poh, S. C., Pan, K. C., & Ping, H. W. (2012). Early development of an innovative building integrated wind, solar and rain water harvester for urban high rise application. *Energy and Buildings, 47*, 201-207.

Chong, W. T., Hew, W. P., Yip, S. Y., Fazlizan, A., Poh, S. C., Tan, C. J., & Ong, H. C. (2014). The experimental study on the wind turbine's guide-vanes and diffuser of an exhaust air energy recovery system integrated with the cooling tower. *Energy Conversion and Management, 87* (Supplement C), 145-155.

Chong, W. T., Muzammil, W. K., Wong, K. H., Wang, C. T., Gwani, M., Chu, Y. J., & Poh, S. C. (2017). Cross axis wind turbine: Pushing the limit of wind turbine technology with complementary design. *Applied Energy, 207*, 78-95.

Chong, W. T., Naghavi, M. S., Poh, S. C., Mahlia, T. M. I., & Pan, K. C. (2011). Techno-economic analysis of a wind–solar hybrid renewable energy system with rainwater collection feature for urban high-rise application. *Applied Energy, 88*(11), 4067-4077.

Chong, W. T., Poh, S. C., Fazlizan, A., Oon, S. & Tiah, C.C. (2011). *Exhaust air and wind energy recovery system for clean energy generation.* Paper presented at the International Conference on Environment and Industrial Innovation, Kuala Lumpur.

University of Malaya

Chong, W. T., Poh, S. C., Fazlizan, A., & Pan, K. C. (2012). Vertical axis wind turbine with omni-directional-guide-vane for urban high-rise buildings. *Journal of Central South University, 19*(3), 727-732.

Chong, W. T., Poh, S. C., Fazlizan, A., Yip, S. Y., Chang, C. K., & Hew, W. P. (2013). Early development of an energy recovery wind turbine generator for exhaust air system. *Applied Energy, 112* (Supplement C), 568-575.

Dalessandro, L., Round, S. D., Drofenik, U., & Kolar, J. W. (2008). Discontinuous Space-Vector Modulation for Three-Level PWM Rectifiers. *IEEE Transactions on Power Electronics, 23*(2), 530-542.

Daly, B. B. (1979). *Woods Practical Guide to Fan Engineering* (2nd ed.). Colchester, England: Woods of Colchester Limited.

Department of Statistical Malaysia (2016). *Current Population Estimates, Malaysia, 2014 to 2016.* Retrieved from https://www.dosm.gov.my/v1/index.php?r=column/ctheme&menu_id=L0pheU43NWJwRWVSZklWdzQ4TlhUUT09&bul_id=OWlxdEVoYlJCS0hUZzJyRUcvZEYxZz09

Fazlizan, A. (2016). *Design and testing of a novel exhaust air energy recovery wind turbine generator.* (Doctoral dissertation, University Malaya). Retrieved from http://studentsrepo.um.edu.my/6405/

Flores-Bahamonde, F., Valderrama-Blavi, H., Martínez-Salamero, L., Maixé-Altés, J., & García, G. (2014). Control of a three-phase AC/DC VIENNA converter based on the sliding mode loss-free resistor approach. *IET Power Electronics, 7*(5), 1073-1082.

Foureaux, N. C., Oliveira, J. H., De-Oliveira, F. D., Filho, B. d. J. C., & De-Faria, R. S. (2015). Command Generation for Wide-Range Operation of Hysteresis-Controlled Vienna Rectifiers. *IEEE Transactions on Industry Applications, 51*(3), 2373-2380.

University of Malaya

Friedli, T., Hartmann, M., & Kolar, J. W. (2014). The Essence of Three-Phase PFC Rectifier Systems - Part II. *IEEE Transactions on Power Electronics, 29*(2), 543-560.

Geurts B.M, Simao Ferreira, C., Van Bussel, G. J. W. (2010). *Aerodynamic Analysis of a Vertical Axis Wind Turbine in a Diffuser*. Paper presented at the 3rd EWEA Conference-Torque 2010: The Science of making Torque from Wind, Heraklion, Crete, Greece.

Geyer, T., Papafotiou, G., & Morari, M. (2009). Model Predictive Direct Torque Control, Part I: Concept, Algorithm, and Analysis. *IEEE Transactions on Industrial Electronics, 56*(6), 1894-1905.

Gitano-Briggs, H. (2010). *Small Wind Turbine Power Controllers, Wind Power* Retrieved from https://www.intechopen.com/books/wind-power/small-wind-turbine-power-controllers

Golecha, K., Eldho, T. I., & Prabhu, S. V. (2011). Influence of the deflector plate on the performance of modified Savonius water turbine. *Applied Energy, 88*(9), 3207-3217.

Hang, L., Zhang, M., Li, B., Huang, L., & Liu, S. (2013). Space vector modulation strategy for VIENNA rectifier and load unbalanced ability. *IET Power Electronics, 6*(7), 1399-1405.

Hansen, A. D., & Hansen, L. H. (2007). Wind turbine concept market penetration over 10 years (1995–2004). *Wind Energy, 10*(1), 81-97.

Hansen, A. D., Iov, F., Blaabjerg, F., & Hansen, L. H. (2004). Review of Contemporary Wind Turbine Concepts and Their Market Penetration. *Wind Engineering, 28*(3), 247-263.

Hepperle, M. (2008). Aerodynamics of Model Aircraft: MH Airfoils. Retrieved from http://www.mh-aerotools.de/airfoils/mh114koo.htm

University of Malaya

Herrman, D. D. (1962). Field tests of fan performance on induced draft cooling towers. *Cooling Tower Institute*.

Hong, Y. Y., Lu, S. D., & Chiou, C. S. (2009). MPPT for PM wind generator using gradient approximation. *Energy Conversion and Management, 50*(1), 82-89.

Hu, J., & Zhu, Z. Q. (2011). Investigation on Switching Patterns of Direct Power Control Strategies for Grid-Connected DC-AC Converters Based on Power Variation Rates. *IEEE Transactions on Power Electronics, 26*(12), 3582-3598.

Hu, K. W., & Liaw, C. M. (2013). *Establishment of an IPMSG system with Vienna SMR and its applications to microgrids.* Paper presented at the IECON 2013 - 39th Annual Conference of the IEEE Industrial Electronics Society.

Hu, K. W., & Liaw, C. M. (2015a). Development of a Wind Interior Permanent-Magnet Synchronous Generator-Based Microgrid and Its Operation Control. *IEEE Transactions on Power Electronics, 30*(9), 4973-4985.

Hu, K. W., & Liaw, C. M. (2015b). Position sensorless surface-mounted permanent-magnet synchronous generator and its application to power DC microgrid. *IET Power Electronics, 8*(9), 1636-1650.

Islam, M., Ting, D. S. K., & Fartaj, A. (2008). Aerodynamic models for Darrieus-type straight-bladed vertical axis wind turbines. *Renewable and Sustainable Energy Reviews, 12*(4), 1087-1109.

Jeong, H. M., Chung, H. S., Bae, K. Y., Kim, S. H., & Shin, Y. S. (2005). Water cooling characteristics in an enclosed vacuum tank by water driven ejector. *Journal of mechanical science and technology, 19*(1), 164-172.

Johnson, M. H., & Aliprantis, D. C. (2014). *Analysis and control of PMSG-based wind turbine with Vienna rectifier near current zero crossings.* Paper presented at the 2014 Power and Energy Conference at Illinois (PECI).

University of Malaya

Jose Rodriguez, P. C. (2012). *Predictive Control of Power Converters and Electrical Drives*. UK: John Wiley & Sons, Ltd, IEEE Press.

Joseph, G., Foreman, J. C., & McIntyre, M. L. (2012). *A variable duty cycle Maximum Power Point Tracking algorithm for Wind Energy Conversion Systems.* Paper presented at the Power Electronics and Machines in Wind Applications (PEMWA), 2012 IEEE.

Justo, J. J., Mwasilu, F., Kim, E. K., Kim, J., Choi, H. H., & Jung, J. W. (2017). Fuzzy Model Predictive Direct Torque Control of IPMSMs for Electric Vehicle Applications. *IEEE/ASME Transactions on Mechatronics, PP*(99), 1-1.

Kazmierkowski, M. P. (2012). Predictive Control of Power Converters and Electrical Drives [Book News]. *IEEE Industrial Electronics Magazine, 6*(4), 67-68.

Kim, D., & Gharib, M. (2013). Efficiency improvement of straight-bladed vertical-axis wind turbines with an upstream deflector. *Journal of Wind Engineering and Industrial Aerodynamics, 115*(0), 48-52.

Kolar, J. W., Ertl, H., & Zach, F. C. (1996). *Design and experimental investigation of a three-phase high power density high efficiency unity power factor PWM (VIENNA) rectifier employing a novel integrated power semiconductor module.* Paper presented at the Applied Power Electronics Conference and Exposition, 1996. APEC '96. Conference Proceedings 1996., Eleventh Annual.we

Kolar, J. W., & Friedli, T. (2013). The Essence of Three-Phase PFC Rectifier Systems - Part I. *IEEE Transactions on Power Electronics, 28*(1), 176-198.

Kolar, J. W., & Zach, F. C. (1994). *A novel three-phase utility interface minimizing line current harmonics of high-power telecommunications rectifier modules.* Paper presented at the Telecommunications Energy Conference, 1994. INTELEC '94., 16th International.

Kot, R., Rolak, M., & Malinowski, M. (2013). Comparison of maximum peak power tracking algorithms for a small wind turbine. *Mathematics and Computers in Simulation, 91*(0), 29-40.

University of Malaya

Lee, J. S., Bak, Y., Lee, K. B., & Blaabjerg, F. (2016). *MPC-SVM method for Vienna rectifier with PMSG used in Wind Turbine Systems.* Paper presented at the 2016 IEEE Applied Power Electronics Conference and Exposition (APEC).

Lee, J. S., & Lee, K. B. (2016a). A Novel Carrier-Based PWM Method for Vienna Rectifier With a Variable Power Factor. *IEEE Transactions on Industrial Electronics, 63*(1), 3-12.

Lee, J. S., & Lee, K. B. (2016b). Performance Analysis of Carrier-Based Discontinuous PWM Method for Vienna Rectifiers With Neutral-Point Voltage Balance. *IEEE Transactions on Power Electronics, 31*(6), 4075-4084.

Lee, J. S., & Lee, K. B. (2017). Predictive Control of Vienna Rectifiers for PMSG Systems. *IEEE Transactions on Industrial Electronics, 64*(4), 2580-2591.

Li, D., Wang, S., & Yuan, P. (2010). *A Review of Micro Wind Turbines in the Built Environment.* Paper presented at the 2010 Asia-Pacific Power and Energy Engineering Conference.

Li, X., Sun, Y., Wang, H., Su, M., & Shoudao, H. (2017). A Hybrid Control Scheme for Three-Phase Vienna Rectifiers. *IEEE Transactions on Power Electronics, PP*(99), 1-1.

Lie, X., & Cartwright, P. (2006). Direct active and reactive power control of DFIG for wind energy generation. *IEEE Transactions on Energy Conversion, 21*(3), 750-758.

Martin, G., & Roux, J. (2010). *Wind Turbines: Types, Economics and Development*: Nova Science.

Mathapati, S., & Bocker, J. (2013). Analytical and Offline Approach to Select Optimal Hysteresis Bands of DTC for PMSM. *IEEE Transactions on Industrial Electronics, 60*(3), 885-895.

University of Malaya

Maughmer, M.D. & Somers, D. M. (2003). Theoretical Aerodynamic Analyses of Six Airfoils for Use on Small Wind Turbines Airfoils, Inc. Port Matilda, Pennsylvania: National Renewable Energy Laboratory NREL.

Mirecki, A., Roboam, X., & Richardeau, F. (2007). Architecture Complexity and Energy Efficiency of Small Wind Turbines. *Industrial Electronics, IEEE Transactions on, 54*(1), 660-670.

Mohamed, M. H., Janiga, G., Pap, E., & Thévenin, D. (2010). Optimization of Savonius turbines using an obstacle shielding the returning blade. *Renewable Energy, 35*(11), 2618-2626.

Mohamed, M. H., Janiga, G., Pap, E., & Thévenin, D. (2011). Optimal blade shape of a modified Savonius turbine using an obstacle shielding the returning blade. *Energy Conversion and Management, 52*(1), 236-242.

Nasiri, M., Milimonfared, J., & Fathi, S. H. (2014). Modeling, analysis and comparison of TSR and OTC methods for MPPT and power smoothing in permanent magnet synchronous generator-based wind turbines. *Energy Conversion and Management, 86*(0), 892-900.

Novaes Menezes, E. J., Araújo, A. M., & Bouchonneau da Silva, N. S. (2018). A review on wind turbine control and its associated methods. *Journal of Cleaner Production, 174* (Supplement C), 945-953.

Ogawa, T., Yoshida, H., & Yokota, Y. (1989). Development of Rotational Speed Control Systems for a Savonius-Type Wind Turbine. *Journal of Fluids Engineering, 111*(1), 53-58.

Radomski, G. (2007). *Voltage Space Vector Control System of Vienna Rectifier I.* Paper presented at the EUROCON, 2007. The International Conference on Computer as a Tool.

Rajaei, A., Mohamadian, M., & Varjani, A. Y. (2013). Vienna-Rectifier-Based Direct Torque Control of PMSG for Wind Energy Application. *IEEE Transactions on Industrial Electronics, 60*(7), 2919-2929.

University of Malaya

Ren, Y., & Zhu, Z. Q. (2015). Enhancement of Steady-State Performance in Direct-Torque-Controlled Dual Three-Phase Permanent-Magnet Synchronous Machine Drives With Modified Switching Table. *IEEE Transactions on Industrial Electronics, 62*(6), 3338-3350.

Rodriguez, J., Bernet, S., Steimer, P. K., & Lizama, I. E. (2010). A Survey on Neutral-Point-Clamped Inverters. *IEEE Transactions on Industrial Electronics, 57*(7), 2219-2230.

Rodriguez, J., Kazmierkowski, M. P., Espinoza, J. R., Zanchetta, P., Abu-Rub, H., Young, H. A., & Rojas, C. A. (2013). State of the Art of Finite Control Set Model Predictive Control in Power Electronics. *IEEE Transactions on Industrial Informatics, 9*(2), 1003-1016.

Schiffer, H. W. (2016). World Energy Resources 2016. Retrieved from https://www.worldenergy.org/wp-content/uploads/2016/10/World-Energy-Resources-Full-report-2016.10.03.pdf

Shafie, S. M., Mahlia, T. M. I., Masjuki, H. H., & Andriyana, A. (2011). Current energy usage and sustainable energy in Malaysia: A review. *Renewable and Sustainable Energy Reviews, 15*(9), 4370-4377.

Shikha, Bhatti, T. S., & Kothari, D. P. (2003a). *A new vertical axis wind rotor using convergent nozzles.* Paper presented at the Large Engineering Systems Conference on Power Engineering, 2003.

Shikha, Bhatti, T. S., & Kothari, D. P. (2003b). Vertical Axis Wind Rotor with Concentration by Convergent Nozzles. *Wind Engineering, 27*(6), 555-959.

Shikha, Bhatti, T. S., & Kothari, D. P. (2005). Early Development of Modern Vertical and Horizontal Axis Wind Turbines: A Review. *Wind Engineering, 29*(3), 287-299.

University of Malaya

Siami, M., Khaburi, D. A., Rivera, M., & Rodriguez, J. (2017). An Experimental Evaluation of Predictive Current Control and Predictive Torque Control for a PMSM fed by a Matrix Converter. *IEEE Transactions on Industrial Electronics, PP*(99), 1-1.

Stout, C., Islam, S., White, A., Arnott, S., Kollovozi, E., Shaw, M., . . . Bird, B. (2017). Efficiency Improvement of Vertical Axis Wind Turbines with an Upstream Deflector. *Energy Procedia, 118*(Supplement C), 141-148.

Takao, M., Kuma, H., Maeda, T., Kamada, Y., Oki, M., & Minoda, A. (2009). A straight-bladed vertical axis wind turbine with a directed guide vane row - Effect of guide vane geometry on the performance *Journal of Thermal Science, 18*(1), 54-57.

Takao, M., Takita, H., Saito, Y., Maeda, T., Kamada, Y., & Toshimitsu, K. (2009). Experimental Study of a Straight-Bladed Vertical Axis Wind Turbine With a Directed Guide Vane Row. *ASME Conference Proceedings, 2009*(43444), 1093-1099.

Tenaga Nasional (2017). *Pricing and tariffs*. Retrieved from https://www.tnb.com.my/commercial-industrial/pricing-tariffs1

Tenaga Suruhanjaya. (2017). *Peninsular Malaysia electricity supply outlook 2017*. Malaysia.

Tiwari, R., & Babu, N. R. (2016). Recent developments of control strategies for wind energy conversion system. *Renewable and Sustainable Energy Reviews, 66*(Supplement C), 268-285.

Trinh, Q. N., & Lee, H. H. (2010). *Fuzzy Logic Controller for Maximum Power Tracking in PMSG-Based Wind Power Systems.* Paper presented at the Advanced Intelligent Computing Theories and Applications. With Aspects of Artificial Intelligence, Berlin, Heidelberg.

UIUC Airfoil Coordinate Database (2014). UIUC Applied Aerodynamics Group, University of Illinois. Retrieved from http://aerospace.illinois.edu/m-selig/ads/coord_database.html

University of Malaya

Vazquez, S., Rodriguez, J., Rivera, M., Franquelo, L. G., & Norambuena, M. (2017). Model Predictive Control for Power Converters and Drives: Advances and Trends. *IEEE Transactions on Industrial Electronics, 64*(2), 935-947.

Wang, Z., Yuwen, B., Lang, Y., & Cheng, M. (2013). Improvement of Operating Performance for the Wind Farm With a Novel CSC-Type Wind Turbine-SMES Hybrid System. *IEEE Transactions on Power Delivery, 28*(2), 693-703.

Wenxi, Y., Zhengyu, L., Ming, Z., & Zhuang, L. (2014). *A novel SVPWM scheme for Vienna rectifier without current distortion at current zero-crossing point.* Paper presented at the 2014 IEEE 23rd International Symposium on Industrial Electronics (ISIE).

Wenxiang, S., Shengkang, L., Xiaoxin, W., & Yi, R. (2017). An Improved Model Predictive Direct Torque Control for Induction Machine Drives. *JOURNAL OF POWER ELECTRONICS, 17*(3), 674-685.

Wong, K. H., Chong, W. T., Sukiman, N. L., Poh, S. C., Shiah, Y. C., & Wang, C. T. (2017). Performance enhancements on vertical axis wind turbines using flow augmentation systems: A review. *Renewable and Sustainable Energy Reviews, 73* (Supplement C), 904-921.

Xia, C., Wang, S., Wang, Z., & Shi, T. (2016). Direct Torque Control for VSI-PMSMs Using Four-Dimensional Switching-Table. *IEEE Transactions on Power Electronics, 31*(8), 5774-5785.

Zheng, Z. W., Chen, Y. Y., Huo, M. M., & Zhao, B. (2011). An Overview: the Development of Prediction Technology of Wind and Photovoltaic Power Generation. *Energy Procedia, 12*(0), 601-608.

Zhong, L., Rahman, M. F., Hu, W. Y., & Lim, K. W. (1997). Analysis of direct torque control in permanent magnet synchronous motor drives. *IEEE Transactions on Power Electronics, 12*(3), 528-536.

University of Malaya

LIST OF PUBLICATIONS AND PAPERS PRESENTED

Journals:

1) W.T. Chong, W.P. Hew**, S.Y. Yip**, A. Fazlizan, S.C. Poh, C.J. Tan, H.C. Ong The experimental study in the wind turbine's guide-vanes and diffuser of an exhaust air energy recovery system integrated with the cooling tower, Energy Conversion and management, 112 (2013) 601-609.

2) W.T. Chong, **S.Y. Yip**, A. Fazlizan, S.C Poh, W.P. Hew, E.P Tan, T.S. Lim, Design of an exhaust air energy recovery wind turbine generator for energy conservation in commercial buildings, Renewable Energy, 67(2014), 252-256.

3) W.T. Chong, S.C. Poh, A. Fazlizan, **S.Y. Yip**, C.K. Chang, W.P. Hew, Early development of an energy recovery wind turbine generator for exhaust air system, Applied Energy, 112 (2013) 568-575.

4) W.T. Chong, S.C. Poh, A. Fazlizan, **S.Y. Yip**, M.H. Koay, W.P. Hew, Exhaust Air Energy Recovery System for Electrical Power Generation in Future Green Cities, International Journal of Precision Engineering and Manufacturing, 14 (2013) 1029-1035.

Conferences and symposium:

1) "Investigation on the effect of diffuser and guide-vanes on an exhaust air energy recovery turbine for energy conservation", The 2013 International Conference on Advances in Energy Research (ICER 2013), 25-28 August 2013, Coex, Seoul, South Korea.

2) "Design and numerical study of the integration of omni-directional shroud with vertical axis wind turbine", 3rd IET International Conference on Clean Energy and Technology (CEAT 2014), 24th-26th November 2014, Sarawak, Malaysia.

3) "Power optimization model of adjustable guide-vane for an exhaust wind energy recovery system", 2015 IEEE Conference on Control Applications (CCA), 21-23 September 2015, Sydney, NSW, Australia.

4) "Model Predictive Direct Torque Control for Permanent Magnet Synchronous Wind Turbine Generator Using Vienna rectifier." UMPEDAC Postgraduate Research on Energy (PRoE) Symposium, 6 – 7 September 2017, Kuala Lumpur, Malaysia.

University of Malaya